université
PARIS-SACLAY

Cold nuclear matter effects in Drell-Yan process and charmonium production

Thèse de doctorat de l'université Paris-Saclay

École doctorale n° 576, Particules, Hadrons, Energie, Noyau, Instrumentation, Imagerie, Cosmos et Simulation (PHENIICS)
Spécialité de doctorat: Physique
Unité de recherche: Université Paris-Saclay, CEA, Département de Physique Nucléaire, 91191, Gif-sur-Yvette, France
Référent: Faculté des sciences d'Orsay

Thèse présentée et soutenue en visioconférence totale le 30/10/2020 par

Charles-Joseph Naïm

Composition du jury:

Elena Ferreiro Professeure, Universidade de Santiago de Compostela, Spain	Présidente du jury
Ginés Martinez Garcia Directeur de recherche, Subatech (CNRS)	Rapporteur
Emilie Maurice Professeure Assistant, Laboratoire Leprince-Ringuet (Ecole Polytechnique)	Examinatrice
Stefano Panebianco Ingénieur chercheur, CEA/Saclay	Examinateur
Stéphane Peigné Chargé de recherche, Subatech (CNRS)	Examinateur
Ingo Schienbein Maître de Conférences, Université Grenoble Alpes	Rapporteur
François Arleo Chargé de recherche, Laboratoire Leprince-Ringuet (CNRS)	Co-directeur
Stéphane Platchkov Ingénieur chercheur, CEA/Saclay	Directeur

Thèse de doctorat

Le courage, c'est d'aimer la vie et de regarder la mort d'un regard tranquille ; c'est d'aller à l'idéal et de comprendre le réel ; c'est d'agir et de se donner aux grandes causes sans savoir quelle récompense réserve à notre effort l'univers profond, ni s'il lui réserve une récompense. Le courage, c'est de chercher la vérité et de la dire ; c'est de ne pas subir la loi du mensonge triomphant qui passe, et de ne pas faire écho, de notre âme, de notre bouche et de nos mains aux applaudissements imbéciles et aux huées fanatiques.

— Jean Jaurès, « Discours à la Jeunesse », Albi (France), 1903.

Remerciements

Jean Jaurès incarna avec splendeur l'idéal républicain. Baigné par la justice, il chercha continûment à faire jaillir l'espoir d'un monde meilleur. Pacifiste, fédérateur et réformateur, il fut un défenseur omniprésent de la République sociale. La flamme de son héritage demeure toujours veillée par toute la patrie reconnaissante. Voici par les mots de qui j'ai voulu débuter ce manuscrit. La définition du courage qu'il légua à la jeunesse de France en 1903 à Albi constitua une source profonde d'inspiration. Encore aujourd'hui, elle est pour moi l'écho de cet *univers profond* face aux tumultes de l'existence. Alors merci pour ces mots qui ornent *mon jardin*, ils ont été si souvent réconfortants...

Voilà maintenant l'instant le plus difficile, du moins le plus délicat. Comment résumer en quelques lignes l'ensemble des interactions qui m'ont amené aujourd'hui à écrire ces remerciements ? Bien que la motivation soit un moteur indispensable à l'accomplissement des plus vastes projets, elle n'est pas suffisante, loin de là. Les rencontres, parfois sous l'auspice du fabuleux hasard, et les proches en constituent le second moteur. Et je crois que l'idée de m'engager vers la physique me fut donnée par Mme Charliat dont j'ai eu l'honneur de croiser le chemin. Elle fut ma professeure de mathématiques en classe de 4ème au collège St-Joseph de Reims. Une professeure dont on se souvient aisément tant elle marqua le jeune esprit, parfois rêveur, que j'étais. De là, je remercie également M. Kalité, mon professeur de physique de lycée, pour m'avoir poussé au travail et à la rigueur ainsi que Mme Alardet, ma professeure d'anglais, pour sa bienveillance et ses précieux conseils. Le premier aperçu de la recherche en physique me fut donné lors de mon stage de 3ème à l'Institut d'Astrophysique de Paris (IAP). Je remercie donc chaleureusement Elisabeth Vangioni pour m'avoir donné l'opportunité de concrétiser ce qui n'était encore qu'imaginé.

Plus tard, pendant mes premières années à Sorbonne Université (ex-Université Pierre et Marie Curie), j'y ai découvert un lieu où la richesse individuelle nourrit une richesse collective. Un endroit où l'autonomie et la curiosité sont au service de la réussite. Je remercie l'ensemble de l'équipe pédagogique, et en particulier le Professeur Patrick Boissé, pour m'avoir donné la chance de grandir dans un environnement scientifique de très haute qualité.

La présente thèse n'aurait pas pu voir le jour sans ma rencontre en master 1 avec Stéphane Platchkov qui fut par la suite mon co-directeur. Tu as été le premier lien entre la physique des particules et moi : ta patience, ta bienveillance et ta richesse scientifique ont permis à un jeune étudiant de s'orienter vers une thèse de doctorat. Alors merci ! Ta rencontre avec François Arleo,

bien loin d'ici, au Chili, a donné naissance à une superbe collaboration qui nous a tous les trois réunis. Je crois que je ne pouvais pas rêver d'un meilleur encadrement, donc merci de m'avoir donné la possibilité de travailler à vos côtés pendant ces 3 années. Merci à toi François pour m'avoir donné l'opportunité d'apercevoir ton travail au quotidien : tu m'as transmis le sens et l'intuition physique nécessaire à tout physicien. Stéphane, merci à toi, tu m'as appris la rigueur qu'impose une mesure expérimentale. Votre apport complémentaire à ma formation scientifique fut colossal. L'articulation entre l'aspect expérimental et théorique m'a permis d'avoir une vision large et fidèle du métier de physicien. Cette expérience très enrichissante a été nourrie par votre très grande expertise scientifique et surtout votre patience.

Je remercie l'ensemble du jury pour avoir pris le temps de commenter et juger mes travaux de recherche. Ce fut un honneur.

Merci aussi à vous, Fabienne, Yann, Nicole et Damien, pour m'avoir apporté un environnement scientifique au quotidien de très haute qualité.

Thank you also to the entire COMPASS collaboration: working within an international collaboration was much more than an asset, it was structuring both from a human and a scientific point of view! I would like to express my deep appreciation to Professor Wen-Chen Chang, Chia-Yu, Yu-Shiang, Marco, Vincent, Evgenii, Catarina and Bakur: working by your side was exciting!

Rien de tout cela n'aurait été possible sans le CEA. Grâce à qui, j'ai pu réaliser ma thèse dans de parfaites conditions, alors merci à vous Franck, Christophe et Hervé M.. Merci à l'ensemble du département : vous avez chacun d'entre vous participé à l'obtention de ce diplôme. Un profond merci à toi, Danielle : ta bienveillance et ton attention ont été indispensables au bon déroulement de cette thèse. Je ne compte pas le nombre de cafés pris dans ton bureau tant ton écoute fut essentielle. Merci à toi Isabelle, c'est grâce à des gens comme toi qu'on prend plaisir à (re)venir au travail ! Merci aussi à l'École Polytechnique ainsi qu'au LLR pour leurs accueils. Je tiens également à remercier l'Université Paris-Saclay et le Labex P2IO pour leurs soutiens matériels et financiers.

Merci à toi, Marine, pour m'avoir donné l'occasion de travailler à tes côtés pendant les Travaux en Laboratoire. Ton dynamisme, ta gentillesse, ta rigueur et ta pédagogie m'ont beaucoup appris. Merci à toi, Michael, pour ta bienveillance, ta passion pour la physique fut très enrichissante !

Un profond merci à toi, Christopher, pour ta gentillesse, ton courage, ton aide constante et ta bonne humeur permanente. Merci à toi Antoine V. pour toutes ces discussions, ces moments de partage et de rire. Merci Benjamin pour ton écoute et ces cafés. L'humain est au cœur de la pratique scientifique et ces 3 ans à tes côtés me l'ont démontré. Merci à vous, Robin et Florian,

pour toutes ces aventures et ces bières. Merci à vous tous et toutes, Brian, Vladimir, Zoé, Hervé D., Aurore, Medhi, Eve, Noëlie, Pierre et Nancy, pour votre présence !

Une profonde reconnaissance pour toi, Stefano. Ton intelligence scientifique et humaine m'ont touché, je te remercie infiniment pour ta présence dans les moments de doute. Ton regard percutant, sensible et sincère m'a été indispensable.

Merci à toutes les personnes qui m'ont accompagné tout au long de ces 3 années et même bien plus. Leur soutien indéfectible m'a montré combien la vie n'est pas un processus solitaire. Bien au contraire. Rien de tout cela n'aurait été possible sans elles.

Merci à ma famille, ma grand-mère, mes parents, mes frères, Héloïse, Jean-Marc et toutes celles et ceux qui ne sont plus. Vous avez chacun à votre manière participé à ce que je suis devenu. Le temps passe ou plutôt, les choses passent dans le temps et pourtant, votre appui reste permanant malgré *les éclats des vieilles tempêtes*. Merci à mes proches dont la présence quotidienne a été décisive et remarquable. Un incommensurable respect à Antoine R., Kevin et Clémence. Je vous dois tout.

Je ne pouvais pas conclure ces remerciements sans mentionner Quiberon, ces longs instants devant l'océan et son horizon apaisant ; merci pour tous ces moments.

Enfin, un insondable remerciement à cet *univers profond* pour m'avoir donné la possibilité de croiser le chemin de personnes extraordinaires.

Figure 1: Côte Sauvage de la presqu'île de Quiberon .

Divisant la hauteur d'un arbre incertain, un invisible oiseau s'ingéniait à faire trouver la journée courte, explorait d'une note prolongée la solitude environnante, mais il recevait d'elle une réplique si unanime, un choc en retour si redoublé de silence et d'immobilité qu'on aurait dit qu'il venait d'arrêter pour toujours l'instant qu'il avait cherché à faire passer plus vite.

— Marcel Proust, « Du côté de chez Swann », 1913.

Résumé en français

Introduction

Le phénomène de perte d'énergie des quarks et des gluons se propageant dans un milieu en interaction forte a été mis en évidence pour la première fois dans les collisions d'ions lourds par les expériences auprès des accélérateurs RHIC et LHC. Une autre manière de sonder les propriétés de la matière nucléaire est d'étudier la production de processus durs dans les collisions hadron-noyau. En effet, dans ce cas, le milieu nucléaire est simple : sa densité ainsi que sa taille sont connues. Dans cette thèse, le processus Drell-Yan et la production de J/ψ ont été étudiés à travers une analyse expérimentale et phénoménologique. La collaboration COMPASS au CERN a collecté un nombre significatif d'événements Drell-Yan et J/ψ en utilisant un faisceau de pions négatifs d'énergie égale à 190 GeV sur deux cibles nucléaires ; l'une composée de noyaux légers, l'aluminium (A=27) et l'autre, de noyaux lourds, le tungstène (A=184).

Le processus Drell-Yan décrit l'annilihation entre deux quarks en un photon virtuel : ce processus est purement électromagnétique à l'ordre dominant en théorie des pertubations (voir Fig. 2). Le photon se désintègre par la suite en une paire de leptons, dans notre cas, des muons.
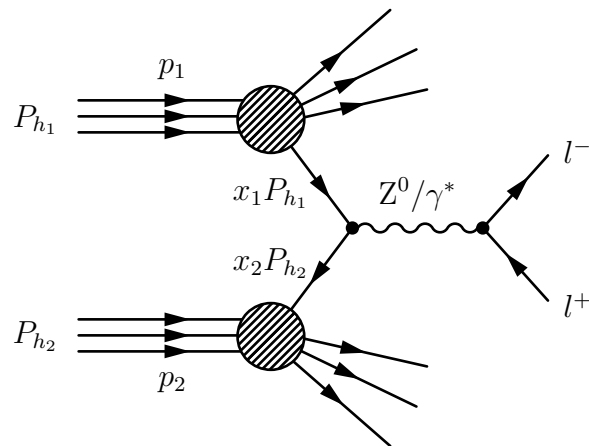

Figure 2: Processus Drell-Yan à l'ordre dominant dans les collisions hadroniques.

En parralèle de ce processus, nous avons également étudié la production de charmonium : un méson composé d'un quark c et d'un antiquark $\bar{c}$. Dans ce processus, l'état initial décrit l'annihilation entre deux partons (quarks ou gluons) en une paire $c\bar{c}$ dans l'état final (voir Fig. 3) s'hadronizant en un méson J/ψ, l'état fondamental du charmonium. Ce dernier se désintégre par la suite en une paire de muons. Contrairement au processus Drell-Yan, la production de

charmonium est un processus purement intéraction forte composé de quarks (ou de gluons) à la fois dans l'état initial et final. La complémentarité de ces deux processus nous renseigne quant à la dépendance de l'état partonique dans l'intéraction avec le milieu nucléaire.
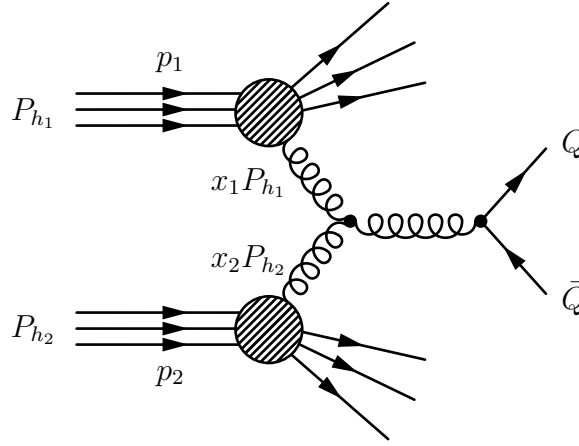

Figure 3: Exemple de production d'une paire $c\bar{c}$ dans les collisions hadroniques.

Partie expérimentale

L'objectif de l'analyse expérimentale est d'extraire le facteur de modification nucléaire, c'est à dire le rapport entre la section efficace calculée dans les collisions pion-tungtène (π^-W) et pion-aluminium (π^-Al). En effet, en choisissant, un noyau lourd, le tungstène, et un noyau léger, l'aluminium, il est possible d'isoler l'effet dû au milieu nucléaire. Cette observable est définie comme suit

$$R_{\pi^-\text{A}}(\text{W/Al}) = \frac{N_{\text{W}}^{\mu^+\mu^-}(x_{\text{F}}, p_\perp)}{\epsilon_{\text{W}} \cdot \mathcal{L}^{\text{W}}} / \frac{N_{\text{Al}}^{\mu^+\mu^-}(x_{\text{F}}, p_\perp)}{\epsilon_{\text{Al}} \cdot \mathcal{L}^{\text{Al}}}, \tag{1}$$

avec $N^{\mu^+\mu^-}(x_{\text{F}}, p_\perp)$ le nombre d'événements dimuons dans le *bin* $(x_{\text{F}}, p_\perp)$ et ϵ l'acceptance du spectromètre. La luminosité est définit comme

$$\mathcal{L} = \alpha^i \Phi^0 \times L_{\text{eff}}^i \times \rho^i \times \frac{\mathcal{N}_A}{M^i} \tag{2}$$

où Φ^0 est le flux absolu initial, α^i est la fraction du flux absolu initial à l'entrée de chaque cible i (voir Fig. 4) et ρ^i est la densité de la cible i. Le nombre d'Avogadro et la masse molaire de la cible i sont notés $\mathcal{N}_A$ et M^i respectivement. La luminosité effective pour la cible i est notée L_{eff}^i et s'exprime comme

$$L_{\text{eff}} = \frac{\lambda_{\text{int}}}{\rho} \left[1 - e^{\frac{-\rho L}{\lambda_{\text{int}}}} \right], \tag{3}$$

avec λ_{int}^i la longueur d'intéraction du pion dans la cible i et L sa longueur. Pour chaque processus, il est nécessaire d'extraire le nombre d'événements de dimuons détectés par l'expérience COMPASS. Pour ce faire, une série de coupures cinématiques a été appliquée afin de ne garder
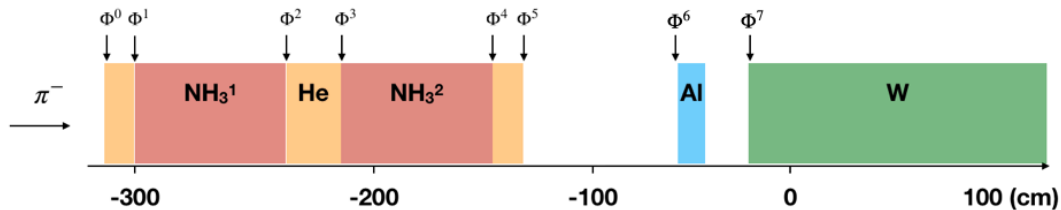
Figure 4: Dispositif expérimental des cibles nucléaires à COMPASS.

que les événements pertinents pour l'analyse. De cette manière, il a été possible de tracer le spectre de masse invariante des dimuons produits à la fois pour la cible d'aluminium et de tungstène. Au total, 9 périodes de données ont été analysées, représentant $\sim 4 \times 10^4$ événements dimuons dans la cible d'aluminium et $\sim 2.3 \times 10^6$ événements dimuons dans la cible de tungstène.

L'extraction des événements J/ψ consiste à réaliser un ajustement du spectre de masse invariante. Pour ce faire, il est nécessaire de décrire de manière correcte le bruit de fond, c'est à dire tous les événements qui ne font pas partis du signal mais qui, malgré tout, sont présents dans les données. Pour cela, l'ensemble des distributions physiques connues participant au spectre de masse invariante ont été simulées à l'aide d'une simulation Monte-Carlo : Open-Charm, Drell-Yan, J/ψ, ψ' et le bruit combinatoire (CB). L'extraction du signal J/ψ a été réalisée en ajustant le spectre de masse invariante avec l'ensemble des composantes physiques issues du Monte-Carlo (méthode «*cocktail*») dans différents *bins* en $x_{\rm F} \in (0, 0.9)$ (7 *bins*) et $p_\perp \in (0, 4)$ GeV (8 *bins*) à la fois pour la cible de W et de Al (voir Fig. 5).

A l'*instar* de l'analyse J/ψ, le nombre d'événements Drell-Yan a été extrait à l'aide de la même méthode *cocktail* sauf qu'il a été décidé d'étudier ce processus dans une région en masse invariante où le bruit de fond est quasi inéexistant. Il a été montré que la région haute masse $M_{\mu^+\mu^-} \gtrsim 4$ GeV est composée à plus de 90% d'événements purs Drell-Yan. Après avoir extrait les événements de chacun des processus J/ψ et Drell-Yan dans les bins cinématiques pertinents, ceux-ci ont été corrigés par une acceptance totale déterminée à l'aide d'une simulation Monte-Carlo comprenant l'acceptance géométrique, l'efficacité de reconstruction, l'efficacité des *triggers* et l'efficacité des détecteurs du spectromètre COMPASS. Enfin, la section efficace dans les collisions π^-W normalisée par la section efficace dans les collisions π^-Al des processus Drell-Yan (en noir) et J/ψ (en bleu) suivant Eq. (1) est montrée en Fig. 6. On observe une dépendance en $x_{\rm F}$ et $p_\perp$ qui dépend du processus. En effet, les données J/ψ montrent une suppression nettement plus importante que les données Drell-Yan dans la cible de tungstène. Les données préliminaires Drell-Yan montrent, quant à eux, un rapport assez plat dans toute la gamme en $x_{\rm F}$ excepté dans le dernier *bin* où une faible suppression peut être observée. En raison des erreurs statistiques et statistiques importantes, ce comportement est compatible avec aucune suppression.
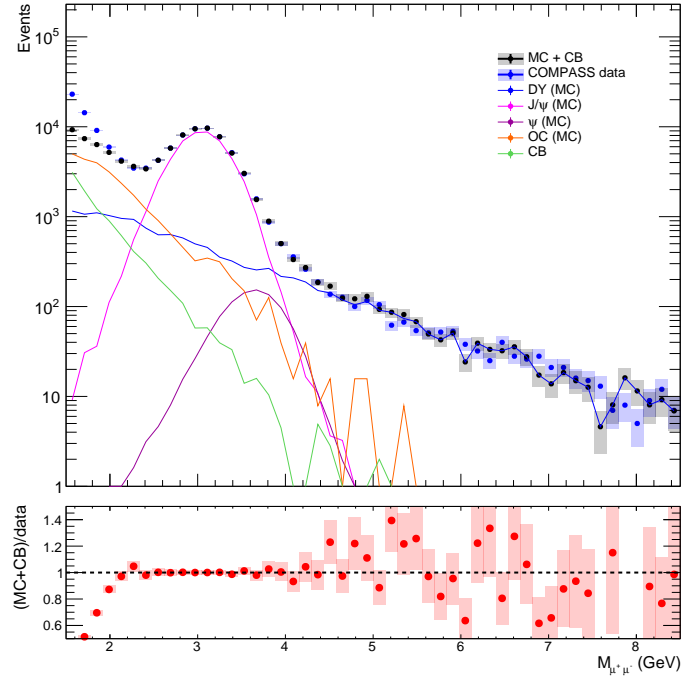
Figure 5: Ajustement du spectre de masse invariante à l'aide des contributions physiques provenant d'une simulation Monte-Carlo.
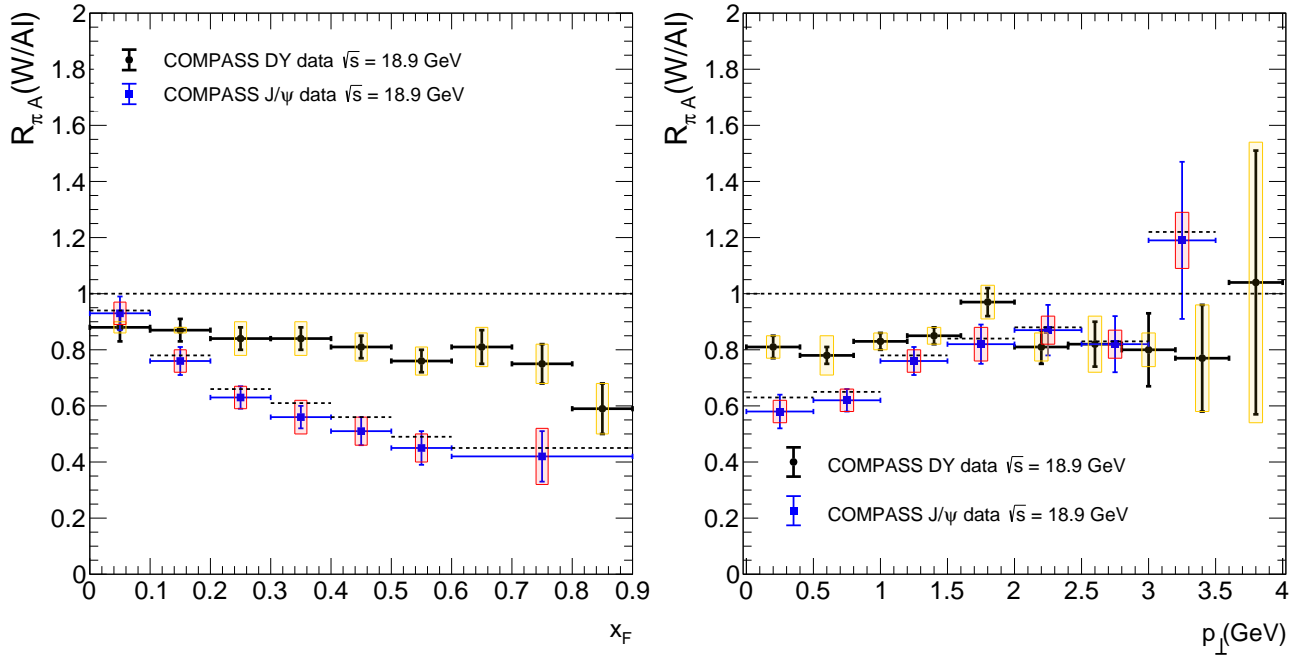

Figure 6: Rapport des sections efficaces dans les collisions $\pi^- W$ et $\pi^- Al$ pour les processus Drell-Yan (en noir) et J/ψ (en bleu) incluant les erreurs statistiques (ligne) et systématiques (rectangle).

Partie phénoménologique

En parallèle des analyses expérimentales, deux autres analyses phénoménologiques ont été réalisées dont l'objectif est (i) d'étudier l'effet de perte d'énergie initiale dans les données Drell-Yan [1] et

(ii) d'extraire une valeur précise du coefficient de transport (noté $\hat{q}_0$) en analysant l'ensemble des données $\Delta p_\perp^2$ [1] des processus Drell-Yan et J/ψ existantes [2].

L'analyse des données Drell-Yan aux énergies du SPS dans les collisions proton-noyau (pA) et pion-noyau (πA) a été réalisée afin de mettre en évidence le phénomène de perte d'énergie initiale d'un quark dans la matière nucléaire froide : l'effet Landau-Pomeranchuk-Migdal (LPM). Le rapport préliminaire entre la section efficace Drell-Yan dans les collisions proton-tungstène (pW) et proton-carbone (pC) en fonction de x_F de l'expérience E906/SeaQuest ($E_{faisceau}$ = 120 GeV) montre une suppression pour tout x_F (Fig. 7 à gauche). Ces données préliminaires indiquent un désaccord net avec l'effet des Fonctions de Distribution de Partons (PDF) nucléaires (en bleu). *A contrario*, le modèle de perte d'énergie (en rose) montre un accord qualitatif. C'est la première fois que l'effet de perte d'énergie initiale est aussi clairement mis en évidence dans des données Drell-Yan dans les collisions proton-noyau. Par ailleurs, l'analyse du rapport entre la section efficace Drell-Yan dans les collisions proton-tungstène (pW) et proton-beryllium (pBe) de l'expérience E866/NuSea ($E_{faisceau}$ = 800 GeV) démontre qu'à plus haute énergie, l'effet de perte d'énergie initiale devient négligeable excepté à grand $x_F \sim 0.9$ (Fig. 7 à droite).

Enfin, l'analyse globale des données $\Delta p_\perp^2$ des processus Drell-Yan et J/ψ en collisions pion-noyau
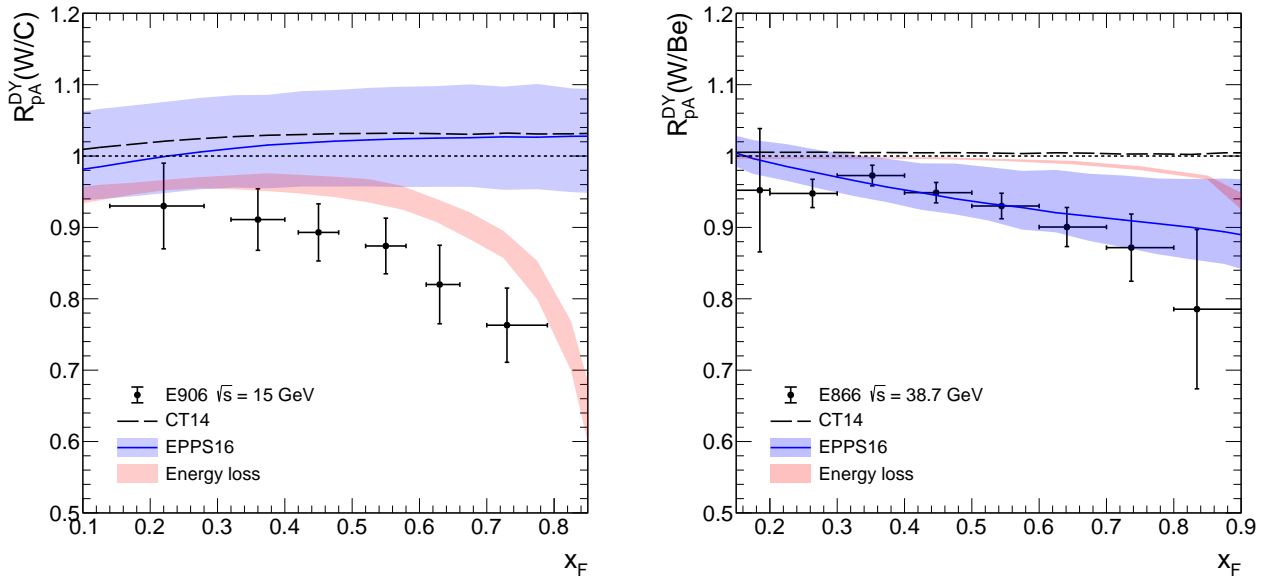

Figure 7: La section efficace Drell-Yan dans les collisions proton-tungstène (pW) normalisée par la section efficace dans les collisions proton-carbone (pC) pour l'expérience E906 (à gauche) et proton-bérillium (pBe) pour l'expérience E866 (à droite) en fonction de x_F. Les calculs théoriques utilisant la PDF nucléaire EPPS16 (noté EPPS16), l'effet d'isospin (noté CT14) et la perte d'énergie initiale (noté Energy loss) sont montrés avec une bande bleu, une ligne en pontillée et une bande rose respectivement.

et proton-noyau des énergies du SPS au LHC a été réalisée. A partir d'hypothèses simples

---

[1] $\Delta p_\perp^2 = \left\langle p_\perp^2 \right\rangle_{hA} - \left\langle p_\perp^2 \right\rangle_{hp}$.

concernant les facteurs de couleur des processus en jeu, la taille des noyaux et la pente de $xG(x)$, une extraction précise du coefficient de transport de la matière nucléaire froide $\hat{q}_0$ pour chaque expérience est montrée en Fig. 8. L'extraction du coefficient de transport réalisée est compatible avec les études de pertes d'énergies radiatives [3, 4, 1]. Les résultats préliminaires
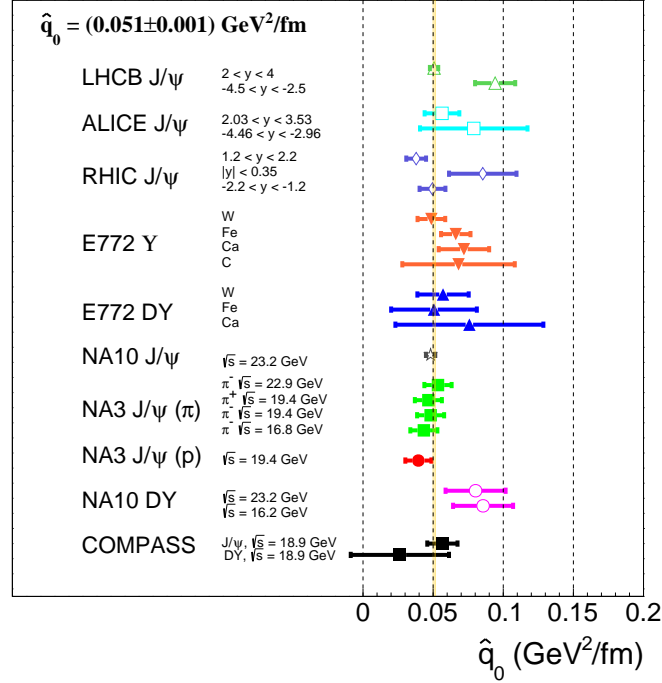

Figure 8: Extraction du coefficient de transport $\hat{q}_0$ à l'aide des données Drell-Yan, J/ψ et Υ en collisions hadron-noyau.

de l'expérience COMPASS présentés dans cette thèse ont également été comparés et montrent un accord remarquable avec les autres expériences.

Conclusion

Les différentes étapes d'analyse, de l'extraction des données aux simulations Monte-Carlo, des processus Drell-Yan et J/ψ à COMPASS dans les collisions $\pi^- A$ sont décrites de manière précise dans cette thèse. Les résultats préliminaires du rapport des sections efficaces $\pi^- W$ et $\pi^- Al$ en fonction de x_F et $p_\perp$ montrent une dépendance nucléaire différente en fonction du processus.

Par ailleurs, l'analyse des pertes d'énergie radiative initiales dans le processus Drell-Yan permet de mettre en évidence pour la première fois sans ambiguité un désaccord entre l'effet de PDFs nucléaires et les données préliminaires de l'expérience E906/SeaQuest. Cette étude montre que la perte d'énergie initiale joue un rôle clef dans l'interprétation des données Drell-Yan aux énergies du SPS dans les collisions hadron-noyau. Enfin, l'analyse globale de l'effet de *broadening* permet d'extraire avec précision le coefficient de transport $\hat{q}_0$ de la matière nucléaire froide montrant un accord remarquable avec les données utilisées. La valeur du coefficient de transport obtenue est compatible avec les précédentes études. Les données préliminaires de l'expérience COMPASS présentent également un très bon accord avec cette extraction.

Contents

List of Figures

1

Dilepton production in hadron-hadron collisions

Contents

1.1 Introduction

1.1.1 Historical remarks

In 1970, a group working at the Alternating-gradient Synchrotron (AGS) at Brookhaven National Laboratory (BNL) proposed to study the massive dimuon pair production in hadronic collisions using a proton beam on uranium (U) target, $pU \rightarrow \mu^+\mu^- + X$ at $E_{\text{beam}} = 22$ to 29.5 GeV

[5]. The differential cross section measured was found to follow a simple power law as a function of the dimuon mass like [6]

$$\frac{\mathrm{d}\sigma}{\mathrm{d}M} \approx \frac{10^{-32}}{M_{\mu^+\mu^-}^5} \mathrm{cm}^2 / \left(\mathrm{GeV}/c^2\right). \tag{1.1}$$

A few months earlier that same year, Sidney Drell and Tung-Mao Yan [7] introduced a formalism based on the newly proposed parton model (Feynman, 1969 [8]). This formalism describes the production of a virtual photon decaying into two leptons in hadron-hadron collisions. The data were then compatible with the predicted continuum. This process is now known as the Drell-Yan process.

On the other hand, in addition to the presence of this continuum, the collected data did not exhibit a resonant structure but a shoulder around $M \sim 3$ GeV. The latter was interpreted as being a phase space effect. It was probably due to a bad mass resolution due to the thickness of the uranium target.[1] Few years later, in November 1974, new data in proton-beryllium (Be) collisions, pBe $\rightarrow e^+e^- + X$, using a proton beam with $E_{\mathrm{beam}} = 30$ GeV highlighted a resonance state in the e^+e^- invariant mass spectrum in the same mass region $M \sim 3$ GeV [9]. The lack of dilepton continuum observed was therefore inconsistent with the Drell-Yan cross section calculation and more generally with the parton model. This discovery was independently discovered by the same observation in e^+e^- collisions at the Stanford Linear Accelerator Center (SLAC) [10]. This major discovery was called the November revolution.[2]

Later, this particle was identified as a bound state composed by a charm (c) and an anti-charm quark ($\bar{c}$) [12]. Since, it has been called J/ψ meson, the ground state of the charmonium meson, with $m_{J/\psi} \approx 3.091$ GeV. The first excited state, ψ', was discovered some time after in the same year in e^+e^- collisions with $m_{\psi'} \approx 3.695$ GeV at SLAC [13]. In the rest of this chapter, the formalism to describe the Drell-Yan and charmonium productions in hadron-proton collisions is introduced. I will expose their interest but also the questions which are still under study.

1.1.2 Parton Model

In the Breit frame or *infinite momentum frame*[3], where the partons are considered free in the hadrons i.e. $Q^2 \rightarrow \infty$, the longitudinal momentum fraction x is defined as [14]

$$\mathrm{p}_{\mathrm{parton}} = x\mathrm{P}_{\mathrm{hadron}}, \tag{1.2}$$

---

[1]When the pair of muons is produced, it crosses a length of the target. The muons lose energy, proportionally to the atomic number of the target, due to elastic collisions. It is therefore difficult to precisely reconstruct the energy of the pair of muons from the hard process. Due to this uncertainty, the energy resolution can be degraded and therefore attenuate the expected peak resulting from the disintegration of a bound nuclear state. I will return to this point in detail later in this thesis.

[2]Bjorken said then of this revolution [11]: "The November revolution just set everything in motion toward the standard model that we have now."

[3]Where the hadron mass can be neglected in the collision with $E_h \gg m_h$. In addition, the parton transverse momentum component according to the direction of propagation of the hadron is considered negligible.
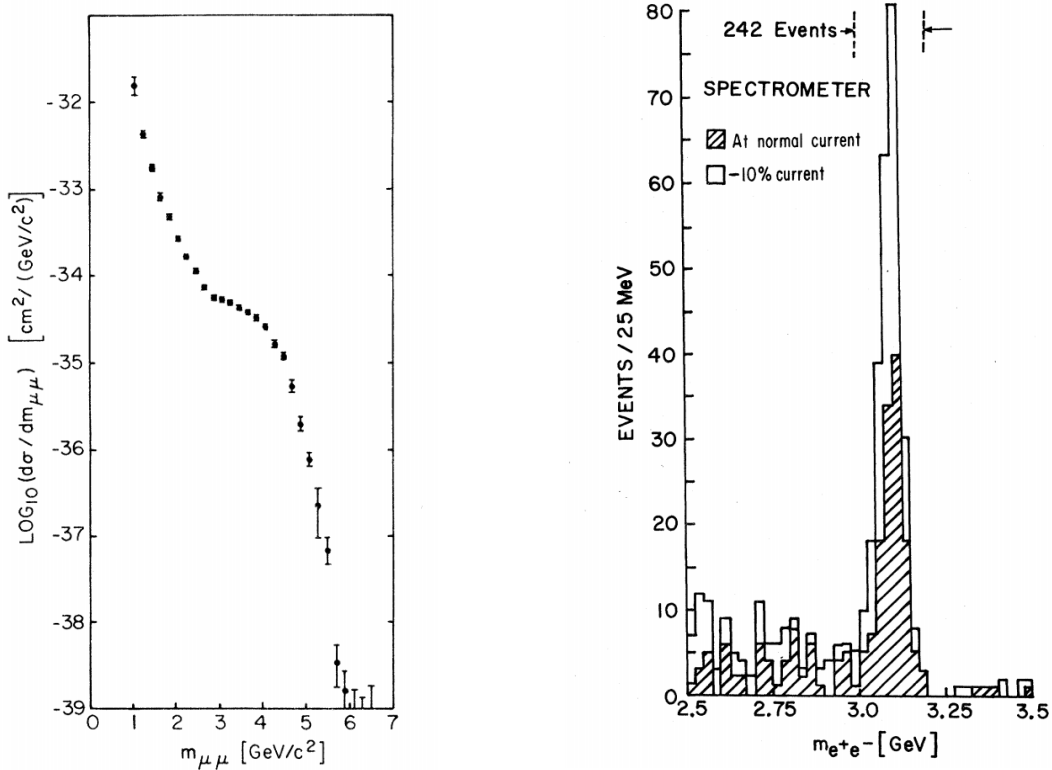
Figure 1.1: Differential cross section as a function of dimuon mass in proton-uranium collisions at $E_{\text{beam}} = 29.5$ GeV from the experimental alternating-gradient synchrotron (AGS) at Brookhaven National Laboratory (BNL) published in 1970 [6] (left panel). Number of events as a function of e^+e^- mass in proton-beryllium collisions published in 1974 [9] (right panel).

where p_{parton} is the four-momentum of the parton in the hadron, P_{hadron} is the four-momentum of the hadron and x, the fraction of momentum carried by the parton inside the hadron and defined in the $0 < x \leq 1$ interval. The partons inside the hadron interact between themselves by soft gluons exchange. This dynamic of the interaction creates a momentum distribution for each parton encoded in the Parton Distribution Function (PDF) directly sensitive to x-Bjorken variable and defined as $f_i(x)\delta x$, i.e. the probability to find a parton with a flavour i with a longitudinal momentum in $(x, x + \delta x)$.

1.1.3   Running coupling constant

Hadronic collisions are relevant to access the hadronic structure via the PDF describing the momentum distribution of partons (quarks and gluons) inside the hadrons. In a hard process, i.e. when the scattering scale $Q \gg \Lambda_{\text{QCD}} \sim 0.2$ GeV, where Λ_{QCD} is the Quantum ChromoDynamics (QCD) scale, the strong coupling constant (α_s) is considered in the asymptotic regime. In this regime, when $\alpha_s(Q^2 \to \infty) \to 0$, the partons inside the hadron are considered free [15, 16]. In contrast at low scale, when $Q^2 \sim 1$ GeV^2, $\alpha_s \gg 1$, the QCD perturbation theory cannot be used. The partons are captured in the hadron, this regime is called confinement. The strong
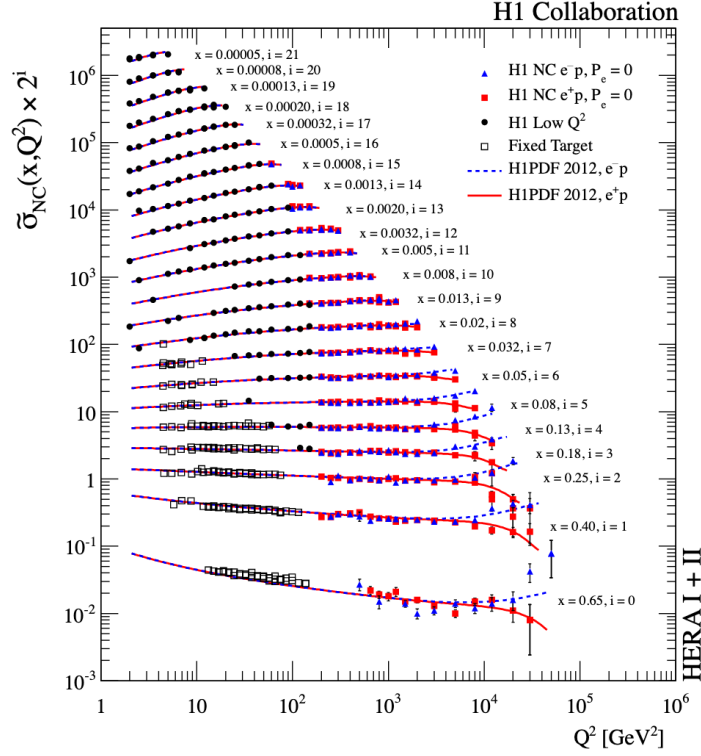
Figure 1.2: Differential cross section for neutral current $e^{\pm}p \to e^{\pm}X$ as a function of Q^2 (GeV^2) from the H1 collaboration [17].

coupling constant α_s, which characterises the interactions between quarks and gluons, depends on the energy scale Q and can be expressed at leading order (LO) as

$$\alpha_{\mathrm{S}}\left(Q^2\right) = \frac{12\pi}{(33 - 2N_f)\ln\frac{Q^2}{\Lambda_{\mathrm{QCD}}^2}}, \tag{1.3}$$

where N_f is the number of quarks flavour.

1.1.4 QCD improved Parton Model

1.1.4.a Scaling violation of structure function in Deep inelastic scattering (DIS)

In the parton model, the partons are considered free. But in QCD, the value of α_s is not zero when $Q \gg \Lambda_{\mathrm{QCD}}$. The perturbative QCD can be applied. The H1 collaboration collected inclusive deep inelastic scattering data allowing for probing the proton structure ($ep \to eX$, $ep \to \nu X$[4]) using an electron-proton collider at $E_{\mathrm{beam}}^{e^{\pm}} = 27.6$ GeV and $E_{\mathrm{beam}}^p = 920$ GeV covering a large Q^2 and x domain, from 60 to 50000 GeV^2 and from $x = 0.00005$ to $x = 0.65$ respectively [17]. In Fig. 1.2, the data show the Q^2 and x dependence of the proton structure. The structure function $F_2(x) = x\sum_q e_q^2 q(x)$ depends weakly on Q^2 for intermediate values of

---

[4]$ep \to eX$ and $ep \to \nu X$ processes describe a diffusion of a lepton on a proton by exchanging a virtual photon and a W boson respectively.

$x \sim 10^{-1}$. For both large and small x values, a clear Q^2 dependence is observed highlighting a scaling violation in the proton structure. This observation leads to the conclusion that the structure functions do not only depend on x but also on the energy scale Q at which it is probed. The dynamics of the evolution as a function of Q^2 of the hadronic structure[5] lies in the interaction of quarks and gluons between them, via the gluons exchange. In the next section, the perturbative QCD corrections will be introduced allowing to predict the scale evolution the structure functions and more generally of the PDF.

1.1.5 Perturbative QCD corrections

In hadron-hadron collisions, the hard partonic cross section $\hat{\sigma}_{ij}$ has a perturbative expansion in α_s such as [18]

$$\sigma(\mathrm{h_1 h_2}) = \sum_{n=0}^{\infty} \alpha_s^n \left(\mu_r^2\right) \sum_{i,j} \int dx_1 dx_2 f_i\left(x_1, \mu_f^2\right) f_j\left(x_2, \mu_f^2\right) \hat{\sigma}_{ij}^{(n)}\left(x_1 x_2 s, \mu_r^2, \mu_f^2\right) \qquad (1.4)$$

where x_1 and x_2 are the Bjorken variables of the hadrons. The $\hat{\sigma}_{ij}$ partonic cross section depends on a non-physical parameter: the renormalisation scale μ_r. This scale is linked to the energy scale which characterises the physical process. Mathematically, it is possible to regularize Ultra-Violet (UV) divergences typically from the parton loop correction when parton momenta $k \to \infty$. The factorisation scale μ_f enables to separate PDFs from the hard partonic cross section, i.e. to separate the long-distance and short-distance physics. This scale is introduced in order to cancel out another type of divergences: InfraRed (IR) divergences i.e. when momenta become soft $k \to 0$. In a cross section calculation, it is generally common to choose a common value for the scales $\mu_r^2 \approx \mu_f^2 \approx Q^2$ to avoid the appearance of large logarithms terms $\ln(Q/\mu) \ll 1$. To estimate an uncertainty on the perturbative calculation, the scales are usually varied between $(\mu_r^2, \mu_f^2) \in (Q^2/4, 4Q^2)$. The expansion in α_s of $\hat{\sigma}_{ij}^{(n)}$ takes into account the QCD corrections with respect to the LO $\hat{\sigma}_{ij}^{(0)}$ cross section. These QCD corrections will be detailed more precisely in the Drell-Yan process in Sec. 1.1.5.

1.1.5.a DGLAP equations

The Q^2 dependence of the PDFs is described by the following DGLAP evolution equations [19, 20],

$$\begin{aligned}
\frac{\mathrm{d}q_i\left(x, Q^2\right)}{\mathrm{d}\ln Q^2} &= \frac{\alpha_s}{2\pi} \int_x^1 \frac{\mathrm{d}x'}{x'} \left[q_i\left(x', Q^2\right) P_{qq}\left(\frac{x}{x'}\right) + g\left(x', Q^2\right) P_{qg}\left(\frac{x}{x'}\right)\right], \\
\frac{\mathrm{d}g\left(x, Q^2\right)}{\mathrm{d}\ln Q^2} &= \frac{\alpha_s}{2\pi} \int_x^1 \frac{\mathrm{d}x'}{x'} \left[q_i\left(x', Q^2\right) P_{gq}\left(\frac{x}{x'}\right) + g\left(x', Q^2\right) P_{gg}\left(\frac{x}{x'}\right)\right]
\end{aligned} \qquad (1.5)$$

where $P_{ij}(x)$ represents the splitting functions, namely, the probability for a parton j (see Fig. 1.3), $q_i(x, Q^2)$ is the quark distribution with the flavour i and $g(x, Q^2)$ is the gluon distribution.

---

[5]$\lambda \sim 1/Q$, where λ is the typical probe wavelength, if $\lambda \ll r_p \sim 1$ fm, it will be possible to access hadronic sub-structures. Consequently, at higher values of Q^2, it is possible to resolve finer detail in hadronic structure.

These splitting functions are calculable in perturbation theory at any order in $\mathcal{O}\left(\alpha_s^n\right)$ (see the 3-loop calculations in [21, 22, 23]). At LO in α_s, these are given by [24]

$$P_{qq}^{(\text{LO})}(z) = \frac{4}{3}\left[\frac{1+z^2}{(1-z)_+} + \frac{3}{2}\delta(1-z)\right],\tag{1.6}$$

$$P_{qg}^{(\text{LO})}(z) = \frac{1}{2}\left[z^2 + (1-z)^2\right],\tag{1.7}$$

$$P_{gq}^{(\text{LO})}(z) = \frac{4}{3}\left[\frac{1+(1-z)^2}{z}\right],\tag{1.8}$$

$$P_{gg}^{(\text{LO})}(z) = 6\left[\frac{z}{(1-z)_+} + \frac{1-z}{z} + z(1-z) + \left(\frac{11}{12} - \frac{N_f}{18}\right)\delta(1-z)\right].\tag{1.9}$$

The plus prescription is defined as (see Eq. (3.2) in [25])

$$[f(x)]_+ \equiv \lim_{\beta \to e}\left\{f(x)\Theta(1-x-\beta) - \delta(1-x-\beta)\int_0^{1-\beta} dz f(z)\right\}.\tag{1.10}$$

The Q^2 evolution of the quarks and gluon PDFs is related by the coupled differential equations
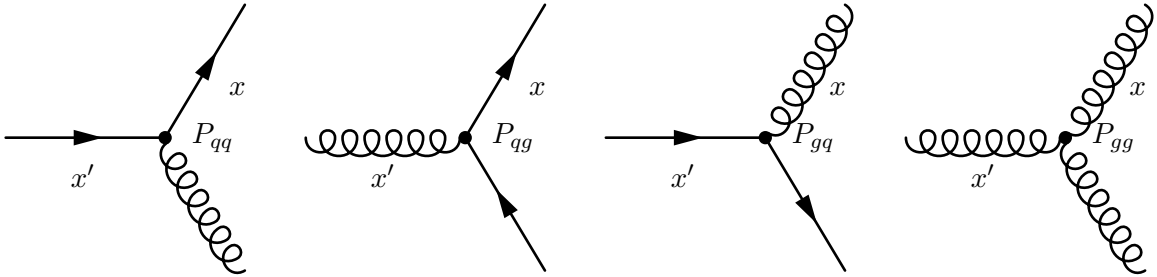
Figure 1.3: Graphical representation of the LO splitting functions P_{qq}, P_{qg}, P_{gq} and P_{gg}.

in Eq. (1.5). Consequently, the information carried by the quarks PDFs at a given x and Q^2 also give an information about the gluon PDF at the same x and Q^2 and *vice versa*.

1.1.6 Parton distribution functions extraction from global fit

DGLAP equations can be numerically solved once the $f_i(x, Q_0^2)$ are given as an input at the starting scale Q_0^2.[6] The PDFs are extracted by performing a global fit of experimental data to determine their shape at a given $Q^2 \gtrsim Q_0^2$. The order in α_s of the extracted PDF will depend on the perturbative development in α_s used to compute the partonic cross section of the hard process and the loop order of the splitting functions. The extraction of the proton and pion PDFs will now be briefly discussed.

---

[6]Typically, the starting scale is defined as $Q_0^2 \simeq 1 - 2 \text{ GeV}^2$ at the limit where the DGLAP evolution equations remains valid.

Proton PDF

Several proton PDFs from global fits are currently available: MMHT2014 [26], CTEQ [27], CT14 [28], NNPDF [29]. These PDFs are highly constrained due to the large amount of data available at the HERA, the Tevatron and LHC colliders. Figure 1.4 shows the proton PDF from CT14 extracted at NLO evaluated at $Q^2 = 10$ GeV^2 and $Q^2 = 10000$ GeV^2 with the error band including all error sets from the global fit. With increasing Q^2, the sea and gluon contributions become important compared to valence quark contributions at small values of x.
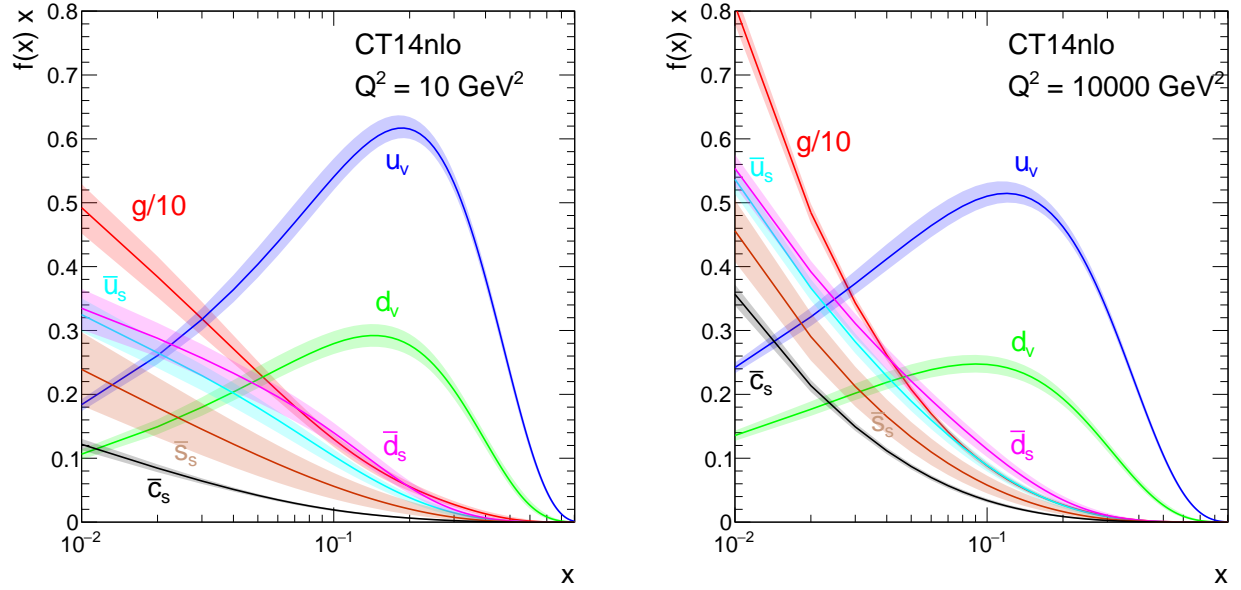
Figure 1.4: Parton distribution functions $xf(x)$ and their associated uncertainties at $Q^2 = 10$ GeV^2 (left) and $Q^2 = 10000$ GeV^2 (right) at NLO using the CT14 parametrization [28].

Pion PDF

The first global fit at LO and NLO of the pion PDF was performed by the SMRS group [30]. They used Drell-Yan data from from NA10 [31], E615 [32] and prompt-photon data from WA70 [33]. The Drell-Yan data are mainly sensitive to the valence distribution, whereas the prompt-photon data probe the gluon distribution.

A second global fit was performed at the same α_s orders by the GRV group [34] and later by the GRSc group [35]. More recently, a global fit including new data from leading neutron production from the HERA experiments [36, 37] was done by the JAM group [38] giving a better constraint in the gluon sector at $x \sim 0.3$. In the π^- PDF, for the valence part, by assuming the SU(2) flavor symmetry

$$\bar{u}_v(x)^{\pi^-} = d_v(x)^{\pi^-}, \tag{1.11}$$

and for the sea part, by assuming the SU(3) flavor symmetry

$$\bar{u}_s(x)^{\pi^-} = u_s(x)^{\pi^-} = \bar{d}_s(x)^{\pi^-} = d_s(x)^{\pi^-} = \bar{s}_s(x)^{\pi^-} = s_s(x)^{\pi^-}. \tag{1.12}$$

Figure 1.5 shows the pion PDF distributions for $\bar{u}_v(x)$, $\bar{u}_s(x)$ and $g(x)$ at $Q^2 = 10$ GeV^2. The pion PDF from the JAM group shows an important reduction of the gluon contribution compared to GRV and SMRS.
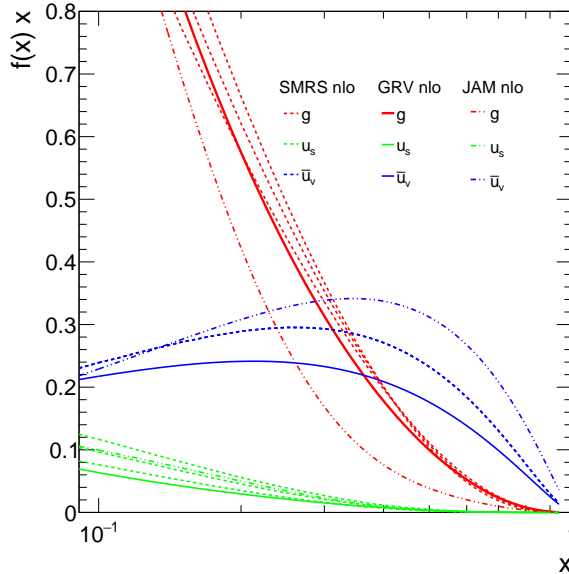
Figure 1.5: Distribution functions of the partons $xf(x)$ for π^- meson at Q$^2 = 10$ GeV^2 at NLO from SMRS [30], GRV [34] and JAM [38] groups.

1.2 Drell-Yan production

1.2.1 Leading order in α_s (LO)

At LO in α_s, the Drell-Yan (DY) partonic cross section $\hat{\sigma}_{q\bar{q}}$ describes the annihilation between a quark and an anti-quark to produce a time-like virtual photon which decays into a lepton pair in the final state, $q\bar{q} \to \gamma^\star \to l^+l^-$ (see Fig. 1.6). The differential partonic cross section reads [39]

$$\frac{\mathrm{d}\hat{\sigma}}{\mathrm{d}M^2}\left(q\bar{q} \to \gamma^\star \to l^-l^+\right) = e_q^2 \frac{4\pi\alpha^2}{3M^2 N_c}\delta\left(x_1 x_2 s - M^2\right), \tag{1.13}$$

where M^2 is the squared lepton invariant mass, $s = (P_{h_1} + P_{h_2})^2$ the center-of-mass energy squared, and e_q, the quark electromagnetic charge e_q and $N_c = 3$, the color factor due to the average over the color initial quarks states. In the hadronic center-of-mass frame, the 4-momenta of the initial state partons coming from the hadrons are defined like

$$p_1 = \frac{\sqrt{s}}{2}\left(x_1, 0, 0, x_1\right), \tag{1.14}$$

$$p_2 = \frac{\sqrt{s}}{2}\left(x_2, 0, 0, -x_2\right) \tag{1.15}$$

with x_1 and x_2 the momentum fractions carried by the parton in hadron h_1 and h_2, respectively. In the hadronic collisions, the partonic cross section in Eq. (1.13) needs to be convoluted with

the PDF of each hadron. The differential cross section of the Drell-Yan process as a function of the dilepton mass M can be written at LO as

$$\frac{\mathrm{d}\sigma}{\mathrm{d}M^2}(\mathrm{h_1h_2})\left(q\bar{q}\to\gamma^\star\to l^-l^+\right) = \sum_{i,j}\int_0^1\mathrm{d}x_1\int_0^1\mathrm{d}x_2\,f_i^{h_1}(x_1)f_j^{h_2}(x_2)\frac{d\hat{\sigma}_{ij}}{dM^2}(x_1,x_2) \quad (1.16)$$

with i,j (with $j=\bar{i}$) are the quark flavours. By multiplying Eq. (1.16) by M^4, the hadronic cross section exhibits a *scaling* as a function of $\tau=\frac{M^2}{s}$,

$$M^4\frac{\mathrm{d}\sigma}{\mathrm{d}M^2}(\mathrm{h_1h_2})\left(q\bar{q}\to\gamma^\star\to e^-e^+\right) = \tau\frac{4\pi\alpha^2}{3N_c}\sum_{i,j}e_i^2\delta_{ij}\int_0^1\mathrm{d}x_1\int_0^1\mathrm{d}x_2\,f_i(x_1)f_j(x_2)\,\delta\left(x_1x_2-\tau\right)$$

$$\equiv \frac{4\pi\alpha^2}{3N_c}F(\tau). \quad (1.17)$$

Note that in this approach, the PDFs are independent from the energy scale at which they are probed: in this Q^2 limit, quarks are point-like. The Drell-Yan cross section at LO depends solely on τ and is therefore totally determined when the squared dilepton mass M^2 and the center-of-the-mass energy squared s are fixed.
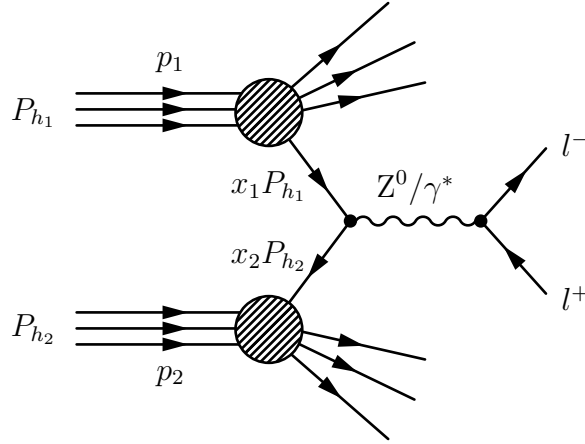
Figure 1.6: Drell-Yan process at leading order (LO).

1.2.2 NLO corrections

The partonic cross section $\hat{\sigma}_{ij}$ at NLO in $\mathcal{O}\left(\alpha^2\alpha_s\right)$ includes real corrections: Compton scattering and annihilation processes, $qg\to q\gamma^\star\to ql^+l^-$ and $q\bar{q}\to g\gamma^\star\to gl^+l^-$. Also virtual corrections, containing self-energy diagrams and vertex corrections, to the Born diagram, $q\bar{q}\to\gamma^\star\to l^+l^-$ are included. The hadronic cross section in Eq. (1.18) can be summed on each partonic channel as

$$\frac{\mathrm{d}\sigma}{\mathrm{d}M^2}(\mathrm{h_1h_2}) = \sum_{i,j}\int_0^1\mathrm{d}x_1\int_0^1\mathrm{d}x_2\,f_i(x_1,\mu_f)f_j(x_2,\mu_f)\frac{\mathrm{d}\hat{\sigma}_{ij}}{\mathrm{d}M^2}(\alpha_s,\mu_r,\mu_f), \quad (1.18)$$

with $\hat{\sigma}_{ij}(\alpha_s)$ which can be written as a perturbative expansion in powers of $\alpha_s\ll 1$,

$$\frac{\mathrm{d}\hat{\sigma}_{ij}}{\mathrm{d}M^2}(\alpha_s) = \frac{\mathrm{d}\hat{\sigma}_{ij}^{\mathrm{LO}}}{\mathrm{d}M^2} + \alpha_s(\mu_r^2)\frac{\mathrm{d}\hat{\sigma}_{ij}^{\mathrm{NLO}}}{\mathrm{d}M^2}(\mu_r^2,\mu_f^2) + O(\alpha_s^2). \quad (1.19)$$

For simplicity, both the normalisation and factorisation scales are set equal to the DY invariant mass[7], $\mu_f^2 = \mu_r^2 = M^2$, where $\Lambda_{\text{QCD}}^2 \ll M^2 \ll s$. The NLO DY cross section $\hat{\sigma}^{\text{NLO}}$ contains two types of divergences that must be taken into account:

- Ultra-violet (UV) divergence from the virtual gluon loop (integration of the infinite momentum) in $q\bar{q} \to \gamma^\star \to l^+l^-$ are treated with the *renormalisation* procedure;

- Infrared (IR) divergence from one soft gluon, i.e. the gluon energy $\omega \to 0$ in the $q\bar{q} \to g\gamma^\star \to l^+l^-$ process.[8] In the general case, the cross section to produce N *soft*, *real* and *independent* gluons by radiation can be written as [40]

$$\mathrm{d}\sigma_N(\alpha_s^N) \propto \int |M_N|^2 \prod_{i=1}^{N} \frac{\mathrm{d}^3 k_i}{2\omega_i} \propto \left(\alpha_s \log^2\right)^N \tag{1.20}$$

where k_i is the soft gluon momentum vector. These terms create double logarithmic divergences. This point will be discussed in Sec. 1.2.2.a.

Let us now describe the differential cross section as a function of the dimuon $p_\perp$ in kinematic regions where $p_\perp \sim M$ and $p_\perp \gg M$.

Transverse momentum dependence in perturbative expansion at fixed order

At LO in α_s, the virtual photon is produced with vanishing transverse momentum. When $p_\perp \gg M$, taking into account the $qg \to q\gamma^\star$ and $q\bar{q} \to g\gamma^\star$ processes where the $q(g)$ is produced at large $p_\perp$, the DY partonic cross section as a function of $p_\perp$ can be parameterized as [41, 42]

$$\frac{d\hat{\sigma}}{dp_\perp^2} \propto \frac{1}{p_\perp^n} \tag{1.21}$$

with $n = 4$ corresponding to an asymptotic limit. When $p_\perp \sim M$, a full description of the $p_\perp$ spectrum is more complex. Figure 1.7 shows the DY differential cross section as a function of $p_\perp$ at NLO (in red) for in pp collisions at $\sqrt{s} = 200$ GeV using CT14 proton PDF [28] integrated between $4.8 < M < 8.2$ GeV. The DY NLO calculation is in reasonable agreement with the data when $p_\perp \sim M$. To improve the description, it possible to take into account higher corrections in α_s^2: the integrated NNLO cross section increases by $\sim 3\%$ compared to the integrated NLO cross section. The NNLO calculation (magenta) is higher compared to NLO calculation and in better agreement with data only at $p_\perp \sim M$. The contribution of higher orders will be much smaller and will not significantly improve the agreement with data, in particular, due to large experimental errors.

---

[7]In the following, the explicit scale dependence is omitted for clarity.

[8]Actually, an additional divergence exists: a collinear divergence from $g \to q\bar{q}$ and $q \to qg$ splitting in the initial state with the gluon transverse momentum $k_\perp \to 0$. These divergences are absorbed by a redefinition of the PDF which become scale-dependent.
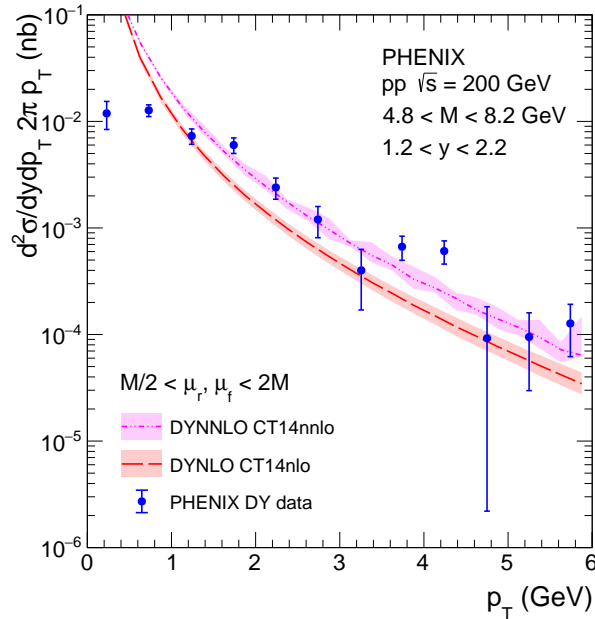
Figure 1.7: Drell-Yan differential cross section as a function of $p_\perp$ at NLO (in red) and NNLO (in magenta) using the DYNNLO software [43] in proton-proton (pp) collisions at $\sqrt{s} = 200$ GeV. In the calculation the CT14 proton PDFs [28] are used by varying the energy scale $M/2 < \mu_r, \mu_f < 2M$. The calculations are compared to the Drell-Yan differential cross section data as a function of $p_\perp$ collected by the PHENIX experiment in pp collisions at $\sqrt{s} = 200$ GeV (blue) [44].

K factor definition

It is also possible to define a theoretical K^{th} factor, defined as the ratio between NLO and LO calculations. It varies between 1.4 to 2 depending on the kinematic domain. Figure 1.8 shows a ratio between NLO and LO DY cross section calculations as a function of x_F at $\sqrt{s} = 50$ GeV (in blue) and $\sqrt{s} = 20$ GeV (in red) in pp collisions using the DYNNLO software [43].

At large x_F ($x_2 \ll x_1$), the Kth increases because the Compton process contribution becomes more important than the $q\bar{q}$ contribution due to an increase of $g(x_2)$ PDF, i.e. $q(x_1)g(x_2) \gg q(x_1)\bar{q}(x_2)$. Consequently, an increased cross section at NLO is expected. Finally, K^{th} diverges because it is dominated by soft gluon emission leading to logarithmically divergent terms $\propto \ln(1 - x_F)$.

1.2.2.a Leading-logarithmic (LL) contribution: the Sudakov factor

The fixed order calculation of the cross section is relevant when $p_\perp^2 \gg M$. For $p_\perp^2 \ll M^2$, the partonic cross section in Eq. (1.22) is dominated by leading logarithmic terms due to soft gluon radiation (see Eq.(1.20)) and is written at all orders in α_s as [45]

$$\frac{1}{\hat{\sigma}} \frac{\mathrm{d}\hat{\sigma}}{\mathrm{d}p_\perp^2} \approx \frac{1}{p_\perp^2} \left[v_1 \alpha_s \ln \left(\frac{M^2}{p_\perp^2} \right) + v_2 \alpha_s^2 \ln^3 \left(\frac{M^2}{p_\perp^2} \right) \cdots + v_n \alpha_s^n \ln^{2n-1} \left(\frac{M^2}{p_\perp^2} \right) + \cdots \right] \quad (1.22)$$

where v_i are theoretically calculable terms. The logarithmic terms come from soft and collinear gluons emission (ng) in the initial-state quarks annihilation, $q\bar{q} \to \gamma^\star ng$ [46]. Consequently, in
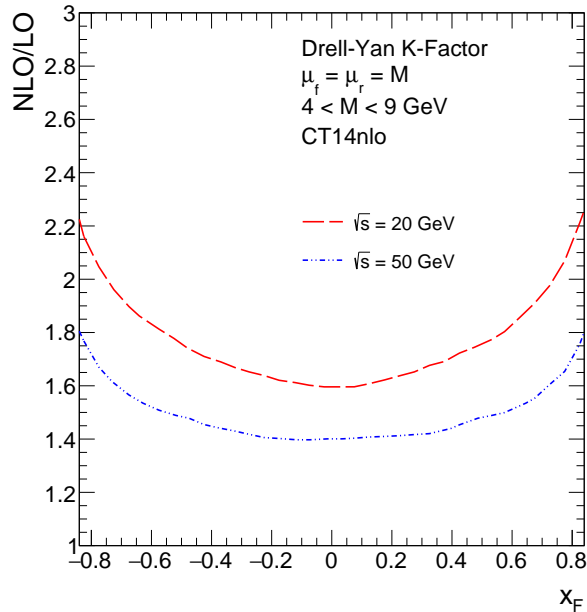
Figure 1.8: Calculation of the ratio between NLO in α_s and LO of DY cross section as a function of x_F using the DYNNLO software [43] using CT14 proton PDF [28] at $\sqrt{s} = 50$ GeV (in blue) and $\sqrt{s} = 20$ GeV (in red) in pp collisions.

Eq. (1.22), the higher order terms are not negligible when $p_\perp^2 \ll M^2$, i.e. when

$$\alpha_\text{S} \ln^2 \left(\frac{M^2}{p_\perp^2} \right) \gtrsim 1. \tag{1.23}$$

These logarithmic terms can be resummed to all orders in perturbation theory as [45]

$$\frac{1}{\hat{\sigma}} \frac{\text{d}\hat{\sigma}}{\text{d}p_\perp^2} \propto \frac{\ln \frac{M^2}{p_\perp^2}}{p_\perp^2} \exp \left(-\frac{\alpha_\text{S}}{2\pi} C \ln^2 \frac{M^2}{p_\text{T}^2} \right) \tag{1.24}$$

with C the Casimir factor of a parton ($C_F = 4/3$ for a quark and $C_A = 3$ for a gluon). The contribution of the logarithmic terms resummed to all orders in α_s contained in the exponential term in (1.24) is called *Sudakov factor*. The cross section in Eq. (1.24) goes to 0 when $p_\perp \to 0$ contrary to what the data show. Indeed, the description of resummation method omits the gluons with momentum $k_i \sim p_\perp$ which satisfies the momentum conservation $\sum_i \vec{k}_i = \vec{p}_\perp$. In other words, the incident parton can emit several very soft gluons while having a transverse momentum equal to 0 as long as the momentum conservation is verified. The complete description of the resummation was proposed by Collins, Soper and Sterman (CSS) in 1985 [47]. The CSS formalism, describing the resummation at all orders in α_s of logarithmic terms by imposing a momentum conservation, provides a finite differential cross section at $p_\perp \to 0$ [46].

In summary, in the calculation, three regions can be distinguished in the differential cross section as a function of $p_\perp$: the resummation term *at all orders* in α_s of soft and collinear gluon emission when $p_\perp^2 \ll M^2$, the perturbative term evaluated *at fixed order* in α_s when $p_\perp^2 \sim \mathcal{O}\left(M^2\right)$ and the asymptotic perturbative term evaluated *at fixed order* in α_s when $p_\perp^2 \gg M^2$.
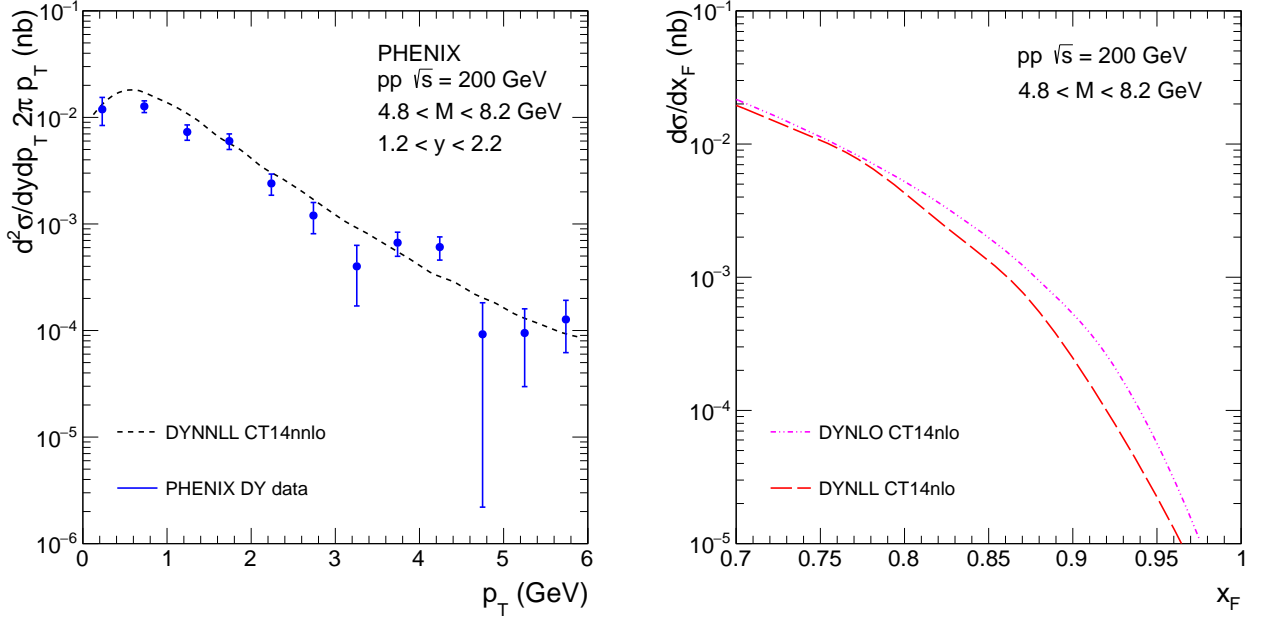
Figure 1.9: Drell-Yan differential cross section as a function of $p_\perp$ at NNLL calculation using the DYRES software [48] in pp collisions at $\sqrt{s} = 200$ GeV using CT14 proton PDF and DY differential cross section as a function of $p_\perp$ collected by PHENIX experiment in pp collisions at $\sqrt{s} = 200$ GeV (blue) [44] (left panel). Drell-Yan differential cross section as a function of x_F at NLO and NLL in pp collisions at $\sqrt{s} = 200$ GeV using CT14 proton PDF (right panel).

The differential cross section in $p_\perp$ can be written as a sum of these three terms as

$$\frac{d\hat{\sigma}}{dp_\perp^2}(\text{total}) = \frac{d\hat{\sigma}}{dp_\perp^2}(\text{resum}) + \frac{d\hat{\sigma}}{dp_\perp^2}(\text{fixed order}) - \frac{d\hat{\sigma}}{dp_\perp^2}(\text{asym}). \qquad (1.25)$$

The comparison between the PHENIX DY data and a Next-to-Next-Leading-Logarithmic (NNLL) calculation is displayed in Fig. 1.9 (left). The cross section calculation at low $p_\perp \ll M$ is finite due to the resummation of logarithmic terms. Figure 1.9 (right) shows the comparison between DY calculations at NLO (in magenta) and NLL (red) as a function of x_F in pp collisions. An important difference between the NLO and the NLL calculation at large x_F is observed due to the resummation terms at small $p_\perp$, see discussion in section 1.2.2. The NLL calculation shows a reduction compared to the NLO calculation on the differential cross section by a factor ~ 2 at $x_F \approx 0.9$.

1.2.3 Kinematics definition in hadron-hadron collisions

Let us now recall the basic kinematic relations in hadron-hadron collisions useful for the next sections. According to the previous sections, generic definitions in a collision[9] between two hadrons (h_1 and h_2) and a production of the two leptons (l and $\bar{l}$) from a hard process $\hat{\sigma}_{ij}$ are defined below.

- $p_1 = (E, \boldsymbol{p_1^i})$ and $p_2 = (E', \boldsymbol{p_2^i})$ the 4-momentum of the hadron 1 and 2;

---

[9]By convention along the z-axis.

- $s = (p_1 + p_2)^2$ the *s-channel* variable, $\sqrt{s}$ the center-of-mass energy in the hadronic frame;

- $x_1 p_1$ and $x_2 p_2$ the 4-momentum of the parton 1 and 2 respectively;

- $x_\mathrm{F} = \frac{p_z}{p_z^{\max}} \approx x_1 - x_2$ the fraction of the maximum longitudinal momentum carried by the dilepton pair;

- $M = \sqrt{x_1 x_2 s}$ the invariant mass of the dilepton pair;

- $M_\perp = \sqrt{M^2 + p_\perp^2}$, the transverse invariant mass of the dilepton pair;

- $y = \frac{1}{2} \ln \left(\frac{E + p_z}{E - p_z} \right) = \ln \left(\frac{E + p_z}{M_\perp} \right)$, the rapidity of dilepton pair.

Bjorken x

The definition of the variables x_1 and x_2 depends on the domain in $p_\perp$ of the dilepton pair produced in a hard process. Indeed, if $p_\perp$ is less than M, the scattering energy scale to probe the physical process is equal to the invariant mass of the dilepton pair where $p_\perp$ is large compared to M, the relevant scattering energy scale becomes dependent on $p_\perp$. Three different kinematics can be defined as

- kinematic $2 \to 1$ ($ij \to k \to l^- l^+ + X$) namely when $0 < p_\perp \lesssim M$: $x_{1/2} \simeq M e^{\pm y} / \sqrt{s}$,

- kinematic $2 \to 2$ ($ij \to kl \to l^- l^+ + X$) when $p_\perp \gtrsim M$: $x_{1/2} \simeq (M_T + p_\perp) e^{\pm y} / \sqrt{s}$

- kinematic $2 \to 2$ ($ij \to kl \to l^- l^+ + X$) when $p_\perp \gg M$: $x_{1/2} \simeq 2 p_\perp e^{\pm y} / \sqrt{s}$.

1.3 Quarkonium production

In this section, we will introduce a second hard process of purely strong interaction: the quarkonium production. The quarkonium production in hadron-hadron collisions proceeds through the QCD scattering of the two partons, as illustrated in Fig. 1.10, in the gluon fusion channel. In the J/ψ case, the ground state of the charmonium meson, the mass of the $c\bar{c}$ pair produced of about 3 GeV is much larger than Λ_{QCD}. Therefore, it is in principle possible to use the perturbative QCD tools combined with factorisation theorems. But, unlike the DY process described above, the quarkonium production is more complex, because it is necessary to describe correctly the hadronisation part. Most quarkonium production models are based on a collinear factorisation between the heavy quark pair $Q\overline{Q}$ production and its subsequent hadronizaton into a charmonium meson. Although the complete description of the production of quarkonium is still a puzzle difficult to solve, the main existing models will be briefly described in the next sections.
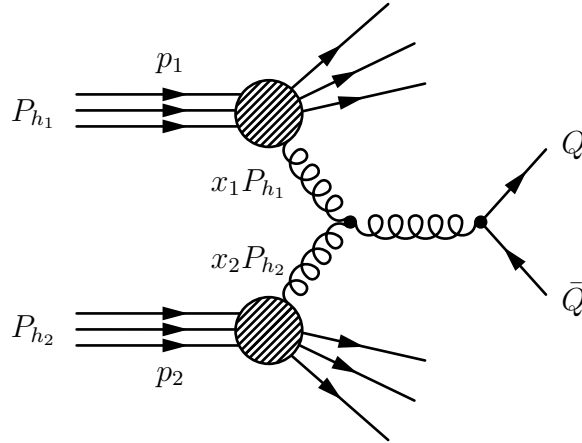
Figure 1.10: Example of $Q\bar{Q}$ pair production in hadron-hadron collisions.

1.3.1   Color state

The quarkonium particle is produced, like all hadrons, in a colourless state, i.e. in a colour singlet state, regardless of the colour state in which the $Q\bar{Q}$ pair is produced. As we will see, there are several models that can describe the quarkonium production in hadron-proton collisions. One of the strong hypotheses lies in the colour state of the $Q\bar{Q}$ pair produced before its hadronisation into quarkonium. Depending on the color state of the quarkonium bound state, the $p_\perp$ dependence of the cross section is different. By considering only lowest order from gluon annihilation processes [49] in the limit $p_\perp \to \infty$, (i.e. with the production of a hard gluon g in the final state), two cases can be distinguished:

1. $Q\bar{Q}$ quarks hadronisation into a colour-singlet state at order α_s^3:
   $g + g \to \left[Q\bar{Q}\right]_1 + g$: $\mathrm{d}\hat{\sigma}/\mathrm{d}p_\perp^2 \propto \frac{\alpha_s^3}{p_\perp^8}$

2. gluon fragmentation into a colour-octet state at order α_s^3:
   $g + g \to \left[Q\bar{Q}\right]_8 + g$: $\mathrm{d}\hat{\sigma}/\mathrm{d}p_\perp^2 \propto \frac{\alpha_s^3}{p_\perp^4}$

The theoretical description of quarkonium presents many delicate issues: identifying the proportions of the production of singlet and octet $Q\bar{Q}$ state, calculating the cross section to an order dominant in α_s. Finally it is necessary to describe the evolution of the $Q\bar{Q}$ pair towards the hadronisation where the factorisation condition is to have the hadronisation time much longer compared to the $Q\bar{Q}$ production time i.e. $t_{had} \gg t_{Q\bar{Q}}$.

1.3.2   Color Evaporation Model

The Color Evaporation Model(CEM) has been suggested to describe the quarkonium production. In this model, the cross section of a quarkonium state H is directly proportional to the heavy

quark pair production cross section integrated between the free $Q\overline{Q}$ mass pair $(2m_Q)$ and open-heavy-flavour hadron pair mass $(2m_{D,B})$. The quarkonium production cross section in the CEM model can be written as [50]

$$\sigma[H + X] = \mathcal{F}_H \int_{2m_Q}^{2m_{D,B}} \frac{d\hat{\sigma}[Q\overline{Q} + X]}{dm_{Q\overline{Q}}} dm_{Q\overline{Q}}, \tag{1.26}$$

where $\sigma[H + X]$ is the production cross section of state H and $\frac{d\hat{\sigma}[Q\overline{Q}+X]}{dm_{Q\overline{Q}}}$ the differential cross section to produce a heavy quark pair $(Q\overline{Q})$ calculable in the perturbative theory. The factor $\mathcal{F}_H$ is determined in a purely phenomenological approach and is related to the fraction of $d\sigma[H + X]$ that produces the quarkonium state H. This model assumes the factorisation between the perturbative production of a $Q\bar{Q}$ pair and the non-perturbative hadronisation process. It is a reasonable assumption in the J/ψ case because $t_f \sim 1/(2m_{c\bar{c}}) \sim 0.1\,\text{fm} \ll 1/(2(M_\psi - M_{J/\psi}))$, where t_f is the H bound state formation time, M_ψ and $M_{J/\psi}$, the ψ and J/ψ bound state masses respectively. Otherwise, the CEM is an average over all color and spin states of the $Q\bar{Q}$ produced. It therefore cannot predict the quantum numbers of the produced bound state J/ψ. On the other hand, a recent improvement of this model (ICEM) was performed to describe the polarisation dependence of the produced quarkonium state H [51]. The ICEM model includes interactions by many soft gluons between $Q\bar{Q}$ and various color sources between its production and its hadronisation into a bound state.

1.3.3 Color-Singlet model

The Color-Singlet Model (CSM) [52] is used to describe the production of a quarkonium state H without evolution of the quantum states between the heavy-quark $Q\bar{Q}$ pair production and its hadronisation. The model assumptions are:

- the $Q\bar{Q}$ pair is produced at a scale $\mu^2 \sim M_{Q\bar{Q}}^2 \gg \Lambda_{\text{QCD}}^2$ justifying a pQCD treatment;

- the $Q\bar{Q}$ pair is produced in the non-relativistic limit with $v \ll 1$, with v the relative velocity of the heavy quarks;

- the state of quarkonium H is produced with the same spin, color and angular-momentum quantum numbers as the $Q\bar{Q}$ pair in a color-singlet ${}^3S_1^{[1]}$ state.

The cross section of quarkonium H production in the CSM model can be written

$$\sigma[H + X] \propto \sigma_{\text{h}_1\text{h}_2 \to (Q\bar{Q})_1} |R_H(0)|^2. \tag{1.27}$$

with $|R_H(0)|$, the non-perturbative parameters describing the hadronisation part and corresponding to the probability of the pair $(Q\bar{Q})_1$ in singlet-state to access to the bound state H. Recently [53], it was shown that $\mathcal{O}\left(\alpha_s^4\right)$ and $\mathcal{O}\left(\alpha_s^5\right)$ corrections to CSM model participate significantly to the total cross section calculation and lead to a relatively good agreement with data at Tevatron and LHC energies in pp collisions at large $p_\perp \gg M_{J/\psi}$.

As we will be described in the next section, the NRQCD model proposes a more complete description that encapsulates the CSM model.

1.3.4 Non-Relativistic QCD model

The Color-Octet Mechanism (COM) in the Non-Relativistic QCD (NRQCD) formalism gives a similar approach as the CSM model. This approach is also based on a factorisation between the hard and soft part. However, the information on the hadronisation part is contained in long distance matrix elements (LDMEs). The cross section of a quarkonium state H production in NRQCD model can be written as [54]

$$d\sigma[H + X] \propto \sigma_{h_1 h_2 \to (Q\bar{Q})_n} \langle O_H^n \rangle. \tag{1.28}$$

where $\sigma_{h_1 h_2 \to (Q\bar{Q})_n}$ is the hadronic cross section part describing the production of $Q\bar{Q}$ pair in spin, color and orbital-angular momentum state denoted n and $\langle O_H^n \rangle$, the non-perturbative parameters describing the hadronisation part and correspond to the probability of the pair $Q\bar{Q}$ to access to the bound state H in a quantum state n. The color-singlet matrix are taken from potential model calculation [55, 56] whereas the octet-matrix elements are extracted in the experimental data [57, 58] at $p_\perp \gg M_{J/\psi}$. In contrast to the CEM model, the NRQCD model includes the radiative decays of exciting states to the J/ψ state. [10] The J/ψ total production cross section can be written as

$$\sigma_{J/\psi} = \sigma_{J/\psi}^{\text{dir}} + \sum_{J=0}^{2} B\left(\chi_{cJ} \to J/\psi + X\right) \sigma_{\chi_{cJ}} + B\left(\psi' \to J/\psi + X\right) \sigma_{\psi'}, \tag{1.29}$$

where $B\left(Q \to J/\psi + X\right)$ is the branching ratio of excited quarkonium state H to J/ψ. Generally, none of the models cited in this section provides a complete description of the production of quarkonium. In particular, the most complete NRQCD model does not reproduce low-energy data at fixed targets [59] especially the quarkonium polarisation.

1.4 Phenomenological aspects of the Drell-Yan and quarkonium production

In this chapter, the framework to describe the production of the Drell-Yan and quarkonium in pp collisions is discussed. These two processes of different but complementary nature make it possible to study the hadronic structure.

1.4.1 Drell-Yan production

As mentioned in Sec. 1.2.2, it is possible to calculate in perturbation theory the DY process in all $p_\perp$ regions. At moderate $p_\perp \sim M$ and large $p_\perp \gg M$ values at fixed order in α_s, the DY cross section is calculated up to NNLO corrections [43] but also at small $p_\perp \ll M$ values, by taking into account the logarithmic corrections up to NNLL corrections [48]. The perturbative calculations allow for reproducing perfectly all observables in pp collisions, as a function of the dilepton mass, rapidity (x_F) or $p_\perp$. To illustrate this point, some comparisons between DY calculations and experimental results will be briefly shown.

---

[10]For more simplicity, the J/ψ quarkonium state is taken for example.

Fixed-target energies

Figure. 1.11 shows the comparison between DY data at $\sqrt{s} = 38.8$ GeV from E866 in pp and pD collisions, E772 in pD collisions and E605 in pCu collision from [60] and DY NLO calculation using two different proton PDFs as a function of dimuon invariant M and x_{F}. This comparison exhibits a perfect agreement showing the success of perturbative calculations in pp collisions.
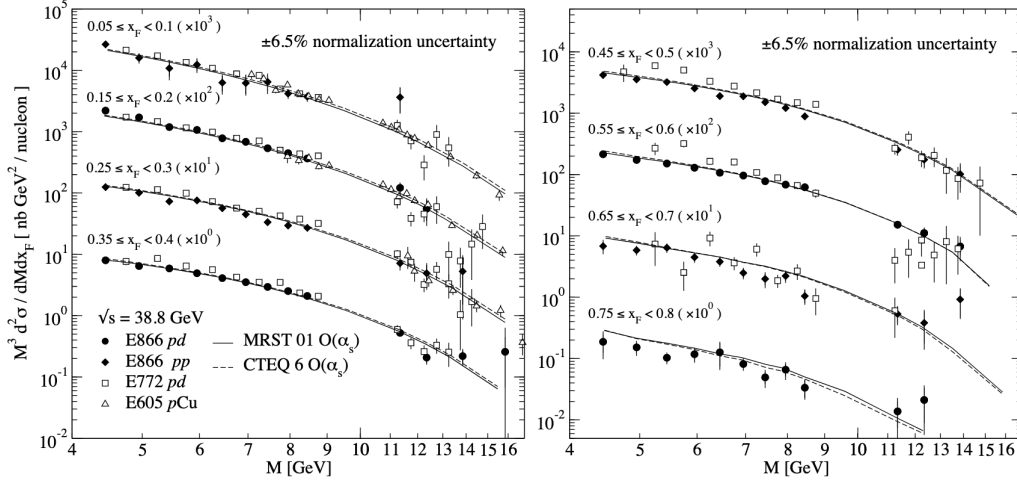
Figure 1.11: Comparison between Drell-Yan data from E866, E772, E605 experiments as a function of dimuon invariant mass M and x_F for different collisions system pp, pD and pCu from [60] and NLO in α_s calculation.

Collider energies

In Sec. 1.2.2 a good agreement at $p_\perp \gtrsim 1$ GeV between Drell-Yan data from PHENIX at $\sqrt{s} = 200$ GeV and calculations is shown. CMS Drell-Yan data as a function of the dilepton (electron and muons) mass at $\sqrt{s} = 13$ TeV [61] also exhibit a perfect agreement with DY NNLO calculation on a large kinematic phase space $20 \lesssim M_{l^+l^-} \lesssim 2000$ GeV. This agreement makes it possible to highlight the solidity of the theoretical formalism of the Drell-Yan process on up to 10 orders of magnitude in the cross section. In addition, the agreement between absolute cross section as a function of $p_\perp$ and calculation up to $p_\perp = 200$ GeV is shown by ATLAS experiment at 7 TeV [62] and CMS experiment at 8 TeV [63]. All these observations allow to one consider the DY process as a clean process to explore new kinematic domains or other collision systems like nuclear collisions.

1.4.2 Quarkonia production

Unlike DY, the quarkonium production in pp collisions is not yet fully understood. None of the models presented do not provide a global description of the data, in particular the $p_\perp$ dependence, both at small $p_\perp \sim M$ and large $p_\perp \gg M$. To demonstrate this point, a few observables are discussed below.

Fixed-target energies

The main part of fixed-target data, typically at SPS energies ($\sqrt{s} \sim$ GeV), is collected in a small $p_\perp$ region, i.e. $p_\perp \ll M$. This kinematic region requires taking into account the logarithmic terms to describe the $p_\perp$ dependence of the cross section.

It was shown [59] that the NRQCD model cannot reproduce fixed-target J/ψ data as a function of the dimuon rapidity due to a too large contribution of the octet color state compared to what was extracted from the Tevatron energies at $\sqrt{s} \sim 1$ TeV .

Collider energies

RHIC experiment compared J/ψ production in pp collisions both at $\sqrt{s} = 200$ GeV and $\sqrt{s} = 510$ GeV [64] [65] with COM, CSM and NRQCD models. At $\sqrt{s} = 200$ GeV, the CSM model underestimates the cross section alone but the Color Octet model (CEM) can reproduce alone all $p_\perp$ values in $2 < p_\perp < 6$ GeV interval. There is no calculation below 2 GeV due to resummation of logarithmic term not taken into account in the calculation. NRQCD model can reproduce only
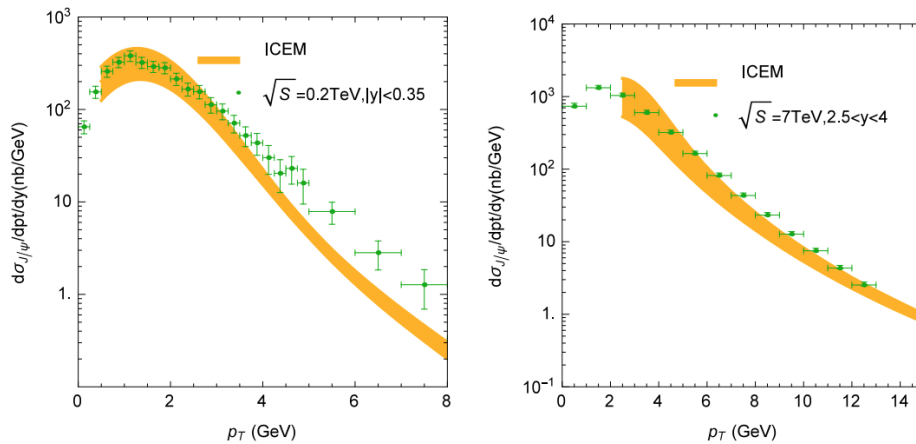
Figure 1.12: Comparison between ICEM model [51] (in orange) and data as a function of $p_\perp$ from prompt J/ψ production in pp collisions at $\sqrt{s} = 200$ GeV and $\sqrt{s} = 7$ TeV from RHIC experiment at mid rapidity [66] and from LHCb experiment at forward rapidity [67] respectively.

large $p_\perp \gtrsim 4$ GeV. Figure 1.12 shows the comparison between ICEM model (in orange) data as a function of $p_\perp$ from prompt J/ψ production in pp collisions at $\sqrt{s} = 200$ GeV and $\sqrt{s} = 7$ TeV from RHIC experiment at middle rapidity [66] and from LHCb experiment at forward rapidity[67] respectively. The agreement between data and ICEM model is good especially at low $p_\perp$ for both energies. The disagreement is accentuated in the large $p_\perp \gtrsim 4$ GeV at RHIC experiment, although the experimental statistical errors are also large.

In Fig. 1.13, the J/ψ production cross section calculated in the CSM, and NRQCD models are compared to the prompt J/ψ data in pp collisions at $\sqrt{s} = 8$ TeV as a function of $p_\perp$ from
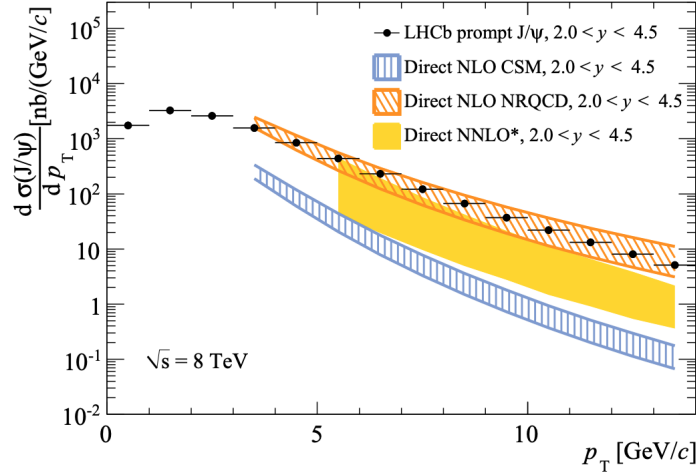
Figure 1.13: Comparison between J/ψ production model calculation at NLO, NRQCD (in orange), CSM (in blue) and CSM at NNLO neglecting a part of the logarithmic terms (in yellow) and prompt J/ψ data in pp collisions at $\sqrt{s} = 8$ TeV as a function of $p_\perp$ from LHCb experiment [68].

LHCb experiment [68]. The CSM NLO calculation underestimates the absolute cross section by an order of magnitude whereas NRQCD at NLO and CSM at NNLO*[11] exhibit a reasonable agreement with data. The absolute cross section description at $p_\perp \lesssim 3$ GeV $\sim M_{J/\psi}$ is not calculated due to the absence of the resummation part. In addition, the agreement between data for other energies at $\sqrt{s}s = 1.96$ and $\sqrt{s}s = 7$ TeV and CSM at NNLO* is confirmed by [53].

In summary, at RHIC and LHC energies, at large $p_\perp \gtrsim M$, CSM model alone at NLO up to α_S^4 underestimates the cross section of at least an order of magnitude while a calculation up to NNLO* up to α_S^5 makes it possible to reproduce the data in a reasonable manner. NRQCD model can also reproduce data in a reasonable way at large at large $p_\perp \gtrsim M$. ICEM model also enables to reproduce all the data for all $p_\perp$. Furthermore, it has been shown that NRQCD model fails to reproduce data at low energies due to a predominance of the color state production.

Predicting the normalisation, the shape of the absolute sections and the polarisation of the quarkonium production is still a puzzle at all energies and in all $p_\perp$ range.

---

[11]NNLO* is not a complete calculation, the logarithmic terms are neglected at small $p_\perp \lesssim M$.

2

Nuclear effects in dilepton production

Contents

Cold nuclear matter can be studied in hadron-nucleus collisions from fixed-target energies ($\sqrt{s} \sim$ GeV) to colliders ($\sqrt{s} \sim$ TeV) energies. Indeed, the nuclear matter is static with a known density. In this thesis, I am interested in the nuclear dependence of the DY and charmonium production via the ratio of nuclear cross sections defined as

$$R_{\text{hA}}\left(\text{A/B}, y\right) \equiv \frac{\text{B}}{\text{A}} \left(\frac{\text{d}\sigma(\text{hA})}{\text{d}y}\right) \times \left(\frac{\text{d}\sigma(\text{hB})}{\text{d}y}\right)^{-1} \tag{2.1}$$

and

$$R_{\text{hA}}\left(\text{A/B}, p_{\perp}\right) \equiv \frac{\text{B}}{\text{A}} \left(\frac{\text{d}\sigma(\text{hA})}{\text{d}p_{\perp}}\right) \times \left(\frac{\text{d}\sigma(\text{hB})}{\text{d}p_{\perp}}\right)^{-1} \tag{2.2}$$

where $\frac{d\sigma(hA)}{dy}$ and $\frac{d\sigma(hA)}{dp_\perp}$ are the cross sections on heavy nucleus (A) over that in a lighter nucleus (B) as a function of y and $p_\perp$ respectiveky. In the next sections, I will describe all effects which can have an impact on the nuclear modification factor R_{hA}.

2.1 A-dependence

2.1.1 Isospin effect

The isospin effect is due to the difference in proton and neutron (in terms of valence quarks) number in a nucleus. In hadron-nucleus collisions (hA) in the absence of nuclear effects, the parton distribution function $f_j^{h_2}$, appearing in general case in Eq. (1.18), should thus be replaced by the corresponding average over proton and neutron partonic densities,

$$f_j^A(x) = Zf_j^p(x) + (A-Z)f_j^n(x) \tag{2.3}$$

where Z and A is respectively the atomic and the mass number of the nucleus A. Depending on the number of proton and neutron in the nucleus, there is a difference between $u_v^A(x)$ and $d_v^A(x)$ creating an *isospin-asymmetry* in the valence region. If the number of proton and neutron is the same, i.e. $A - Z = Z$, the nucleus is called *isoscalar* otherwise *non-isoscalar*. Table 2.1 shows the proton fraction for several light and heavy nuclei. Figure 2.1 shows the distribution of parton

Nucleus	A (nucleons number)	Z (atomic number)	Proton fraction
H	1	1	1
D	2	1	0.50
Be	8	4	0.50
C	12	6	0.50
Fe	56	26	0.46
W	184	74	0.40
Pt	195	78	0.40

Table 2.1: Isoscalarity of several nuclei.

distribution functions of $u_v^A(x)$ and $d_v^A(x)$ normalized by A multiplied by x for deuterium (left panel) isoscalar nucleus and for tungsten (right panel) non-isoscalar nucleus. At large $x \gtrsim 0.1$, the $u_v^A(x)$ and $d_v^A(x)$ distributions exhibit a difference of $\sim 15\%$.

The isospin effect from proton and neutron number in nucleus can play a role in R_{hA} but *only* in the target valence quarks region at large $x_2 \gtrsim 0.1$. In this x_2 region, typically, in πA (or in $\bar{p}p$) collisions, the DY cross section, for instance, is dominated by the parton distribution functions (PDF) from the target valence quarks. This point will be discussed in more detail in sections 2.1.3 and 2.1.4. The isospin effect is the first *trivial* effect participating in the nuclear modification ratio R_{hA} being different than unity. In the next section, a second effect due to the antiquark flavour asymmetry in the proton sea will be introduced.
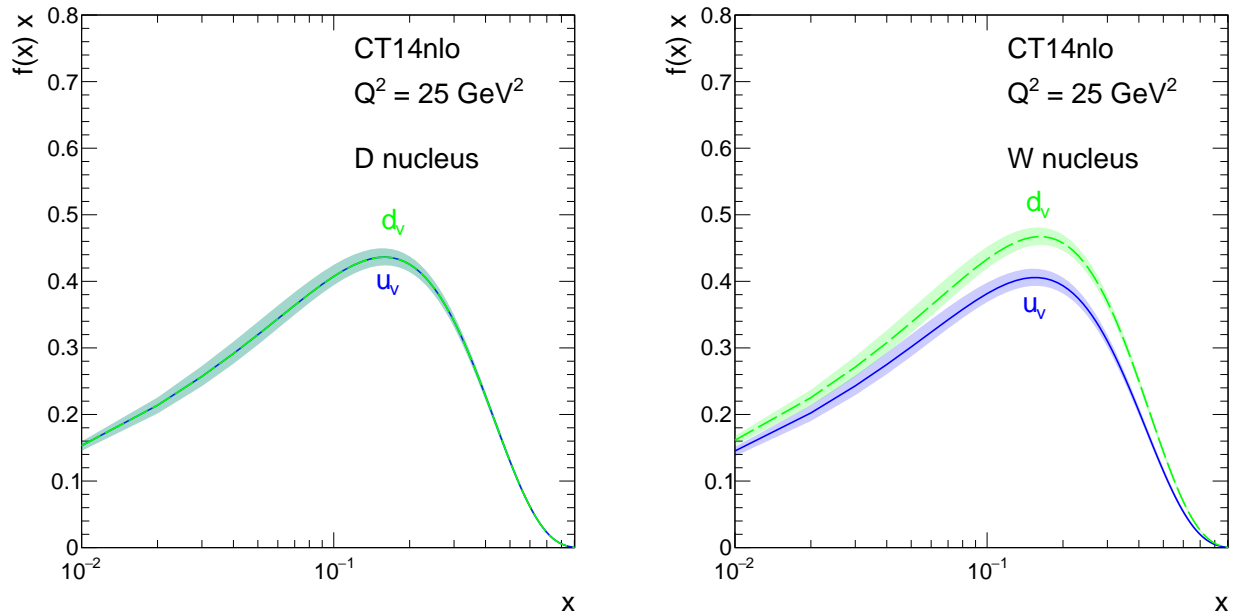
Figure 2.1: Parton distribution functions of $u_v^A(x)$ and $d_v^A(x)$ normalised by A times x and their associated uncertainties at $Q^2 = 25$ GeV^2 for deuterium nucleus (left panel) and tungsten nucleus (right panel) at Next-to-Leading Order (NLO) using CT14 parameterization [28].

2.1.2 Antiquark flavor asymmetry in the nucleon sea

Whereas the isospin effect appears in the target valence quarks region, the antiquark flavour asymmetry effect is the consequence of the difference of the parton distribution functions of $\bar{u}$ and $\bar{d}$ quarks in the nucleon sea. E866/NuSea collected DY data [69] on proton and deuterium targets using a proton beam at E$_{\text{beam}}$=800 GeV to study the antiquark flavour asymmetry. The experimental acceptance coverage is $0.036 < x_2 < 0.312$, $0.044 < x_F < 0.537$, $5.5 < $ M < 12.8 GeV and $0.92 < p_\perp < 1.12$ GeV.

At LO or when $p_\perp \ll M$[1], the DY cross section in pp collisions is proportional to $\bar{u}$ and $\bar{d}$ PDFs. In order to study the contribution from sea quarks from the target only, i.e. $x_1 \gg x_2$ and by assuming $\bar{u}^{\text{p}} = \bar{d}^{\text{n}}$, the DY cross section in pp and pn collisions can therefore be written like

$$\sigma_{\text{pp}}^{\text{DY}} \propto \frac{4}{9} u\left(x_1\right) \bar{u}\left(x_2\right) + \frac{1}{9} d\left(x_1\right) \bar{d}\left(x_2\right), \tag{2.4}$$

$$\sigma_{\text{pn}}^{\text{DY}} \propto \frac{4}{9} u\left(x_1\right) \bar{d}\left(x_2\right) + \frac{1}{9} d\left(x_1\right) \bar{u}\left(x_2\right). \tag{2.5}$$

By considering $d^{\text{p}}(x) \ll 4u^{\text{p}}(x)$, the ratio of DY cross sections between pD and pp collisions can be approximated as

$$\left.\frac{\sigma^{\text{pD}}}{2\sigma^{\text{pp}}}\right|_{x_1 \gg x_2}^{\text{DY}} \approx \frac{1}{2} \frac{\left(1 + \frac{1}{4}\frac{d(x_1)}{u(x_1)}\right)}{\left(1 + \frac{1}{4}\frac{d(x_1)}{u(x_1)}\frac{\bar{d}(x_2)}{\bar{u}(x_2)}\right)} \left(1 + \frac{\bar{d}(x_2)}{\bar{u}(x_2)}\right) \approx \frac{1}{2}\left[1 + \frac{\bar{d}(x_2)}{\bar{u}(x_2)}\right]. \tag{2.6}$$

---

[1]In this $p_\perp$ region, quark-antiquark annihilation process $q\bar{q} \to \gamma^* X$ dominates. At large $p_\perp \gg M$, the Compton scattering process $qg \to q\gamma^\star X$ dominates (see 1.2.3).

Thanks to Eq. (2.6), it is therefore possible to extract the $\bar{d}/\bar{u}$ ratio from the pD over pp cross sections ratio. If the sea is flavor symmetric, $\bar{d}(x_2) = \bar{u}(x_2)$, Eq. (2.6) should be equal to 1. Figure 2.2 shows the ratio of DY cross sections between pp and pD collisions from E866/NuSea experiment as a function of x_2. The ratio depends on x_2 showing a flavour asymmetry between $\bar{d}(x)$ and $\bar{u}(x)$ PDFs. In addition, the comparison between E866/NuSea data and NLO calculations using nCTEQ15 (in red) [70], NNPDF31 (in blue) [29] and CT14 (in magenta) [28] free proton PDFs, which include E866/NuSea data in the global fits, is shown. The $\bar{d}/\bar{u}$ flavour asymmetry magnitude depends a lot on the parametrization used for the global fit: nCTEQ predicts a more important asymmetry effect compared to NNPDF31 and CT14. E866/NuSea data constrain
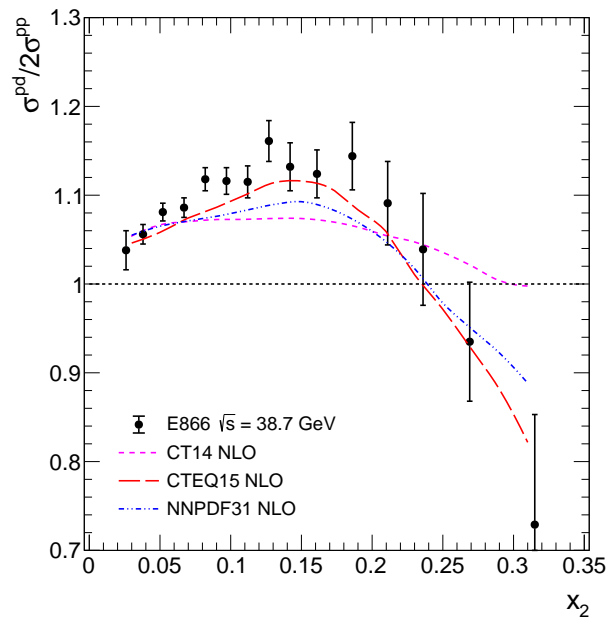
Figure 2.2: Ratio of DY cross section between *pp* and *pd* collisions from E866/NuSea experiment using a proton beam at $E_{\text{beam}} = 800$ GeV (in black) [69] and from calculation using nCTEQ15 (in red) [70], NNPDF31 (in blue) [29] and CT14 (in magenta) [28] free proton PDF at NLO neglecting nuclear effect due to deuterium nucleus.

the $\bar{d}/\bar{u}$ asymmetry in the $0.015 < x < 0.35$ range, obtaining

$$\int_0^1 [\bar{d}(x) - \bar{u}(x)]dx = 0.118 \pm 0.012. \tag{2.7}$$

From April 2014 to July 2017, the E906/SeaQuest experiment collected new DY data [71] using a proton beam at lower beam energy $E_{\text{beam}} = 120$ GeV probing the $\bar{d}/\bar{u}$ ratio at higher x, $0.1 < x < 0.45$. The analysis is still ongoing [72]. In the next section, the nuclear modification ratio R_{hA} for both DY and charmonium processes for different kinematic situation and hadronic projectile cases is studied.

2.1.3 Drell-Yan cross sections ratio

At large positive $x_F > 0$, or $x_1 \gg x_2$, typically in fixed-target configuration, the DY cross section at LO is dominated by the parton distribution functions of the valence quarks from the beam hadron.[2] In pA collisions, the DY cross section is related to the sea quark distributions of the target,

$$\sigma_{pA}^{DY} \propto \frac{4}{9} u^p(x_1)\bar{u}^A(x_2) + \frac{1}{9} d^p(x_1)\bar{d}^A(x_2). \tag{2.8}$$

The cross sections ratio in pA collisions can be written as

$$R_{pA}^{DY} \propto \frac{8\bar{u}^A(x_2) + \bar{d}^A(x_2)}{8\bar{u}^B(x_2) + \bar{d}^B(x_2)}, \tag{2.9}$$

by assuming $u^p(x_1) \approx 2d^p(x_1)$ when x_1 is the order $\mathcal{O}(10^{-1})$ in the proton. In $\pi^- A$ collisions, the DY cross section is dominated by valence quark contributions from the beam and from the target,

$$\sigma_{\pi^- A}^{DY} \propto \frac{4}{9} \bar{u}^{\pi^-}(x_1)u_v^A(x_2) + \frac{1}{9} d^{\pi^-}(x_1)\bar{d}^B(x_2). \tag{2.10}$$

The ratio of nuclear cross sections can be express as

$$R_{\pi^- A}^{DY} \propto \frac{4u^A(x_2) + \bar{d}^A(x_2)}{4u^B(x_2) + \bar{d}^B(x_2)}, \tag{2.11}$$

by assuming $\bar{u}^{\pi^-}(x_1) = d^{\pi^-}(x_1)$ in the pion. Consequently, at forward rapidity $(x_F > 0)$ in the pion beam case, the valence quarks of the target are essentially probed. Consequently, this region is sensitive to the isospin effect. While in pA, the sea quarks of the target is probed mainly sensitive to antiquark flavour asymmetry in the nucleon sea.

2.1.4 Charmonium cross sections ratio

In pA collisions, when $x_F \approx 0$ or $x_1 \approx x_2 \ll 1$, the gluon PDF contribution is dominant compared to quark PDFs contribution, $g(x_2) \gg q(x_2) \simeq \bar{q}(x_2)$, the J/ψ [3] process in all production models can be written as,

$$g^p g^A \rightarrow Q\overline{Q} \rightarrow J/\psi + X. \tag{2.12}$$

The quarkonium production cross section in pA collisions is directly sensitive to the gluon PDF of the target. Assuming QCD factorisation, it can be written (see Eq. (2.13)) as a product of the gluon PDF from the beam[4] and the nucleus and the quarkonium cross section,

$$\frac{d\sigma(pA)}{dy}[J/\psi + X] = \int_0^1 dx_1 \int_0^1 dx_2 \int d\hat{s} \, g^p\left(x_1, \mu_F^2\right) g^A\left(x_2, \mu_F^2\right) \frac{d\hat{\sigma}_{gg \rightarrow J/\psi + X}}{dy} \delta\left(x_1 x_2 s - \hat{s}\right) \tag{2.13}$$

---

[2]At $x_F < 0$, it is the opposite case, the DY cross section at LO is dominated by the PDFs of the valence quarks from the target hadron.

[3]To simplify, the J/ψ meson as the charmonium state is chosen.

[4]It was shown in [73] in Υ data collected by E866/NuSea experiment in pp and pD collisions $\sigma(pD \rightarrow \Upsilon)/2\sigma(pp \rightarrow \Upsilon) \approx \frac{1}{2}\left(1 + \frac{g(x_2)^n}{g(x_2)^p}\right) \approx 1$ with integrated ratio equal to $0.984 \pm 0.026(\text{stat}) \pm 0.01(\text{sys})$ compatible with $g(x_2)^n = g(x_2)^p$.

where $\mu_F^2 \sim M_{J/\psi}^2$. When $x_2 \ll 1$, the cross sections ratio is equal to the ratio of the gluon PDFs of the nucleus A and the nucleus B,

$$R_{pA}^{J/\psi} \propto \frac{g^A(x_2)}{g^B(x_2)}. \tag{2.14}$$

On the other hand, when $x_F \gtrsim 0.8$[5], the $q\bar{q}$ sub-process dominates [50].

In $\pi^- A$ collisions, the dominant partonic sub-process depends on the pion PDF parametrisation as discussed in Sec. 1.1.6. However, at large $x_F \sim x_1$, the cross section is dominated by the valence quark PDFs from the pion beam. The shape of $g(x)$ in the pion decreases quickly at large x like $xg(x)^\pi \sim (1-x)^3$ [74] whereas the shape of $\bar{q}^\pi(x)$ decreases like $x\bar{q}(x) \sim (1-x)$ [30]. Consequently, when the $q\bar{q}$ partonic sub-process dominates, it is reasonable to write the cross sections ratio as

$$R_{\pi^- A}^{J/\psi} \propto \frac{u^A(x_2) + \bar{d}^A(x_2)}{u^B(x_2) + \bar{u}^B(x_2)}. \tag{2.15}$$

Between these two limits, i.e. $0 < x_F \ll 1$, the case is more complex to simply write the cross sections ratio because the relative contribution of $q\bar{q}$ and gg partonic sub-processes depend strongly on which pion PDF is used[6]. The J/ψ cross section at LO can be written as a sum of two terms,

$$\sigma^{\pi^- A}[J/\psi + X] = \sigma_{gg}^{\pi^- A}[J/\psi + X] + \sigma_{\bar{q}q}^{\pi^- A}[J/\psi + X]. \tag{2.16}$$

Figure 2.3 shows a calculation in the CEM model at LO for $\pi^- A$ collisions at the COMPASS experiment with beam energy $E_{beam} = 190$ GeV using two different pion PDFs: GRV [34] and the more recent pion PDF extraction from JAM [38]. Using GRV gives gluon fusion as a dominant channel except at large $x_F \sim 0.8$. In contrast, JAM gives $u(x_1)\bar{u}(x_2) \gg g(x_1)g(x_2)$ at all x_F. However, JAM pion PDF gives a better constraint in the gluon sector at $x \sim 0.3$ thanks to leading neutron data from the HERA experiment [36, 37]. Consequently, as illustrated in Fig. 1.5, the gluon contribution from JAM is lower compared to GRV.

In $\pi^- A$ collisions, the uncertainty of the initial partonic state will have an impact on the interpretation of the experimental data discussed in Sec. 2.5.

2.2 Nuclear parton distribution function

The EMC collaboration highlighted the Nuclear parton distribution function (nPDF) effect in DIS data in 1981 [75]. These data indicated for the first time that the proton PDF in a nucleus (nPDF) is modified compared to the free proton PDF: $f_i^{p/A}(x, Q^2) \neq f_i^p(x, Q^2)$, where $f_i^{p/A}$ is defined as the PDF of the parton of flavour i inside a proton bound in a nucleus. The nuclear modification factor is defined as $R_j^A \equiv f_j^{p/A}/f_j^p$. The magnitude of this nuclear effect

---

[5]This value is modified at very low beam energy.

[6]Certainly, the pion PDF and the hard process order will also change the relative contribution of these two sub-processes.
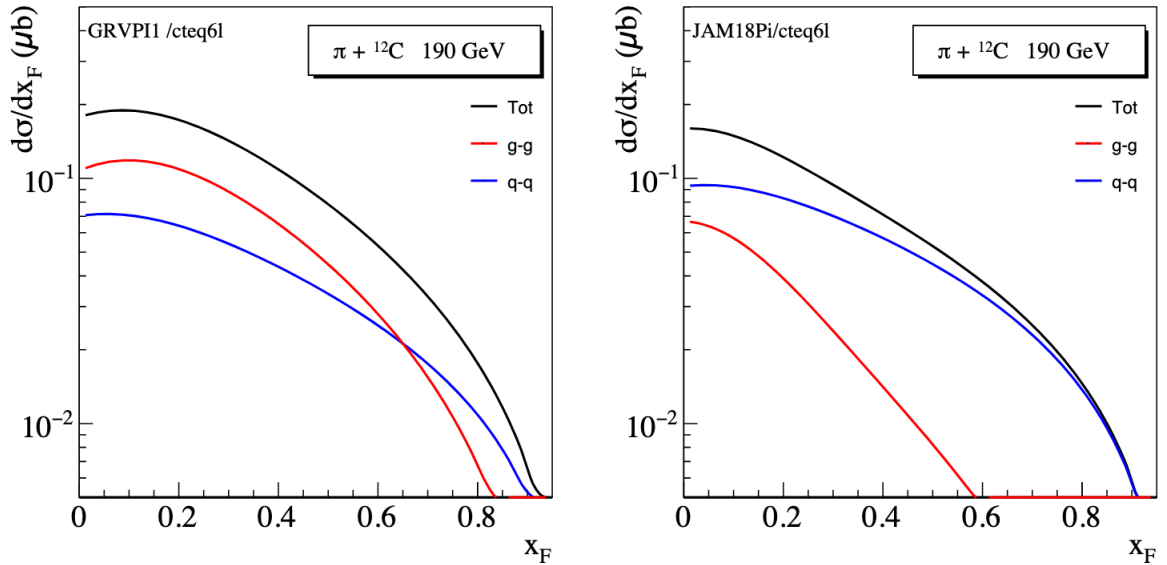
Figure 2.3: Differential J/ψ cross section using the CEM model at LO at E_{beam}=190 GeV in $\pi^- A$ collisions using the GRV (left panel) and JAM pion PDFs (right panel).

depends on the x range probed in the nucleus. At $0.3 < x < 0.7$ (*EMC effect*), the ratio of the nucleon PDFs measured on iron (Fe) and deuterium (D) shows a slight depletion below 1. In contrast at smaller $x \lesssim 0.3$ (*anti-shadowing effect*), the ratio shows an increase higher than 1. Since then, four main regions have been distinguished:

- $x \gtrsim 0.7$: Fermi motion $R^A(x, Q^2) \gtrsim 1$;

- $0.3 \lesssim x \lesssim 0.7$: EMC region[7] $R^A(x, Q^2) \lesssim 1$;

- $0.1 \lesssim x \lesssim 0.3$: Anti-shadowing region $R^A(x, Q^2) \gtrsim 1$;

- $x \lesssim 0.1$: Shadowing region $R^A(x, Q^2) \lesssim 1$.

The latest global fit extractions of nPDF at NLO using DGLAP evolution (see Sec. 1.1.6) was performed by DSSZ [77], nCTEQ15 [70], and EPPS16 [78]. The latter includes for the first time data from the LHC. In order to take into account nPDF effects on dilepton production in hadron-nucleus collisions, f_j^p (f_j^n) needs to be replaced by $f_j^{p/A}$ ($f_j^{n/A}$) in Eq. (2.3),

$$f_j^A(x_2, Q^2) = Z \, f_j^{p/A}(x_2, Q^2) + (A - Z) \, f_j^{n/A}(x_2, Q^2) \,, \tag{2.17}$$

---

[7]Since its discovery the interpretation of the EMC effect remained a puzzle. Recently [76], a new interpretation by CLAS collaboration was suggested. This study shows an universal modification of the nucleon structure in the short range correlation proton and neutron pair in nucleus.

where the bound neutron $f_j^{\mathrm{n/A}}$ nPDF is determined by assuming SU(2) isospin symmetry as,

$$
\begin{aligned}
f_{u,\overline{u}}^{\mathrm{n/A}}\left(x,Q^2\right) &= f_{d,\overline{d}}^{\mathrm{p/A}}\left(x,Q^2\right), \\
f_{d,\overline{d}}^{\mathrm{n/A}}\left(x,Q^2\right) &= f_{u,\overline{u}}^{\mathrm{p/A}}\left(x,Q^2\right), \\
f_{i}^{\mathrm{n/A}}\left(x,Q^2\right) &= f_{i}^{\mathrm{p/A}}\left(x,Q^2\right) \ \ \text{for other flavours.}
\end{aligned}
\tag{2.18}
$$

Let us now briefly describe the data used in different collisions to extract nPDFs:

- DIS data from EMC, SLAC, NMC and CHORUS experiments [78] ($\ell A \to \ell + X$) describe a scattering of a lepton (ℓ) on a nucleus (A) via the production of space-like virtual photon or W boson (in ν_l diffusion). This process enables to probe the quark distributions of the nucleus. Depending on the collision energy, they data help to constrain both sea and valence quark distributions at rather large x, $10^{-2} \lesssim x \lesssim 1$. The largest amount of data used for the nPDF extraction comes from this process [78, 70].

- π^0 production (hA $\to \pi^0 + X$) at $p_\perp \lesssim 16$ GeV from PHENIX and STAR experiments [79, 80] at PHENIX ($\sqrt{s} = 200$ GeV). These data can *a priori* be used to probe the gluon sector nPDF around $10^{-2} \lesssim x \lesssim 10^{-1}$ at mid rapidity for instance.

- Z/W production (pA $\to$ Z and pA $\to$ W via u$\overline{\mathrm{d}} \to$ W$^+$ and d$\overline{\mathrm{u}} \to$ W$^-$) are measured at LHC energies by the ATLAS and CMS experiments at $\sqrt{s} = 5.02$ TeV and $\sqrt{s} = 8.16$ TeV [81, 82, 83]. These data constrain the quark nPDFs in the shadowing and antishadowing region for $10^{-3} \lesssim x \lesssim 10^{-1}$ depending on the decay lepton rapidity.

- Dijet data from CMS experiment [84] at $\sqrt{s} = 5.02$ GeV at large $p_\perp \gtrsim 30$ GeV. These data constrain quark and gluon nPDFs at $x \sim 10^{-2}$ and $x \sim 10^{-1}$ depending on the pseudo-rapidity η_{dijet}[8] probed.

- DY data in pA collisions from E772 [85] and E866 [86] fixed-target experiments at $\sqrt{s} = 38.7$ GeV collected in dilepton mass range $4 < M < 8$ GeV. These data constrain sea quark nPDFs mainly in the shadowing region around $x \sim 0.1$. In addition, DY data in πA collisions from NA10 [87], NA3 [88] and E615 [89] fixed-target experiments from $\sqrt{s} = 16.2$ to 23.1 GeV are used. In these collisions, DY production is sensitive to the valence quark PDFs of the target. These data *a priori* constrain valence quark nPDFs in the EMC and anti-shadowing region for $0.1 \lesssim x \lesssim 0.5$.

A summary of the data used by each group is shown in Table 2.2. In the next sections, I will discuss four different parameterizations of recent nPDFs from the EPPS16, EPS09 [90], nCTEQ and DSSZ groups.

---

[8]The pseudo-rapidity is defined like $\eta = -\ln\left(\tan(\theta/2)\right)$, where θ is the polar angle with respect to the proton beam direction. In ulta-relativistic limit, $y = \eta$.

	EPS09	**DSSZ**	**nCTEQ**	**EPPS16**
e-DIS	✓	✓	✓	✓
ν-DIS		✓		✓
DY pA	✓	✓	✓	✓
RHIC hadrons	✓	✓	✓	✓
LHC data				✓
DY πA				✓

Flavor decomposition			✓	✓
Baseline	CTEQ6.1	MSTW2008		CT14

Table 2.2: Recent global analysis of nuclear PDFs.

2.2.1 EPPS16 and EPS09 global fit

The EPPS16 group used all data discussed above, in particular including the DY data in πA collisions and the data from LHC. Each nPDF is constructed from CT14 free proton PDF [28], named *baseline*, by fitting the nPDF ratio as

$$
R_i^{\mathrm{A}}\left(x, Q_0^2\right) = \begin{cases} a_0 + a_1\left(x - x_a\right)^2 & x \leq x_a \\ b_0 + b_1 x^\alpha + b_2 x^{2\alpha} + b_3 x^{3\alpha} & x_a \leq x \leq x_e \\ c_0 + \left(c_1 - c_2 x\right)\left(1 - x\right)^{-\beta} & x_e \leq x \leq 1 \end{cases} \tag{2.19}
$$

where a_i, b_i, c_i are free parameters and determined by the asymptotic small x limit at $y_0 = R_i^{\mathrm{A}}\left(x \to 0, Q_0^2\right)$, the antishadowing maximum and the EMC minimum are defnined as $y_a = R_i^{\mathrm{A}}\left(x_a, Q_0^2\right)$ and $y_e = R_i^{\mathrm{A}}\left(x_e, Q_0^2\right)$ respectively and $\alpha = 10x_a$. The EPPS16 nPDF A-dependence of y_0, y_a and y_e are parametrized as

$$
y_i(A) = y_i\left(\mathrm{A_{ref}}\right)\left(\frac{\mathrm{A}}{\mathrm{A_{ref}}}\right)^{\gamma_i[y_i(A_{\mathrm{ref}})-1]} \tag{2.20}
$$

where the initial energy scale is $Q_0 = 1.3$ GeV, $\mathrm{A_{ref}} = 12$ and $\gamma_i \geq 0$ is a positive parameter. Figure 2.4 shows the nPDF ratio R_j^{A} for the W nucleus at $Q^2 = 10$ GeV^2 ($Q^2 \sim M_{J/\psi}^2$) at NLO for several parton flavours ($u_{\mathrm{v}}(x)$, $d_{\mathrm{v}}(x)$, $g(x)$, $u_{\mathrm{s}}(x)$ and $d_{\mathrm{s}}(x)$)[9] including the error band (blue band), the individual error sets (blue line) and the best fit extraction (black line). The global fits are performed using 20 free parameters including 5 additional parameters compared to the previous EPS09 nPDF extraction in order to take into account the flavour dependence of quark nPDFs observed in LHC data.[10] EPS09 nuclear modification factor is also shown in Fig. 2.5 for comparison. The EPPS16 nPDFs error band increases, compared to EPS09 as illustrated in Figs. 2.5 and 2.4, because of the additional fit parameters included for each parton flavour to take into account the flavour dependence highlighted in W and Z bosons production at LHC [81, 82, 83].

---

[9]The v and s labels denote respectively valence and sea.

[10]In Z/W production measured at LHC energies, the data point to a difference between $\bar{d}$ and $\bar{u}$ nPDFs [81, 82, 83].
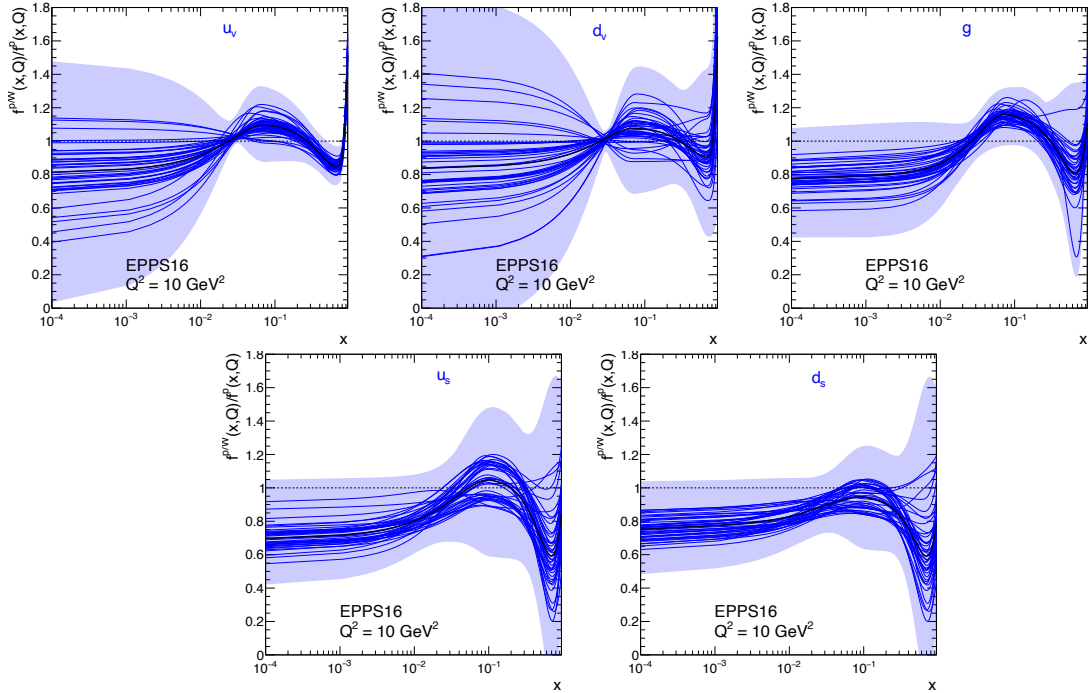
Figure 2.4: nPDF ratio $f^{\mathrm{p/W}}(x,Q)/f^{\mathrm{p}}(x,Q)$, their associated uncertainties (blue band) with the central set (black line) and all error sets (blue lines) at $Q^2 = 10$ GeV^2 using EPPS16 NLO parameterization [78].
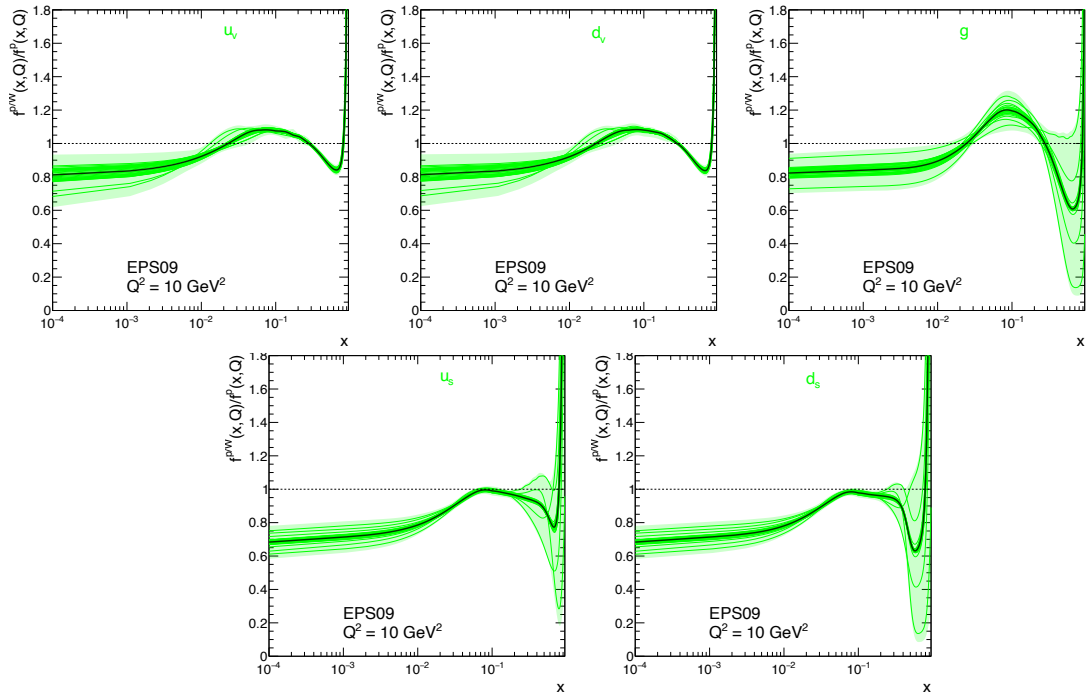
Figure 2.5: nPDF ratio $f^{\mathrm{p/W}}(x,Q)/f^{\mathrm{p}}(x,Q)$, their associated uncertainties (green band) with the central set (green line) and all error sets (green lines) at $Q^2 = 10$ GeV^2 using EPS09 NLO parameterization [90].

In both cases, all error sets are not homogeneously distributed in the nPDFs error band. In some cases, one error set give the whole width of the error band in particular for the gluon

nPDF at $x \gtrsim 10^{-1}$. EPPS16 shows globally significantly larger error bands compared to previous EPS09 extraction. In this sense, the EPPS16 fits are more conservative.

Recently [91], EPPS16 group scrutinised the recent LHCb D^0-meson data in pPb collisions (pA $\rightarrow$ D^0+X) in $0 \lesssim p_\perp \lesssim 10$ GeV interval at forward and backward rapidity. A good agreement was found, within the large error band, with actual nPDF extraction. These data should *a priori* give an important nPDF constrain in gluon sector for $10^{-5} \lesssim x \lesssim 10^{-2}$.

2.2.2   nCTEQ global fit

The nPDFs from nCTEQ collaboration used all data discussed above except the DY data from πA collisions and LHC data. They included 16 free parameters by fitting directly the nPDF $f_i^{\mathrm{p/A}}(x, Q_0^2)$ via the same parametrisation used for the free proton CTEQ fits [27],

$$
\begin{aligned}
x f_i^{\mathrm{p/A}}\left(x, Q_0^2\right) &= c_0 x^{c_1}(1-x)^{c_2} e^{c_3 x}\left(1+e^{x_4} x\right)^{c_5} \\
\frac{\overline{d}\left(x, Q_0^2\right)}{\overline{u}\left(x, Q_0^2\right)} &= c_0 x^{c_1}(1-x)^{c_2}+\left(1+c_3 x\right)(1-x)^{c_4}
\end{aligned}
\tag{2.21}
$$

where the initial energy scale is $Q_0 = 1.3$ GeV, $x f_i^{\mathrm{p/A}}(x, Q_0^2)$ is the bound proton nPDF of a nucleus A for a parton flavour a, c_k is the fit parameters, $\overline{d}(x, Q_0^2)$ and $\overline{u}(x, Q_0^2)$ are the nPDF of $\overline{d}$ and $\overline{u}$ quarks. The $s(x, Q_0^2)$ and $\overline{s}(x, Q_0^2)$ nPDFs are assumed to be the same. The nCTEQ nPDF A-dependence is directly related to the c_i coefficients,

$$
\begin{aligned}
c_k(A) &\equiv c_{k,0}+c_{k,1}\left(1-A^{-c_{k,2}}\right) \\
k &= \{1, \ldots, 5\}.
\end{aligned}
\tag{2.22}
$$

Figure 2.6 shows the nuclear modification factor R_j^{A} for the W nucleus at $Q^2 = 10$ GeV^2 at NLO for several parton flavours ($u_{\mathrm{v}}(x)$, $d_{\mathrm{v}}(x)$, $g(x)$, $u_{\mathrm{s}}(x)$ and $d_{\mathrm{s}}(x)$) including the error band (red band), each error sets (red line) and the best fit extraction (black line). The comparison between nCTEQ, EPS09 and EPPS16 parameterizations, exhibits important differences in particular for the gluon and d valence quark nPDFs.

2.2.3   DSSZ global fit

The nPDFs from the DSSZ group are fitted using 25 free parameters without DY data from πA collisions and LHC data. These nPDFs are extracted directly by fitting the modification factor R_j^A with the baseline for the free proton PDF from MSTW2008 [26]. The nuclear modification factor of valence quark distributions is parametrized as

$$
R_v^{\mathrm{A}}\left(x, Q_0^2\right) = \epsilon_1 x^{\alpha_v}(1-x)^{\beta_1} \times\left(1+\epsilon_2(1-x)^{\beta_2}\right)\left(1+a_v(1-x)^{\beta_3}\right),
\tag{2.23}
$$
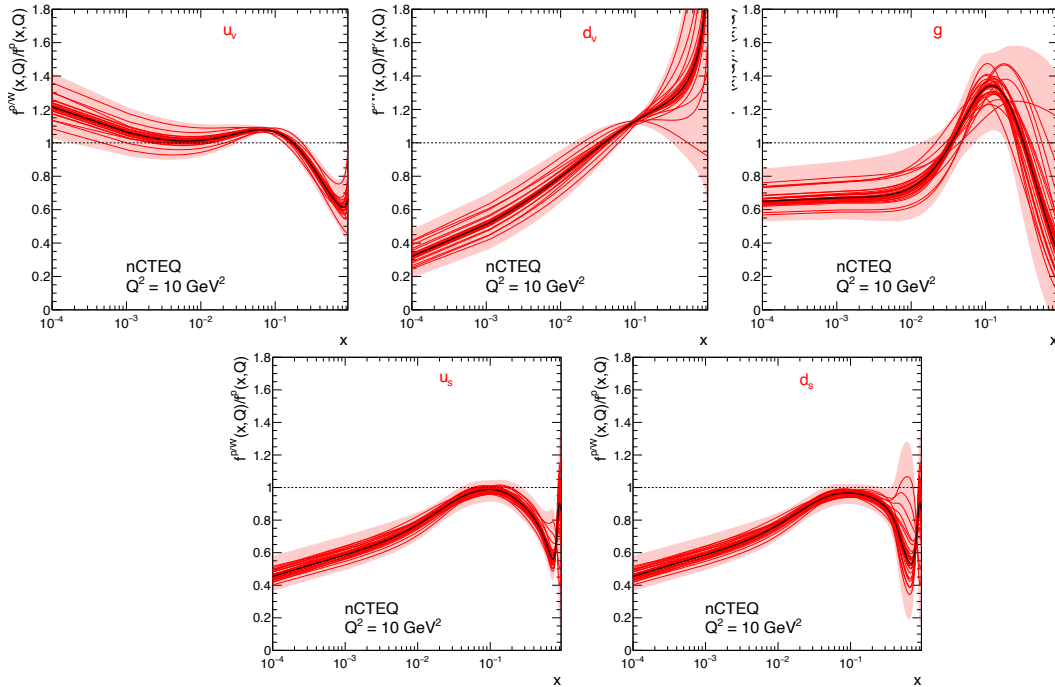
Figure 2.6: nPDF ratio $f^{\text{p/W}}(x,Q)/f^{\text{p}}(x,Q)$, their associated uncertainties (red band) with the central set (black line) and all error sets (red lines) at $Q^2 = 10$ GeV^2 using nCTEQ15 NLO parameterizations [70].

and for the gluon and sea quark distributions, the nuclear modification factor is parametrized using Eq. (2.23) as

$$
\begin{aligned}
R_s^{\text{A}}\left(x,Q_0^2\right) &= R_v^{\text{A}}\left(x,Q_0^2\right) \frac{\epsilon_s}{\epsilon_1} \frac{1 + a_s x^{\alpha_s}}{a_s + 1} \\
R_g^{\text{A}}\left(x,Q_0^2\right) &= R_v^{\text{A}}\left(x,Q_0^2\right) \frac{\epsilon_g}{\epsilon_1} \frac{1 + a_g x^{\alpha_g}}{a_g + 1}
\end{aligned}
\tag{2.24}
$$

with the initial energy scale $Q_0 = 1$ GeV and α_s, α_g, a_s and a_g are free parameters. The $s(x,Q_0^2)$ and $\bar{s}(x,Q_0^2)$ nPDFs are assumed to be the same. The A-dependence nPDF is determined via

$$
\xi = \gamma_\xi + \lambda_\xi \text{A}^{\delta_\epsilon}
\tag{2.25}
$$

with γ_ξ, λ_ξ and δ_ξ and $\xi \in \{\alpha_v, \alpha_s, \alpha_g, \beta_1, \beta_2, \beta_3, a_v, a_s, a_g\}$, the additional free parameters to reproduce the A-dependence. Moreover DSSZ group includes, in neutral pion production data [79, 80], the medium modified fragmentation function in the pion hadronization described in [92]. DSSZ nPDFs show a compatibility with EPS09 nPDF for valence quark distributions. But the more important differences come from the gluon nPDF where the shadowing effect is much lower in DSSZ compared to EPPS16, EPS09 and nCTEQ nPDFs. In particular at $x \sim 10^{-4}$ where $R_g^{\text{A}}(x,Q^2 = 10) \approx 1$[11] as shown in Fig. (14) in [77]. In addition, the anti-shadowing and EMC effects for sea quark distributions predicted by EPPS16, EPS09 and nCTEQ nPDFs is considerable compared to the DSSZ nPDF exhibiting moderate nuclear corrections.

---

[11]At low scale $Q \sim 1$ GeV, DSSZ group shows an important dependence on Q and predicts an important effect in this energy scale region.

After discussing the latest nPDFs extractions, it clear that the nuclear modification factor depends both on the data used and especially on the assumptions regarding nPDF parameterizations. While EPPS16, by adding free parameters, has considerably widened the error bands compared to the previous EPS09 extraction. EPS09 and nCTEQ show significant nuclear effects for all flavours. Finally, DSSZ group predicts a much lower gluons nPDF effect. At the same time, in the EMC and anti-shadowing regions above $x \gtrsim 0.1$, they exhibit less sea quark nPDFs effect compared to the previous groups mentioned. As much as all the groups agree on the presence of a nuclear modification effect at large $x \gtrsim 0.1$ for valence quark distributions, the conclusion for the gluon as well as for the sea quarks nPDFs is not yet clear. The next measurements coming from Electron-Ion-Collider (EIC) in DIS production will be able to probe small $x \lesssim 10^{-4}$ allowing for setting strong constraints on the nPDFs of the sea quarks and gluons [93, 94].

2.3   Nuclear absorption

In this section, a second nuclear effect is introduced: the nuclear absorption. This effect affects only the charmonium production in hA collisions. It describes the probability that a bound state H, typically the J/ψ meson, interacts inelastically with a nucleon from a nucleus (so called absorption). When the produced $Q\bar{Q}$ pair hadronizes within a time t_{had} into a bound state H, this one can be dissociated while its travelling trough the nucleus. The condition for this to take place is that the bound state H is formed inside the nucleus. The following condition must therefore be satisfied

$$t_{had} = \gamma \tau_{had} \lesssim L \tag{2.26}$$

where L is the medium length, $\gamma = \frac{E}{M_H}$ the Lorentz factor, E, M_H and τ_{had} are respectively the energy, the mass of the bound state H and $\tau_{had} \approx 0.2 - 0.4$ fm [95, 96, 97], its formation time in *the nucleus rest frame*. The relation between the J/ψ energy E and the $x_{\rm F}$ value in a $2 \rightarrow 1$ kinematics[12] is given by [4]

$$E\left(x_{\rm F}\right) = E_{\rm beam} \cdot \left[\frac{x_{\rm F}}{2} + \sqrt{\left(\frac{x_{\rm F}}{2}\right)^2 + \frac{M_H^2}{s}} \right], \tag{2.27}$$

where $E_{\rm beam}$ is the beam energy in the nucleus rest frame. To illustrate in which kinematical domain the nuclear absorption can have an impact on the J/ψ cross section in hA collisions, Fig. 2.7 shows the $x_{\rm F}^{\rm abs}$ limit below which the condition from Eq. (2.26) is verified for a typically heavy nucleus W with $A = 184$ (with $L_{\rm W} \approx (3/2)R = 3/2 r_0 A^{\frac{1}{3}} \sim 9.6$ fm) at E866/NuSea ($E_{\rm beam}$ = 800 GeV), COMPASS ($E_{\rm beam}$ = 190 GeV) and E906/SeaQuest ($E_{\rm beam}$ = 120 GeV) beam energy. At low beam energy, *i.e.* when $E_{\rm beam} \lesssim 1$ TeV, the J/ψ nuclear absorption effect can have an impact on the data until relatively high $x_{\rm F}$ values. For instance, at E866 beam energy,

---

[12]The $p_\perp$ dependence in the invariant mass calculation is neglected as far as in fixed-target configuration at these beam energies, we have $p_\perp \ll M$.

the nuclear absorption has an impact only for $x_F \lesssim 0.1$, whereas the more the beam energy decreases, the more this limit shifts towards larger x_F. By taking $\tau_{had}^{J/\psi} = 0.3$ fm, the J/ψ is produced systematically higher than the length (L_W) of the nucleus, $L_W \lesssim t_{had}$ at positive x_F, except at very low beam energy at E_{beam}=190 GeV, where the $t_{had} \lesssim L_W$ when $x_F \lesssim 0.5$ (see Fig. 2.7). This limit changes to $x_F \lesssim 0.8$ at the beam energy of E906 experiment. Note that it is difficult to estimate the exact value of x_F^{abs} limit where the condition in Eq. (2.26) is verified because of the uncertainty on the J/ψ formation time. However, this makes it possible to give a reasonable order of magnitude. Knowing the x_F region where this effect can play a role, the
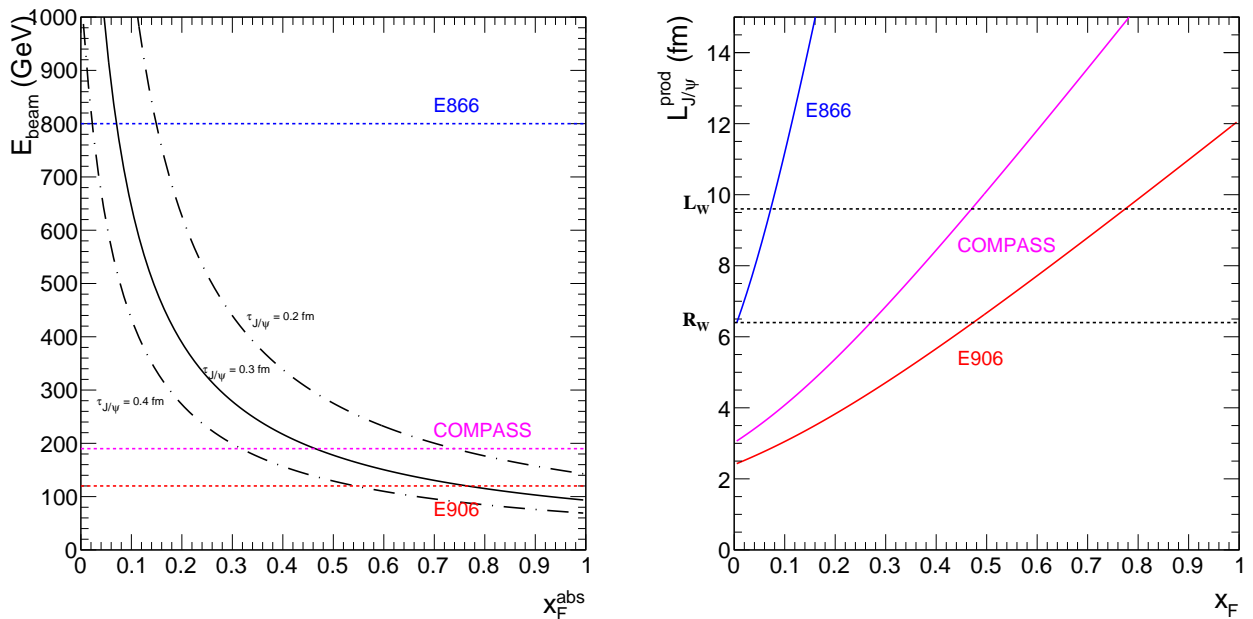
Figure 2.7: x_F^{abs} as a function E_{beam} for different J/ψ formation time $\tau_{had}^{J/\psi} = 0.2$, 0.3 and 0.4 fm (left panel) and J/ψ production at length $L_{J/\psi}^{prod}$ fm as a function of x_F assuming $\tau_{had}^{J/\psi} = 0.3$ fm (right panel).

absorption survival probability by the medium can be computed as [50],

$$S(\sigma_{abs}, l_A) = e^{-\rho\sigma_{abs}l_A} \tag{2.28}$$

where σ_{abs} is the nuclear absorption cross section, l_A the medium length crossed by the J/ψ calculated from the Glauber model [98] and $\rho = 0.17$ fm^{-3} the nuclear density. The global data analysis from SPS to RHIC experiments was done by [99, 100] and the best fit gave the J/ψ nuclear absorption cross section equal to $\sigma_{abs}^{J/\psi N} = 3.5 \pm 0.2$ mb. According to Eq. (2.28), the J/ψ cross section in hA can be written as

$$\frac{d\sigma^{hA}[J/\psi + X]}{dy} = S(\sigma_{abs}, l_A) \times \frac{d\sigma^{hp}[J/\psi + X]}{dy} \times A. \tag{2.29}$$

For illustration, $S(\sigma_{abs}, l_A)$ is evaluated for a W nucleus, by taking $l_A = R_W \sim 6.4$ fm and $\sigma_{abs}^{J/\psi N} = 3.5 \pm 0.2$ mb. The cross section ratio due to nuclear absorption is equal to

$$R_{hA}^{J/\psi, abs} = 0.68 \pm 0.02. \tag{2.30}$$

2.4 Parton energy loss in a QCD medium

Finally, another nuclear effect plays a key role in the nuclear modification ratio: parton energy loss. When a color charge (quark or gluon) passes through a QCD medium - for instance in a confined cold medium like a nucleus or in a hot and deconfined medium like a quark-gluon plasma - the rescattering in the medium induces a gluon radiation spectrum leading to energy loss. This effect was highlighted, for the first time, in heavy ion collisions at RHIC (and later at LHC) through the suppression of hadrons, generically named *jet quenching phenomenon*, see [101, 102, 103, 104]. The effect of energy loss can be simply modelled like

$$\frac{\mathrm{d}N^{\mathrm{out}}(E)}{\mathrm{d}E} = \int_{\epsilon} \mathcal{D}(\epsilon, E) \frac{dN^{\mathrm{in}}(E + \epsilon)}{dE}, \tag{2.31}$$

where $\frac{\mathrm{d}N^{\mathrm{in}}(E)}{\mathrm{d}E}$ and $\frac{\mathrm{d}N^{\mathrm{out}}(E)}{\mathrm{d}E}$ are respectively the initial and final differential energy distributions of a high energetic parton entering in the QCD medium, ϵ the energy loss value, $\mathcal{D}(\epsilon, E)$ is the probability energy loss distribution related to the medium-induced gluon spectra. The
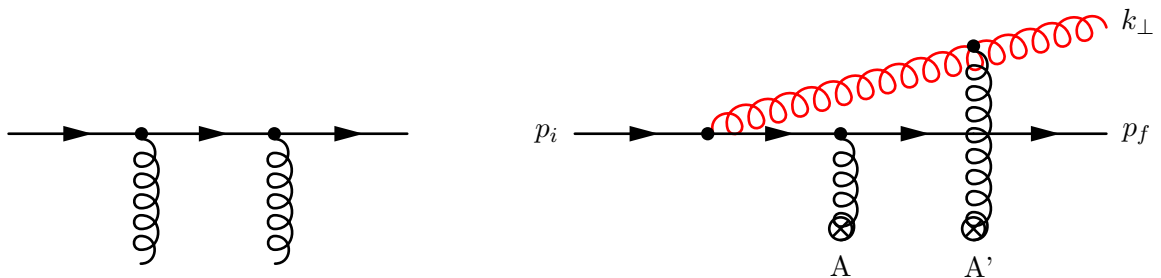
Figure 2.8: Typical diagram for collisional (left panel) and gluon energy loss radiation (right panel) of an energetic quark travelling in a nuclear medium.

scattering center responsible for gluon radiation are considered independently when the typical gluon formation $\tau_f \sim 2\omega/k_\perp^2$ where ω is the gluon energy and $k_\perp$ its transverse momentum [105, 106], becomes $\lambda \lesssim \tau_f \ll L$ where λ is the mean free path of the propagating high energy parton, namely the distance between two scattering centers noted A and A' as illustrated in Fig. 2.8. Each group of τ_f/λ scattering centers acts can be considered as unique coherent source for gluon radiation: this effect is named *Landau-Pomeranchuk-Migdal* (LPM) effect [105, 106]. In contrast, when $\tau_f < \lambda$, each scattering center acts are as an independent source of radiation: this is the *Bethe-Heitler* regime [105, 106]. Finally, the last case $\tau_f \gg L$, all scattering centers in the medium act coherently as a source of radiation. The latest regime is named *fully coherent* and was highlighted in recent years [4, 3, 107]. Several formalism[13] have been developed to describe the energy loss by medium-induced gluon radiation in a dense nuclear matter, namely: Baier, Dokshitzer, Mueller, Peigné, Schiff and Zakharov (BDMPS-Z) formalism [105, 106, 110], Gyulassy, Levai and Vitev formalism (GLV) [111, 112, 113], Wiedemann [114, 115] and Higher

---

[13]Arnold-Moore-Yaffe formalism (AMY) [108, 109] is not included here because it is suitable for a hot nuclear medium at very high temperature, namely in a QGP.

Twist formalism (HT) [116, 117]. In this part, only the BDMPS formalism will be briefly discussed as it will be used in Chapters 6 and 7.

The BDMPS formalism works in the limit of high energy for the incident parton (E) and the soft gluon radiation approximation $\omega \ll E$. It describes the multiple soft scattering induced by the medium, characterised by the transport coefficient $\hat{q} = (d\Delta p_\perp^2)/dL$, where $\Delta p_\perp$ is the transverse momentum acquired by the high energetic parton propagating in the medium per unit path length. The energy of the parton is considered as larger compared to the transverse momentum exchanged during the scattering, knows as *eikonal approximation*:

$$E \gg \mu. \tag{2.32}$$

In addition, the energy of emitted gluon is considered as larger compared to its transverse momentum: $\omega \gg k_\perp$ (*collinear approximation*).

2.4.1 Transport coefficient and broadening effect

When a parton propagates in a nucleus, it is impacted by two related nuclear effects. First, the gluon exchanges with the medium and the parton partially transforms parton longitudinal into transverse momentum, leading to a broadening effect. Secondly, medium induced gluon radiation caused by multiple scattering leads to parton energy loss. These two different nuclear effects are related to the same quantity: the transport coefficient $\hat{q}$, which characterises the scattering properties of the medium. The interaction between a parton and a medium is determined by two quantities: the typical momentum transferred μ in a single scattering and the mean free path $\lambda = [\rho\sigma]^{-1}$ related to nuclear matter density ρ and the single scattering cross section σ. The transport coefficient $\hat{q}$ giving by [105, 106] at LO is

$$\hat{q} \equiv \frac{\mu^2}{\lambda} = \frac{4\pi^2\alpha_s C_R}{N_c^2 - 1}\rho \times xG\left(x, Q^2\right) \tag{2.33}$$

with $Q^2 \sim \Delta p_\perp^2$ and C_R the color charge of parton, i.e. $C_R = \left(N_c^2 - 1\right)/2N_c = 4/3$ for a quark and $C_R = N_c = 3$ for a gluon. Thus the transport coefficient $\hat{q}$ is directly related to the gluon distribution $xG(x)$ of the nucleons and the nuclear density ρ.

Figure 2.9 shows schematically the impact of radiative energy loss and transverse momentum broadening effects on a parton with initial energy E and transverse momentum $p_\perp$. The average accumulated transverse momentum squared acquired by the parton is given by [106]

$$(\Delta\vec{p}_\perp)^2 \approx \mu^2\frac{L}{\lambda} = \hat{q}L \tag{2.34}$$

where L is the effective nuclear length, i.e. the length that the parton travels in the medium. This observable will be discussed in more detail in the Chapter 7.
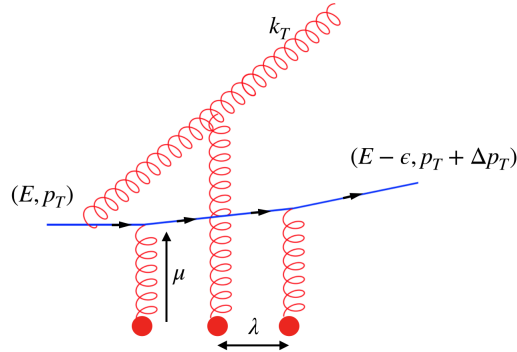
Figure 2.9: Cartoon of radiative energy loss and broadening effect from a hard parton with an energy E and a transverse momentum $p_\perp$ scattering a QCD medium.

2.4.2 Energy loss regimes

The radiative energy loss induces a gluon radiation spectra. The probability that a parton of energy E radiates n gluons with a total energy ϵ has been determined by [105, 106].

Depending on the hard process and therefore the gluon formation time τ_f compared to the length of the medium crossed L, the average energy loss will be different. Two situations stands out:

- The LPM regime, i.e. $\lambda \lesssim \tau_f \ll L$, corresponds to the case where an incoming *or* outgoing high-energy parton crosses the nucleus from a hard collision. The first case is associated to the DY production (hA$\rightarrow \gamma^\star$) and the second case to the SIDIS production (lA$\rightarrow l + h$). The probability $\mathcal{D}(\epsilon)$ to lose an energy ϵ, based on *independent* and *soft* gluons radiations, reads

$$\mathcal{D}(\epsilon) = \sum_{n=0}^{\infty} \frac{1}{n!} \left[\prod_{i=1}^{n} \int d\omega_i \frac{dI(\omega_i)}{d\omega} \right] \delta \left(\epsilon - \sum_{i=1}^{n} \omega_i \right) \cdot \exp \left[- \int_0^{+\infty} d\omega \frac{dI(\omega)}{d\omega} \right], \qquad (2.35)$$

with n, the number of gluon emission emitted by the hard parton and $\frac{dI(\omega_i)}{d\omega}$ is the medium-induced gluon spectrum [105],

$$\left(\omega \frac{dI}{d\omega} \right)_{\text{LPM}} \sim \alpha_s N_c \frac{L}{\tau_f} = \frac{\alpha_s N_c}{\pi} \sqrt{\frac{\hat{q} L^2}{\omega}}. \qquad (2.36)$$

In the LPM regime when $\lambda \lesssim \tau_f \ll L$, the average energy loss is [105, 106]

$$\langle \epsilon \rangle_{\text{LPM}} \equiv \int_0^\infty d\epsilon D(\epsilon) \epsilon \propto \alpha_s \hat{q} L^2. \qquad (2.37)$$

The effects of initial-state (or, final-state) energy loss in nuclear matter should be negligible at high energy, $\langle \epsilon \rangle_{\text{LPM}} \ll E$, as the particle energy *in the nucleus rest frame* gets large, $E \propto s$ leading to $\Delta E/E \rightarrow 0$. The LPM regime in DY process will be studied in more detail in Chapter 6.

- The *Fully Coherent Energy Loss* (FCEL) regime [4, 3, 107], i.e. $\tau_f \gg L$, has an impact in the case where one incoming *and* one outgoing high-energy parton is produced in the nucleus. While the two partons undergo the initial and final LPM energy loss, the FCEL energy loss dynamic is generated by the interference term between the both partonic states. The medium-induced gluon spectrum in this regime is [4]

$$\left(\omega\frac{\mathrm{d}I}{\mathrm{d}\omega}\right)_{\mathrm{FCEL}} = \frac{N_c\alpha_s}{\pi}\left\{\ln\left(1+\frac{\Delta q_\perp^2 E^2}{M_\perp^2\omega^2}\right) - \ln\left(1+\frac{\Lambda_\mathrm{p}^2 E^2}{M_\perp^2\omega^2}\right)\right\}\Theta\left(\Delta q_\perp^2 - \Lambda_\mathrm{p}^2\right), \quad (2.38)$$

with $M_\perp = \left(M^2 + p_\perp^2\right)^{\frac{2}{2}}$ the transverse mass momentum and $\Lambda_\mathrm{p}^2 = \max\left(\Lambda_\mathrm{QCD}^2, \Delta q_\perp^2\right)$. The FCEL energy loss average leads to

$$\langle\epsilon\rangle_{\mathrm{FCEL}} \propto \sqrt{\hat{q}L}/M_\perp \cdot E. \quad (2.39)$$

This energy loss regime plays a role in the hadron production[14] in hA$\to q/g(\to h') + X$ collisions. The LPM energy loss regime is significantly lower than the FCEL regime in high energy limit, $\langle\epsilon\rangle_{\mathrm{LPM}} \ll \langle\epsilon\rangle_{\mathrm{FCEL}}$. Since the mean energy loss in LPM regime is independent of parton energy E whereas the mean energy loss FCEL regime depends on it.

Energy loss	Process	Regime	$\langle\epsilon\rangle$
Initial-state	hA $\to \ell^+\ell^- + X$ (LO DY)	$\tau_f \lesssim L$ (LPM)	$\propto \hat{q}L^2$
Final-state	eA $\to e + h + X$ (SIDIS)	$\tau_f \lesssim L$ (LPM)	$\propto \hat{q}L^2$
Fully coherent	hA $\to [Q\bar{Q}(g)]_8 + X$ (quarkonium)	$\tau_f \gg L$	$\propto \sqrt{\hat{q}L}/M \cdot E$

Table 2.3: LPM and FCEL energy loss regimes.

2.5 Empirical observations

2.5.1 Data

In this section, the nuclear dependence as a function of the rapidity (or x_F) and the transverse momentum of DY and charmonium data from fixed-target to collider experiments will be commented in light of the nuclear effects introduced previously. The fixed target configuration provides a higher luminosity compared to colliders allowing for data samples within large statistics. In addition, thanks to the boost of the center-of-mass of the reaction, the collected data make it possible to access very large values of x_F in the $0 \lesssim x_\mathrm{F} \lesssim 1$ interval. A systematic comparison will be made between the nuclear dependence of DY and J/ψ data. Below are some observations from the data displayed in Table 2.4.

---

[14]Typically in J/ψ production.
[14]These data will be available in the future.

Exp.	Beam	$\sqrt{s}$ (GeV)	Process	A	Dependence	Ref.
E906	p	15	DY	Fe, W	x_{F}	[118]
COMPASS	π^-	18.9	DY	NH3, Al, W	$x_{\mathrm{F}}, p_\perp$	[119]
			J/ψ	NH3, Al, W	$x_{\mathrm{F}}, p_\perp$	
NA3	p	19.4	J/ψ	H, Pt	$x_{\mathrm{F}}, p_\perp$	[120]
	π^-	16.7/19.4/22.9				
	π^+	19.4				
	π^-	16.7/19.4/22.9	DY	Pt	$x_{\mathrm{F}}, p_\perp$	[87, 121]
NA10	π^-	16.2/23.1	DY	W	$x_{\mathrm{F}}, p_\perp$	[122, 88]
		23.1	J/ψ	D, W		
E772	p	38.7	DY	Ca, Fe, W	$x_{\mathrm{F}}, p_\perp$	[123]
			Υ	Ca, Fe, W	$p_\perp$	
E866	p	38.7	DY	Be, Fe, W		[124]
			J/ψ	Be, Fe, W	$x_{\mathrm{F}}, p_\perp$	[86]
PHENIX	d	200	J/ψ	Au	y, $p_\perp$	[125]
ALICE	p	5020	J/ψ	Pb	y, $p_\perp$	[126, 127]
LHCb	p	8160	J/ψ	Pb	y, $p_\perp$	[128]

Table 2.4: Data sets from experiment for DY and quarkonia nuclear dependence.

Drell-Yan data

- Preliminary DY data from the **E906/SeaQuest** experiment using a proton beam at E_{p} = 120 GeV show $R_{\mathrm{pA}}^{\mathrm{DY}} < 1$ along x_{F}, in particular at large x_{F}. The suppression is more important in the W compared to Fe nuclear targets (both normalised to the Be target).

- The **NA3** experiment collected DY data using a negative pion beam at E_{π^-} = 150 GeV, $R_{\pi\mathrm{A}}^{\mathrm{DY}}$ exhibit a small x_1 dependence. In addition, at all beam energies, the $p_\perp$ dependence shows no target dependence. Due to a large error bar, these data are compatible with the absence of nuclear effects (besides isospin effect).

- DY data from the **NA10** experiment show as a function of x_2, $R_{\pi^-\mathrm{A}}^{\mathrm{DY}}(\sqrt{s} = 16.2 \text{ GeV}) \lesssim R_{\pi^-A}^{DY}(\sqrt{s} = 23.1 \text{ GeV})$ despite large error bars.

- DY data from the **E866** experiment (and E722 experiment) indicate a small x_{F} and $p_\perp$ dependencies in DY data as illustrated in Figs. 2.10 and 2.11. The amplitude of the suppression depends on the nucleus size.

J/ψ data

- J/ψ data from the **NA10 experiment** show that the suppression is greater by using a proton beam than a pion beam $R_{pA}^{J/\psi} < R_{\pi A}^{J/\psi}$ at the same beam energy. An important suppression is observed at large x_F in both cases.

- J/ψ data from the **E866** experiment (and previously from the E722 experiment) indicate a strong suppression as a function of x_F. The amplitude of suppression depends on the nucleus size, like in DY data, as illustrated in Fig. 2.10.

- The **NA3** experiment shows no beam energy dependence in $\langle p_\perp^2 \rangle_{\pi W}^{J/\psi}$ but at the same beam energy $\langle p_\perp^2 \rangle_{pW}^{J/\psi} > \langle p_\perp^2 \rangle_{\pi W}^{J/\psi}$;

- The **PHENIX** experiment did not observe a rapidity dependence between forward and backward rapidity in the $\langle p_\perp^2 \rangle_{dAu}^{J/\psi}$ - $\langle p_\perp^2 \rangle_{pp}^{J/\psi}$ but an increase at mid rapidity with large error bars. The R_{pA} as a function of y exhibits a more important suppression at forward compared to backward rapidity.

- In J/ψ data from **ALICE** and **LHCb** experiments, $R_{pA}^{J/\psi}$ exhibits more suppression at forward compared to backward region. In addition, $\langle p_\perp^2 \rangle_{pPb}^{J/\psi}$ is higher at forward compared to backward data.
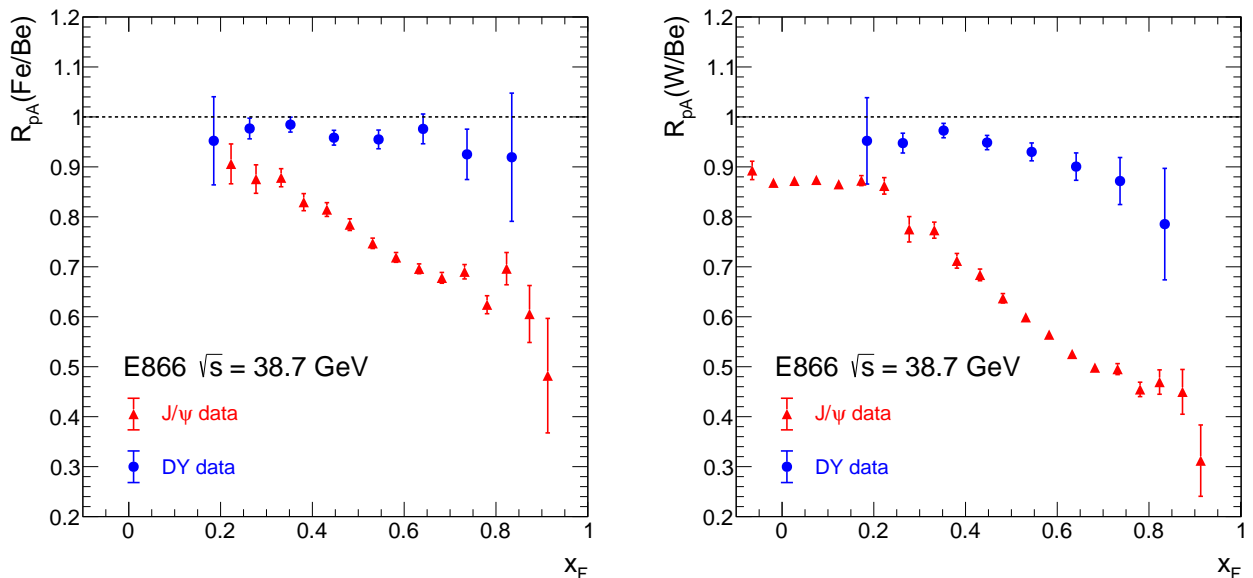
Figure 2.10: Ratio of DY (in blue) $(4 < M < 8.5$ GeV) and J/ψ (in red) data measured in pA collisions at $\sqrt{s}$=38.7 GeV as a function of the x_F from E866/NuSea experiment in Fe (left panel) and W (right panel) nucleus, both normalised to the Be target.
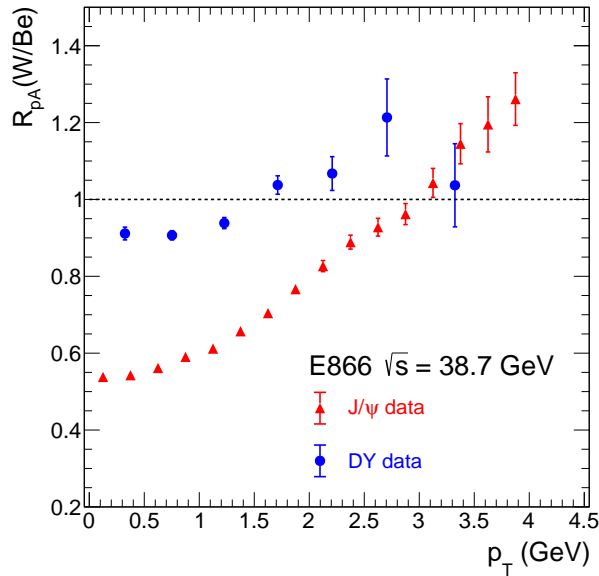
Figure 2.11: Ratio of DY (in blue) data ($4 < M < 8.5$ GeV) and J/ψ (in red) data ($0.3 \leq x_F \leq 0.93$) measured in pA collisions at $\sqrt{s}$=38.7 GeV as a function of the dimuon $p_\perp$ from E866/NuSea experiment.

2.5.2 Data interpretation

Each data shown in Table 2.4 will not be described individually, but some elements of interpretation will be given to demonstrate that these data can not be described by the nuclear absorption for J/ψ data and nPDF effects:

1. In $2 \rightarrow 1$ kinematic ($p_\perp \lesssim M$), namely in $gg \rightarrow J/\psi$ or $q\bar{q} \rightarrow \gamma^\star$ processes, the $p_\perp$ dependence of dimuon in x_2 and Q^2 can be neglected. Consequently, the nuclear cross section ratio in hA as a function of $p_\perp$ can be written as

$$R_{\mathrm{hA}}(y, p_\perp) \simeq R_j^{\mathrm{A}} \left(x_2 = \frac{M_\perp}{\sqrt{s}} e^{-y}, Q^2 = M_\perp^2 \right). \qquad (2.40)$$

The Cronin peak observed in all data in R_{hA} is around $p_\perp \lesssim 1 - 2$ GeV. From Eq. (2.40). I assume $p_\perp = 0$ GeV in nPDF leading to a constant R_{hA} unlike data. These data cannot be explained by nPDF by considering $p_\perp = 0$ GeV (see Fig. 2.11).

2. The E866 J/ψ data [86] probe a x_2 range $10^{-2} \lesssim x_2 \lesssim 10^{-1}$ and are sensitive to shadowing and anti-shadowing of the gluon nPDF. In Fig. 2.4, the gluon nPDF from EPPS16 at $Q^2 = M_{J/\psi}^2$ gives $0.7 \lesssim R_g^{\mathrm{W}}(x_2, Q^2) \lesssim 1$ for all error sets at $x_2 \sim 10^{-2}$ equivalent to very large x_F in Fig. 2.10. In contrast, the data exhibit $R_{\mathrm{pA}}^{J/\psi}(\mathrm{W/Be}, x_F) \sim 0.4$. These data cannot be explained by nPDF alone as illustrated in Fig. 2.12. In addition, it is possible to evaluate the impact of nuclear absorption in E866 J/ψ data according to Eq. (2.30) for a W nucleus. The calculation from Eq. (2.30) shows that the nuclear absorption cannot explain the data in E866/NuSea experiment in Fig. 2.10, in particular at large $x_F \gtrsim 0.2$ where $0.2 \lesssim R_{\mathrm{pA}}(\mathrm{W/Be}) \lesssim 0.8$.

3. The preliminary E906 DY data [118] probe a x_2 range $0.1 \lesssim x_2 \lesssim 0.3$ and are sensitive to anti-shadowing of mainly of the $\bar{u}(x_2)$ nPDF where $R_{\bar{u}}^A(x_2) \gtrsim 1$ is expected but at large x_F equivalent to $x_2 \sim 0.1$, the data show $R_{pA}(W/Be, x_F) \sim 0.75$.
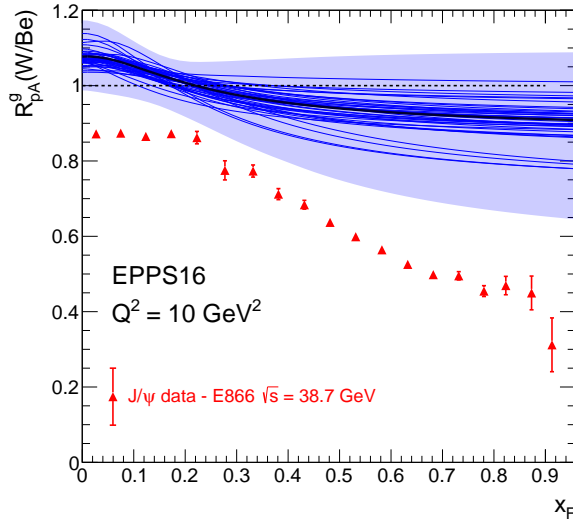
Figure 2.12: Comparison between E866/NuSea J/ψ data (in red) and $R^g(W/Be)$ ratio of W and Be gluon nPDFs from EPPS16 (in blue) at NLO as a function of x_F.

2.5.3 Phenomenological approach

Throughout this chapter, the most important nuclear effects have been introduced. Some elements showed that the J/ψ data for example could neither be explained by nPDF or by nuclear absorption alone. Recent phenomenological energy loss studies carried out had a great success in explaining J/ψ suppression data from fixed-target to LHC energies following the highlighting of a new energy loss dynamics in quarkonia production in these collisions: FCEL effect [4, 3, 107].

Figure 2.13 shows the comparison between nuclear cross sections ratios R_{pA} (W/Be) from E866 J/ψ data [86] and a calculation including only the FCEL effect from [4] as a function of x_F. The energy loss model alone can explain the suppression of the J/ψ data as a function of x_F. A precise value of the transport coefficient was extracted by fitting these data obtaining a reference value $\hat{q} = 0.075$ GeV^2/fm. As discussed in Sec. 2.2, it is possible to have a nPDF effect in these data due to shadowing effect contributing to the normalisation mainly of R_{pA} (see Fig. 2.12). The nPDF and radiative energy loss effects may appear as a product [4]

$$R_{pA}(x_F) = R_{pA}^{E.loss}(x_F) \times R_g^{nPDF}(x_F) \tag{2.41}$$

where R_g^{nPDF} is the gluon nuclear modification factor in the J/ψ pA data case. The nPDF effect contributes to R_{pA} normalisation by $\sim 10\%$ using the EPPS16 nPDF central set [78] .

In Fig. 2.14, the $p_\perp$ dependence of R_{pA} (W/Be) from the E866 J/ψ data is reproduced by taking into account the both broadening and energy loss effect from [129]. The radiative energy
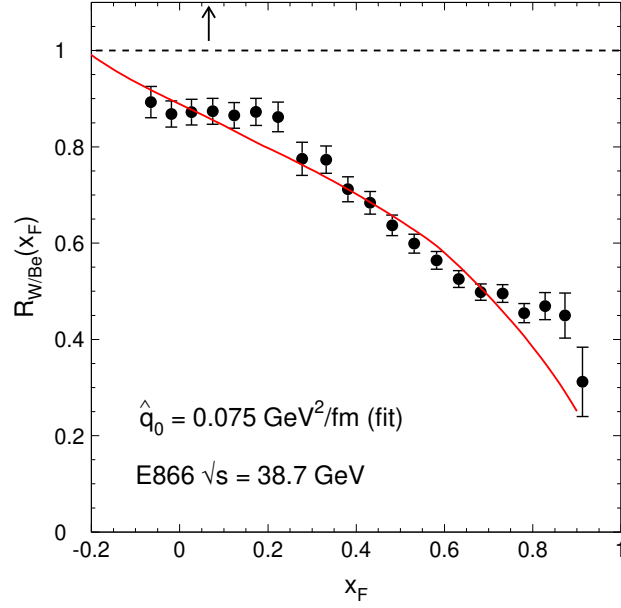
Figure 2.13: Comparison between R_{pA} (W/Be) from E866 J/ψ data [86] and energy loss model in FCEL regime from [4] as a function of x_F.
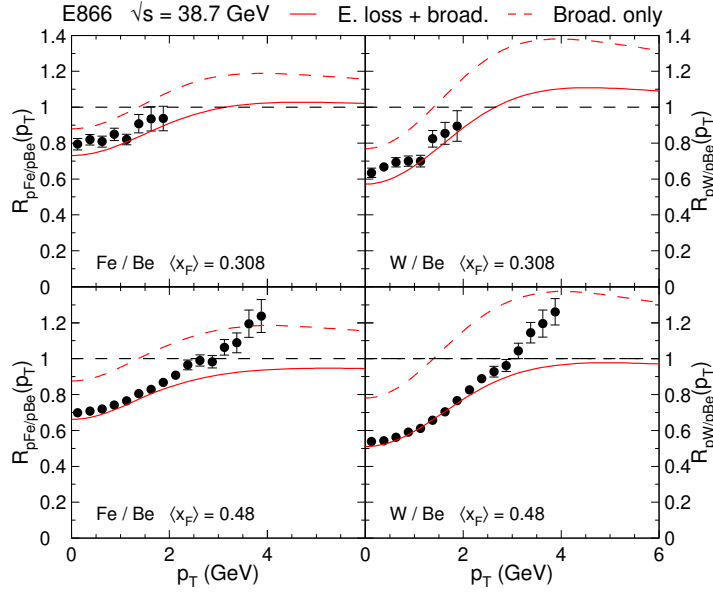
Figure 2.14: Comparison between R_{pA} (W/Be) from E866 J/ψ data [86] and broadening/energy loss model in FCEL regime from [129] as a function of $p_\perp$.

loss effect has an impact on $p_\perp$ due to the $M_\perp$ dependence of mean radiative energy loss value $\langle\epsilon\rangle_{\rm FCEL} \propto 1/M_\perp$. In Eq. (2.42), when $p_\perp \lesssim M$, $R_{pA}^{\rm E.loss}(y, p_\perp)$ varies slowly as a function of $p_\perp$ therefore affecting the normalisation of the calculation taking into account $R_{pA}^{\rm Broadening}(p_\perp)$ alone :

$$R_{pA}(p_\perp) = R_{pA}^{\rm E.loss}(x_F, p_\perp) \times R_{pA}^{\rm Broadening}(p_\perp) \tag{2.42}$$

This phenomenological success was confirmed in all J/ψ data from fixed target to the LHC energies. As we have also seen other nuclear effects than the energy loss can have an impact on the nuclear modification factor: nPDF and nuclear absorption for instance. Because of the many uncertainties regarding these effects as discussed, it is difficult from a single observable to establish the relative contributions although attempts have been made to do so throughout the chapter.

In the next chapter of this thesis, I will present the J/ψ and DY analysis at COMPASS experiment using a pion beam on two nuclear targets, Al and W, at $\sqrt{s} = 18.9$ GeV in Chapters 3, 4 and 5. I will discuss initial state energy loss and show how this impacts the DY data in fixed targets in πA and pA collisions in Chapter 6. Finally, the study of the transverse momentum broadening in the world data in hA collisions has been carried out and will be discussed in the Chapter 7.

3

COMPASS experiment

Contents

3.1 Introduction

COMPASS/NA58 (COmmon Muon and Proton Apparatus for Structure and Spectroscopy) is a fixed target experiment located in the north area at CERN. It uses hadron and muon beams produced by the Super Proton Synchrotron (SPS). Dedicated to hadron structure and spectroscopy, the COMPASS experiment is contributing to many still open QCD problems. The first COMPASS experiment proposal was accepted in 1998. One of its main goals was to measure directly the gluon polarisation [130, 131]. In 2010, an addendum to the experimental program

was approved by the CERN SPS advisory committee [132]. The new program was decomposed mainly in three physics topics: General Parton Distributions (GPD) study via the Deep Virtual Compton Scattering (DVCS) process, unpolarized PDF and Transverse Spin-Dependent (TMD) studies in Semi-Inclusive Deep Inelastic Scattering (SIDIS) and Drell-Yan (DY) experiments.

In this chapter, I will describe the essential components of the DY COMPASS setup. I will start by describing the front part of the spectrometer related to the beam and the targets in Sec. 3.2 and Chap. 3.3, then I will describe some characteristic detectors used in the reconstruction of the particles trajectories in Sec. 3.4. Finally, I will be interested in more detail on the Drift Chamber detectors in Chap. 3.7.

3.2 Beam

The DY COMPASS setup used a secondary negative hadron beam with an energy of about 190 GeV through the M2 extraction line of the Super Proton Synchrotron (SPS). The SPS provided a high intensity proton beam ($\approx 10^{13}$ beam protons in one or two 5 s spills for a SPS cycle of 32-48 s) with an energy equal to 400 GeV. The primary proton beam interacts with a Beryllium target (T6) of 500 mm thickness. Along the beam line, a number of dipole and quadruple magnets allow to select only the negatively charged hadrons produced following this interaction. The relative composition of the negative hadron beam produced depends on the beam energy, as illustrated in Table 3.1. At 190 GeV, the hadron beam is essentially composed of negative pions (≈ 96.8 %), negative kaons (≈ 2.4 %) as well as antiprotons (≈ 0.8 %).

	Negative beam		
Momentum (GeV)	π^- (%)	K^- (%)	$\bar{p}$ (%)
100	95.8	1.80	2.40
160	96.6	2.30	1.10
190	**96.8**	**2.40**	**0.80**
200	96.9	2.40	0.70

Table 3.1: The relative composition of the hadron beam at the COMPASS experiment for some typical momenta calculated from [133].

A dedicated pilot run at low beam intensity ($\sim 10^6$ beam particles per second) in 2014 allowed to determine the momentum of the incident beam used for DY data taking thanks to the Beam Momentum Station (BMS). The BMS is composed of six scintillator hodoscopes (BM01-BM06) located upstream and downstream of a dipole magnet (B6) surrounded by four quadrupoles (Q29-Q32) as illustrated in Fig. 3.1. The main characteristics of the detectors composing the BMS are shown in Table 3.2. The measurements of momentum distribution gave a beam momentum of 190.9 GeV with a standard deviation of 3.2 GeV [135].
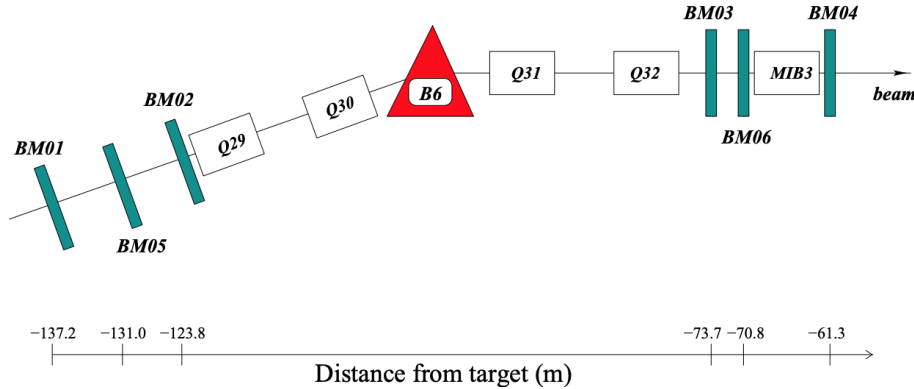
Figure 3.1: Layout of the BMS at the end of the M2 beam line [134]. The BMS detectors are in green boxes, the bend 6 magnet is in red triangle labelled B6 and quadruple magnets are in white boxes.

Detector	Active area	Resolution
BM01-04	$6 - 12 \times 9 - 23$	σ_s=1.3-2.5 mm, σ_t=0.3 ns
BM05	12×16	σ_s= 0.7 mm, σ_t=0.5 ns
BM06	12×16	σ_s= 0.4 mm, σ_t=0.5 ns

Table 3.2: The main characteristics of the detectors composing the BMS [134].

3.3 Targets

The DY COMPASS setup includes 4 nuclear targets one behind the other: two mix helium-ammonia, aluminium and tungsten targets as illustrated in Fig. 3.2.
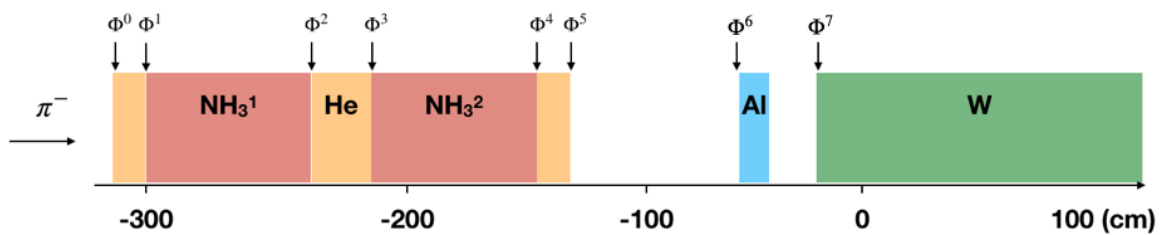
Figure 3.2: An illustration of targets position in DY COMPASS setup.

3.3.1 NH₃ targets

The two most upstream targets of the spectrometer are composed of a mixture of liquid helium (^{3}He and ^{4}He) and solid ammonia crystals, noted NH_3^1 and NH_3^2 in Fig. 3.2. The NH_3 targets consist of cylindrical cells of 55 cm length each and a diameter of 4 cm. The two cells are separated by a 20 cm gap. The NH_3 material was chosen in order to polarize the targets and measure transverse spin-dependent asymmetries in the DY process.

The amount of solid ammonia in each NH_3 targets is defined by the packing factor[1] p_{factor}, which is determined experimentally by the target group. In 2018, the packing factors were $p_{factor}^{NH_3^1} = 0.5677 \pm 0.0242$ for the NH_3^1 target and $p_{factor}^{NH_3^2} = 0.4814 \pm 0.0205$ for the NH_3^2 target. The volume distribution of solid ammonia and liquid helium in each target is considered to be homogeneous. All information about the density (ρ) and the atomic number (A) for each element independently are summarised in Table 3.5. The density of each NH_3^1 and NH_3^2 target

	State	A (g.mol^{-1})	ρ (g.cm^{-3})
^{3}He	liquid	3.02	0.154
^{4}He	liquid	2.00	0.154
NH_3	solid	17.04	0.850

Table 3.3: Target parameters of pure NH_3, He_3 and He_4.

must take into account the mixture of solid ammonia and liquid helium elements. The density of a target composed of n elements is defined as

$$\rho^{Mix} = \sum_i^n \rho^i p_F^i, \tag{3.1}$$

where p_F^i and ρ^i are respectively the packing factor and the nuclear density of the element i. The effective atomic number of a target composed of n elements is defined as

$$A_{eff}^{Mix} = \frac{\rho^{Mix}}{\sum_i^n \frac{\rho^i p_F^i}{A^i}} \tag{3.2}$$

where A^i is the atomic number of the element i. All information about the mix of ammonia-helium targets, NH_3^1 and NH_3^2, are summarized in Table 3.4. In 2018, the position of NH_3^1 was $Z \in [-294.50, -239.40]$ cm and of NH_3^2 was $Z \in [-219.10, -163.90]$ cm as illustrated in Fig. 3.2.

	A$_{eff}$ (g.mol^{-1})	ρ (g.cm^{-3})
NH_3^1	12.43	0.54 ± 0.02
NH_3^2	11.35	0.48 ± 0.02

Table 3.4: Target parameters of the mix of ammonia-helium NH_3^1 and NH_3^2 targets [136].

3.3.2 Al and W targets

A hadron absorber is located after the ammonia-helium targets. Its goal is to stop all the hadrons produced in large quantities during hadronic interactions. It is mainly composed of ten layers (19 cm long each) of alumina (Al_2O_3) tiles as shown in Fig. 3.3. The hadron

---

[1]By definition, the packing factor is the volume ratio between the volume occupied by the solid ammonia and the total volume of the target.
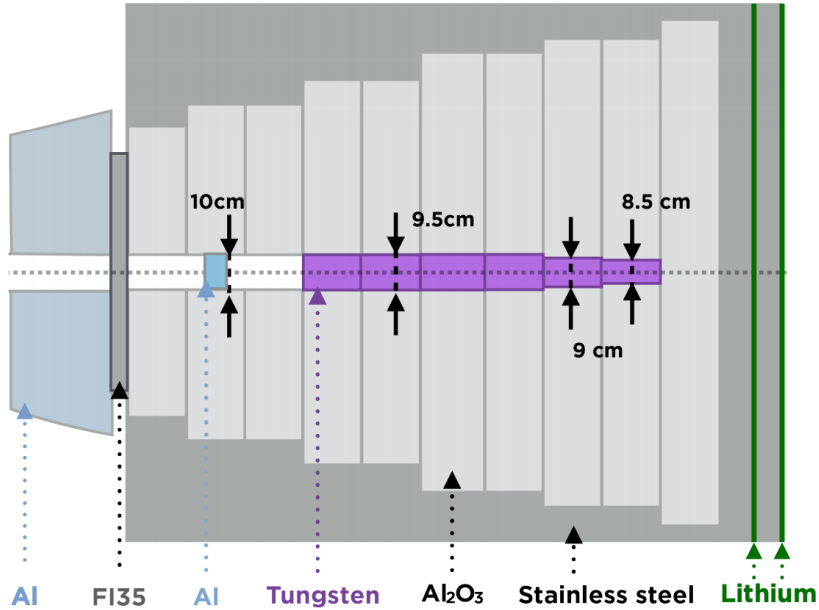
Figure 3.3: Illustration of the hadron absorber [135].

absorber encapsulates a cylindrical aluminium (Al) target of 7 cm long with a diameter of 10 cm and a tungsten (W) beam plug composed of 3 blocks of 80, 20 and 20 cm. The Al and the W targets are made of pure ^{27}Al and ^{184}W elements respectively. Only the first 10 cm of the W target will be used in the data analysis.

All information about density and atomic number are summarized in Table 3.5. In 2018, the position of the Al and W targets was $Z \in [-73.50, -66.50]$ cm and $Z \in [-30, -20]$ cm respectively.

	State	M $(g.mol^{-1})$	ρ $(g.cm^{-3})$
^{27}Al	solid	26.98	2.70 ± 0.01
^{184}W	solid	183.84	19.30 ± 0.01

Table 3.5: Target parameters of pure the Al and W targets [136].

3.3.3 Beam attenuation

When hadron beam particles enters a nuclear target, a fraction of it interacts inelastically and is absorbed by the target. The mean distance between two inelastic interactions is defined as the interaction length $\lambda_{\text{int}} \propto 1/\sigma^{\text{inelastic}}$. The larger the atomic number A of the target, the more important is the geometrical inelastic cross section $\sigma^{\text{inelastic}} \propto A^{2/3}$. The attenuation function $\mathcal{C}^{\text{attenuation}}$ of the pion beam in a target of density ρ and interaction length λ_{int}[2] is defined as

$$\mathcal{C}^{\text{attenuation}}(z) = e^{\frac{-\rho z}{\lambda_{\text{int}}}}, \tag{3.3}$$

---

[2]By convention the attenuation length is expressed in g.cm^{-2}.

where Z is the target position defined between 0, the entry of the target and L, its length. The information about the pion interaction length for each DY COMPASS setup target is summarized in Table 3.6. The pion interaction length of a hadron traversing a target composed of n elements is defined as

$$\lambda_{\mathrm{Mix}} = \frac{\rho^{\mathrm{Mix}}}{\sum_{i}^{n} \frac{\rho^{i} p_{F}^{i}}{\lambda^{i}}}. \tag{3.4}$$

The beam attenuation rate depends on the atomic number of the target and its length as

Target	$\lambda_{\mathrm{int}}^{\pi}$ $(g.cm^{-2})$
NH_3^1	110.50 ± 0.01
NH_3^2	110.38 ± 0.01
Al	136.70 ± 0.01
W	218.70 ± 0.01

Table 3.6: Target parameters of pure Al and W targets [136].

illustrated in Fig. 3.4. After travelling 10 cm, the pion beam loses $\sim 10\%$ of intensity in the Al target against $\sim 60\%$ in the W target. The beam absorption is an effect to be taken into account
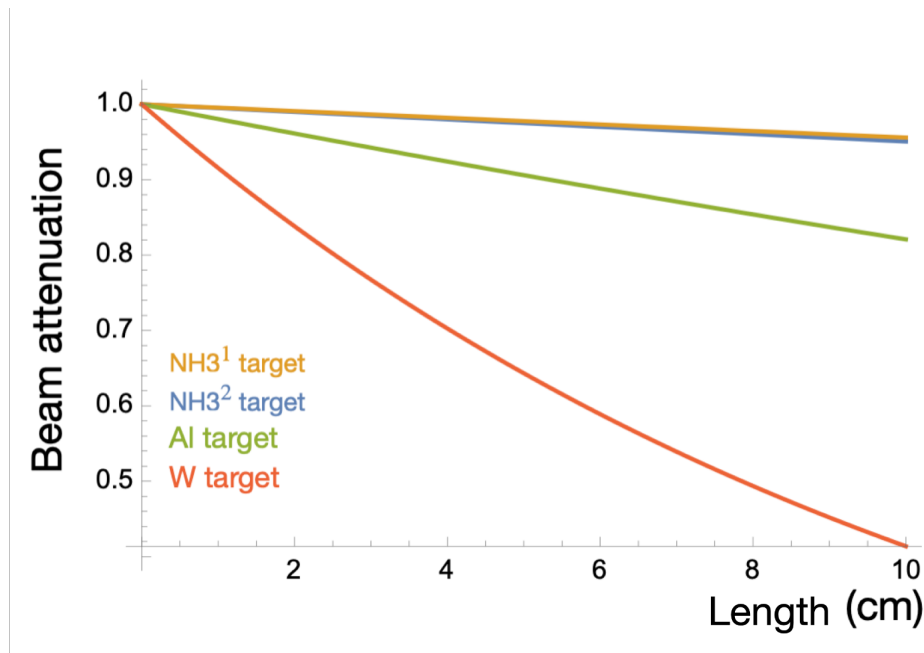
Figure 3.4: An illustration of the beam attenuation as a function of target length (cm) for W, Al, NH_3^1 and NH_3^2 targets based on Eq.(4.3).

when calculating the beam flux at the entrance of each target (noted Φ^i in Fig. 3.2). Consequently, the beam flux Φ^i entering in the target i depends on the beam absorption in the previous targets

$$\Phi^i = \Phi^0 \prod_{k=1}^{i} \mathcal{C}_k^{\mathrm{attenuation}}, \tag{3.5}$$

where Φ^0 is the initial beam flux as illustrated in Fig. 3.3. All information related to target characteristics and beam attenuation for DY COMPASS setup in 2018 data taking are summarised in Table 3.7.

	Luminosity information			
	Density ρ (g.cm^{-3})	Length (cm)	λ_{int} (g.cm^{-2})	Fraction of incident beam Φ_i
He	0.12	7	103.60	Φ^0
NH$_3^1$	0.54	55.1	110.50	0.99 Φ^0
He	0.12	19.8	103.60	0.76 Φ^0
NH$_3^2$	0.52	55.2	110.38	0.74 Φ^0
He	0.12	7.0	103.60	0.57 Φ^0
Al	2.70	7.0	136.70	0.57 Φ^0
W cell1	19.30	10	218.70	0.49 Φ^0

Table 3.7: Target characteristics and beam attenuation in the DY data taking in 2018 [136].

3.4 Spectrometer

The DY COMPASS setup is composed of two stages: the Large Angle Spectrometer (LAS) and the Small Angle Spectrometer (SAS) for a polar angular coverage 8 mrad $< \theta <$ 180 mrad. A sketch of the COMPASS setup used for DY data taking is shown in Fig. 3.5. Several detectors present were not used for DY data taking because not useful for muon detection such as ECAL/HCAL (Electromagnetic/Hadronic CALorimeter) and RICH (Ring Imaging CHerenkov detector). The LAS part is build around the SM1 magnet of 1T are to deviate large momentum particles while the SAS part is build around the SM2 magnet of 4.4T enabling ing to deviate small momentum particles. The large angular coverage results from the combination of three tracking regions:

1. Very Small Area Trackers (VSAT) region which covers the beam region up to a radial distance of 2.5-3 cm. In this region, the detectors are able to support high-particle flux ($\sim 10^7$ Hz or higher);

2. Small Area Trackers (SAT) region which covers the beam region up to a radial distance of 2.5 cm to 30 - 40 cm. It uses to detect particles at small angles. In this region, the detectors are able to support moderate-particle flux ($\sim 10^5$ Hz);

3. Large Area Trackers (LAT) region covering the largest angles. This region corresponds to the lowest particle flux ($\sim 10^4$ Hz).
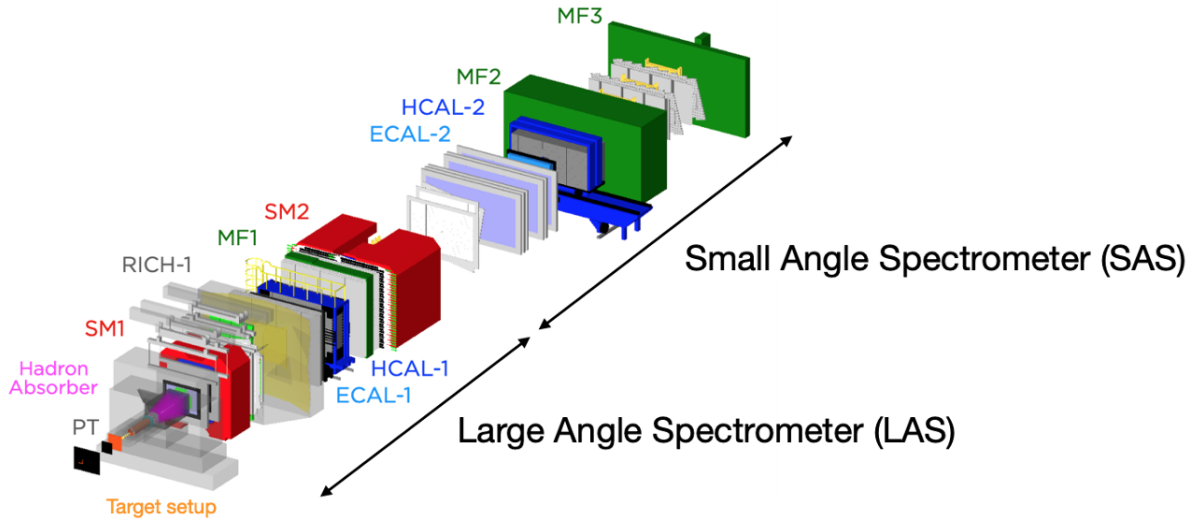
Figure 3.5: COMPASS setup used for the DY data taking.

3.4.1 Very Small Area Tracking

The Very Small Area Trackers (VSATs) region covers the beam region up to a radial distance of 2.5-3 cm. It therefore enables very small angle tracks to be reconstructed ($\theta \to 0$ mrad). The high beam rate $\sim 10^7$ Hz requires detectors with excellent time resolution. During the DY run, only the Scintillating Fibres (SciFi) detectors were in use. This region is composed by Scintillating Fibres (SciFi) and Microstrips detectors.

There are 14 planes of detection of Scintillating Fibres detectors (SciFi) with an active area from 4×4 cm^2 to 12×12 cm^2. In DY data taking, three SciFi stations (FI01, FI15, and FI03) composed the beam telescope and were placed upstream of the target setup to measure the beam trajectory and provide timing information. The typical time resolution is equal to 400 ps.

The Silicon microstrip detectors were not used in the DY run.

3.4.2 Small Angle Trackers

In the Small Angle region, tracker detectors cover a few tens of centimeters from the beam axis where the rate drops to $\sim 10^5$ Hz. The SAT trackers include Micromegas (micromesh gaseous structure) and GEM (Gas Electron Multipliers) gaseous detectors.

- *Gas Electron Multi-plier (GEM) detectors*
  There are eleven Gas Electron Multiplier (GEM) stations composed of four projection planes. They are all located after the SM1 magnet, throughout the COMPASS spectrometer. All eleven detectors are composed by an active area of 31×31 cm^2 with a 5 cm diameter dead zone.

The COMPASS GEM detectors consist of three amplifications stages, called GEM. Each of them is made of a 50 μm thick Kapton mesh composed by holes of 70 μm diameter spaced by 170 μm. The GEM stages are separated by transfer gaps of 2 mm height each. Primary electrons are created in the drift gap and are amplified in each GEM. This technology enables to share the charges amplifications to limit electrical discharges. It permits to collect quickly ions produced associated ensuring good time resolution. The typical time and spatial resolutions are, respectively, equal to 12 ns and 70 μm.

- *Micromegas*

  There are three Micromegas stations (MP01, MP02, MP03) composed by four detectors (one for each projection: horizontal, vertical and inclined by $\pm$ 45 degrees) located between the targets and the SM1 magnet. Each detection plan is composed by a active plane of 40×40 cm^2 with a 5 cm diameter dead zone. A Micromegas detector consists of a mesh separating the ionization and the amplification areas as illustrated in Fig. 3.6. The holes of the mesh are 30 to 50 μm large [137]. An incoming charged particle ionises the gas and creates primary electron-ion pairs. Due to the electric field ($\sim$ 1 kV/cm), the primary electrons drift to the mesh electrode. They enter in the amplification area where they are accelerated under the effect of a stronger electric field ($\sim$ 40 kV/cm). This acceleration induces a multiplication of ionisation: the *avalanche effect*. The drift of electrons induces an electric signal and the amplified signal is then read out on strips.

  The Micromegas detectors track particles not only at small angles, but also in the region in and around the beam in which the hit rate becomes really high, i.e. up to 2 MHz/cm^2 [138]. To cope with this high rate, a pixelized readout with pixels of 1 mm^2 was chosen. In addition, a GEM foil was inserted in the ionization area. The GEM foil acts as a pre-amplification stage, therefore reducing the gain of the amplification gap and, accordingly, the number of discharges by up to two orders of magnitude. In order to have a reasonable number of readout channels, the detector design is a combination of small-pixel, large-pixel and long-strip areas. The pixel areas (50×50 mm^2) are equipped with 0.4×2.5 mm^2 strips in the beam region and 0.4×6.25 mm^2 around. The remaining of the 40×40 cm^2 active area is subdivided in three slices. The central and the two lateral slice is equipped with 20 cm long and 0.4 mm thick and with 40 cm long and 0.48 mm thick strips, respectively. The designs of the detector and of its central region are shown in Fig. 3.7. The total number of channels is equal to 2560. The typical time and spatial resolutions are equal to 9 ns and 90 µm respectively.
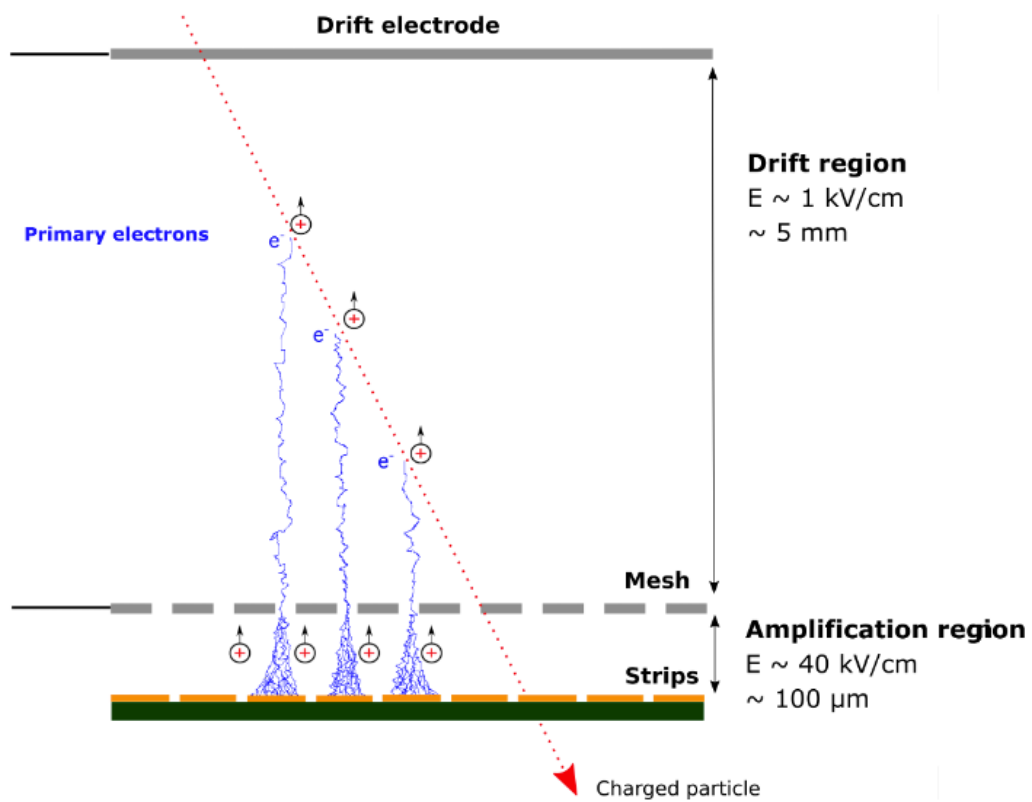
Figure 3.6: Micromegas detector.
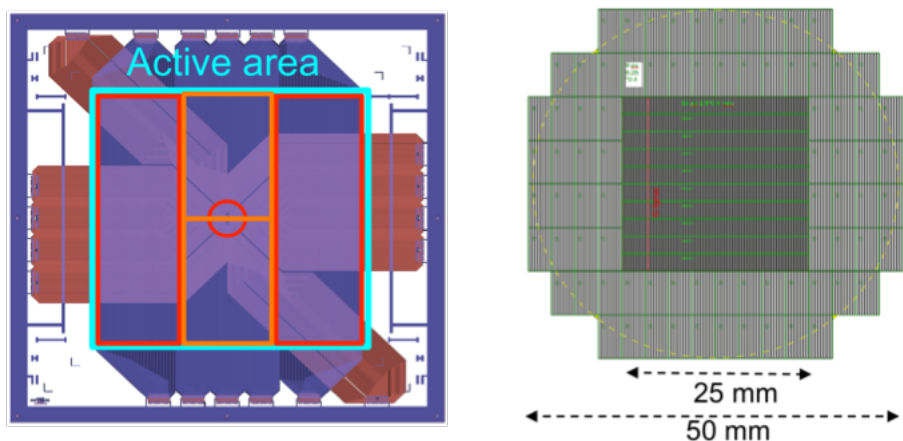
Figure 3.7: Sketch of alarge pixelised Micromegas.

3.4.3 Large Area Trackers

In the Large Area region, tracker detectors cover the largest angles dominated by low particle fluxes $\sim 10^4$ Hz. The particle flux is lower in this region, compared to previous area trackers, thus making it possible to use gaseous detectors with wires. Their dead zones nearly coincide

with the SAT region. This region includes Drift Chamber (DC) and Straw tube detectors.

- *Drift Chamber*

  A Drift Chamber (DC) is a gaseous detector composed a series of wires spaced 4 mm. They used to measure the spatial coordinates of charged particles crossing the detector. There are four DCs located downstream of the targets named DC00, DC01, DC04 and DC05. The two first (small DCs) have active areas of 180×127 cm^2 with a 30 cm diameter dead zone. They are located upstream of SM1. DC04 and DC05 (large DCs) are located downstream of SM1 and have an active area of 240×204 cm^2 with a 30 cm diameter dead zone.

  The detection active area is composed by a gaseous volume separated by two cathode planes and one wire plane as illustrated in Fig. 3.8. The detection principle is based on the ionization of the gas along the incident charged particle flight path. Under the effect of an electric field, the ionized electrons movement induces an electric current. By measuring their drift time and their arrival position on the electrode, it is possible to obtain spatial information on the charged particle. The geometry of a DC chamber is defined with three parameters:

  - the wire diameter of cathode (100 μm) and anode (20 μm);
  - the distance c between two cathode wires (8 mm): one cell;
  - the distance d between two cathode plans (4 mm).
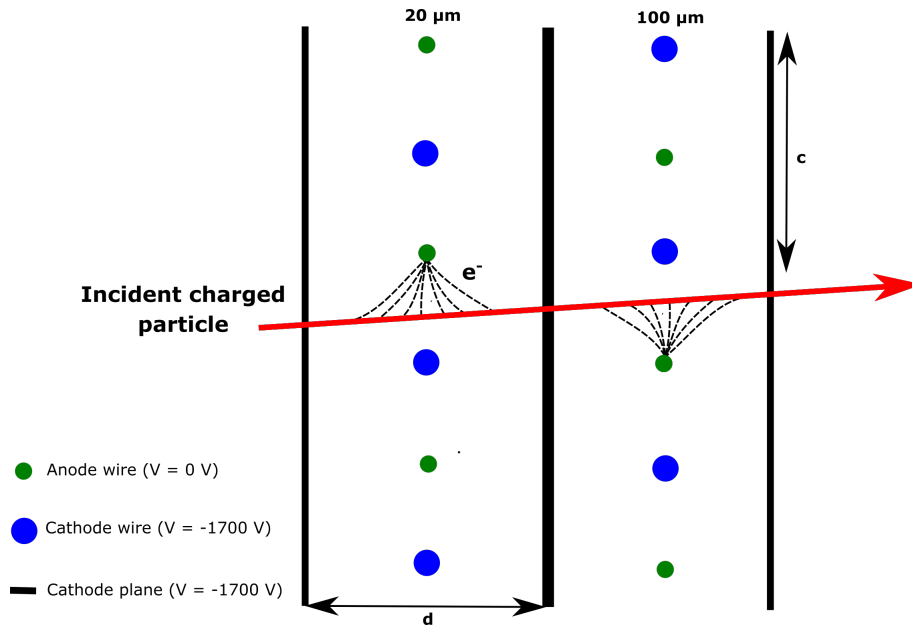
Figure 3.8: Schema of the detection principle of a charged particle crossing a Drift Chamber.

The characteristics of the DC detectors will be discussed in more details in Chap. 3.7.

- *Straw tube chambers*

  There are two Straw tube chambers (ST03 and ST05) located downstream of SM1. They consists of an assembly of Kapton tubes of 6 mm diameter. A single straw tube is composed by an inner layer of Carbon loaded Kapton (40 μm thickness), an outer layer of aluminized Kapton (12 μm thickness) and a glue film (7 μm thickness). In center of each tube is placed an anode wire made of gold-plated tungsten of 30 μm diameter and brought to a high potential. These detectors are based on the same principle compared to DC detectors. Indeed, a electrons cascade is produced when an ionising particle crosses a tube. It collected by the anode wire.

  Straw tube chambers consist of two stations with six projection views and with an active area 350×243 cm^2 including a central dead zone of 20×20 cm^2. The spacial resolution for these detectors is about of 190 μm.

- Multi-Wire Proportional Chamber (MWPC)

  The MWPC detectors are 14 stations, 6 in the LAS region and 8 in the SAS region. There are composed of an an active area 178×120 cm^2. Their dead zone increases according to their position along the beam line from 16 cm to 22 cm diameter. The typical spatial resolution of the MWPC detector is equal to $\sigma_\mathrm{s} = 1.6$ mm.

Station	Number of det.	Planes per det.	Channel par det.	Active area (cm^2)	Resolution
Micromegas	12	4	1024	40×40	$\sigma_\mathrm{s} \sim 90~\mu m$, $\sigma_t \sim 9$ ns
Small DC	2	4	1408	180×127	$\sigma_\mathrm{s} \sim 190~\mu m$
Large DC	2	4	500	240×204	$\sigma_\mathrm{s} \sim 500~\mu m$
Straw	2	4	892	320×260	$\sigma_\mathrm{s} \sim 190~\mu m$

Table 3.8: Main characteristics of the small and large area trackers [134].

3.4.4 Muon identification

Among all the particles detected by the tracking detectors described above, it is necessary to identify for those which are muons only. For this, 2 dedicated muon filters are used. They include an absorber layer in iron surrounded by trackers stations (MW). Thus, the incoming hadrons are stopped by the absorber while the muons are identified when a track upstream and downstream of the absorber can be reconstructed. The first Muon Wall (MW1) is located in the LAS region in front of SM2. As for the second, MW2, it is located at the very end of the SAS region.

3.5 Trigger and veto system

The trigger system enables to select the relevant physic event candidates. It is composed by scintillator hodoscopes distributed along the spectrometer allowing a large angular coverage. Also, a veto system permits to suppress ambiguous events involving the detection of muons from the halo beam[3]. It is located upstream of the targets as illustrated in Fig. 3.9. Sin-
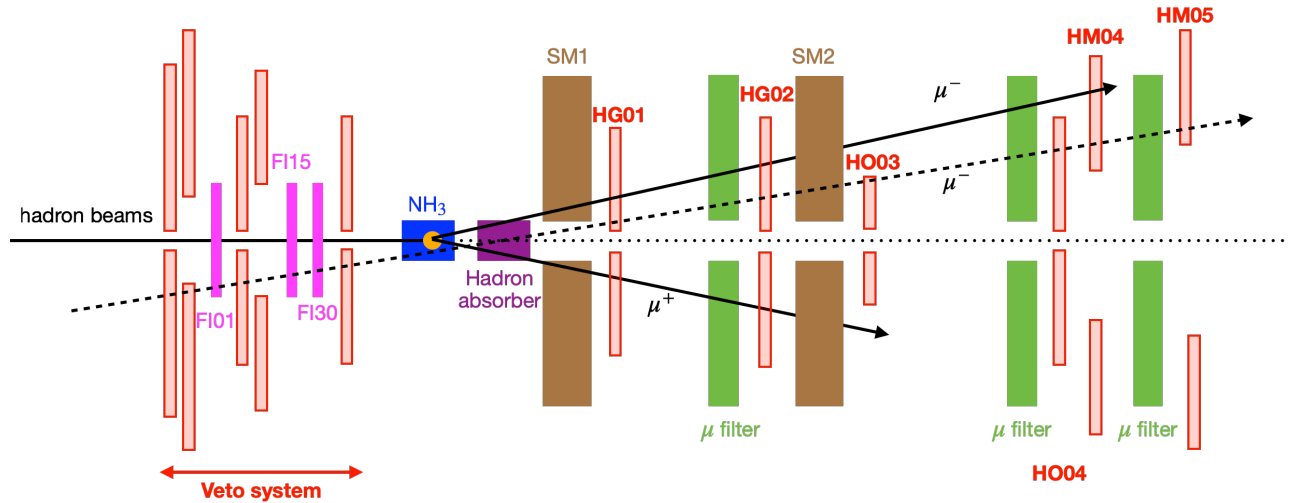
Figure 3.9: Location of trigger system hodoscopes downstream of the target and veto system hodoscopes upstream of the target during DY data taking. The figure shows the production of a dimuon correlated pair (in black line) and one muon from the beam decay (dotted black line) rejected by the veto system.

gle muon DY triggers include

- **LAS** (Large Angle Spectrometer) trigger consists of two hodoscope planes H1 (HG01Y1) and H2 (HG02Y1, HG02Y2). The H1 and H2 planes is composed of 32 slabs. They are located between SM1 and SM2;

- **Outer** trigger consists of two hodoscope planes H3O (HO03Y1) and H4O (HO04Y1, HO04Y2). The first is composed of 18 slabs and is located after SM2 whereas H4O is composed of 16 slabs ans is located at the end of the LAS region;

- **Middle** trigger consists of two hodoscope stations HM04Y1 and HM05Y1. Both hodoscopes stations are located in the SAS region and are composed of 32 slabs each.

The trigger system used during the DY data taking is based on the detection of dimuon events, i.e. the activation of two single-muon triggers, namely a coincidence of either *LAS and LAS*, *LAS and Outer* or *LAS and Middle* triggers is required. Figure 3.10 shows dimuon events as a function of dimuon longitudinal momentum p_Z (GeV) for each dimuon trigger. At large p_Z, corresponding to small polar $\theta_{\mu^+\mu^-}$ angle, the number of events is dominated by events from

---

[3]$\pi^- \to \mu^- + \bar{\nu}_{\mu^-}$.
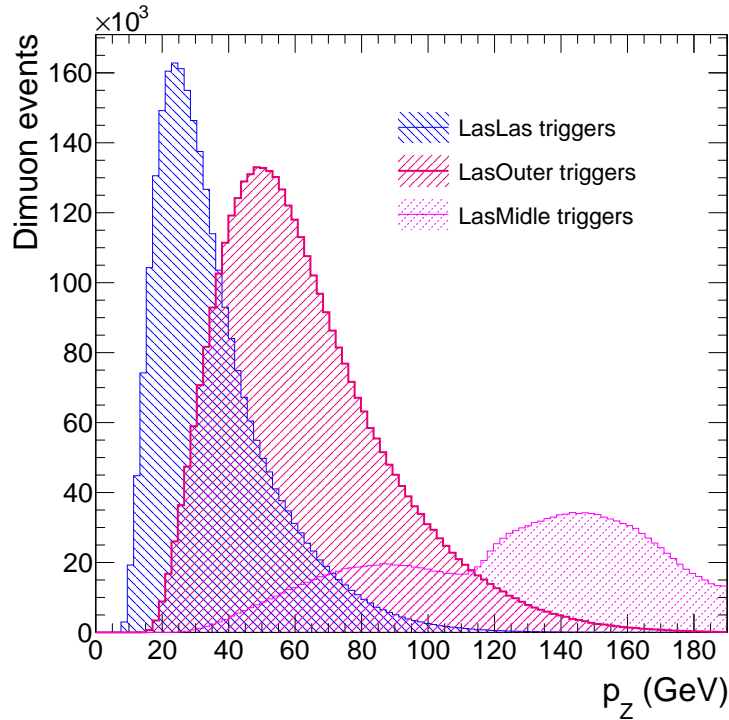
Figure 3.10: Typical dimuon events distribution as a function of p_Z in all dimuon invariant mass phase space $M \in (1;10)$ GeV from DY data taking.

LAS and Middle triggers whereas at small p_Z, corresponding to large $\theta_{\mu^+\mu^-}$ angles, the events are dominated by *LAS and Las* triggers. In addition, a bump is observed at large $p_Z \sim 150$ GeV for *LAS and Middle* triggers. These events comes mainly from pions/kaons decay.

3.6 Data acquisition

The data acquisition system (DAQ) [134] collects data from the over 250,000 detector channels during an event. A typical COMPASS event size is ~ 45 kB. The DAQ system was designed to quickly process information from physical events and to minimize the deadtime associated with data collection and transfer. Signals from the detectors are preamplified and digitised via Analog to Digital Converters (ADCs) or Time to Digital Converters (TDCs). In the second time, these information are sent to readout driver modules GANDALF (Generic Advanced Numerical Device for Analog and Logic Functions), CATCH (COMPASS Accumulate, Transfer and Control Hardware) or GeSiCA (GEM and Silicon Control and Acquisition). The data are transferred via optical fibres to FPGA (Field Programmable Gate Array) multiplexing cards, where they are buffered for one spill while merging it into sub-events. Finally, data files (~ 1 GB size) are copied on the tapes of the CERN central computer centre (CASTOR).

3.6.1 Reconstruction

To be analysed, the data are retrieved from CASTOR and are processed via the COMPASS reconstruction program, which is a fully C++ object-oriented program: the COMPASS Reconstruction and AnaLysis (CORAL) program. The reconstruction consists in starting from the hits in the detectors to reconstruct the trajectory of the muons and thus the vertex where the muon was typically produced in the different targets. COMPASS does not have an operational vertex detector, this point will be discussed in Chapters 4 and 5. Consequently, the location of the vertex is then identified by extrapolating the reconstructed muons tracks. After reconstruction has been realised by CORAL, the data are stored in data structured trees (DSTs). These data in this form are ready to be analysed via the COMPASS analysis program, PHAST (PHysics Analysis Software Tool).

3.7 The Drift Chamber detector

This section aims to describe the Drift Chambers (DC00, DC01, DC04) for which CEA/Saclay is responsible. During the 2015 and 2018 data taking, our group ensured the proper functioning of the DCs on the one hand. On the other hand, all the calibrations necessary for the reconstruction of the events were carried out for all the data taking years (2016, 2017 and 2018). Finally, the repair of the DC04 chamber occupied part of the year of 2020.

3.7.1 Characteristics

The DY COMPASS setup includes four Drift Chambers (DC00, DC01, DC04 and DC05) located in the LAS region upstream of the SM2 magnet as illustrated in Fig. 3.11. These detectors allow to detect muons produced at large polar angles. My thesis work mainly focused on the DC04 chamber. Now, I will discuss the characteristics of this detector in more detail. Below, some parameters regarding the large DC04 chamber [139] at COMPASS:

- Active area $\sim 248 \times 208 \times 12.5 \mathrm{cm}^3$;

- Gaz used: $\mathrm{Ar}/\mathrm{C}_2\mathrm{H}_6/\mathrm{CF}_4$ (45/45/10%)

- 8 plans (YY', XX', VV', UU') = (90°, 0°, -10°, +10°) with respect to the vertical axis;

- In the same doublet, the two planes are offset by half a cell to remove the right-left ambiguity during the reconstruction of the tracks (see Fig. 3.8 and 3.12);

- Number of drift cells per plane: 256;

- Space between cathode wires: 8 mm;

- Beam killer: diameter 28.6 cm.
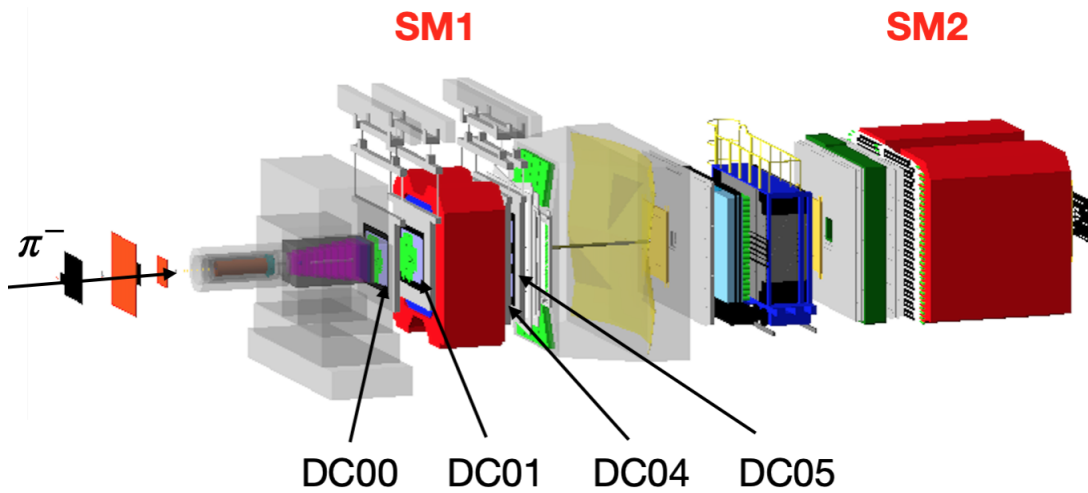
Figure 3.11: Location of the DCs in the DY COMPASS setup in the LAS part.

Figure 3.12 left shows the four Drift Chamber doublets (YY', XX', VV' and UU')[4] of the DC04 chamber. The plane doublet closest to the beam is therefore UU' plans. The orientation of the doublet planes facing the beam is shown on the right panel. Each plane doublet is oriented at an angle of 10 degrees in order to maintain a power of discrimination during the tracks reconstruction.
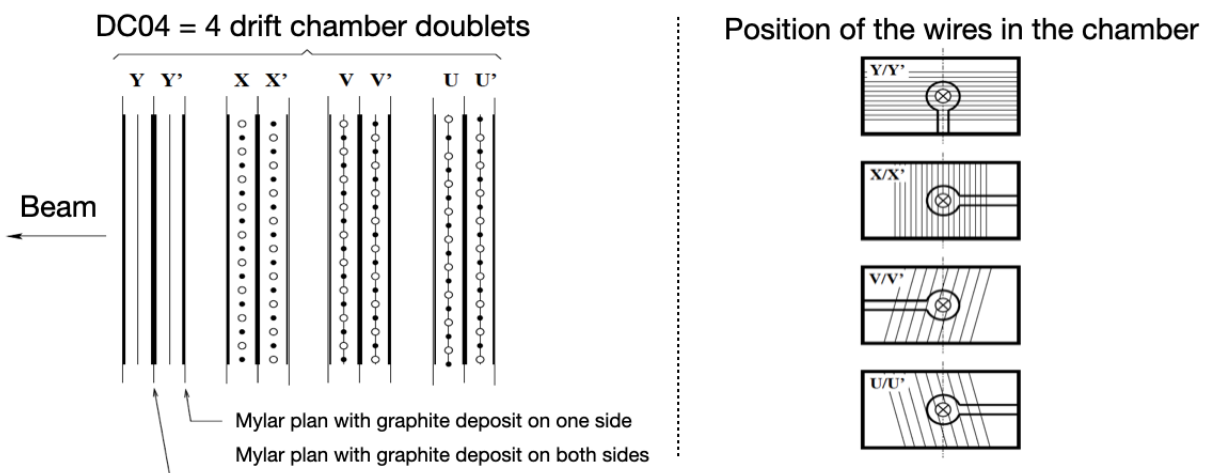
Figure 3.12: Plan of the DC04 chamber [139].

---

[4]In the following, we will note Y as Y1 and Y' as Y2 and the same for other plans.

3.7.2 Formation and processing of the electrical signal

When a charged particle, typically a muon, crosses a gas volume, it ionises the atoms present along its path. The probability of electromagnetic interaction between the incident particle and the electrons of the electric procession of atoms will depend essentially on the nature of the gas. The incident particle will transmit part of its energy and allow the ionisation. When electrons are created, under the effect of the potential difference between anode and cathode wire, they migrate and acquire a kinetic energy greater than the ionization potential of the gaz. Consequently, the primary electrons will be able to ionize in turn the gas by creating other electrons which in turn will also ionize the gas etc., this phenomena is called *avalanche* (see Fig. 3.8). The charge amplification process is characterized by the gain defined as

$$G = \frac{N}{N_0} = e^{\alpha(E)L} \tag{3.6}$$

with N_0 the number of primary electrons and N the number of electrons from the avalanche, L the length of the amplification area, and α the first Townsend coefficient. This coefficient depends, in first approximation, on the electric field E, the pressure P, and parameters A and B which depend on the nature of the gas mixture [140]:

$$\frac{\alpha}{P} = Ae^{-\frac{BP}{E}}. \tag{3.7}$$

The gas mixture is composed by a noble gas and a polyatomic gas, called *quencher*. The electronic layers of a noble gas are full so it has few excited states. The ionization process is therefore favored over the excitation process. The electron created by ionization is generally accompanied by the emission of a photon which can ionize the gas in turn by the photoelectric effect. Consequently, a polyatomic gas is used, with multiple modes of rotation and vibration, in order to reduce risks of discharge by absorbing the UV photons emitted by the noble gas in the amplification area. The gas used for the COMPASS Drift Chamber is Ar $\sim$ 45 %(noble gas), $C_2H_6 \sim$ 45 % (polyatomic gas or quencher) and $CF_4 \sim$ 10 % (allowing to increase the electron drift velocity by reducing the transverse diffusion cross section). In this configuration, the number of primary electrons created at nominal voltage $\sim$ -1700 V is of the order of 100.

The drift of the electrons under the electric field towards the wire induces an electric current. The electron drift time is of the order of a nanosecond (see Sec. 3.7.3.a). In contrast, the ions created at the same time as the electrons migrate towards the cathode in a much longer time of the order of 100 ns due to their mass.[5]

---

[5]The drift velocity without magnetic field is proportional to 1/m, $\vec{v}_D = \frac{e\tau}{m}\vec{E}$ with τ the mean time between two collisions, and m the particle's mass.

Front-end Electronics

When the signal is created, it is processed by the front-end electronics of the chamber. The part responsible of signal processing is made up of two modules: ASD8 and F1 supplied respectively by a low voltage delivering ± 6 V and ± 8 V. ASD8 module provides an analog signal processing including a pre-amplifier, an amplifier and a discriminator. The signal from the ASD8 module is sent to the F1 cards aiming to digitize signal transit times (Time to Digital Converter). It is designed to digitize more than 6 million signals per second with a precision of the order of 100 ps [141].

3.7.3 Calibration

3.7.3.a Space and time (RT) relation

When a particle ionises the DC gas volume, the trigger system opens a time gate of 310 ns (corresponding to 2400 TDC channels), during which the F1 cards measures the time signal induced by the drift electrons. Fig. 3.13 shows the time distribution for a high intensity run in 2015 DY data taking for the DC00U1 and the DC01U1 views. Because the DC01 detector is further downstream of the spectrometer, the events rate is lower compared to the DC00 detector by a factor ~ 1.7. The time distributions exhibit a constant background due to fortuitous tracks that are not included in the event for which the trigger was activated but which induced an electrical signal on the wires. In contrast, the time correlated signals are highlighted by a peak with a width of ~ 60 ns. The electron drift time is between 0 and 60 ns, the maximum drift time
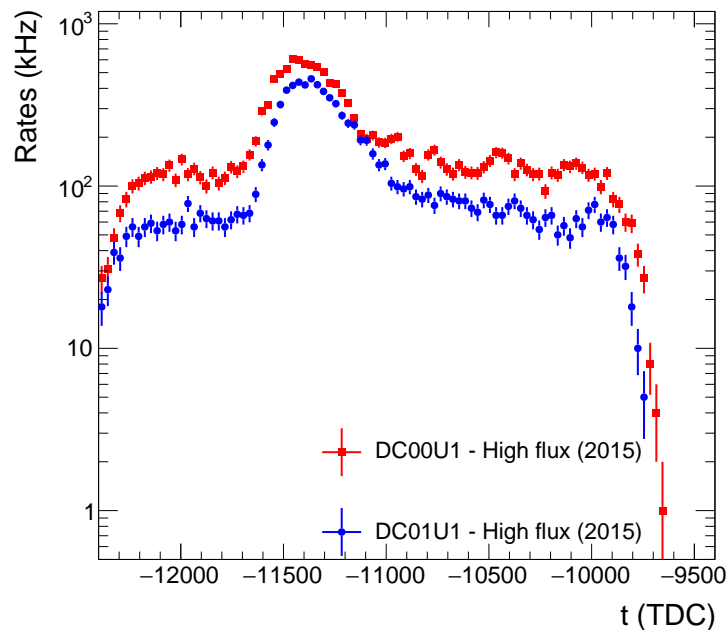
Figure 3.13: Drift time distribution for DC00U1 (in red) and DC01U1 (in blue) at high flux as a function of TDC channel (128 ps per channel).

corresponding to the extreme case where the electrons are produced near the cathode wire. The

typical drift velocity obtained from RT relation is 12 ns/mm as illustrated in Fig. 3.14. In order
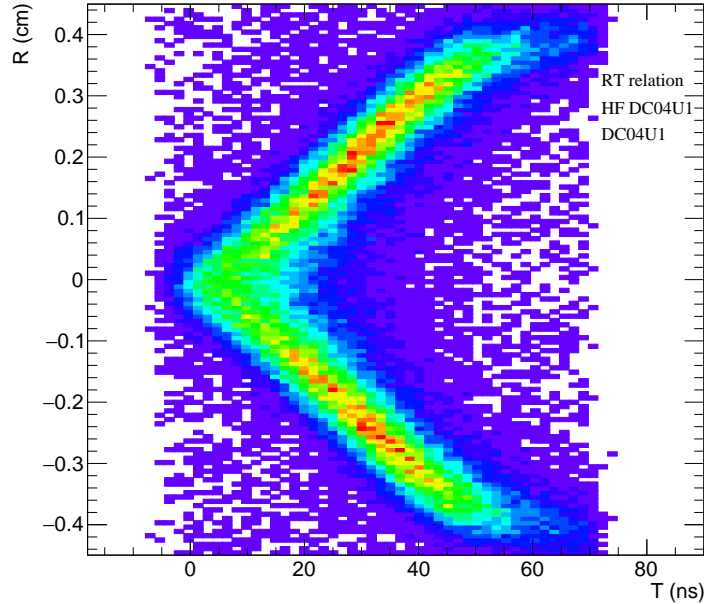
Figure 3.14: Relation between time (ns) and the wire distance R (cm) for the DC04U1 plane at high flux intensity during the DY data taking in 2015.

to identify the exact position of the particle crossing the Drift Chamber, it is necessary to know the relation between the drift time T (ns) and the distance R (cm) travelled by the electrons between the cathode and the anode as illustrated in Fig. 3.7. In practice, this RT relation is divided into time intervals of 2 ns and the distribution obtained as a function of R (cm) is fitted using a Gaussian function in order to extract the mean value. These results are then put into the form of a table which will be used by the CORAL tracks reconstruction software.

3.7.3.b   Efficiency

A fraction of all particles passing through a DC detector will not be detected and therefore not reconstructed. In order to calculate the detection efficiency of DC detector plane, it is deactivated in the tracking during the reconstruction process by CORAL software. The plane inefficiency is therefore defined as the probability that the plane does not detect the passage of particle while other planes in the chamber did. Figure 3.15 shows the 2D efficiency map of DC04U1 and DC04U2 views during a high-intensity run of DY data taking. First of all, a totally ineffective central zone appears in the central area corresponding to the presence of the *beam killer*. Second, some areas are in the form of a straight line where the efficiency is lower compared to the rest of the chamber, this is due to the nylon wires. Generally, the efficiency obtained during a DY data taking run in high flux conditions is greater than 90% for DC04 detector.
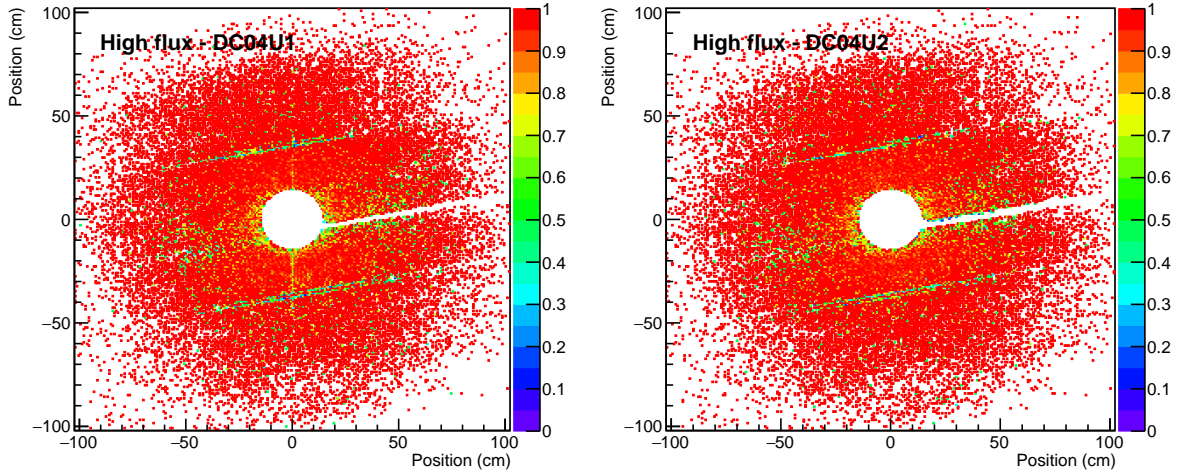
Figure 3.15: Efficiency map of DC04U at high flux during the DY data taking.

3.7.3.c   Spatial resolution

The spatial resolution of a detector σ_a can be calculated from the spatial resolution of the residual and the uncertainty of track reconstruction position thanks to other detectors. These sources of uncertainty are completely independent and can be summed up in a quadratic way as

$$\sigma^2 = \sigma_a^2 + \sigma_t^2. \tag{3.8}$$

In order to get rid of the uncertainty of track reconstruction position depending on the set of detectors of the spectrometer, it is possible to use the fact that each view is divided in 2 planes (see Fig. 3.12). The two planes from each view are staggered by a half a cell, i.e. 4 mm. The uncertainty of reconstruction of the track for these two planes can therefore be considered to be identical. Consequently, it possible to define the double layer residual to determine the spatial resolution of each detector plane as

$$\delta\Delta u_{\text{double residual}} = (u_{\text{plane 1}} - u_{\text{track}}) - (u_{\text{plane 2}} - u_{\text{track}}) = u state_{\text{plane 1}} - u_{\text{plane 2}} \tag{3.9}$$

where $u_{\text{plane 1(2)}}$ is the hit position on plane 1(2) and u_{track} is the hit position determined from reconstruction. The double layer residual is independent of the track resolution and only dependent of the difference of hit position between the plane 1 and plane 2. Figure 3.16 shows the double residual for the plane DC04U1 during the 2015 DY data taking in high flux condition. To determine the resolution, the distribution is fitted with one Gaussian function and one constant to reproduce the background. In Fig. 3.16, a Gaussian function is fitted on the distribution in order to extract the value of the resolution of the plane. The resolution of the DC04U plane can be written by assuming that the distribution of the residuals are the same for the two planes as

$$\sigma_{\text{double residual}}^2 = \sigma_{\text{plane 1}}^2 + \sigma_{\text{plane 2}}^2 = 2\sigma_{\text{plane 1}}^2 = 2\sigma_{\text{a}}^2 \tag{3.10}$$
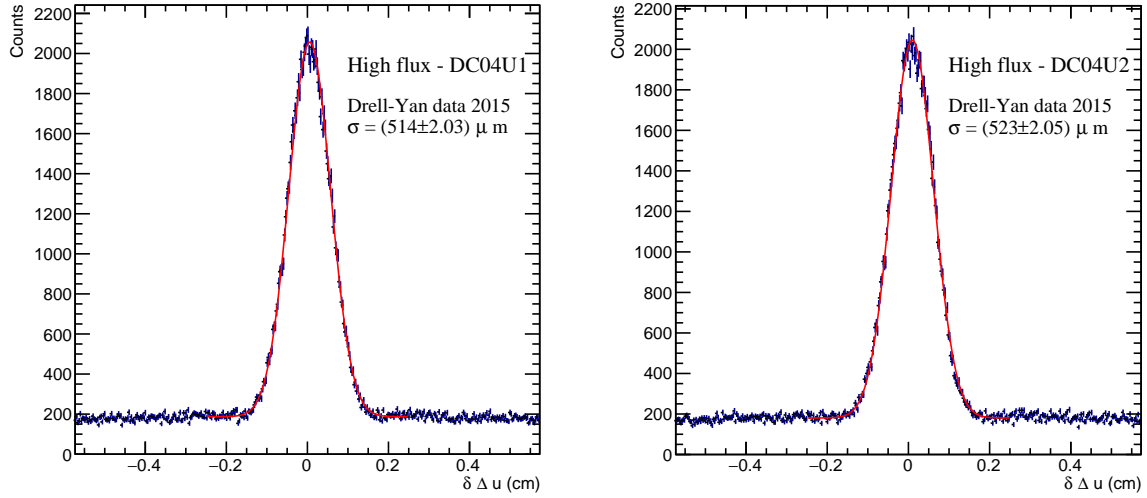
Figure 3.16: Double residue distribution of DC04U1 and DC04U2 in a high flux data taking run.

The fit results for DC04U1 and DC04U2 give approximately the same standard deviation (see Fig. 3.16). Consequently, the resolution for the DC04U plane during a typical run of DY data taking in high flux for the DC04U is equal to $\bar{\sigma}_a \approx (367 \pm 2)\mu m$. The values of efficiency and resolution of the DC04 detector for each plane and each view are summarized in Table 3.9.

DC	Efficiency (%)	Standard deviation (μm)
DC04U1	93.67 ± 0.08	514 ± 2
DC04U2	93.7 ± 0.1	523 ± 2
DC04V1	92.8 ± 0.1	424 ± 2
DC04V2	94.0 ± 0.1	411 ± 2
DC04Y1	94.0 ± 0.1	533 ± 2
DC04Y2	94.0 ± 0.1	535 ± 3
DC04X1	92.0 ± 0.1	443 ± 2
DC04X2	91.0 ± 0.1	446 ± 2

Table 3.9: Characterisation of the DC04 detector in high flux intensity (HI) in 2015 data taking.

4

Analysis of J/ψ production in πA collisions

Contents

In this chapter, I present the data analysis for the J/ψ production in $\pi^- $A collisions, for the W and the Al targets nuclei. Results for the ratio of nuclear cross section W/Al are given as a function of $x_{\rm F}$ and $p_\perp$. The analysis is based on real data (RD) accumulated in 2018. It includes the selection of events, the calculation of the acceptance of the setup using a Monte-Carlo (MC) simulation, the extraction of the cross-sections ratio and the study of systematic errors.

4.1 Observable

The double differential cross section of J/ψ production is given by

$$\frac{\mathrm{d}^2\sigma^{\pi^-A}}{\mathrm{d}x_\mathrm{F}\mathrm{d}p_\perp}(J/\psi) = \frac{N^{\mathrm{J/\psi}}_{\mathrm{events}}(x_\mathrm{F},p_\perp)}{\epsilon^\mathrm{A}\cdot\mathrm{BR}\cdot\Delta x_\mathrm{F}\cdot\Delta p_\perp\cdot\mathcal{L}} \tag{4.1}$$

where $N^{\mathrm{J/\psi}}_{\mathrm{events}}$ is the number of J/ψ events in the $(x_\mathrm{F},p_\perp)$ kinematic bin, $\mathrm{BR} = (5.971\pm0.032)\%$ the branching ratio of the decay $\mathrm{J/\psi}\to\mu^+\mu^-$, ϵ is the acceptance calculation including geometrical acceptance, detector efficiency, trigger efficiency and reconstruction efficiency, Δx_F and $\Delta p_\perp$ are the x_F and $p_\perp$ bin widths. The luminosity $\mathcal{L}$ is

$$\mathcal{L} = \alpha^i\Phi^0\times L^i_{\mathrm{eff}}\times\rho^i\times\frac{\mathcal{N}_A}{M^i} \tag{4.2}$$

where Φ^0 is the initial absolute beam flux and α^i, the fraction of initial beam flux entering in the target i, ρ^i the i target density. The Avogadro number and molar mass of the target i are noted $\mathcal{N}_A$ and M^i respectively. The effective luminosity L^i_{eff} takes into account the beam attenuation inside target i and λ^i_{int} the interaction length of pion in target i and defined as

$$L_{\mathrm{eff}} = \frac{\lambda_{\mathrm{int}}}{\rho}\left[1 - e^{\frac{-\rho L}{\lambda_{\mathrm{int}}}}\right]. \tag{4.3}$$

The relevant observable to study the nuclear dependence of J/ψ process is the ratio of nuclear cross sections between a heavy nucleus (A) and a light nucleus (B),

$$R^{J/\psi}_{\pi^-\mathrm{A}}(\mathrm{W/Al}) = \frac{N^{J/\psi}_\mathrm{W}(x_\mathrm{F},p_\perp)}{\epsilon_\mathrm{W}\cdot\alpha^\mathrm{A}\times L^\mathrm{W}_{\mathrm{eff}}\times\rho^\mathrm{W}}\Big/\frac{N^{J/\psi}_\mathrm{Al}(x_\mathrm{F},p_\perp)}{\epsilon_\mathrm{Al}\cdot\alpha^\mathrm{Al}\times L^\mathrm{Al}_{\mathrm{eff}}\times\rho^\mathrm{Al}}. \tag{4.4}$$

The $R^{J/\psi}_{\pi^-\mathrm{A}}(\mathrm{W/Al})$ ratio does not depend on the absolute beam flux Φ^0. The information concerning the flux is contained in the fraction of the incident flux at the entrance of the target, noted α, and also in the effective luminosity which takes into account its absorption along the target.

The $R^{J/\psi}_{\pi^-\mathrm{A}}(\mathrm{W/Al})$ ratio will be discussed as a function of $p_\perp$ and x_F. An additional observable, which will be calculated, is the mean transverse momentum, $\langle p^2_\perp\rangle$ of the J/ψ process.

4.2 Data sample

The 2018 data set used in the present analysis corresponds to 9 periods (P00 to P08) of the t2 production, i.e. the second production of the 2018 data with the alignment of the spectrometer updated compared to the first production t1. These data were collected using a high intensity beam of about 6×10^7 hadrons.s^{-1}. Data analysis was performed using the PHAST software after processing the raw data with the CORAL reconstruction software.

Analysis cuts
(1) $\mu^+\mu^-$ tracks pair (X/X0>30) from primary vertex, $M_{\mu^+\mu^-} > 1.5$ GeV + Badspill list
(2) $Z_{\text{First}} < 300$ cm & $Z_{\text{Last}} > 1500$ cm
(3) Mean time of track t defined
(4) $\left\| t_{\mu^+} - t_{\mu^-} \right\| < 5$ ns
(5) χ^2 track / ndf < 10
(6) Trigger validation and (LL and LO) dimuon triggers
(7) $0 < x_F < 0.9$
(8) $0 < p_T < 4$ (GeV)
(9) W: $-30 < Z_{vtx} < -20$ (cm) and $R_{\text{elipsoid}} < 1$ (cm)
(10) Al: $-73.5 < Z_{vtx} < -66.5$ (cm) and $R_{\text{elipsoid}} < 1$ (cm)

Table 4.1: List of kinematics cuts used for a dimuon event in 2018.

4.2.1 Event selection

To extract the J/ψ cross section, it is necessary to apply kinematic cuts in order to select only muon particles that correspond to a true physics event. The kinematic cuts are determined in order to select a pair of muons correlated in time resulting from the interaction between the pion beam and the nuclear target (see Table 4.1). The cuts applied in the present analysis are explained below:

(1) Two oppositely charged particles μ^+ and μ^- with more than 30 radiation lengths (X/X0) from a common CORAL best primary vertex, i.e. a reconstructed vertex with an associated beam particle. If there is no best primary vertex, the reconstructed vertex with the closest reduced-χ^2 to 1 is selected. At this step, the bad spill rejection cut ensures the beam flux stability in data;

(2) The first point of measurement of the particles tracks must be at less than 300 cm and more than 1500 cm along the beam axis to ensure that the particles have positions upstream of the first spectrometer magnet and downstream of the first muon filter;

(3) The timings of the oppositely charged muons is defined. It ensures that a trigger time is associated with each muon;

(4) Selection of oppositely charged muons that difference in time is less than 5ns, related to the trigger time, enabling to reject uncorrelated oppositely charged muons;

(5) The spatial χ^2 of muon track must be less than 10 to ensure the quality of the reconstruction

(6) Selection of the muons associated with the fired trigger. This cut is applied after extrapolating the muon track down to the two fired hodoscopes in order to determine if the muon is in its geometric acceptance

(7) and (8) Selection of oppositely charged muons that value of x_{F} is positive[1]. Selection of oppositely charged muons whose value of $p_\perp$ is between 0 and 4 GeV;

(9) and (10) Selection of dimuon events from the first 10 cm of the W target. Selection of dimuon events from the Al target. Figure 4.1 shows the impact of the radial cut in the *xy* plane of the vertex position.

The data analysis is performed by using the 9 periods of the 2018 data. Table 4.2 shows
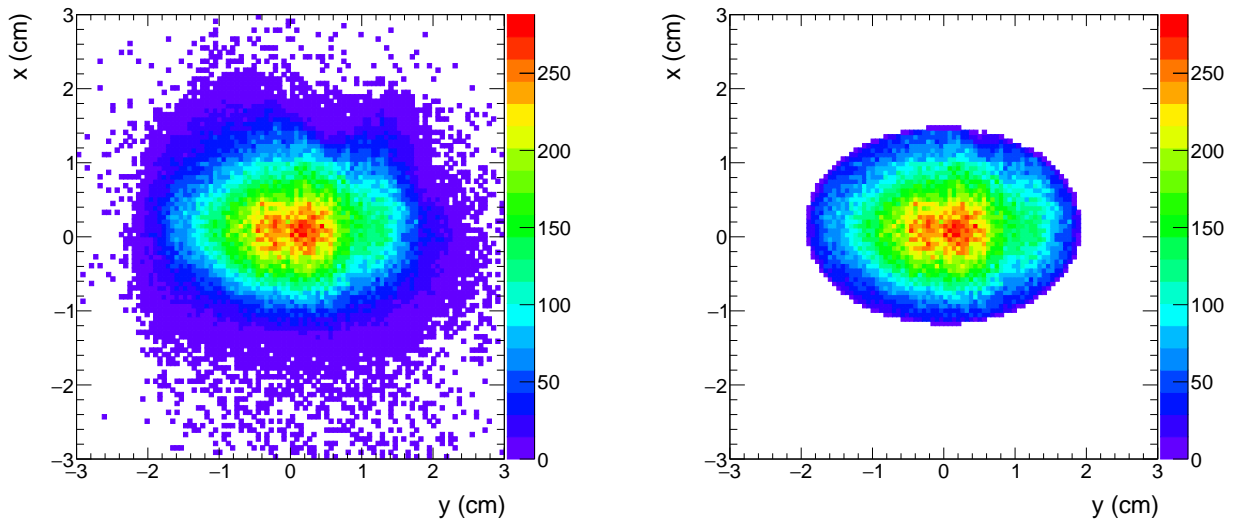
Figure 4.1: Radial vertex distribution in the W target.

the evolution of the number of events for each period according to the kinematic cuts applied throughout the selection. After all the cuts, there are on average five times more events in the W target compared to the Al target integrated in $1.5 < M < 8.5$ GeV.

4.2.2 Dimuon invariant mass

After applying all selection criteria, I can start comparing the data from the different targets. Figure 4.2 shows the dimuon events as a function of the invariant mass for *LasLas or LasOuter* triggers for the four COMPASS targets for the period P01. Before initiating the details of the analysis, several comments can be made on this invariant mass spectrum. First of all, the normalization of each dimuon mass distribution depends on the target, which shows that

---

[1]The rejection of x_{F} values between 0.9 and 1 is due to the edge effects of phase space whose acceptance is poorly controlled. I come back to this point later.

Selections	P00	P01	P02	P03	P04	P05	P06	P07	P08
	General selections of dimuon events								
(1)	1.55301e+07	7.99067e+06	1.61287e+07	1.21514e+07	1.09503e+07	7.15226e+06	8.18908e+06	1.39557e+07	5.02053e+06
(2)	1.50536e+07	7.73835e+06	1.55943e+07	1.17552e+07	1.06538e+07	6.87648e+06	7.91197e+06	1.34766e+07	4.8452e+06
(3)	1.49459e+07	7.67827e+06	1.54764e+07	1.16661e+07	1.05882e+07	6.82165e+06	7.8539e+06	1.33773e+07	4.8084e+06
(4)	1.05282e+07	5.86996e+06	1.2101e+07	9.15094e+06	1.0509e+07	5.26634e+06	6.05618e+06	1.02259e+07	3.6605e+06
(5)	1.0444e+07	5.82692e+06	1.2011e+07	9.08981e+06	8.13291e+06	5.22888e+06	6.01657e+06	1.01561e+07	3.63419e+06
(6)	8.32992e+06	4.7662e+06	9.84962e+06	7.37048e+06	8.07781e+06	4.3115e+06	5.01756e+06	8.43529e+06	3.05939e+06
(7)	6.04522e+06	3.50942e+06	7.32899e+06	5.49105e+06	4.93754e+06	3.21985e+06	3.77516e+06	6.3174e+06	2.28976e+06
(8)	6.04264e+06	3.50817e+06	7.32644e+06	5.48917e+06	4.93615e+06	3.21874e+06	3.77393e+06	6.31523e+06	2.289e+06
	Al target selections								
(09)	54328	36786	76401	56982	50839	34012	39374	66479	23987
	W target selections								
(10)	276905	192656	404666	298319	267741	179285	212733	351660	127813

Table 4.2: The statistics of the dimuon events for each of the 9 periods, following the cuts defined in Table 4.1.
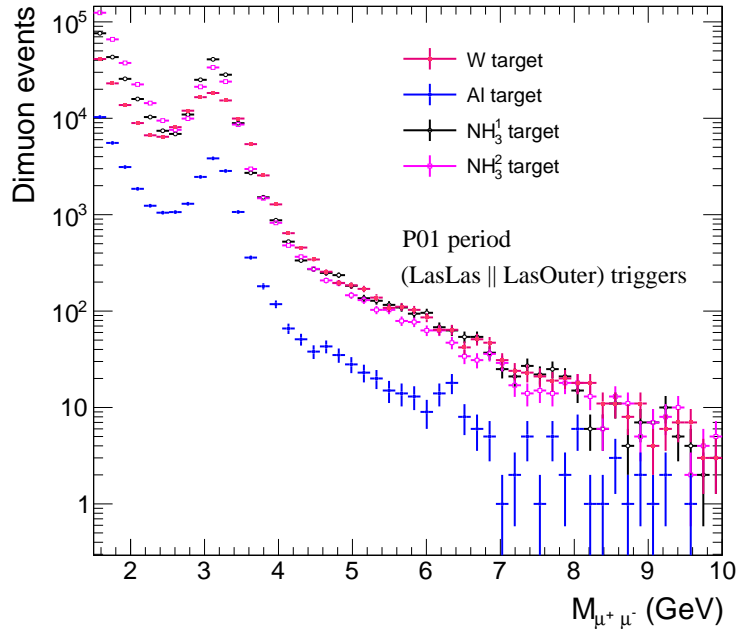
Figure 4.2: Dimuon events as a function of the invariant mass M (GeV) for the W (in red), Al (in blue), NH_3^1 (in black) and NH_3^2 (in magenta) targets in the period P01.

the acceptance of the spectrometer and the luminosity will be important corrective factors to access to the J/ψ absolute cross section. In addition, the resolution of the J/ψ peak around $M \sim 3$ GeV varies depending on the target as well worsening when going from the lighter to the heavier targets.

4.3 J/ψ signal extraction

In order to extract the number of J/ψ events for each target, there are essentially two methods. The first consists in finding a parametrization of the background and the J/ψ signal as a function of the dimuon invariant mass. This method is model-dependent insofar as a strong assumption is made concerning the values of the background. Often, the background evolves according to kinematic variables, it is sometimes difficult to find a single parameterization. The second

method consists in reproducing the dimuon invariant mass spectrum using the distributions from known physical processes (DY, Open-Charm, Charmonium) calculated using a MC simulation. This method makes it possible to use a parameterization of the background based on physical considerations and the spectrometer responses. It enables for taking into account the background evolution as a function of the kinematic parameters chosen. This method, which is more descriptive from a physical point of view, depends on the different inputs introduced during the MC simulation but also on the control of the response of the spectrometer. This method will be the method discussed and used to extract the J/ψ signal in the present analysis.

4.3.1 Invariant mass reconstruction

The dimuon invariant mass distribution for each target is analysed as a superposition of several physics process contributions, named "cocktail" method. The dimuon invariant mass contribution is evaluated by simulating each physics process with the PYTHIA8 event generator [142]. The dimuon invariant mass at COMPASS beam energy is composed by:

- Open-Charm (OC) semi-leptonic decays process dominant at $M \sim 2$ GeV;

- J/ψ ($M_{J/\psi} = 3.096$ GeV) and ψ' ($M_{\psi'} = 3.686$ GeV) processes dominant when $2 \lesssim M \lesssim 4$ GeV. Indeed, while the decay of a bound state results in the formation of a peak at the exact position of its mass[2], due to the resolution of the spectrometer, its distribution extends beyond its mass value;

- Drell-Yan (DY) process dominant when $M \gtrsim 4$ GeV.

For dimuon invariant masses lower than $M \lesssim 2$ GeV, the mass spectrum is dominated by uncorrelated decays of pions and kaons calculated from data, named Combinatorial Background (CB). The J/ψ, ψ', DY and OC contribution distributions are obtained by a TGEANT Monte-Carlo simulation[3] including a complete description of the DY COMPASS 2018 setup with effects induced by resolution, energy loss in the detectors and trigger requirements. All processes discussed in the next section are simulated by using the GRV pion [34] and the CT14 free proton PDFs [28] at NLO.

4.3.1.a Open-Charm contribution

The first process that participates in the invariant mass spectrum is the Open-Charm semi-leptonic process contribution. It describes the production of $D\bar{D}$ pair decaying into muons. This process constitutes a source of correlated[4] dimuon pairs produced from the partonic processes

$$ij \to D\bar{D} \to \mu^+ \mu^- \tag{4.5}$$

---

[2]In fact, there is width related to its lifetime.

[3]TGEANT software is a Geant4 based Monte Carlo simulation for the COMPASS-II experiment.

[4]The mean life of $D^\pm$ and D^0 are $(1040 \pm 7) \times 10^{-15}$ s and $(410.1 \pm 1.5) \times 10^{-15}$ s respectively.

where (i, j) are quarks or gluons. All channels giving a dimuon pair are simulated i.e. $D\bar{D}$, $\Lambda_{c\bar{c}}$, χ_c and ω_{c0} decays. Table 4.3 indicates the integrated cross section values provided by PYTHIA8 in $\pi^- n$ and $\pi^- p$ collisions. According to Table 4.3, the gg partonic channel is about $\sim 50\,\%$

Partonic channel	$\sigma_{\pi^-\mathrm{p}}(\mathrm{mb})$	$\sigma_{\pi^-\mathrm{n}}(\mathrm{mb})$
gg	$(2.006 \pm 0.014) \times 10^{-3}$	$(2.010 \pm 0.013) \times 10^{-3}$
$q\bar{q}$	$(1.299 \pm 0.016) \times 10^{-3}$	$(8.216 \pm 0.083) \times 10^{-4}$
sum	$(3.305 \pm 0.018) \times 10^{-3}$	$(2.831 \pm 0.015) \times 10^{-3}$

Table 4.3: The OC integrated cross section estimated by PYTHIA8.

larger than the $q\bar{q}$ channel in π^-p collisions. The simulation of Open-Charm contribution is quite
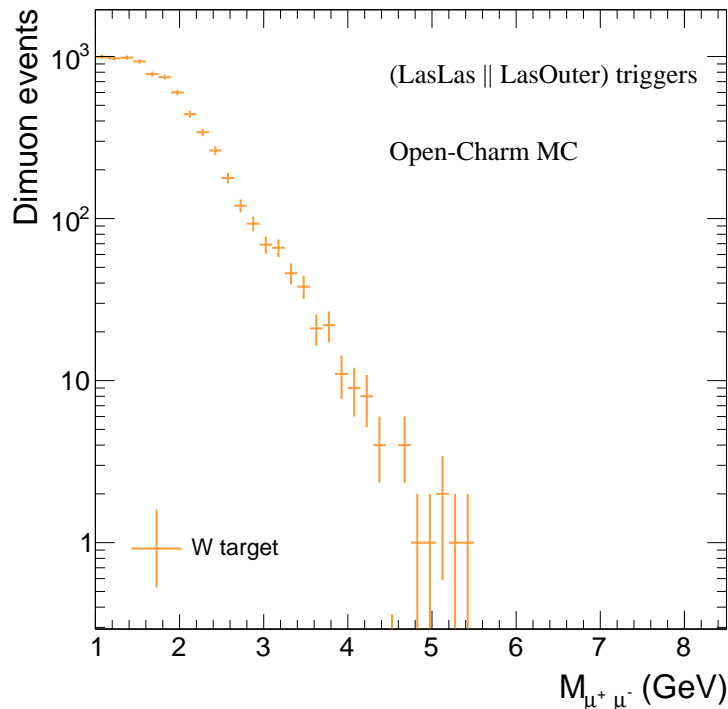
Figure 4.3: Open-Charm MC dimuon *reconstructed events* for the W target

complicated for several reasons. First, the cross section decreases rapidly as a function of the dimuon invariant mass. The OC distribution is dominated by dimuon mass with a mass $M \lesssim 2$ GeV. It becomes negligible in the high-mass region $M \gtrsim 5$ GeV, as illustrated in Fig. 4.3. Secondly, all possible channels decaying into $D\bar{D}$ pair must be taken into account. When $M \gtrsim 2$ GeV, the OC contribution follows a simple exponential law as a function of the dimuon invariant mass.

4.3.1.b   Charmonium process contribution

The second process describes the production of two charmed resonances, namely J/ψ and ψ' mesons decaying into muons. There are produced from the partonic processes

$$ij \to c\bar{c} \to J/\psi \to \mu^+\mu^- \tag{4.6}$$

where (i, j) are quarks or gluons. The initial partonic dominant channel depends on the incoming hadron but also on the production model as discussed in Chap. 2. The production model used by PYTHIA8 to calculate of charmonium production cross section is NRQCD. Because the relative cross section ratio between J/ψ and ψ' is not well known, these two processes were simulated independently.[5] The evolution of prompt-J/ψ[6] and prompt-ψ' integrated cross section are summarized in Table 4.4. Some comments are given: (i) the integrated values of the prompt-J/ψ and prompt-ψ' cross sections differ by 20% only and (ii) the comparison between the integrated cross section in π^-p and π^-n indicates that the *gg* channel dominates the absolute cross section in PYTHIA8 generator[7].

Process	$\sigma_{\pi^-\text{p}}(\text{mb})$	$\sigma_{\pi^-\text{n}}(\text{mb})$
Prompt-J/ψ	$(6.75 \pm 0.03) \times 10^{-5}$	$(6.60 \pm 0.04) \times 10^{-5}$
Prompt-ψ'	$(7.54 \pm 0.04) \times 10^{-6}$	$(7.38 \pm 0.04) \times 10^{-6}$

Table 4.4: The charmonium absolute cross section estimated by PYTHIA8.

Despite the ignorance of the production model of charmonium, the invariant mass spectrum is mainly sensitive to the resolution of the spectrometer. However, the mass resolution is correlated to the angular resolution of the muons produced and therefore indirectly to the production model. Depending on the angular distribution of the muons produced, the response of the spectrometer could be different and consequently, the J/ψ and ψ' mass resolution also. This effect is considered as negligible compared to the spectrometer effects (the resolution effect for instance).

The J/ψ and ψ' distributions are shown separately in Fig. 4.4 as a function of the dimuon invariant mass in the W target. The distribution of dimuon events is at first approximation a Gaussian shape. A fit of the J/ψ and ψ' distributions gives a resolution in the W target of $\sigma_{J/\psi} = (0.362 \pm 0.001)$ GeV and $\sigma_{\psi'} = (0.372 \pm 0.001)$ GeV.

Effect on the resolution on charmonium distribution Figure 4.5 shows the effect of the reconstruction of the MC J/ψ distribution for three different targets. First, the more the target in upstream position, the more the resolution improves. In order to estimate the dimuon mass resolution, the MC J/ψ distribution is fitted with a single Gaussian function. The fit results are summarised in Table 4.5. The reduced χ^2 degrades quickly with the resolution because of the J/ψ distribution doesn't follow the Gaussian shape approximation. In addition, the position of the peak of J/ψ is the same for the NH_3^2 and Al targets while for the W target, the average position is shifted towards a lower mass.

---

[5] The J/ψ and ψ' processes are simulated independently so as not to depend on the their relative cross sections ratio given by PYTHIA8 generator.

[6] As discussed In Sec. 1.3.4, the NRQCD model enables to describe the direct production of J/ψ, named prompt-J/ψ, but also the indirect production via the decay of excited states of charmonium into J/ψ state.

[7] Indeed, if $\sigma_{\pi^-\text{p}} \approx \sigma_{\pi^-\text{n}}$, it implies that the valence quark PDFs does not contribute in the J/ψ cross section.
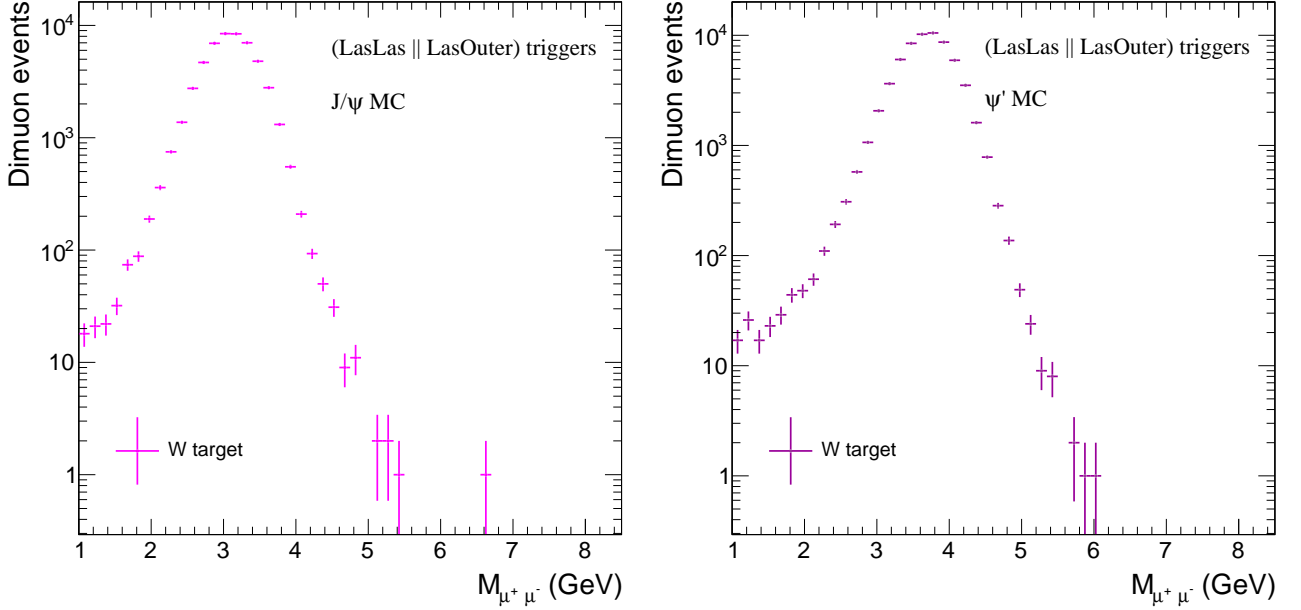
Figure 4.4: J/ψ (left panel) and ψ' (right panel) MC distributions as a function of dimuon invariant mass.

Target	$\langle M \rangle$ (GeV)	$\sigma_{J/\psi}$ (MeV)	χ^2/ndf
NH_3^2	3.135 ± 0.006	194 ± 0.06	144
Al	3.135 ± 0.006	212 ± 0.02	44
W	3.095 ± 0.017	362 ± 0.01	19

Table 4.5: Estimation of the J/ψ resolution for NH_3^1, Al and W targets by fitting the dimuon invariant mass from MC with a Gaussian function.

Secondly, at low dimuon invariant masses $M \lesssim 2$ GeV, a shoulder appears for the Al target. While the distribution decreases more smoothly in the NH_3^2 target. This effect is less pronounced in the W target. It is explained by the fact that the muons produced lose their energy depending on their polar angles, the energy losses in the the absorber are different.

4.3.1.c   Uncorrelated background contribution

The dominant background for $M \sim 2$ GeV is due to the decay of kaons and pions via

$$
\begin{aligned}
\pi^+ &\to \mu^+ + \nu_\mu \\
\pi^- &\to \mu^- + \bar{\nu}_\mu \\
K^+ &\to \mu^+ + \nu_\mu \\
K^- &\to \mu^- + \bar{\nu}_\mu.
\end{aligned}
\tag{4.7}
$$

Uncorrelated muons can accidentally be combined in the track reconstruction and satisfy the trigger and cut requirements generating the uncorrelated background events, named *Combinatorial Background* (CB). After collecting the single muons, the number of dimuons is calculated via the
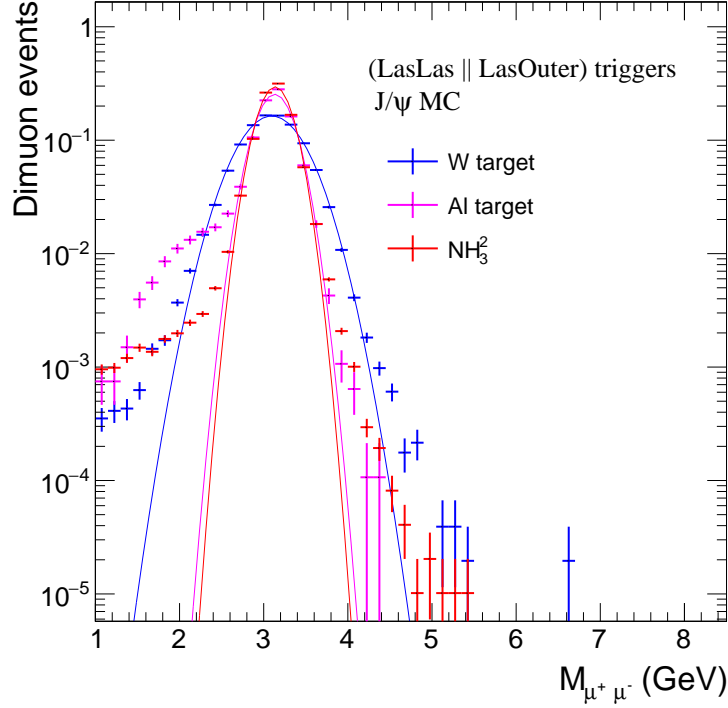
Figure 4.5: J/ψ MC distribution in the W (in blue), Al (in magenta) and $\mathrm{NH_3^2}$ (in red) targets.

technique of event mixing used in [143]. The event-mixing method is based on two assumptions: (1) the muon tracks come from different physical processes and (2) they are completely independent of each other. The total number of uncorrelated dimuon pairs $N_{\mu^+\mu^-}^{\mathrm{CB}}$ is equal to

$$\frac{\mathrm{d}N_{\mathrm{CB}}^{+-}}{\mathrm{d}M} = 2\sqrt{\frac{\mathrm{d}N^{++}}{\mathrm{d}M}\frac{\mathrm{d}N^{--}}{\mathrm{d}M}} \cdot \frac{A^{+-}}{\sqrt{A^{++}A^{--}}} \tag{4.8}$$

where A^{+-}, A^{++} and A^{--} are the acceptances of opposite-sign and like-sign dimuon pairs. In order to make the acceptances of the spectrum independent of the charge of the detected muon, an additional cut, *image cut*, is applied to the data such as $\frac{A^{+-}}{\sqrt{A^{++}A^{--}}} = 1$. Figure 4.6 shows the contributions of $\mu^+\mu^+$ and $\mu^-\mu^-$ pairs for the period P01 as a function of the dimuon invariant mass. The uncorrelated dimuon pairs contribute essentially for $M \lesssim 5$ GeV. In the high-mass region, the uncorrelated background contributes for less than 1% of the dimuon number of events.

4.3.1.d Drell-Yan contribution

The last process participating in the dimuon invariant mass spectrum is the DY process. At LO, it describes the annihilation between a quark and an antiquark into a virtual photon,

$$q\bar{q} \rightarrow \gamma^\star \rightarrow \mu^+\mu^-. \tag{4.9}$$

The integrated DY absolute cross sections from PYTHIA8 as a function of the dimuon invariant mass are summarized in Table 4.6. At high-mass $4 \lesssim M \lesssim 9$ GeV, the ratio between $\sigma_{\pi^-p}^{\mathrm{DY}}$
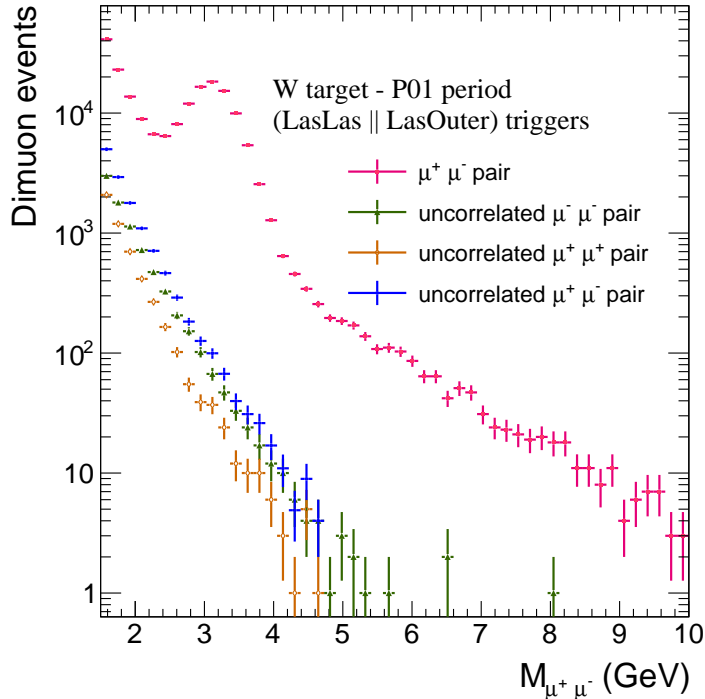
Figure 4.6: Dimuon mass distribution including total dimuon pairs with opposite sign (in red), uncorrelated dimuon pairs with same sign (in green and yellow), combinatorial background calculation (in blue).

and $\sigma_{\pi^- n}^{\mathrm{DY}}$ is around 1.9. Indeed, by considering $\langle M \rangle \sim 4$ GeV, $\langle x_2 \rangle \sim 0.2$, the DY cross section is dominated by the contribution of the valence u quark PDFs of the nucleon where $u(x_2)^p \approx 2u(x_2)^n$. Figure 4.7 shows the *reconstructed events* from MC simulation for the DY

Invariant mass region (GeV)	$\sigma_{\pi^- p}^{DY}$(nb)	$\sigma_{\pi^- n}^{DY}$(nb)
$1 - 11$	0.2524 ± 0.0004	0.1366 ± 0.0002
$4 - 9$	0.1521 ± 0.0002	0.0787 ± 0.0001

Table 4.6: The DY absolute cross section estimated by PYTHIA8.

process as a function of the dimuon invariant mass in the W target. For $M \lesssim 2$ GeV, at the edge of phase space, *reconstructed events* exhibit an elbow due to the resolution effect. It is therefore necessary to generate events in a dimuon mass phase space sufficiently large to avoid resolution degradation in the mass range fit considered. In this case, the MC sample is generated for $M \in (1, 11)$ GeV. The distribution of the DY contribution follows an exponential law in $M \gtrsim 2$ GeV region.[8] The simple form of this contribution will enable to constrain its normalisation during the reconstruction of mass spectrum by comparing the high-mass region between the

---

[8]The DY contribution distribution as a function of dimuon mass is fitted with a single exponential function in $M \gtrsim 2$ GeV. The fit result gives $\propto e^{\alpha M}$, with $\alpha =$ -0.83 $\pm$ 0.01 and χ^2/ndf = 1.1 for the W target.
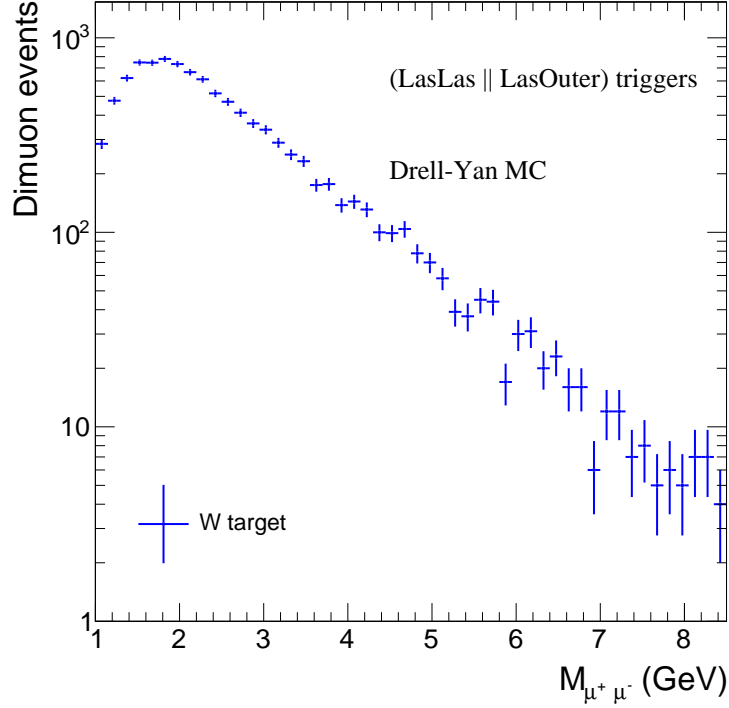
Figure 4.7: Drell-Yan MC dimuon *reconstructed events* in the W target

real data (RD) and MC simulation. Indeed, the other contributions described above do not contribute in the dimuon invariant mas region when $M \gtrsim 5$ GeV.

4.3.2 Fit procedure

In order to reproduce the dimuon invariant mass spectrum, the contributions OC, DY, J/ψ, ψ' are fitted to the RD spectrum. The normalisation of the uncorrelated background contribution (CB) is fixed to 1 because this contribution is calculated from the RD following Eq. (4.11). In addition, to take into account the fact that the resolution can be underestimated in MC simulation, the J/ψ MC distribution is multiplied by a Gaussian function

$$f(M)^{J/\psi}_{\text{MC+Gaussian}} = f(M)^{J/\psi}_{\text{MC}} \times \mathcal{N}e^{-\frac{(M-\mu)^2}{2\sigma^2}} \qquad (4.10)$$

where σ, $\mathcal{N}$ and μ are free parameters. The final fit function for $M > 2$ GeV region is

$$f(M)_{\text{fit}} = \alpha_1 f(M)^{J/\psi}_{\text{MC+Gaussian}} + \alpha_2 f(M)^{\psi'}_{\text{MC}} + \alpha_3 f(M)^{\text{OC}}_{\text{MC}} + \alpha_4 f(M)^{\text{CB}}_{\text{RD}} \qquad (4.11)$$

where α_i with $i \in 1, 2, 3$ are free parameters and α_4 value is fixed to 1.

4.3.2.a Invariant mass fit for the W target

The dimuon invariant mass fit for $M \in (2 - 8.5)$ GeV for each of the nine periods in the W target is performed according to (4.11) as illustrated in Fig. 4.8. The normalisation of the DY
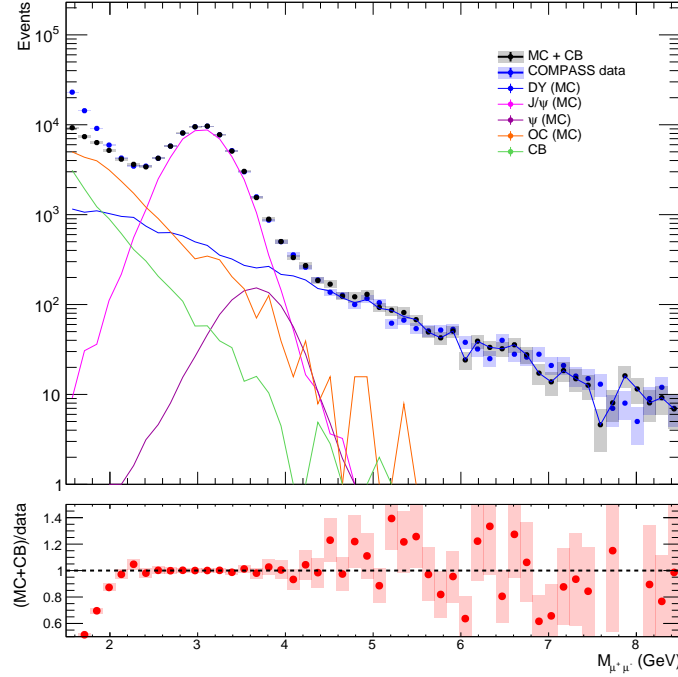
Figure 4.8: Invariant mass for the period P01 and the W target (top) and ratio between MC calculation and RD (bottom).

Period	Number of J/ψ events	χ^2/ndf	μ (GeV)	σ (GeV)
P00	$110311 \pm (332)_{\text{stat}}$	4.8	3.08 ± 0.01	0.78 ± 0.02
P01	$77333 \pm (278)_{\text{stat}}$	3.2	3.13 ± 0.01	0.76 ± 0.03
P02	$163402 \pm (404)_{\text{stat}}$	5.3	3.12 ± 0.01	0.78 ± 0.02
P03	$118758 \pm (345)_{\text{stat}}$	3.8	3.12 ± 0.01	0.75 ± 0.02
P04	$104921 \pm (323)_{\text{stat}}$	4.1	3.08 ± 0.01	0.73 ± 0.02
P05	$70813 \pm (266)_{\text{stat}}$	3.6	3.10 ± 0.01	0.75 ± 0.03
P06	$84935 \pm (291)_{\text{stat}}$	3.9	3.13 ± 0.01	0.79 ± 0.03
P07	$141143 \pm (376)_{\text{stat}}$	5.3	3.10 ± 0.01	0.78 ± 0.02
P08	$51215 \pm (226)_{\text{stat}}$	2.4	3.08 ± 0.01	0.79 ± 0.04

Table 4.7: Number of J/ψ events from the W target extracted using the "cocktail method" for each of the nine periods. Here, μ and σ are the parameters of the Gaussian function from J/ψ fit according to Eq. (4.10).

contribution is fixed by fitting the high-mass regions $M \gtrsim 5$ GeV where the contribution is dominant. The fit results for each period in the W target are summarized in Table 4.7. Figure 4.8 shows a perfect agreement between the "cocktail" method and the RD in J/ψ region where $2 \lesssim M \lesssim 4$ GeV. The values obtained of μ and σ parameters in Gaussian function multiplied to the J/ψ MC distribution are summarized in Table 4.7. They show that it is necessary to add a Gaussian function in the MC in order to reproduce the RD: that is to degrade the J/ψ mass resolution. The dominant background in the J/ψ region, i.e. $2 \lesssim M \lesssim 5$ GeV, comes mainly

from the OC (17%), the DY (13%) and the CB (3%), see Table 4.8. The confidence in the

Process	Contribution (%)
J/ψ	66%
OC	17%
DY	13%
CB	3%
ψ'	1%

Table 4.8: Contribution of each process integrated for $M \in (2-5)$ GeV for the period P01 in the W target.

DY contribution normalisation is important insofar as it is constrained by $M \gtrsim 5$ GeV region. For $M < 2$ GeV region, excluded from the fit, it is shown that the background is not correctly described by "cocktail" fit method. Several elements can explain this observation:

- The dimuon invariant mass shape of the RD in the region where $M < 2$ GeV follows approximately an exponential law, just like the CB contribution. The OC cross section could therefore be overestimated;

- The mass resolution in this region is degrading enormously. Other processes could participate in the reconstruction of the mass spectrum like light mesons decays (ω and ρ mesons);

- The OC distribution distribution may be wrong since this process is difficult to control in PYTHIA.

These elements show the limits of the "cocktail" method. Although it is based on physical considerations, it is confronted with a lack of knowledge of the simulated processes.

4.3.2.b Invariant mass fit for the Al target

The dimuon invariant mass fit for each of the nine periods in the Al target is performed according to Eq. (4.11) as illustrated in Fig. 4.9 following the same procedure as for W target. The fit results are summarised in Table 4.10 for the Al target. The best reduced χ^2/ndf is obtained in the Al target without adding a Gaussian function. The mass resolution is therefore well reproduced by the MC in this specific target. The $M < 2$ region is just as poorly described in the Al as in the W target. While the relative contribution of the CB in $2 \lesssim M \lesssim 5$ GeV region is about 3% for the W target, it is almost 10% for the Al target. Otherwise, the relative contribution of the OC is identical $\sim 17\%$, see Table 4.9.
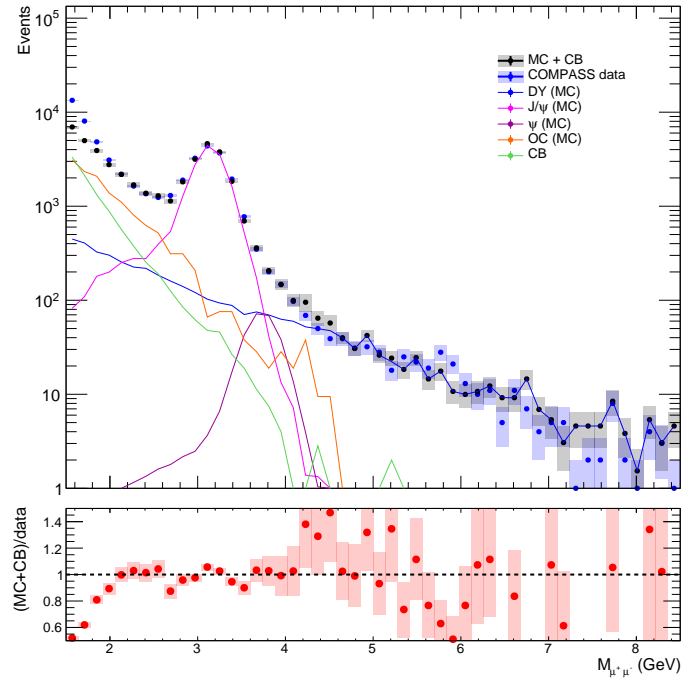
Figure 4.9: Invariant mass for the period P01 and the Al target (top) and the ratio between the MC simulation and RD (bottom).

Process	Contribution (%)
J/ψ	64%
OC	17%
DY	8%
CB	10%
ψ'	1%

Table 4.9: Contribution of each process for $M \in (2-5)$ GeV for the period P01 in the Al target.

4.3.3 J/ψ resolution estimation from Monte-Carlo simulation

Using a Monte-Carlo simulation, it is possible to quantify the resolution of each kinematic variable in order to determine the relevant binning choice for x_{F} and $p_{\perp}$ distributions. A part of all *generated events* is not detected by the spectrometer due to the geometric acceptance. Another part is detected, named *true-generated events*, then reconstructed, *reconstructed events*, by the reconstruction software. They include all the reconstruction effects including the resolution effects. It is therefore possible to compare each reconstructed track with the associated generated track. If the track has been reconstructed at $Z_{\mathrm{vtx}}^{\mathrm{reconstructed}}$ given, its associated generated track will be positioned at another $Z_{\mathrm{vtx}}^{\mathrm{generated}}$. The difference between these two positions is related to the resolution effects of the spectrometer.

Period	Number of J/ψ events	χ^2/ndf
P00	$16672 \pm (129)_{\text{stat}}$	3.7
P01	$11925 \pm (109)_{\text{stat}}$	2.9
P02	$24235 \pm (155)_{\text{stat}}$	5.0
P03	$17731 \pm (133)_{\text{stat}}$	3.4
P04	$15692 \pm (125)_{\text{stat}}$	2.7
P05	$10464 \pm (102)_{\text{stat}}$	3.5
P06	$12016 \pm (110)_{\text{stat}}$	2.8
P07	$20596 \pm (144)_{\text{stat}}$	5.3
P08	$7284 \pm (85)_{\text{stat}}$	2.4

Table 4.10: Number of J/ψ events from the Al target extracted using the "cocktail method" for each of the nine periods.

Consequently, the resolution is determined by calculating the difference between *true-generated events* and *reconstructed events* associated. The distribution is fitted with two Gaussian functions: one in order to extract the resolution of the kinematic variable and one to estimate the background caused by the mis-associations between *true-generated* and reconstructed events. These values are estimates and only make sense if the Monte-Carlo reproduces in a faithful manner the real conditions of the data taking. An example of a fit for the x_{F} variable for the W target is shown in Fig. 4.10. Table 4.11 summarizes the resolution values determined by the MC simulation for the main variables. The invariant mass and Z_{vtx} position resolutions depend

Kinematics variables	Nuclear targets		
	Ammoniac (NH$_3$)	Aluminium (Al)	Tungsten (W)
x_{vtx} (cm)	0.028 ± 0.001	0.038 ± 0.001	0.044 ± 0.001
y_{vtx} (cm)	0.024 ± 0.001	0.035 ± 0.001	0.043 ± 0.001
Z_{vtx} (cm)	10.4 ± 0.18	2.79 ± 0.09	5.65 ± 0.006
M (GeV)	0.143 ± 0.001	0.223 ± 0.004	0.351 ± 0.002
x_{F}	0.011 ± 0.001	0.014 ± 0.001	0.025 ± 0.001
$p_\perp$ (GeV)	0.108 ± 0.001	0.228 ± 0.004	0.290 ± 0.002

Table 4.11: Estimated resolutions for the J/ψ′ process.

strongly on the nuclear target considered. The Z_{vtx} resolution decreases by a factor of two between the most upstream target, NH$_3$, and the most downstream target, W. This is mainly due to the fact that the dimuon tracks have to be extrapolated to their vertex. The further upstream the target is, the greater the associated error, as the corresponding polar angles are small in the geometrical acceptance of the spectrometer.
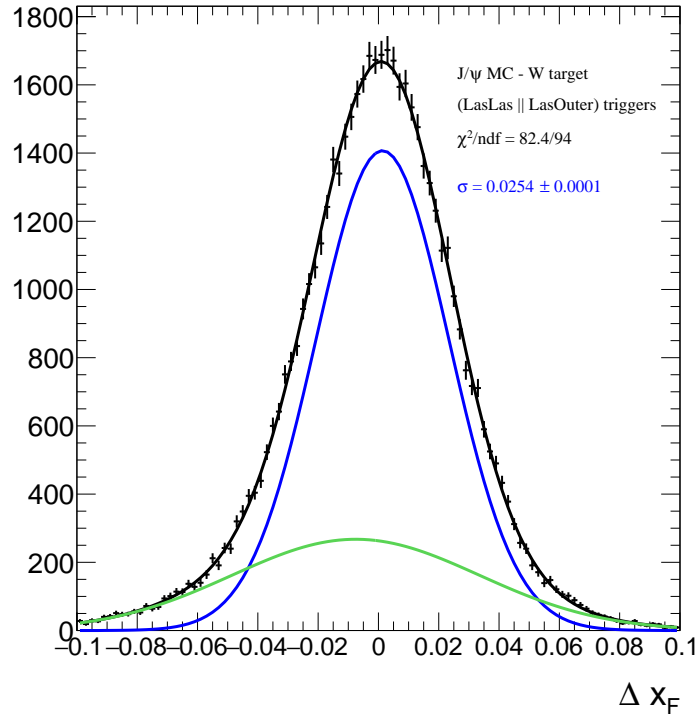
Figure 4.10: Difference between *true-generated events* and *reconstructed events* associated, Δx_F, for x_F kinematic variable. In blue, the Gaussian function used to estimate the kinematic resolution in the W target. In green, the Gaussian function used to estimate the background caused by the mis-associations.

4.3.4 J/ψ **2D extraction method**

In order to extract the number of J/ψ as a function of x_F and $p_\perp$, an invariant mass fit is performed in each 2D (x_F and $p_\perp$) kinematic bin. The limit of the width of the binning chosen is determined in accordance with the resolution summarized in Table 4.11. For the study of cross sections ratio, the target with the lowest resolution, i.e. the W target, will constrain the limit of the width of the possible binning. The binning used for the present analysis is $x_\mathrm{F} \in [0 - 0.1, 0.1 - 0.2, 0.2 - 0.3, 0.3 - 0.4, 0.4 - 0.5, 0.5 - 0.6, 0.6 - 0.9]$ and $p_\perp \in [0 - 0.5, 0.5 - 1.0, 1.0 - 1.5, 1.5 - 2.0, 2.0 - 2.5, 2.5 - 3.0, 3.0 - 3.5, 3.5 - 4.0]$ GeV.

4.3.4.a   **W target**

In each 2D (x_F, $p_\perp$) bin value, an invariant mass fit for $M \in (2 - 8.5)$ GeV is performed using the "cocktail method". The results of the fit are shown in Fig. 4.11 as a function of $p_\perp$ for the x_F interval (0.1 - 0.2). Table 4.12 shows the χ^2/ndf values for each 2D (x_F, $p_\perp$) bin value. A χ^2/ndf value of $\varnothing$ indicates an empty 2D bin.

The fit shows a reasonable agreement in $M \gtrsim 2$ GeV. Despite a significant number of physical contributions in the fit. It is possible to correctly reproduce a wide range in dimuon mass. In contrast for $M \lesssim 2$ GeV, a disagreement between the fit and RD is observed. It varies as a
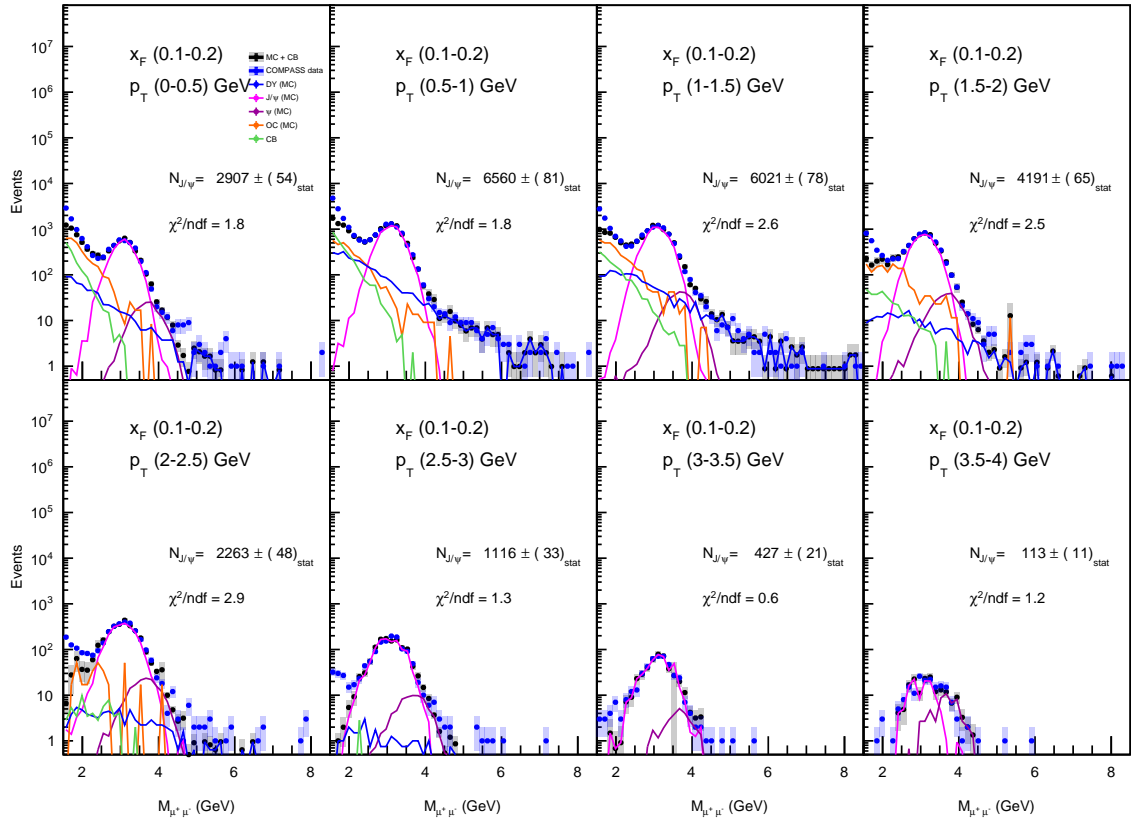
Figure 4.11: Number of J/ψ events as a function of the dimuon mass for different $p_\perp$ bins for $x_F \in (0.1 - 0.2)$ extracted thanks an invariant mass fit with "cocktail" method for the period P01 in the W target.

$p_\perp$ \ x_F	0-0.5	0.5-1	1-1.5	1.5-2	2-2.5	2.5-3	3-3.5	3.5-4
0-0.1	4.5	1.6	2.0	2.2	2.2	1.3	0.9	∅
0.1-0.2	1.8	1.8	2.6	2.5	2.9	1.3	0.6	1.2
0.2-0.3	1.7	2.4	1.9	3.2	2.5	1.1	0.9	∅
0.3-0.4	2.0	3.2	5.9	3.3	1.7	1.2	0.8	∅
0.4-0.5	3.5	4.3	2.7	1.5	0.8	0.9	∅	∅
0.5-0.6	2.5	3.0	2.4	1.7	0.4	∅	∅	∅
0.6-0.9	2.0	2.0	1.9	2.6	∅	∅	∅	∅

Table 4.12: χ^2/ndf obtained by using the "cocktail method" for the W target and for the period P01. A χ^2/ndf value of ∅ indicates an empty 2D bin.

function of $p_\perp$ and tends to decrease for the region with large $p_\perp$. This point shows that a physical effect is possibly not taken into account in the "cocktail" method or that one of the contribution is poorly known. Two potential candidates are the OC and the CB contributions as discussed In Sec. 4.3.2.a. In addition, the total background varies as a function of $p_\perp$: decrease with $p_\perp$

vanishing for the last $p_\perp$ bin. Only the contribution of charmonium contributes to the dimuon mass spectrum. The extraction of the number of J/ψ as a function of $p_\perp$ and x_F proves essential to take properly into account the evolution of the background in the various kinematic bins.

The correlation map for the J/ψ events as a function of x_F and $p_\perp$ is shown in Fig. 4.12. The large $x_F \to 0.9$ region is dominated by small $p_\perp \lesssim 1$ GeV values while large $p_\perp \approx 4$ GeV values are dominated by the moderate $x_F \sim 0$ values. Figure 4.13 (left panel) shows the J/ψ
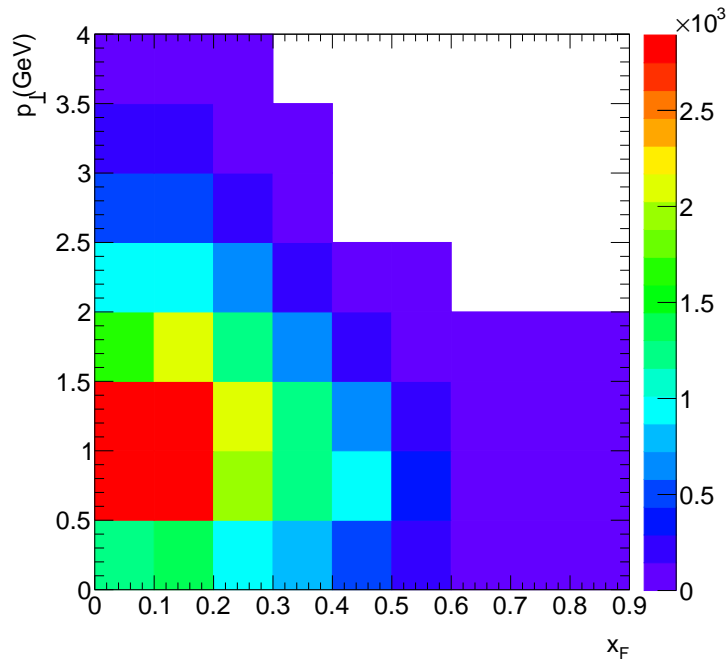
Figure 4.12: Number of J/ψ events as a function of $p_\perp$ and x_F extracted using an invariant mass fit with "cocktail" method for the period P01 for the W target.

events as a function of the x_F integrated over the $p_\perp$ range, $0 < p_\perp < 4$ GeV and (right panel) the number of J/ψ events as a function of $p_\perp$ integrated over the x_F range, $0 < x_F < 0.9$. The mean value of x_F and $p_\perp$ distributions are $\langle x_F \rangle = 0.20$ and $\langle p_\perp \rangle = 1.22$ GeV respectively.

4.3.4.b Aluminium target

In the same way as the W target, an invariant mass fit in each 2D $(x_F, p_\perp)$ bin is also performed to extract the J/ψ events for $M \in (2 - 8.5)$ GeV for the Al target. The analysis is strictly identical to that of the W target concerning the extracting method of the J/ψ number. Table 4.13 shows the χ^2/ndf values for each 2D $(x_F, p_\perp)$ bin value.

Figure 4.14 shows the correlation between $p_\perp$ and x_F in the Al target. The mean value obtained of x_F distribution is $\langle x_F \rangle = 0.22$ and $p_\perp$ distribution is $\langle p_\perp \rangle = 1.10$ GeV. The x_F $(p_\perp)$ distribution integrated for all $p_\perp$ (x_F) values for the period P01 and the Al target is shown in Fig. 4.15.
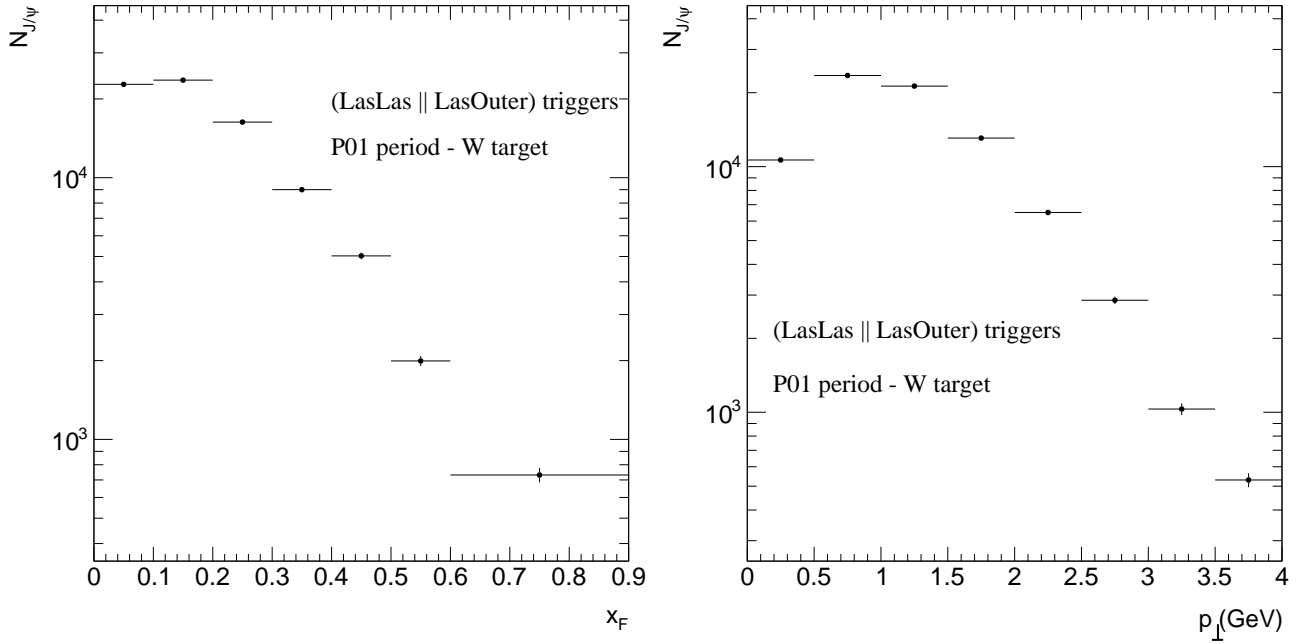
Figure 4.13: Number of J/ψ events collected during the period P01 for the W target as a function of x_F and $p_\perp$.
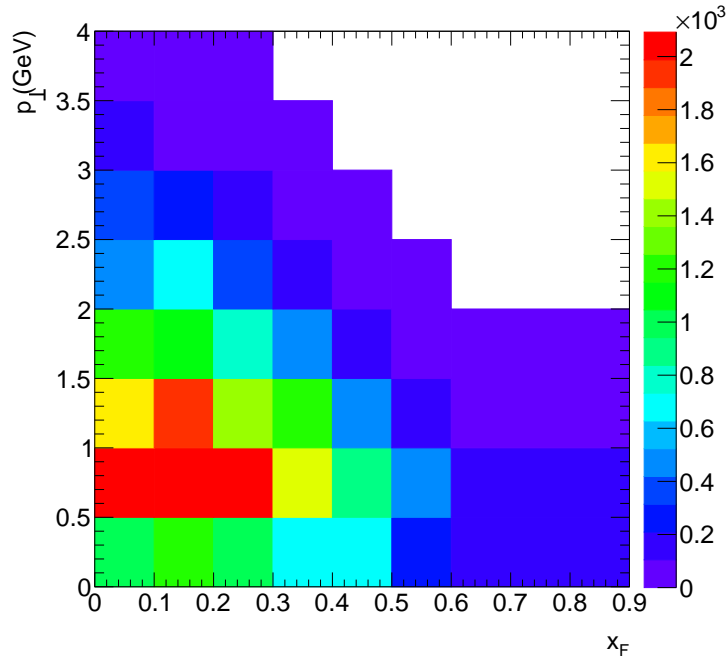
Figure 4.14: Number of J/ψ events as a function of $p_\perp$ and x_F extracted using an invariant mass fit with "cocktail" method for the period P01 for the Al target.

4.3.4.c Event migration as a function of Z_{vtx}

Due to the absence of a vertex detector, it is difficult to reconstruct the precise position of the vertex of the dimuon tracks. Depending on the dimuon invariant mass and the Z_{vtx} position,

x_{F} \ $p_\perp$	0-0.5	0.5-1	1-1.5	1.5-2	2-2.5	2.5-3	3-3.5	3.5-4
0-0.1	2.1	2.0	2.7	1.3	2.0	1.0	∅	∅
0.1-0.2	1.7	3.8	1.5	1.0	1.5	1.6	∅	∅
0.2-0.3	0.5	2.1	1.3	0.8	0.6	0.4	2.3	∅
0.3-0.4	2.1	1.9	0.8	0.8	0.9	∅	∅	∅
0.4-0.5	1.4	1.4	1.4	1.4	0.7	∅	∅	∅
0.5-0.6	1.5	2.1	1.1	0.3	∅	∅	∅	∅
0.6-0.9	0.8	0.9	0.7	∅	∅	∅	∅	∅

Table 4.13: χ^2/ndf obtained by using the "cocktail method" for the Al target and for the period P01. A χ^2/ndf value of ∅ indicates an empty 2D bin.
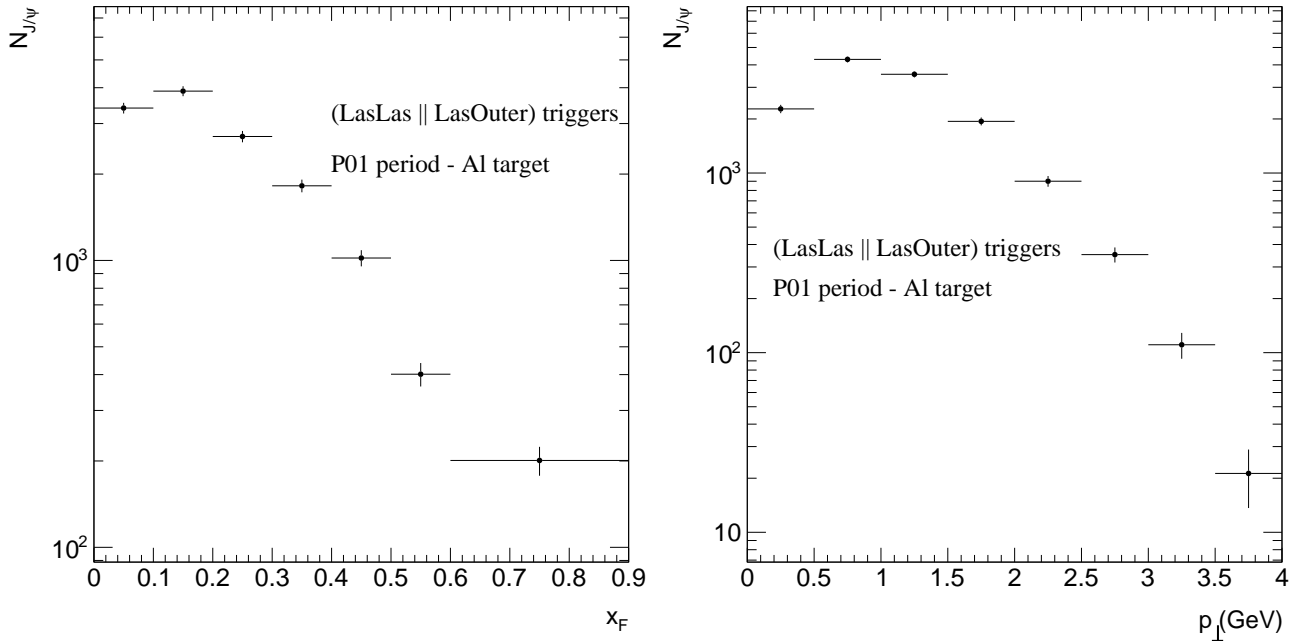
Figure 4.15: Number of J/ψ events collected during the period P01 for the Al target as a function of x_{F} and $p_\perp$.

the resolution of the spectrometer may deteriorate and generate a migration effect. Figure 4.16 shows the position of *reconstructed events* as a function of Z_{vtx} from MC J/ψ simulation. A fraction of *generated events* in $Z_{vtx} \in (-30, -20)$ cm, i.e. from the W target, migrates to Z_{vtx} position corresponding to the Al target position. Consequently, it is possible to estimate the fraction of events contamination in the Al target coming from the W target. The results are summarized in Table 4.14 and 4.15 for the x_{F} and $p_\perp$ integrated bins, respectively.

The contamination of J/ψ events, coming from the W migrating to the Al target, depends on the value of the x_{F} or $p_\perp$ bin. At the edge of the phase space in both $\perp$ and x_{F} variables, the contamination fraction is the lowest.
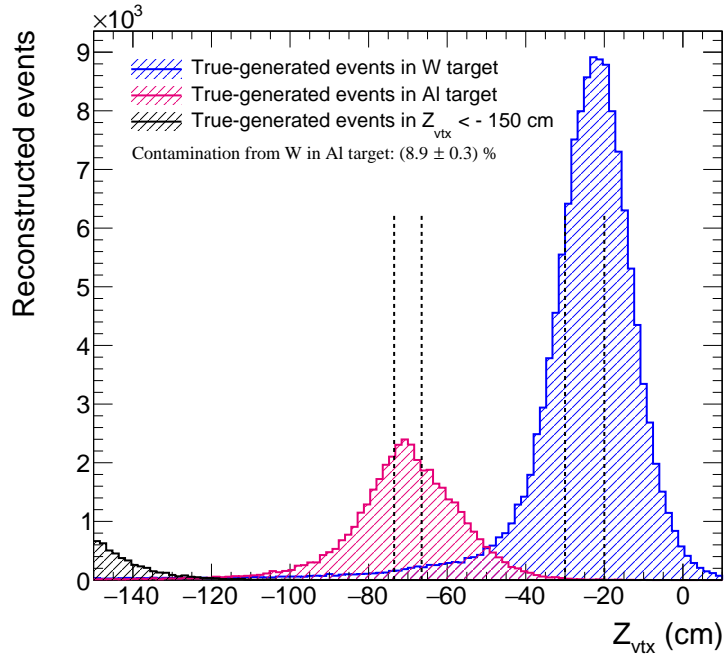
Figure 4.16: Reconstructed dimuon events as a function of Z_{vtx} from the J/ψ MC simulation. In red, *reconstructed events* from *true-generated events* associated inside Al target and in blue, *reconstructed events* from *true-generated events* associated inside W target.

x_{F}	Fraction of contamination
0-0.1	0.028 ± 0.003
0.1-0.2	0.053 ± 0.004
0.2-0.3	0.110 ± 0.006
0.3-0.4	0.150 ± 0.001
0.4-0.5	0.167 ± 0.013
0.5-0.6	0.137 ± 0.017
0.6-0.9	0.086 ± 0.002

Table 4.14: Estimation of events contamination in the Al target from the W target for each x_{F} kinematic bin.

$p_{\perp}$ (GeV)	Fraction of contamination
0-0.5	0.160 ± 0.010
0.5-1	0.110 ± 0.010
1-1.5	0.081 ± 0.006
1.5-2	0.054 ± 0.004
2-2.5	0.034 ± 0.004
2.5-3	0.032 ± 0.005
3-3.5	0.090 ± 0.001
3.5-4	0.080 ± 0.003

Table 4.15: Estimation of events contamination for the Al target from the W target for each $p_{\perp}$ kinematic bin.

As discussed in Sec. 4.3.3, the x_F region in which the contamination is the highest, namely for $x_F \in (0.2 - 0.5)$, corresponds to the low values of $\theta^{\mu^-} \lesssim 0.04$ rad (see Fig. 5.2 (left panel)). In the same way, the $p_\perp$ region including the highest contamination rate, namely for $p_\perp \in (0 - 1.5)$ GeV, contains the low values of θ^{μ^-} muons polar angles, $\theta \lesssim 0.04$ rad (see Fig. 5.2 (right panel)).
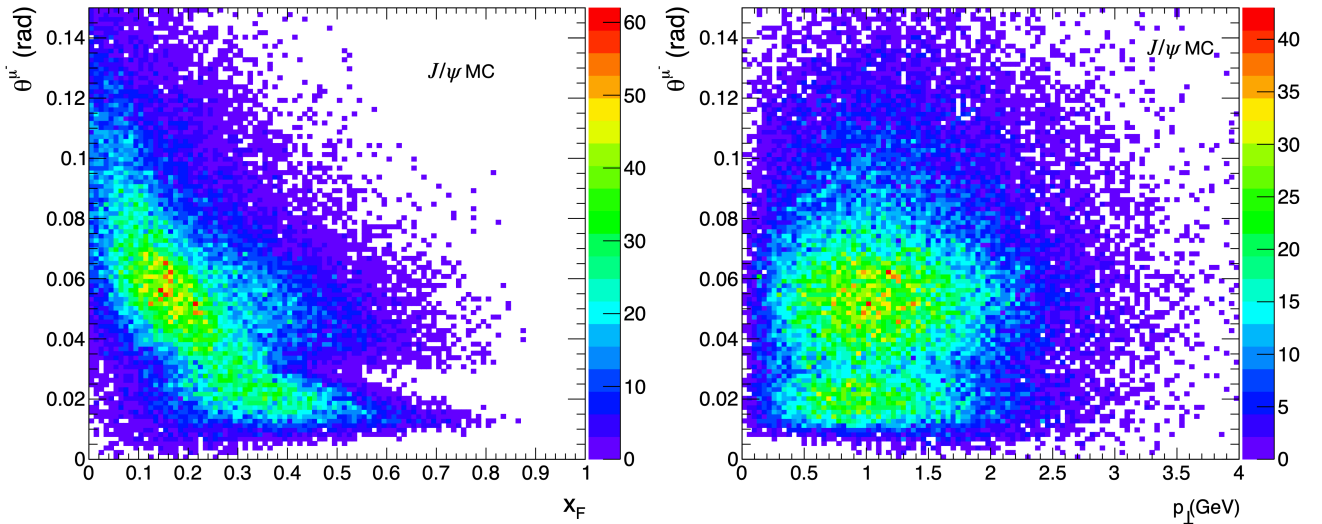
Figure 4.17: θ^{μ^-} muon polar angle as a function of x_F (left panel) and $p_\perp$ (right panel) from the J/ψ MC for the W target.

In order to gain confidence in the contamination fraction rates, it is necessary to verify that the MC reproduces the RD correctly. Due to the method of extraction over the full dimuon mass range, it is difficult to directly compare kinematic distributions between MC and RD due to the background contribution. On the other hand, it is possible to consider a limited dimuon mass range, $M \in (3; 3.3)$ GeV, where the J/ψ process is dominant. The J/ψ purity in the Al target data sample is about 95%[9]. The Z_{vtx} distribution shown is normalised by the number of events. If the resolution in the MC correctly reproduces the RD, then the event migration are taken into account in the acceptance correction discussed in the next section. At this level, it is possible to demonstrate that this is not the case through two observations. First, it is necessary to multiply the J/ψ distribution from the MC with a Gaussian function. Second, Fig. 4.18 shows the comparison between J/ψ MC and RD events for $M \in (3 - 3.3)$ normalised by the integral of the respective distributions as a function of Z_{vtx}. The ratio of the MC and RD events for the Al target is not flat suggesting that the J/ψ Z_{vtx} resolution is not perfectly reproduced by the MC compared to the RD. In addition, the ratios between MC and RD events for the Al and W targets differ by as much as 30%. This point can be explained by several things: (i) the beam flux absorption in the Al and W targets could be not correctly reproduce in the MC, (ii) a problem in the acceptance calculation as a function of Z_{vtxt} and (iii) the J/ψ cross

---

[9]This value is obtained by the ratio between the integral between 3 to 3.3 GeV of J/ψ and total contributions in Fig. 4.9.
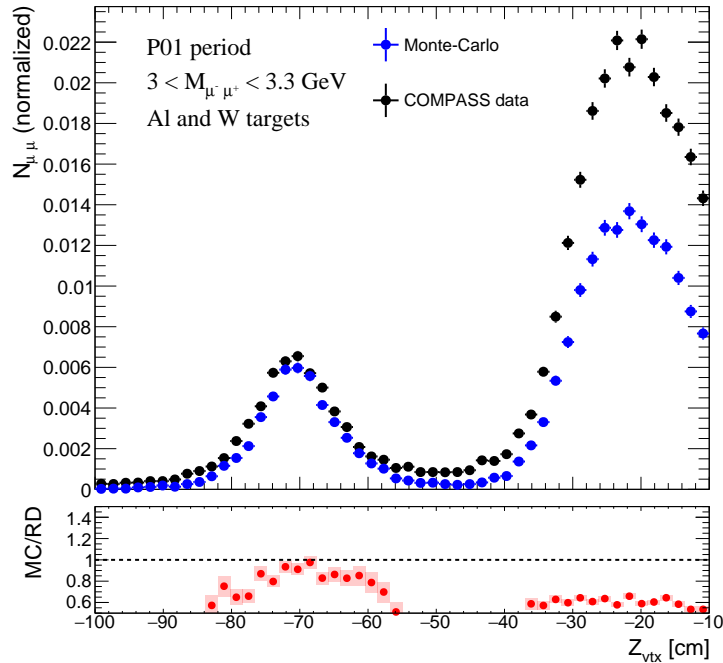
Figure 4.18: Comparison between the J/ψ MC (blue) and the P01 RD (black) for $M \in (3 - 3.3)$ events normalised by the integral of the respective distributions as a function of Z_{vtx}.

section evaluation in π^-Al and π^-W collisions in the PYTHIA generator could be wrong as discussed in Sec. 4.3.1.b. Indeed, the fact that the dominant channel given by PYTHIA in the J/ψ production is gg fusion, the cross section therefore does not depend on the atomic number of the target. In order to verify this, several possible studies be conducted: (i) verifying that the beam flux absorption in the targets is correctly reproduced in the MC and (ii) by changing the J/ψ production model for instance. [10] It is possible to roughly estimate the impact of the disagreement between the RD and the MC distributions as a function of Z_{vtxt} on the event contamination. According to Fig. 4.18, the event contamination from the W in Al target is, in each x_{F} and $p_\perp$ kinematic bins, possibly underestimated by 30%.

4.3.4.d   Events migration as a function of the dimuon mass

The shoulder appearing in the MC J/ψ distribution for $M \lesssim 2$ GeV in the Al target can be explained by the fact that at low masses the Z_{vtx} resolution deteriorates and the migration from the W to Al target increases. Figure 4.19 shows the impact of the migration on the J/ψ distribution for $M \lesssim 2$ GeV. Without the migration events from the W in the Al target, the J/ψ distribution is close to a Crystal Ball function, like in the NH$_3$ targets. These migration effects are not in themselves a concern if and only if the MC can correctly reproduce them. However, it has

---

[10]It possible to use the CEM model. Figure 2.3 shows a calculation using the CEM model at LO with two different pion PDF. The initial partonic state in the J/ψ production in π^-A collisions depends strongly both on the model and also on the pion PDF.
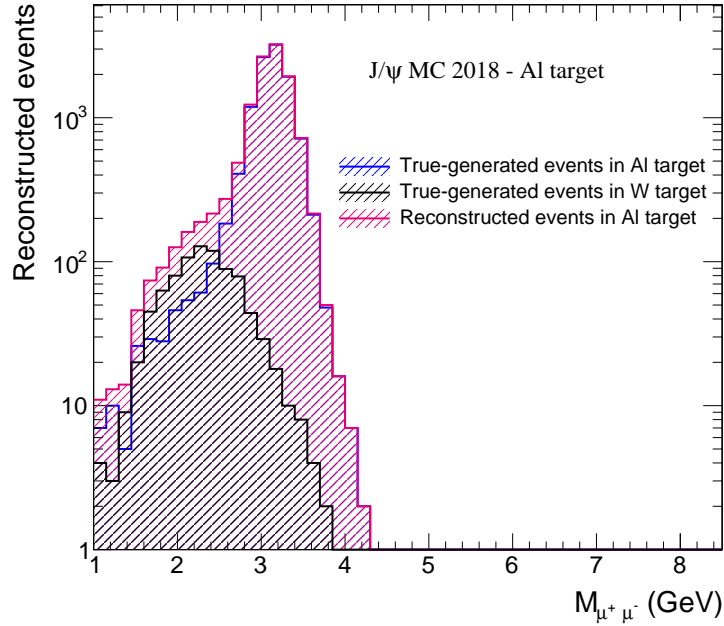
Figure 4.19: *Reconstructed events as a function of dimuon mass from the J/ψ MC. In red, the reconstructed events from the true-generated events in the Al target, in blue, the reconstructed events from the true-generated events in the W target and in black the reconstructed events from the true-generated events in $Z_{\text{vtx}} < -150cm$ region.*

been shown that both as a function of the invariant mass but also as a function of Z_{vtx} that this was not the case. The migrations are therefore included in the acceptance, but not completely. Accordingly, the number of J/ψ events extracted for the Al target is probably underestimated.

4.4 J/ψ cross section extraction method

In order to access the physical observable, the number of J/ψ events as a function of x_{F} and $p_\perp$ distributions need to be corrected by the acceptance of the spectrometer, noted ϵ, including

- the geometrical acceptance of the spectrometer. It is defined as the ratio between *true-generated events* and *generated events* in a specific bin, i.e. without resolution effect due to the reconstruction:

$$\varepsilon^{\text{geometrical}} = \frac{N_{\text{MC}}^{\text{true}-\text{generated}}}{N_{\text{MC}}^{\text{generated}}} \tag{4.12}$$

where $N_{\text{MC}}^{\text{true}-\text{generated}}$ is the number of *true-generated events* (i.e. entering in the acceptance of the spectrometer) and $N_{\text{MC}}^{\text{generated}}$ is the number of all generated events. This acceptance reduces to a purely angular acceptance of the produced muons;

- the trigger efficiency $\epsilon^{\text{trigger}}$. It is composed of two parts: the hodoscope efficiency and the coincidence matrix efficiency. The latter corresponds to the efficiency of the coincidence

system when two hodoscope slabs are in coincidence during the passage of a muon.[11] The $\epsilon^{\text{trigger}}$ factor is implemented in the MC and is directly related to the hardware efficiency of the hodoscope slabs as described in Sec. 3.5;

- reconstruction effects $\epsilon^{\text{reconstruction}}$. This factor encodes both the reconstruction efficiency of muon tracks and the resolution effects at the vertex position;

- the detectors efficiency $\epsilon^{\text{detectors}}$. This efficiency takes into account the fact that the detectors which enable to reconstruct the muon tracks do not have an efficiency of 100% as discussed in the section 3.7 where the example of the Drift Chamber is mentioned. The 2D efficiency of each detector plane from RD is included in the simulation as illustrated in Fig. 3.16. In the present analysis, only 1D efficiencies were used. In the future, in order to improve the description of the spectrometer in the MC, a 2D detectors efficiency map description will be necessary.

Finally, the ϵ corrective factor is determined by using a J/ψ MC simulation of the COMPASS spectrometer as discussed In Sec. 4.3.1. In the present J/ψ analysis, the 2D acceptance as a function of x_{F} and $p_{\perp}$ is

$$\varepsilon_{x_{\text{F}},p_{\perp}} = \frac{N(x_{\text{F}},p_{\perp})^{\text{rec}}_{\text{MC}}}{N(x_{\text{F}},p_{\perp})^{\text{gen}}_{\text{MC}}} \tag{4.13}$$

where $N(x_{\text{F}},p_{\perp})^{\text{rec}}_{\text{MC}}$ is the number of *reconstructed events* by the spectrometer in $(x_{\text{F}},p_{\perp})$ kinematic bin and $N(x_{\text{F}},p_{\perp})^{\text{rec}}_{\text{gen}}$ is the number of *all generated events* in the same $(x_{\text{F}},p_{\perp})$ kinematic bin. *All generated events* include only the Z_{vtx} and dimuon mass selection criteria. The *reconstructed events* from MC undergo exactly the same analysis as the RD. These data are reconstructed using the CORAL software under the same conditions as the RD and analysed by PHAST software applying the same kinematic cuts (see Table 4.1). In this way, the ratio between reconstructed and generated events represents the fraction of event accepted by the spectrometer, in other words the kinematic phase space defined by the spectrometer. The condition for determining a realistic acceptance is to generate a sufficiently large phase space (larger than that of the RD) in order not to have a finite acceptance value for a given kinematic bin. Figure 4.20 shows an illustration of the phase spaces generated in the MC and derived from the RD as a function of the x_{F} and $p_{\perp}$ variables. This illustration can be generalised to n variables. Ideally, for the acceptance to be completely independent of the event generator and therefore of the generated phase space, it would be necessary to generate a flat MC in order to uniformly populate all the regions of the kinematic phase space. Such a method would require a huge simulation time. Instead, a physics event generator was used. This approach presents the risk of not correctly describing the correlations between the kinematic variables. The phase space

---

[11]For instance, in LAS single muon trigger case for instance, it refers to coincidence between HG01Y1 and HG02Y1 or HG01Y1 and HG02Y2 slabs.
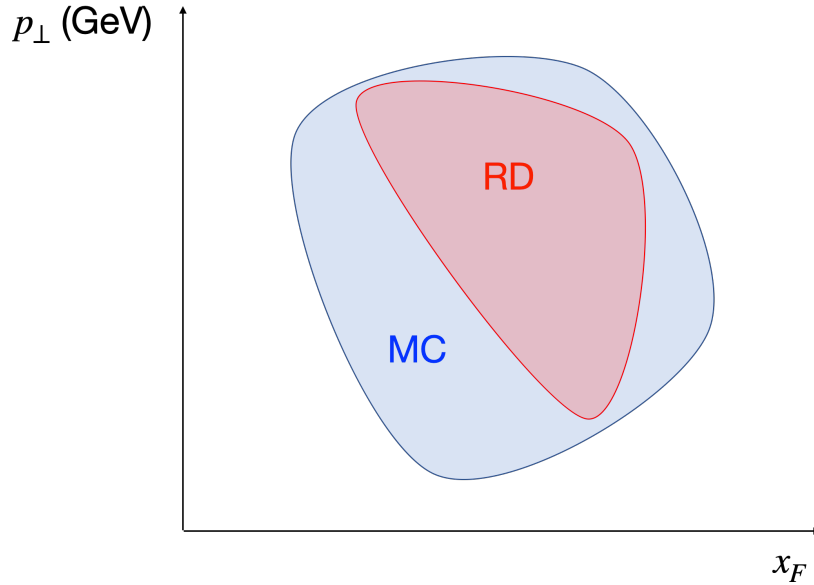
Figure 4.20: Illustration of MC and RD phase space as a function of $p_\perp$ and x_{F}.

covered by the main J/ψ kinematic variables of *reconstructed events* from the MC used in the present analysis is shown in Fig. 4.21. A strong dependence between x_{F} (or x_1, x_2) and $p_\perp$ in *reconstructed events* J/ψ MC is observed. This variable is therefore very little dependent on the physics event generator. These observations enable to conclude (1) on the weak dependence of the physics generator with regard to the J/ψ extraction via a fit of the invariant mass spectrum and (2) on the fact that x_{F} and $p_\perp$ are two natural variables for the acceptance correction calculation.

4.4.1   2D acceptance as a function of $p_\perp$ and $x_{\mathbf{F}}$

A 2D extraction of J/ψ events in the W and the Al targets has been performed. These events must now be corrected by the corresponding 2D acceptance in order to extract a physical observable.

4.4.1.a   W target

The acceptance ϵ is computed by using the MC J/ψ simulation used for the dimuon mass fit. Because the fit is performed in (2-8.5) GeV dimuon mass range, in addition to the cuts summurized in Table 4.1, the same mass cut is included in the MC *reconstructed events*. This is in order to correspond to the J/ψ extraction dimuon invariant mass phase space. Figure 4.22 shows the acceptance calculation according to (5.3) as a function of x_{F} and $p_\perp$. For $p_\perp \lesssim 2$ GeV, the acceptance is nearly flat for all x_{F} bins. For $p_\perp \gtrsim 2$ GeV, it smoothly increases, at least for x_{F} values below 0.5. In the last three bins in x_{F}, the acceptance of the spectrometer goes to zero at large $p_\perp \gtrsim 2$ GeV. This observation explains the behavior already noticed in Fig. 4.11.
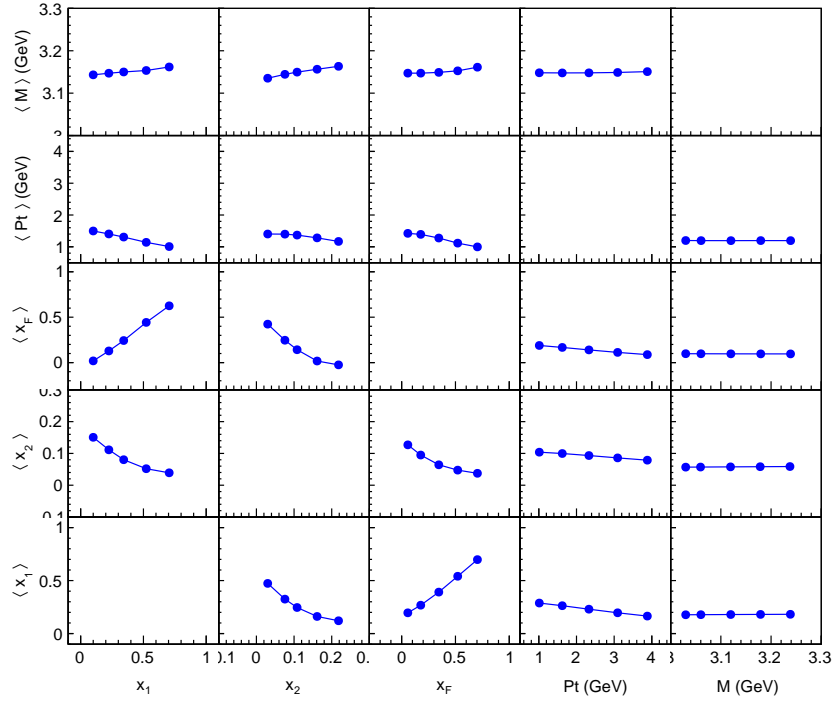
Figure 4.21: Correlation of *reconstructed events* from prompt-J/ψ MC for the W target.
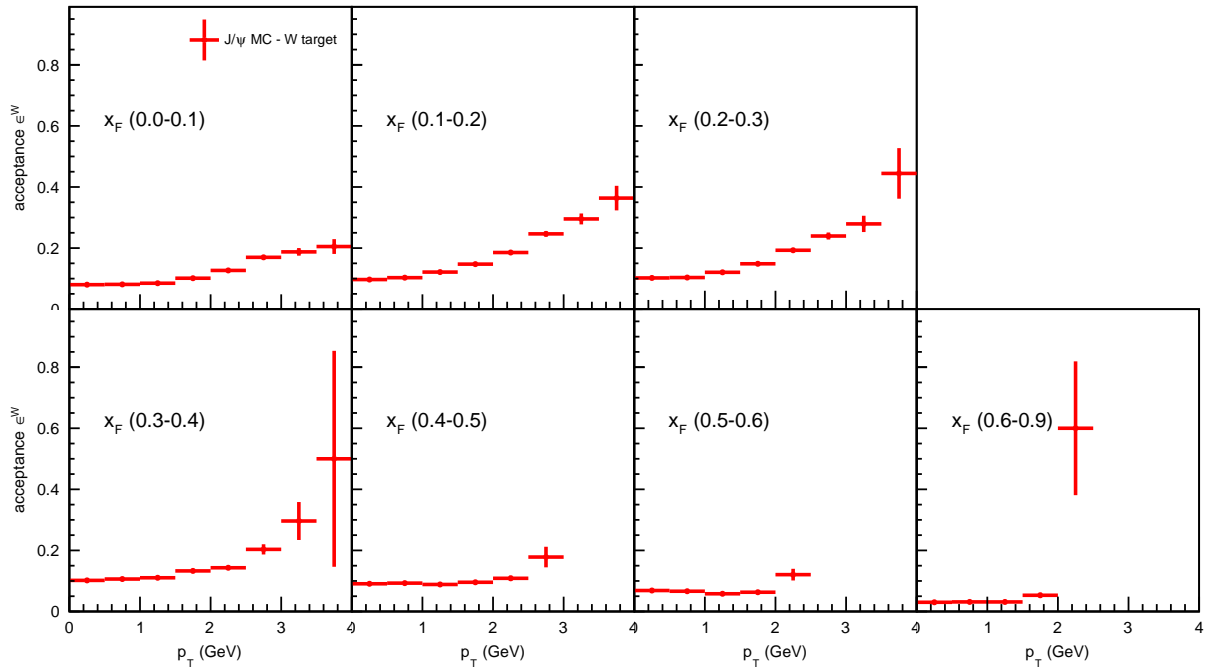
Figure 4.22: Acceptance for the W target as a function of x_F and $p_\perp$.
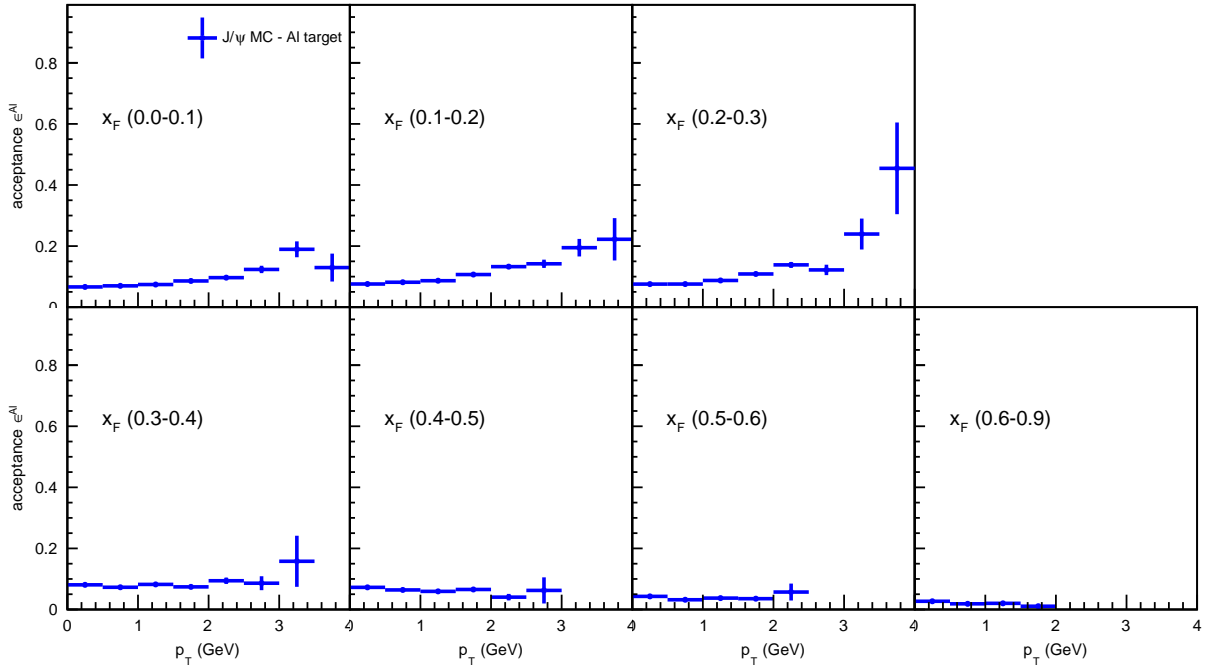
Figure 4.23: Acceptance for the Al target as a function of x_F and $p_\perp$ calculated with J/ψ MC simulation.

4.4.1.b Al target

Just like for the W target, the acceptance at small $p_\perp \lesssim 3$ GeV for all x_F bins is nearly flat as illustrated in Fig. 4.23. In general, the acceptance for the Al target is lower compared to the W target. Fig. 4.24 shows the ratio between ϵ^W and ϵ^{Al}. The ratio is fitted with a p_0 constant parameter. The p_0 factor increases as a function of x_F bins, except for the last bin $x_F \in (0.6\text{-}0.9)$ but at the same time the statistical uncertainties increase. The x_F where the variation of the normalization is the strongest compared to the others x_F bins are for $x_F \in (0.0\text{-}0.1)$ and $x_F \in (0.5\text{-}0.6)$.

Migration and acceptance correction As discussed, the acceptance correction is determined via Eq. (5.3) of which the numerator contains the information of the reconstructed events. When calculating cross sections, i.e. when the events are corrected for acceptance, the migration effects included in the acceptance calculation should cancel out with those in the data. This is true if and only if the effects of the spectrometer are correctly simulated. However, several elements tend to show that the resolution is underestimated in the MC. Therefore, the migration of the J/ψ events from the W target to the Al target is probably underestimated and the acceptance correction of the RD did not enable this effect to be fully taken into account.
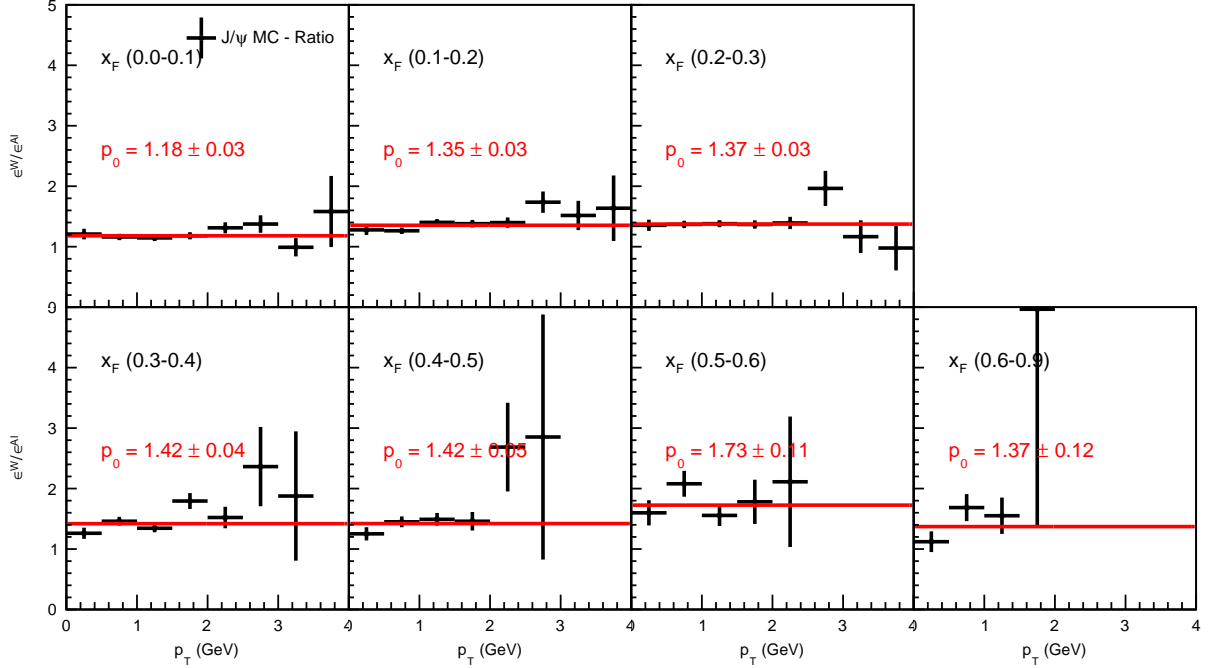
Figure 4.24: In black, ratio of ϵ acceptance in the W and Al targets as a function of x_F and $p_\perp$. In red, zero degree polynomial fit function with p_0 parameter.

4.4.2 J/ψ cross section as a function of $p_\perp$ and x_F

After the 2D acceptance correction as a function of $p_\perp$ and x_F as well as the correction of the luminosity except the initial absolute flux Φ_0, it is now possible to extract the following quantity

$$\frac{\mathrm{d}\sigma^{\pi^- A}}{\mathrm{d}x_F \mathrm{d}p_\perp}(J/\psi) \times \Phi_0 = \frac{N_{\mathrm{events}}^{J/\psi}(x_F, p_\perp)}{\epsilon^A \times \mathcal{L}} \times \Phi_0. \tag{4.14}$$

The observable discussed here corresponds to an absolute cross section multiplied by the initial absolute cross section multiplied by the initial absolute flux Φ_0. Because in the absolute cross sections ratio, Φ_0 is cancelled out, it is not necessary to take it into account. Figure 4.25 shows the number of J/ψ corrected by the acceptance and the luminosity information and multiplied by the initial absolute flux Φ_0[12] according to Eq. (4.14) for the W target and the period P01. The mean values of x_F and $p_\perp$ absolute cross sections are $\langle x_F \rangle = 0.20$ and $\langle p_\perp \rangle = 1.09$ GeV respectively. Figure 4.26 shows the J/ψ absolute cross section multiplied by the initial absolute flux Φ_0 for the Al target and the period P01. The mean value of x_F absolute cross section is $\langle x_F \rangle = 0.23$ and $p_\perp$ distribution is $\langle p_\perp \rangle = 1.01$ GeV for the Al target. The comparison between the absolute cross section as a function of x_F in W and Al targets shows a steeper slope in the W target. By using a parametric function in form $\propto (1 - x_F)^\alpha$, it possible to quantify the difference in the slope between the two targets. The fit results give $\alpha^W = 2.747 \pm 0.054$ and $\alpha^{Al} = 1.994 \pm 0.102$. The x_F distribution in the W target is more suppressed by $\sim 30\%$ compared to Al target.

---

[12]The normalization by the initial absolute flux Φ_0 is simply a notation in order to use the cross section notation in labelling of the legend.
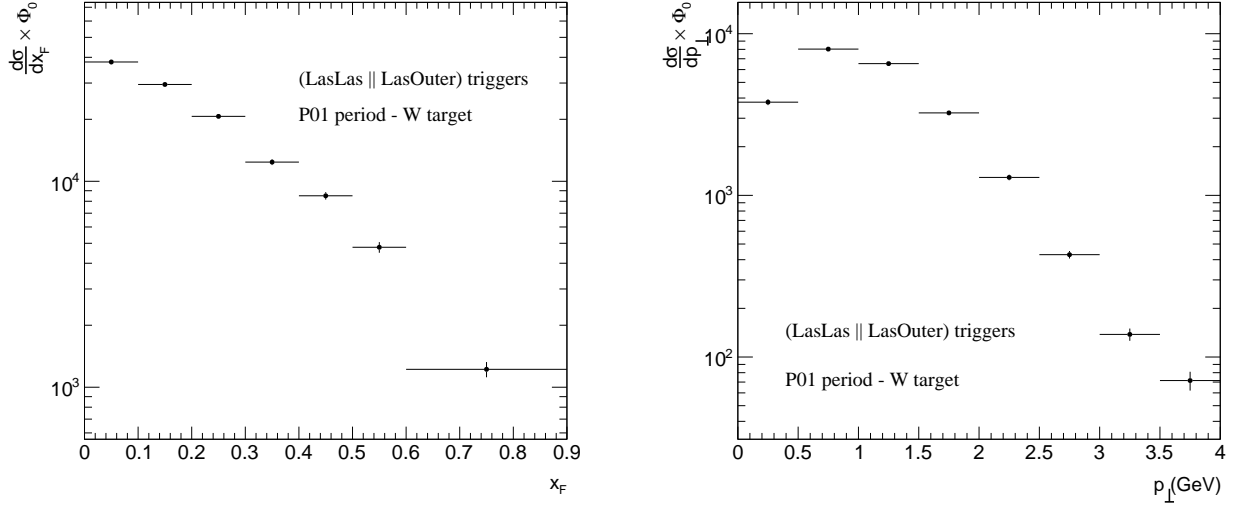
Figure 4.25: Absolute cross section as a function of x_F (left panel) and $p_\perp$ (right panel) multiplied by the initial absolute flux Φ_0 for the W target in the period P01.
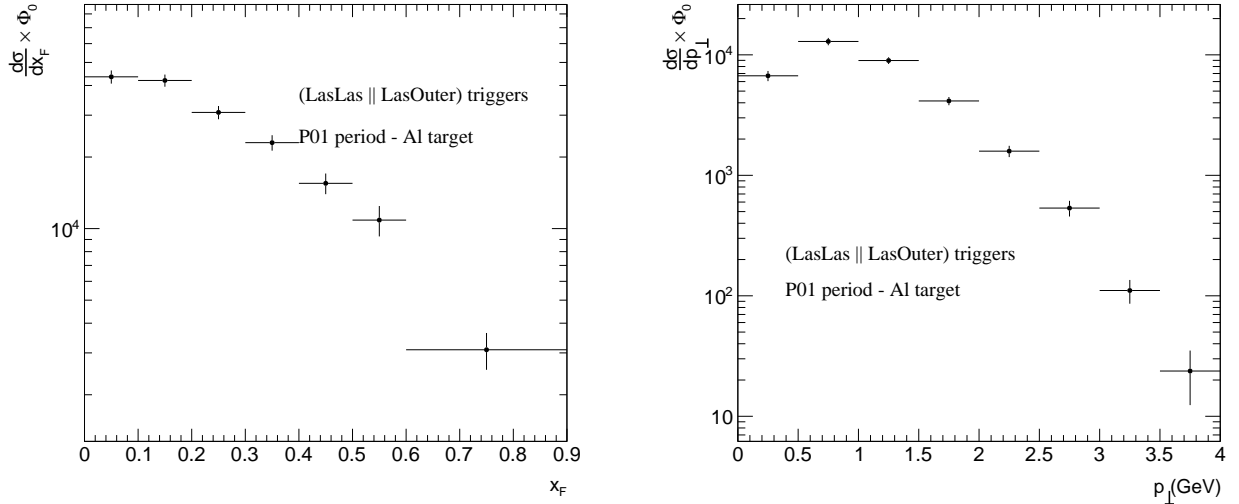
Figure 4.26: Absolute cross section as a function of x_F (left panel) and $p_\perp$ (right panel) multiplied by the initial absolute flux Φ_0 for the Al target in the period P01.

4.4.3 Ratio of cross sections for J/ψ production for the W and Al targets

From Figs. 4.25 and 4.26, it possible to calculate the J/ψ production ratio in πW, normalised to πAl collisions for the period P01. This, in order to extract the nuclear effects as a function of x_F and $p_\perp$. Figure 4.27 (left panel) shows the J/ψ nuclear dependence as a function of x_F. A strong suppression of the cross section is observed in the W target compared to the Al target. In the last x_F bin, the ratio is $\mathrm{R}_{\pi\mathrm{A}}^{J/\psi}(\mathrm{W/Al}) = 0.39 \pm 0.08$. Tables 4.16 and 4.17 shown the ratio values for the period P01 as a function of x_F and $p_\perp$ respectively.
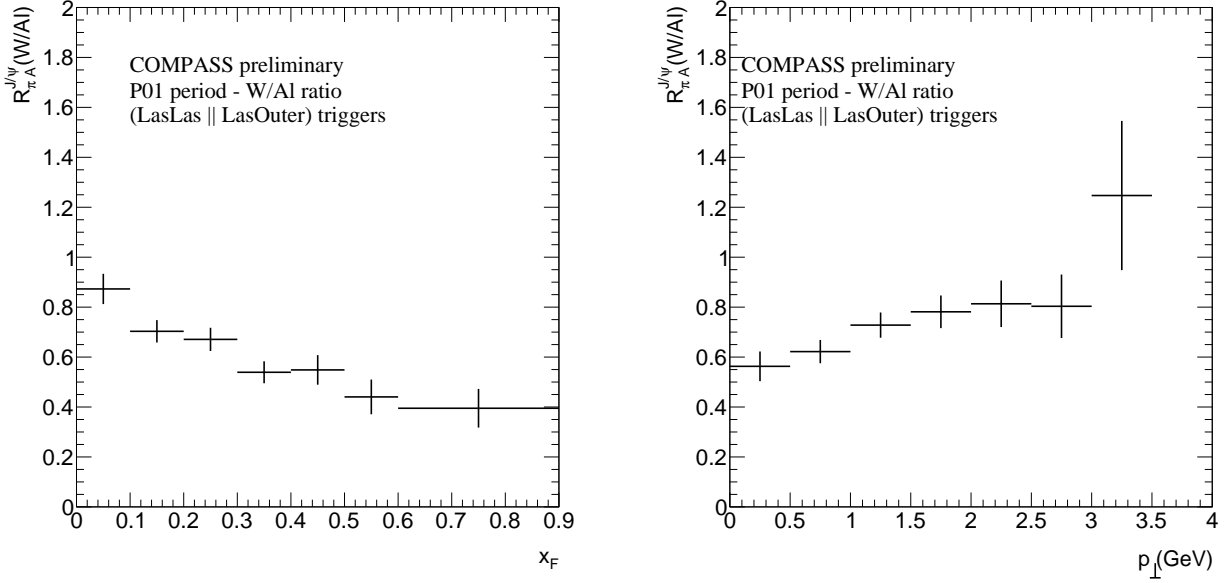
Figure 4.27: J/ψ nuclear production ratio measured in πW normalised to πAl collisions as a function of x_F (left panel) and $p_\perp$ (right panel) for the period P01. The error bars include statistical uncertainties only.

x_F	$R_{\pi A}^{J/\psi}(\mathrm{W/Al})$
0-0.1	0.87 ± 0.06
0.1-0.2	0.70 ± 0.04
0.2-0.3	0.67 ± 0.05
0.3-0.4	0.54 ± 0.04
0.4-0.5	0.55 ± 0.06
0.5-0.6	0.44 ± 0.07
0.6-0.9	0.39 ± 0.08

Table 4.16: J/ψ nuclear production ratio measured in πW normalised to πAl collisions as a function of x_F for the period P01. The error bars include statistical uncertainties only.

$p_\perp$ (GeV)	$R_{\pi A}^{J/\psi}(\mathrm{W/Al})$
0-0.5	0.56 ± 0.06
0.5-1	0.62 ± 0.05
1-1.5	0.72 ± 0.05
1.5-2	0.78 ± 0.06
2-2.5	0.81 ± 0.09
2.5-3	0.80 ± 0.12
3-3.5	1.25 ± 0.30
3.5-4	3.01 ± 1.50

Table 4.17: J/ψ nuclear production ratio measured in πW normalised to πAl collisions as a function of $p_\perp$, normalised to Al, for the period P01. The error bars include statistical uncertainties only.

4.4.4 Nuclear transverse momentum broadening

In order to determine the nuclear transverse momentum broadening, $\langle p_\perp^2 \rangle$ defined in Eq. (7.6) is calculated with different methods (see sections 4.4.4 and 7.2.2 for more details). The *Kaplan method* is used by fitting the absolute cross section as a function of $p_\perp$ with the Kaplan function. The advantage of this method is that it is free itself from experimental acceptance by integrating the parameterization of the absolute cross section as a function of $p_\perp$ between 0 and infinity. The second method, *bin method*, consists in summing the experimental absolute cross section
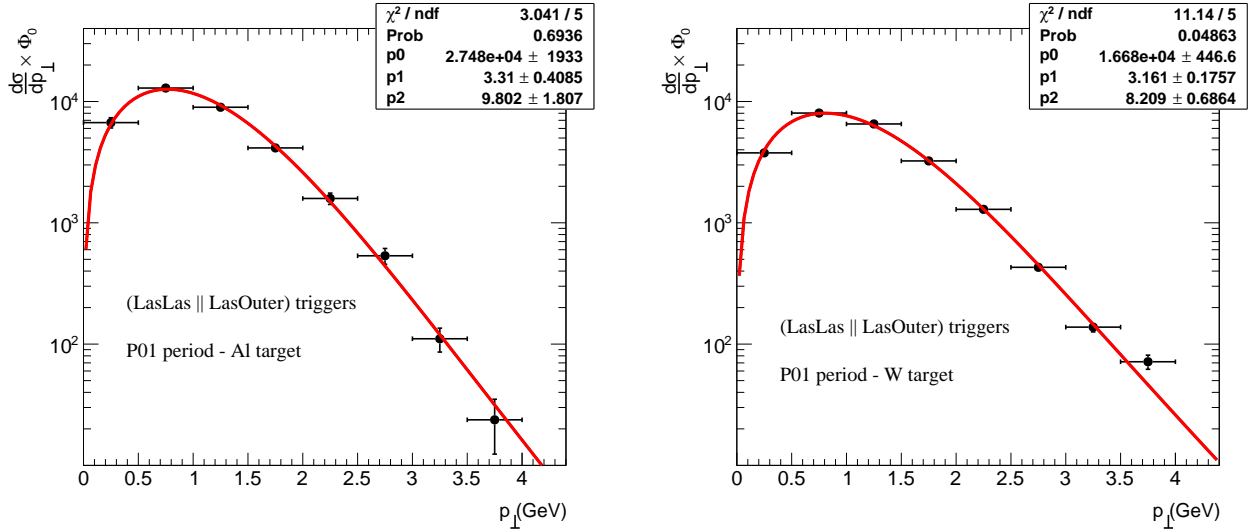
Figure 4.28: Kaplan fit of the absolute cross section as a function of $p_\perp$ (GeV) multiplied by the initial absolute flux Φ_0 for the Al (left panel) and the W (right panel) target in the P01. The error bars include statistical uncertainties only. The p_0, p_1 and p_2 are respectively the parameters to the fit results corresponding to $\mathcal{N}$, p_0 and m in Eq. (7.8).

as a function of $p_\perp$ from the first to the last experimental bin. The $p_\perp$ value appearing in the integral calculation can be determined in two cases: by using the $p_\perp$ value corresponding to the median of the experimental bin or the $p_\perp$ value corresponds to the $p_\perp$ mean value in the corresponding bin determined by the integral of the Kaplan cross section parameterization in this bin. The second case makes it possible to overcome the width of the experimental bin by taking into account the behaviour of the absolute cross section in this same bin. Figure 4.28 shows the Kaplan fit of the absolute cross section multiplied by the initial absolute flux Φ_0 as a function of $p_\perp$ for the Al (left panel) and W (right panel) targets for the period P01. The transverse momentum broadening values calculated are summarized in Table 4.18. The transverse momentum broadening value $\Delta p_\perp^2$ for the three methods are compatible. Furthermore, the $\langle p_\perp^2 \rangle$ calculated with the *bin method* using a mean $p_\perp$ value is systematically below the values obtained by the *bin method* using a median $p_\perp$ value (3% difference) and by the *Kaplan method* (5% difference). In the following, only the *Kaplan method* will be used. The $\Delta p_\perp^2$ value obtained from the W and Al targets for period P01 for J/ψ process is equal to 0.21 ± 0.04 GeV^2.

Method	$\langle p_\perp^2 \rangle_{\mathrm{W}}$ (GeV^2)	$\langle p_\perp^2 \rangle_{\mathrm{Al}}$ (GeV^2)	$\Delta p_\perp^2$ (GeV^2)
Kaplan	1.61 ± 0.02	1.40 ± 0.04	0.21 ± 0.04
Bin (median)	1.58 ± 0.02	1.37 ± 0.04	0.21 ± 0.04
Bin (mean)	1.54 ± 0.02	1.33 ± 0.04	0.21 ± 0.04

Table 4.18: Determination of $\Delta p_\perp^2$ with different methods in the W and Al targets for the period P01.

4.5 Systematic uncertainties estimation

In this section, the systematic errors associated with the different steps of the extraction of the J/ψ absolute cross sections will be quantified. The four most important sources of systemic error in this analysis come from (1) the method of extracting the number of J/ψ events, (ii) the acceptance calculation (iii) the Z_{vtx} dependence of the cross section and (iv) the period-by-period compatibility. The systematic error for an observable x is defined as

$$\sigma_x = \sqrt{\frac{1}{n} \sum_{i=1}^{n} (x_i - \bar{x})^2} \tag{4.15}$$

where n is the number of results obtained for an observable, x_i the observable value x determined for period i and $\bar{x}$, its mean value.

4.5.1 Signal extraction

It possible to quantify the impact of the mass range fit on the J/ψ extraction. Indeed, in the present analysis, the chosen mass interval is between 2 and 8.5 GeV. This interval is determined in order to avoid including an artificial systematic error from the poorly reproduced $M < 2$ GeV region. In order to explore the impact of this ignorance, it is possible to relax the fit parameter of the CB contribution and widen the mass interval of the fit between 1.5 and 8.5 GeV. Figure 4.29 shows the fit result for the Al (left panel) and the W (right panel) targets by leaving the CB contribution free for the period P01. In this configuration, the dominant contribution for $M \lesssim 2$ is the CB while the OC contribution is normalised with a negative coefficient from the fit, not visible in the figure. In the case of the Al target, the CB alone can reproduce the region $M \lesssim 2$ GeV. Fluctuations around the J/ψ mass show that this region is difficult to simulate, possibly due to the contamination rate of events from the W target in this region. In addition, the χ^2/ndf degrades by almost 50%. The mass interval changes results in a 4% increase of the total number of J/ψ (see Table 4.19). In this context, it is possible that the increase in χ^2/ndf leads to an error in extracting the number of J/ψ. The same observations are made in the case of the W target. In this case, the agreement over the entire dimuon mass range improves considerably, particularly for $M \lesssim 2$ where the ratio between the MC and RD is close to 1 (see Fig. 4.29). The χ^2/ndf obtained improves by almost 25%. The mass interval change results in a 5% increase in the total number of J/ψ (see Table 4.20). Only the χ^2/ndf from the invariant mass spectrum fit in the W
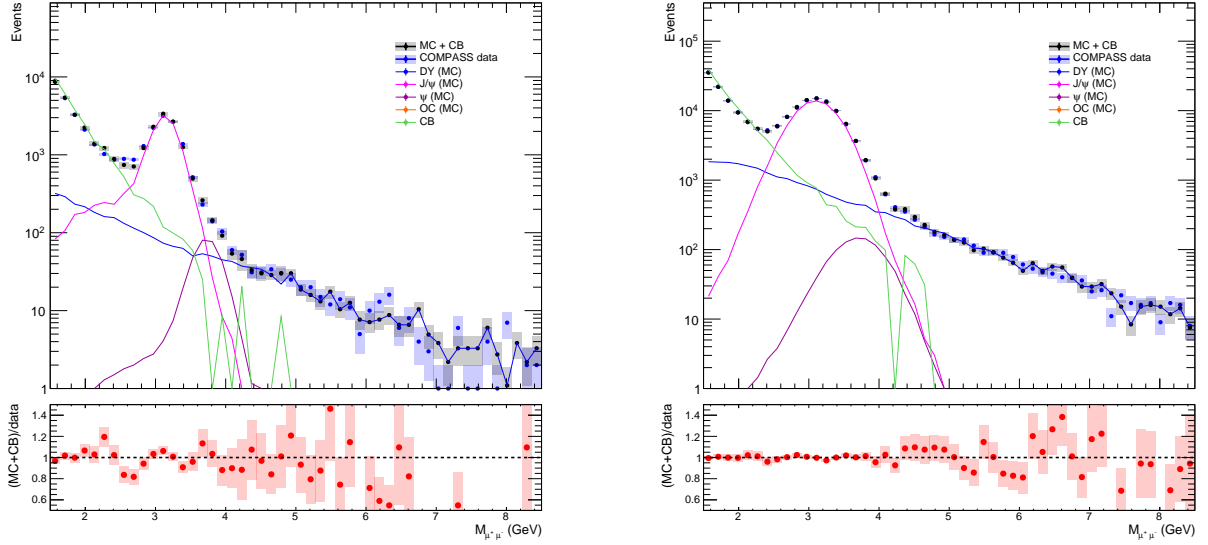
Figure 4.29: Dimuon invariant mass fit between 1.5 et 8.5 GeV for the Al (left panel) and the W (right panel) targets using the "cocktail" method by leaving free CB normalisation.

Mass range (GeV)	Number of J/ψ events	χ^2/ndf
2-8.5	11925 $\pm(109)_{\text{stat}}$	2.9
1.5-8.5	12416 $\pm(111)_{\text{stat}}$	5.2

Table 4.19: J/ψ extraction with "cocktail" method in different mass range for the Al target in the period P01.

target is improved, impacting the total number of J/ψ events by 5%. In view of the degradation of χ^2/ndf from the invariant mass spectrum fit in the Al target, it is difficult to consider that the error in the J/ψ number extraction for the Al target is 5% as well. Fig. 4.30 shows the impact of the mass interval fit in the $R_{\pi A}^{J/\psi}$(W/Al) as a function of x_F (left panel) and $p_\perp$ (right panel).

Mass range (GeV)	Number of J/ψ events	χ^2/ndf
2-8.5	77333 $\pm(278)_{\text{stat}}$	3.2
1.5-8.5	81350 $\pm(285)_{\text{stat}}$	2.4

Table 4.20: J/ψ extraction with "cocktail" method in different mass range for the W target in the period P01.

The average systematic error of the mass interval fit in the calculation of $R_{\pi A}^{J/\psi}$(W/Al) is about 4%. This estimate is an integrated average over the whole range in x_F (left panel) and $p_\perp$. It constitutes an upper limit. In particular because the enlargement of the cut in dimuon mass interval for the Al target generates a degraded χ^2/ndf artificially increasing the systematic error on the J/ψ extraction.
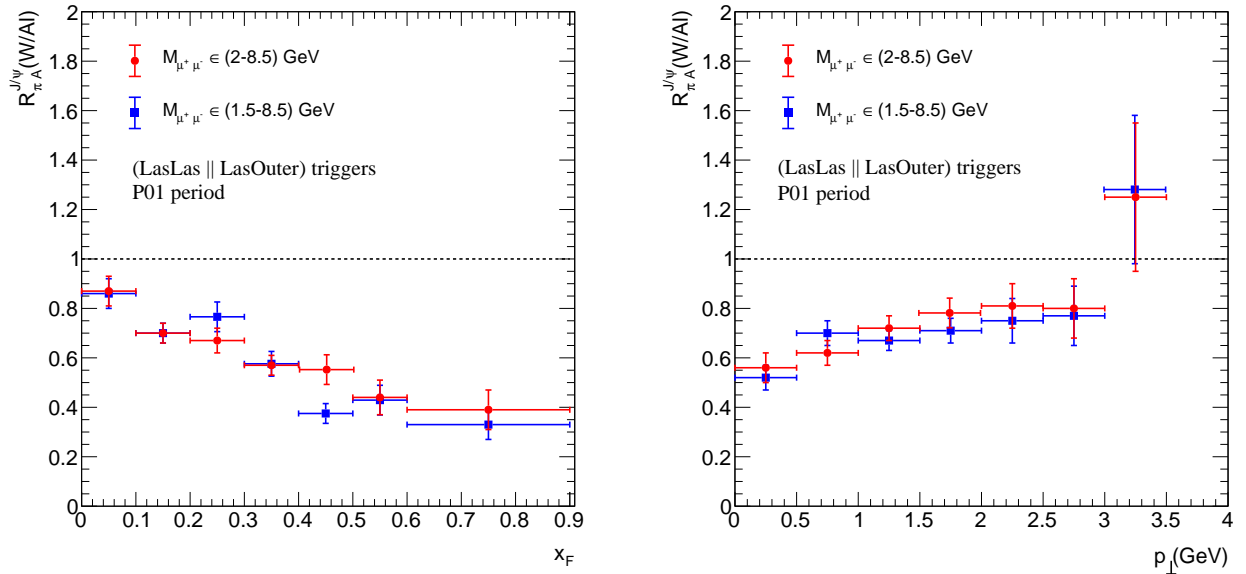
Figure 4.30: Impact of the mass range fit on the $\mathrm{R}_{\pi\mathrm{A}}^{J/\psi}(\mathrm{W/Al})$ ratio as a function of x_{F} (left panel) and $p_\perp$ (right panel). In blue, J/ψ extracted by fitting the dimuon invariant mass between 1.5 and 8.5 GeV and in red, J/ψ extracted by fitting the dimuon invariant mass between 2 and 8.5 GeV.

4.5.2 Impact of the Z_{vtx} position in the W target

In order to check the consistency of the calculation of the $\mathrm{R}_{\pi\mathrm{A}}^{J/\psi}(\mathrm{W/Al})$ ratio as a function of x_{F} and $p_\perp$, it is possible to check the impact of the cut in Z_{vtx} in particular for the W target. Indeed, this target measures 120 cm. By comparing the $R_{\pi^-\mathrm{A}}$ value obtained for different slices, an estimate of the systematic error due both to the attenuation of the beam in the target and the acceptance dependence as a function of Z_{vtx} can be quantify.

Figure 4.31 shows the impact on the $\mathrm{R}_{\pi\mathrm{A}}^{J/\psi}(\mathrm{W/Al})$ ratio as a function of x_{F} (left panel) and $p_\perp$ (right panel) calculated for the first 5 cm and for the second 5 cm of W target. The results obtained are compatible with the central value calculated for the first 10 cm of the W target. The systematic error associated with the variation of the cut in Z_{vtx} for the W is small compared to the statistical error and is equal to 2%.

4.5.3 Acceptance systematic error

To estimate the systematic due to the acceptance calculation, it possible to use different pion PDF in the J/ψ MC simulation. Fig. 4.32 shows the impact on the pion PDF choice on the $\mathrm{R}_{\pi\mathrm{A}}^{J/\psi}(\mathrm{W/Al})$ ratio as a function of x_{F} (left panel) and $p_\perp$ by using an acceptance calculation using GRVP1 (NLO) (central value in the present analysis) and GRVP0 (LO) pion PDF [34]. The choice to modify the order of the PDF comes from the fact that the J/ψ process is dominated by the gg channel in PYTHIA (see section 4.3.1). Therefore, the J/ψ process simulated in COMPASS kinematics will be directly sensitive to the gluon PDF of the pion beam.
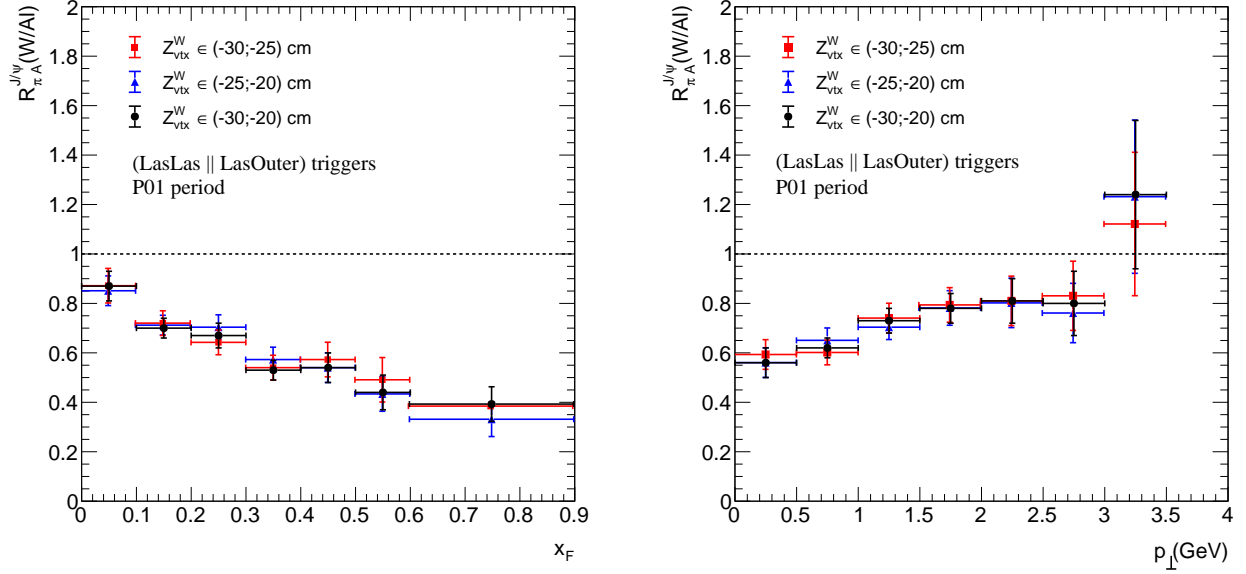
Figure 4.31: Impact of the Z_{vtx} cut in the W target on the $R_{\pi A}^{J/\psi}(W/Al)$ ratio as a function of x_F and $p_\perp$. In blue, J/ψ extracted by fitting the dimuon invariant mass in second 5 cm in the W target. In red, J/ψ extracted by fitting the dimuon invariant in first 5 cm in the W target and in black, the first 10 cm.
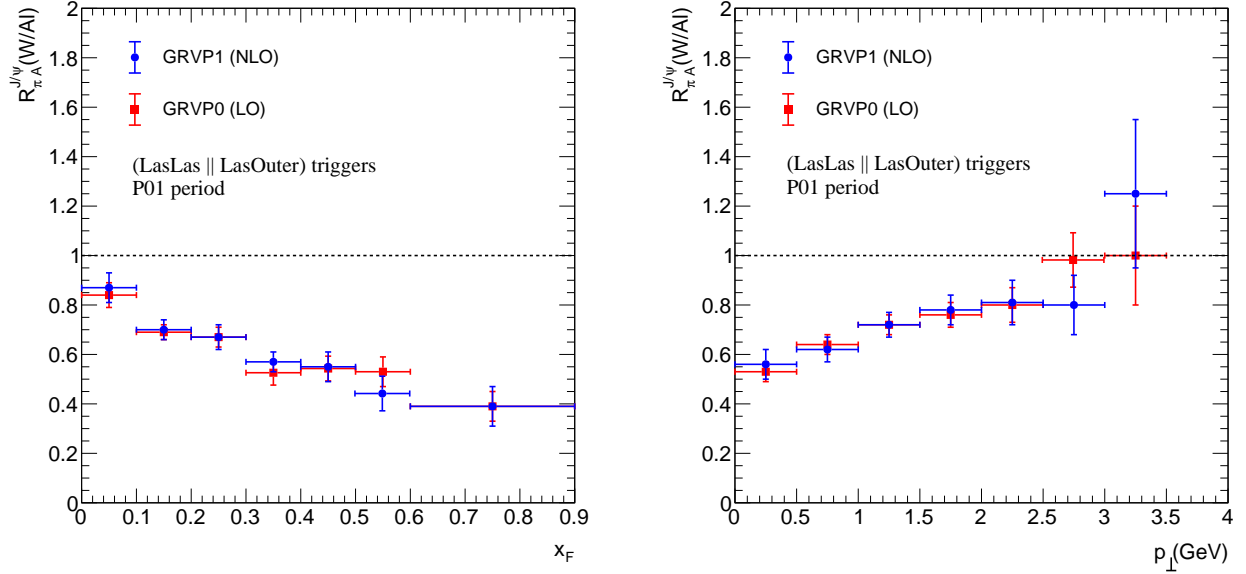
Figure 4.32: Impact of the pion PDF used in J/ψ MC simulation on the $R_{\pi A}^{J/\psi}(W/Al)$ ratio as a function of x_F (left panel) and $p_\perp$ (right panel). In blue, $R_{\pi A}^{J/\psi}(W/Al)$ ratio using an acceptance calculation using GRVP1 (NLO) and in red, using an acceptance calculation using GRVP0 (LO) [34].

The comparison gives an mean systematic error for both $R_{\pi A}^{J/\psi}(W/Al)$ ratio as a function of x_F and $p_\perp$ equal to 2%. No impact on the acceptance calculation was found using different free proton PDFs at NLO (CT14 [28] and NNPDF [29]). Indeed, at large x_2, in the COMPASS kinematics, these PDFs are well known. In summary, all information about the estimation of systematic errors in $R_{\pi A}^{J/\psi}(W/Al)$ ratio are summarized in Table 4.21.

Systematic error	Number of J/ψ events
Signal extraction	4%
Acceptance	2%
Z_{vtx} dependence	2%
Luminosity	$< 1\%$

Table 4.21: Summary of systematic error estimation in $\mathrm{R}_{\pi\mathrm{A}}^{J/\psi}(\mathrm{W/Al})$ ratio as a function of x_{F} and $p_{\perp}$.

4.5.4 Period compatibility

So far only the results for the period P01 have been shown. It is necessary to ensure that each period gives results compatible both for the A-dependence as a function of x_{F} and $p_{\perp}$ but also for the value of the nuclear transverse momentum broadening value. $\mathrm{R}_{\pi\mathrm{A}}^{J/\psi}(\mathrm{W/Al})$ ratios as a function of x_{F} (left panel) and $p_{\perp}$ (right panel) for each period (P00 to P08) are shown in Fig. 4.33 and 4.34. The ratio between the results for each period and for the reference period P01 is also shown at the bottom of the figures. The agreement between each period is satisfactory. No deviation of more than 20% is observed except at the edge of the phase space, in the last bin in x_{F} and $p_{\perp}$.
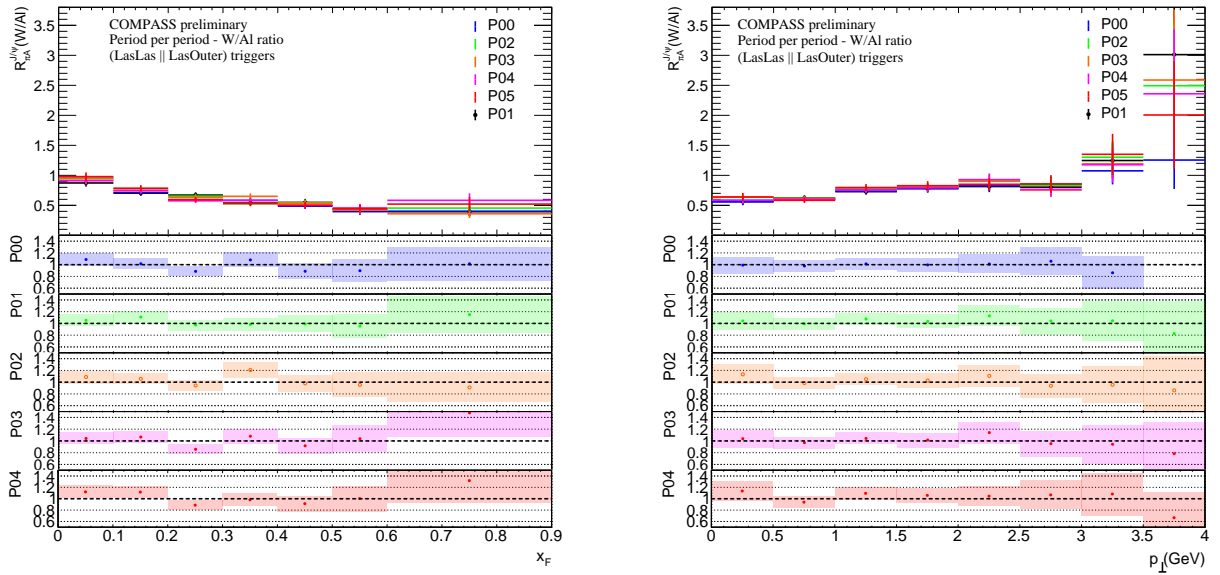
Figure 4.33: $\mathrm{R}_{\pi\mathrm{A}}^{J/\psi}(\mathrm{W/Al})$ as a function of x_{F} (left panel) ans $p_{\perp}$ (right panel) from the different periods (P00, P01, P02, P03 and P04) and the statistical uncertainties associated (top). The ratio between $\mathrm{R}_{\pi\mathrm{A}}^{J/\psi}(\mathrm{W/Al})$ as a function of x_{F} (left panel) ans $p_{\perp}$ (right panel) from different periods (P00, P01, P02, P03 and P04) normalized by the period P01.

In Table 4.22, the $\langle p_{\perp}^2 \rangle_{\mathrm{W}}$, $\langle p_{\perp}^2 \rangle_{\mathrm{Al}}$ and $\Delta p_{\perp}^2$ values are shown for all periods. They are compatible period per period. The standard deviation of the $\langle p_{\perp}^2 \rangle_{\mathrm{W}}$, $\langle p_{\perp}^2 \rangle_{\mathrm{Al}}$ and $\Delta p_{\perp}^2$ obtained are equal to 0.01 GeV, 0.01 GeV and 0.01 GeV^2 respectively. These error values are small and can be neglected, compared to the other uncertainties.
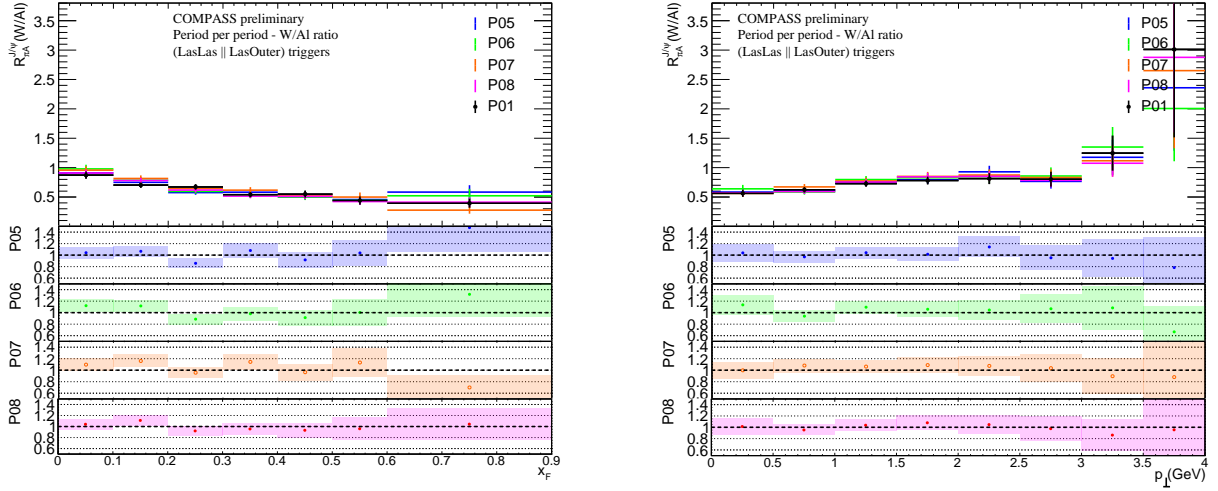
Figure 4.34: $R_{\pi A}^{J/\psi}(\text{W/Al})$ as a function of x_F (left panel) ans $p_\perp$ (right panel) from the different periods (P05, P06, P07 and P08) and the statistical uncertainties associated (top). The ratio between $R_{\pi A}^{J/\psi}(\text{W/Al})$ as a function of x_F (left panel) ans $p_\perp$ (right panel) from different periods (P05, P06, P07 and P08) normalized by the period P01.

Period	$\langle p_\perp^2 \rangle_{\text{W}}$ (GeV^2)	$\langle p_\perp^2 \rangle_{\text{Al}}$ (GeV^2)	$\Delta p_\perp^2$ (GeV^2)
P00	1.58 ± 0.02	1.39 ± 0.04	0.19 ± 0.04
P01	1.61 ± 0.02	1.40 ± 0.04	0.21 ± 0.04
P02	1.59 ± 0.02	1.37 ± 0.04	0.22 ± 0.04
P03	1.59 ± 0.02	1.40 ± 0.04	0.19 ± 0.04
P04	1.58 ± 0.02	1.36 ± 0.04	0.22 ± 0.04
P05	1.60 ± 0.02	1.39 ± 0.04	0.21 ± 0.04
P06	1.61 ± 0.02	1.40 ± 0.04	0.21 ± 0.04
P07	1.59 ± 0.02	1.37 ± 0.04	0.22 ± 0.04
P08	1.60 ± 0.02	1.37 ± 0.05	0.23 ± 0.05
Mean	1.59 ± 0.02	1.38 ± 0.04	0.21 ± 0.04

Table 4.22: Determination of the $\langle p_\perp^2 \rangle_{\text{W}}$, $\langle p_\perp^2 \rangle_{\text{Al}}$ and $\Delta p_\perp^2$ with the *Kaplan method* method in the W and the Al targets from the nine periods.

4.5.5 Results

Ratio of cross sections

The final results of the nuclear ratio as a function of x_F (left panel) and $p_\perp$ (right panel) of the J/ψ process are shown in Fig. 4.35. For each kinematic bin, the mean value from each period with the systematic error associated including the impact of the period-per-period compatibility and the signal extraction[13] are summarized in Table 4.23 and 4.24.

---

[13]The other systematic errors summarized in Table 4.21 are negligible.
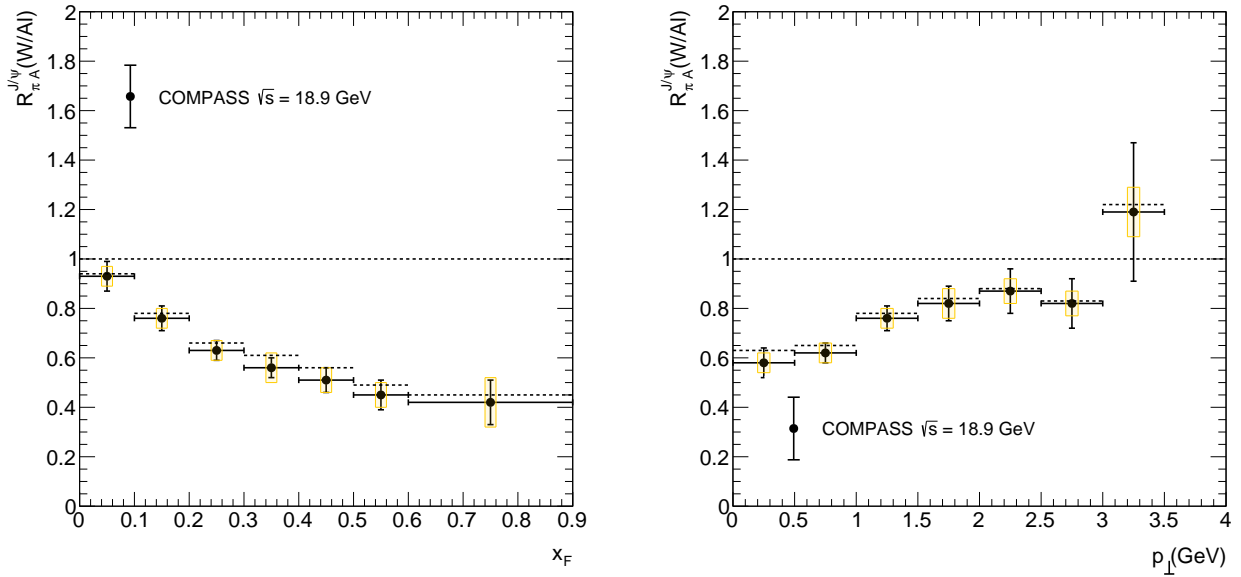
Figure 4.35: $R_{\pi A}^{J/\psi}(W/Al)$ mean values as a function of x_F (left panel) and $p_\perp$ (rght panel) from nine periods. The black errors bars and the yellow squares represent the statistical and systematic uncertainties, respectively. The black dotted line corresponds to the low limit due to the underestimation of the contamination of the J/ψ events due to the migration from the W to the Al target.

x_F	$R_{\pi A}^{J/\psi}(W/Al)$
0-0.1	$0.93 \pm (0.06)_{stat} \pm (0.05)_{syst}$
0.1-0.2	$0.76 \pm (0.05)_{stat} \pm (0.04)_{syst}$
0.2-0.3	$0.63 \pm (0.04)_{stat} \pm (0.05)_{syst}$
0.3-0.4	$0.56 \pm (0.04)_{stat} \pm (0.05)_{syst}$
0.4-0.5	$0.51 \pm (0.05)_{stat} \pm (0.03)_{syst}$
0.5-0.6	$0.45 \pm (0.06)_{stat} \pm (0.09)_{syst}$
0.6-0.9	$0.42 \pm (0.09)_{stat} \pm (0.10)_{syst}$

Table 4.23: $R_{\pi A}^{J/\psi}(W/Al)$ mean values as a function of x_F from the nine periods and the statistical and systematic uncertainties associated.

$p_\perp$ (GeV)	$R_{\pi A}^{J/\psi}(W/Al)$
0-0.5	$0.58 \pm (0.06)_{stat} \pm (0.04)_{syst}$
0.5-1	$0.62 \pm (0.04)_{stat} \pm (0.04)_{syst}$
1-1.5	$0.76 \pm (0.05)_{stat} \pm (0.04)_{syst}$
1.5-2	$0.82 \pm (0.07)_{stat} \pm (0.06)_{syst}$
2-2.5	$0.87 \pm (0.09)_{stat} \pm (0.05)_{syst}$
2.5-3	$0.82 \pm (0.12)_{stat} \pm (0.05)_{syst}$
3-3.5	$1.19 \pm (0.28)_{stat} \pm (0.10)_{syst}$
3.5-4	$2.40 \pm (1.11)_{stat} \pm (0.50)_{syst}$

Table 4.24: $R_{\pi A}^{J/\psi}(W/Al)$ mean values as a function of $p_\perp$ from the nine periods and the statistical and systematic uncertainties associated.

Nuclear transverse momentum broadening

The mean values from each period are $\langle p_\perp^2 \rangle_{\rm W} = (1.59 \pm 0.02)$ GeV^2, $\langle p_\perp^2 \rangle_{\rm Al} = (1.38 \pm 0.04)$ GeV^2 and $\Delta p_\perp^2 = 0.21 \pm 0.04$ GeV^2.

4.6 Conclusion

In this chapter, preliminary J/ψ data of the COMPASS experiment were analysed. From the event selection to the Monte-Carlo (MC) analysis, the extraction of the J/ψ cross sections ratio between π^-W and π^-Al collisions was discussed. The J/ψ extraction was performed by fitting the dimuon mass spectrum using the "cocktail" method for different $x_{\rm F}$ and $p_\perp$ bins. This method enables to take into account the background evolution.

A good agreement was found in a large dimuon mass fit interval, $M \in (2 - 8.5)$ GeV in both Al and W targets data sample. However, some tensions appeared in the low dimuon mass region $M \in (1.5 - 2.0)$ GeV due to several reasons: (i) a large event migration $\sim 10\%$ from the W to Al targets was highlighted, (ii) the low dimuon mass region is dominated by the Open-Charm (OC) contribution that is not very well known in the PYTHIA generator and (iii) the low dimuon mass region could contain other processes not included in the "cocktail" method like the decay of light mesons (ω and ϕ mesons). Nevertheless, the variation of the dimuon mass interval fit changes slightly $\sim 4\%$ the extraction of the J/ψ cross sections ratio between π^-W and π^-Al collisions.

The preliminary J/ψ data show a strong suppression as a function of $x_{\rm F}$ and $p_\perp$ in π^-W compared to π^-Al collisions. Otherwise, the transverse momentum broadening effect between π^-W and π^-Al collisions is equal to $\Delta p_\perp^2 = 0.21 \pm 0.04$ GeV^2. It exhibits an important nuclear effect due to the W target. These preliminary results highlight strong nuclear effects in the J/ψ data. In Chap. 6 and 7, an interpretation of these data based on the theoretical framework exposed in Chap. 2 will be proposed.

Analysis of Drell-Yan production in πA collisions

Contents

5.1 Observable

The double differential cross of Drell-Yan (DY) production is

$$\frac{\mathrm{d}^2\sigma^{\pi^- A}}{\mathrm{d}x_{\mathrm{F}}\mathrm{d}p_{\perp}}(\mathrm{DY}) = \frac{N_{\mathrm{events}}^{\mathrm{J}/\psi}(x_{\mathrm{F}}, p_{\perp})}{\epsilon^{\mathrm{A}} \cdot \Delta x_{\mathrm{F}} \cdot \Delta p_{\perp} \cdot \mathcal{L}} \tag{5.1}$$

where $N_{\mathrm{events}}^{\mathrm{DY}}$ is the number of Drell-Yan events in the $(x_{\mathrm{F}}, p_{\perp})$ kinematic bin, ϵ is the acceptance calculation including reconstruction efficiency, trigger efficiency, geometrical efficiency and detectors efficiency, Δx_{F} and $\Delta p_{\perp}$ are the x_{F} and $p_{\perp}$ bin width. The luminosity $\mathcal{L}$ is defined

in Eq. (4.3). The nuclear dependence for the DY process can be accessed when considering the ratio between the W and the Al target as a function of $x_{\rm F}$ and $p_\perp$:

$$R_{\pi^- {\rm A}}^{\rm DY}({\rm W/Al}) = \frac{N_{\rm W}^{\rm DY}(x_{\rm F}, p_\perp)}{\epsilon_{\rm W} \cdot \alpha^{\rm W} \Phi^0 \times L_{\rm eff}^{\rm W} \times \rho^{\rm W}} \Big/ \frac{N_{\rm Al}^{\rm DY}(x_{\rm F}, p_\perp)}{\epsilon_{\rm Al} \cdot \alpha^{\rm Al} \Phi^0 \times L_{\rm eff}^{\rm Al} \times \rho^{\rm Al}}. \tag{5.2}$$

As for the J/ψ analysis, the initial absolute flux Φ^0 cancels out in (5.2). The information concerning the flux is contained in the fraction of the incident flux at the entrance of the target, α, and also in the effective luminosity which is taken into account using the effective target length, $L_{\rm eff}$ (see Eq. (4.3)).

In this chapter, the extraction of the DY nuclear cross section ratios between the W target and the Al target will be discussed. All the steps of the analysis, from the extraction of DY events to the calculation of acceptance thanks to the Monte-Carlo simulation (MC), will be detailed. Finally, the preliminary results of $R_{\pi^- {\rm A}}$ as a function of $x_{\rm F}$ and $p_\perp$ will be shown.

5.2 Drell-Yan signal extraction

As discussed in the Sec 4, the dimuon mass spectrum consists of a mixture of different physical contributions: Open-Charm (OC), Combinatorial Background (CB), Charmonium (J/ψ and ψ') and DY. In order to study a specific process, it is necessary to evaluate the signal to background ratio in order (i) to minimise the systematic errors due to the background extraction and (ii) to maximise the signal number of events.

In the high-mass region $M \gtrsim 4$ GeV, the dimuon mass spectrum is dominated by the DY contribution in both W and Al targets (see Fig. 4.8 and Fig. 4.9). This very clean dimuon mass region is suitable for studying the DY process. The choice of the best dimuon mass interval for this study will depend on the evaluation of the DY process purity level.

5.2.1 Data sample

In order to determine the number of DY events, it is necessary to select the relevant invariant dimuon mass region where the purity of DY is high enough to minimise the systematic error due to the background subtraction. From the invariant mass fit shown in Fig. 4.9 for the Al target and in Fig. 4.8 for the W target, the integral of each physical contribution is calculated. The information about the background as a function of dimuon invariant mass is shown in Table 5.2 for the Al target and in Table 5.1 for the W target.

The dimuon invariant mass region best suited to study the DY process is $4.4 < {\rm M} < 8.5$ GeV for the Al target and $4.7 < {\rm M} < 8.5$ GeV for the W target. It is therefore obvious that the target which has the most restrictive dimuon mass interval constrains the final mass cut, i.e. $4.7 < {\rm M} < 8.5$ GeV. The DY number of events after the final dimuon invariant mass cut are summarised in Table 5.3.

After applying all selection criteria, the extracted kinematic distributions contain only DY events. The background is already subtracted thanks to the dimuon mass cut. A bin by bin DY

Dimuon invariant mass (GeV)	DY (%)	OC (%)	CB (%)	J/ψ (%)	ψ' (%)
4.2-8.5	84	8	< 1	2	5
4.3-8.5	88	8	< 1	1	4
4.4-8.5	91	6	< 1	< 1	3
4.5-8.5	94	6	< 1	< 1	1
4.6-8.5	95	5	< 1	< 1	1
4.7-8.5	97	3	< 1	< 1	< 1
4.8-8.5	100	0	0	0	0

Table 5.1: Contribution of each process integrated in x_{F}, $0 < x_{\mathrm{F}} < 0.9$, $p_\perp$, $0 < p_\perp < 4$ GeV for the W target.

Dimuon invariant mass (GeV)	DY (%)	OC (%)	CB (%)	J/ψ (%)	ψ' (%)
4.2-8.5	92	7	< 1	< 1	< 1
4.3-8.5	97	3	< 1	< 1	< 1
4.4-8.5	100	0	0	0	0

Table 5.2: Contribution of each process integrated in $0 < x_{\mathrm{F}} < 0.9$ and $0 < p_\perp < 4$ GeV for the Al target.

Selections	P00	P01	P02	P03	P04	P05	P06	P07	P08
Al target selections									
4.7 < M < 8.5 GeV	326	244	500	384	289	223	256	401	171
W target selections									
4.7 < M < 8.5 GeV	2303	1600	3294	2426	2043	1474	1737	2855	1016

Table 5.3: The statistics of dimuon events period by period according to Table 4.1.

extraction as a function of x_{F} and $p_\perp$ could also have been performed like in the J/ψ analysis. However due to the low statistics in the high-mass region, the statistical fluctuations at the edge of dimuon phase space of the other processes (as discussed in Sec 4.3.1), in particular for the OC process, would have caused an artificial systematic error. The present method of DY extraction in this analysis therefore seems the most relevant. Moreover, for reasons of low statistics, in particular for the Al target, all the periods will be merged in the remaining of this chapter.

5.2.2 Monte-Carlo simulation

The DY process is simulated and reconstructed using the COMPASS's complete analysis chain (PYTHIA, TGEANT, CORAL and PHAST software). The DY process is generated at LO in α, i.e. $q\bar{q} \rightarrow \gamma^\star \rightarrow \mu^+\mu^-$. The description of the DY process, simulated in the PYTHIA8 generator, is described in Sec 4.3.1.d. The generation of the $p_\perp$ spectra is carried out using a Gaussian

transverse momentum broadening function whose parameters are chosen phenomenologically[1]. The GRV pion [34] and the CT14 free proton PDFs [28] at NLO were used.

5.2.2.a Kinematics correlations

The correlation of DY MC events in the high-mass region as a function of the main variables are shown in Fig. 5.1. In the same way as in the J/ψ analysis, a strong dependence between x_F (or x_1, x_2) and $p_\perp$ in *reconstructed events* DY MC is observed. Consequently, the 2D extraction of the DY process as a function of x_F and $p_\perp$ enables to take into account the dependence of the spectrometer acceptance on them. The DY acceptance of the spectrometer covers the
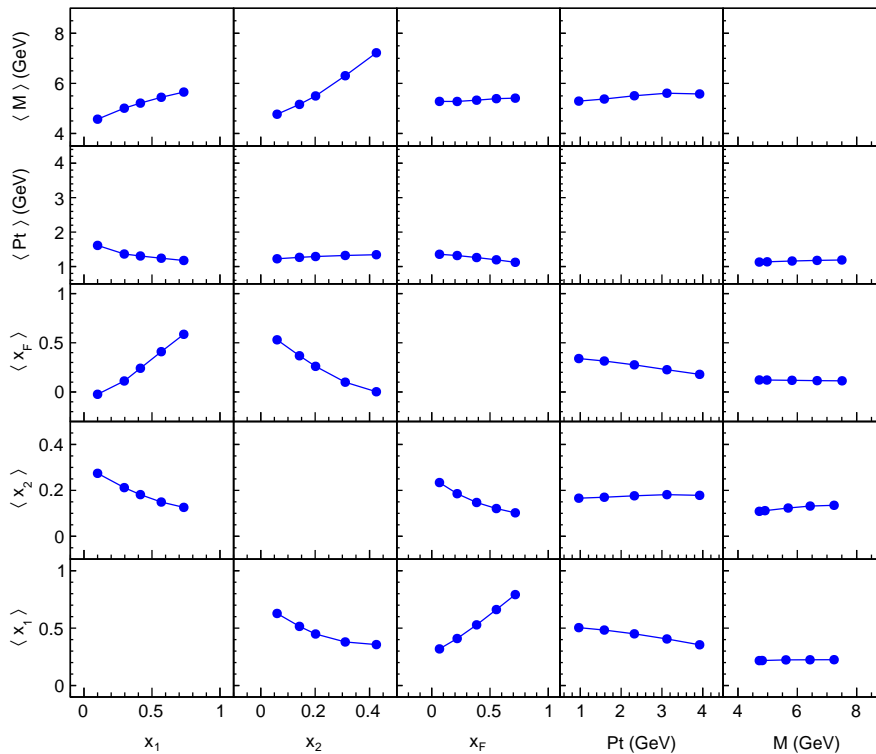
Figure 5.1: Correlation of *reconstructed events* from the DY MC for M $\in$ (4.7-8.5) GeV for the W target.

kinematic domain in $x_2 \in (0.05-0.4)$ corresponding to the anti-shadowing and EMC regions. The acceptance explores the $x_1 \in (0.1\text{-}0.8)$ interval. The DY cross section is essentially dominated by the valence quark PDFs of the pion beam in this region.

5.2.2.b Resolution and migration effects

Using the high-mass DY MC simulation, it is possible to estimate the resolution of kinematic variables. For each *reconstructed event*, the information of the associated *generated events* is also

---

[1]The parameters for generating this spectrum in the PYTHIA are not based on physical considerations. It is a matter of finding a set of parameters, non-physical though, which correctly reproduces the RD.
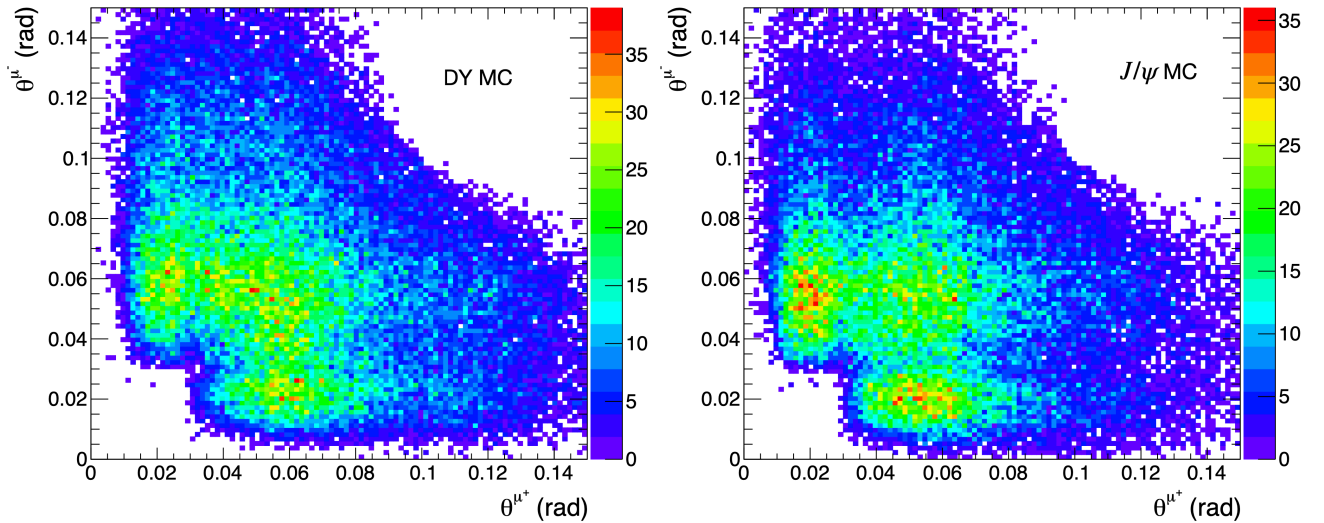
Figure 5.2: Muon angles from high-mass DY MC (left panel) and J/ψ MC (right panel).

kept. The calculation of the difference of these two quantities enables to quantify the impact of the spectrometer, i.e. all experimental effects (see Fig. 4.10).

Table 5.4 shows the resolution estimation in $M \in (4.7\text{-}8.5)$ GeV of the vertex position (X_{vtx}, Y_{vtx}, Z_{vtx}), the dimuon invariant mass M, x_{F} and $p_\perp$. Overall, the DY resolution on M, x_{F} and $p_\perp$ are slightly modified compared to the J/ψ process. On the other hand, the DY Z_{vtx} vertex position is improved by ~ 25 to 30 % respectively in NH$_3$ and W targets. Muon angles are slightly shifted

	Nuclear targets		
	Ammoniac (NH$_3$)	Aluminium (Al)	Tungsten (W)
X_{vtx} (cm)	0.025 ± 0.001	0.038 ± 0.001	0.040 ± 0.001
Y_{vtx} (cm)	0.023 ± 0.001	0.037 ± 0.001	0.043 ± 0.001
Z_{vtx} (cm)	7.99 ± 0.06	2.74 ± 0.01	4.05 ± 0.01
M (GeV)	0.164 ± 0.001	0.206 ± 0.002	0.358 ± 0.001
x_{F}	0.013 ± 0.001	0.017 ± 0.001	0.03 ± 0.001
$p_\perp$ (GeV)	0.110 ± 0.006	0.190 ± 0.005	0.293 ± 0.001

Table 5.4: Estimated resolutions for DY MC in $M \in (4.7\text{-}8.5)$ GeV.

to large angles compared to the J/ψ process as illustrated in Fig. 5.2. The mean value obtained are $\left\langle \theta^{\mu^+} \right\rangle_{\text{DY}} \approx \left\langle \theta^{\mu^-} \right\rangle_{\text{DY}} \sim 0.061$ mrad and $\left\langle \theta^{\mu^+} \right\rangle_{J/\psi} \approx \left\langle \theta^{\mu^-} \right\rangle_{J/\psi} \sim 0.057$ mrad. In the absence of a vertex detector, each vertex position is reconstructed by extrapolating the muon tracks. For larger angles, like in the high-mass DY process compared to the J/ψ process, the error associated with the tracks extrapolation at the vertex point will be smaller and therefore the resolution better.

Migration effect

The facts that (1) the target of Al is too close to the target of W and that (2) the resolution

as a function of Z_{vtx} is of the order of a centimeter, an event migration coming from the W causes contamination of the Al target. As shown in Tables 5.4 and 4.11 the resolution on Z_{vtx} depends strongly on the dimuon invariant mass. In the high-mass DY region, the Z_{vtx} resolution in W increases by 30% compared to J/ψ process[2]. The direct impact of improving the resolution
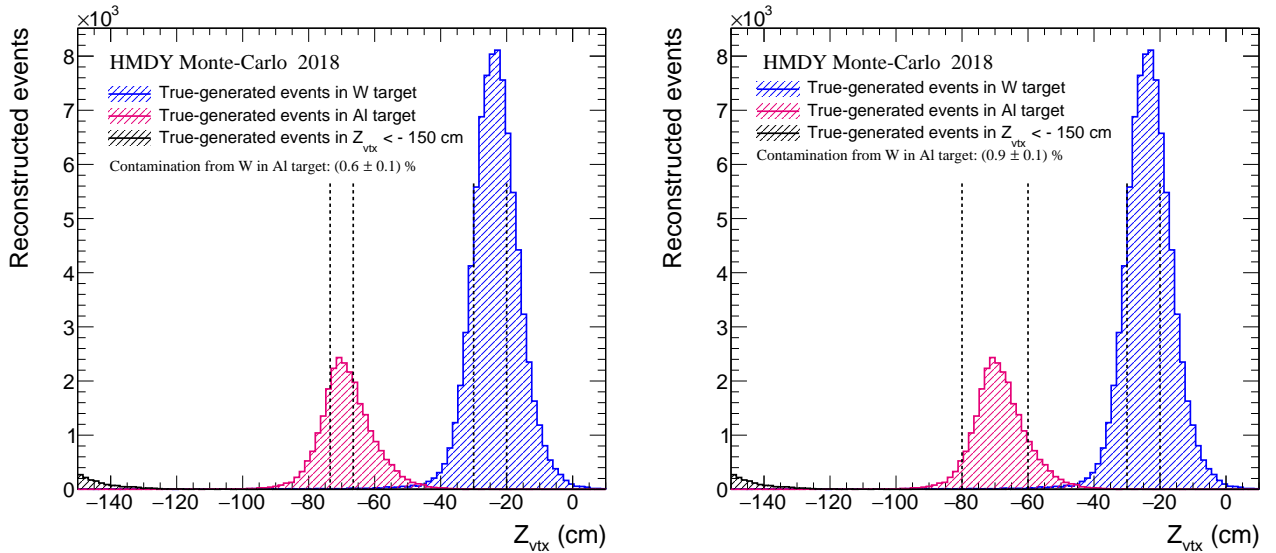
Figure 5.3: Reconstructed events as a function of Z_{vtx} from high-mass DY MC. In red, the *reconstructed events* from the *true-generated events* in Al target, in blue, the *reconstructed events* from the *true-generated events* in W target and in black, the *reconstructed events* from the *true-generated events* in $Z_{\text{vtx}} < -150 cm$ region.

on Z_{vtx} in high-mass DY MC results in a decrease in the contamination rate of events coming from the W target to the Al target $< 1\%$, as illustrated in Fig. 5.3 (left panel).

The resolution and small migration effects enable us to enlarge the cut limits of the Al target. Thus, it is possible to significantly increase the number of events from the Al target and to minimise the contamination coming from the W target, as illustrated in Fig. 5.3 (right panel). Indeed, the ratio of the *true-generated* distributions in between the enlarged and the standard cuts of the Al target is ~ 2, according to Fig. 5.3. The W target contamination for the Al target is still lower than 1% despite the widening of the cut. An extension of the downstream Z_{vtx} limit will risk adding a more significant contamination that is not under control. Similarly an extension of the upstream Z_{vtx} limit does not give a significant gain in the number of events. The difference in number of events period by period by using the Al standard cut and the Al enlarged cut is summarised in Table 5.5. A 50% gain in the number of events is observed. In the rest of the analysis, the Al enlarged cut will be used.

---

[2]Regarding the J/ψ analysis, although the Z_{vtx} average resolution (integrated over the entire dimuon mass range) approaches the high-mass DY Z_{vtx} resolution, the W contamination for the Al target is dominated by the low mass $M \lesssim 2$ GeV region.

Selections	P00	P01	P02	P03	P04	P05	P06	P07	P08
Al target selection -73.5 < Z_{zvtx} < -66.5 cm									
4.7 < M < 8.5 GeV	326	244	500	384	289	223	256	401	171
Al enlarge target selection -80 < Z_{zvtx} < -60 cm									
4.7 < M < 8.5 GeV	696	462	999	756	590	455	512	832	320

Table 5.5: The statistics of dimuon events period by period for the Al target after applying the dimuon mass cut.

5.2.3   Validity of the Monte-Carlo simulation

In order to ensure the validity of the MC in this analysis, a comparison between the high-mass DY MC and the Real Data (RD) is mandatory. The comparison must be made for identical kinematics conditions. Therefore, the same kinematic cuts are applied both in the *reconstructed events* from the high-mass DY MC and in the RD (Tables 4.1 and 5.5).

W target

Figure 5.4 shows the comparison between the MC and RD data as a function of x_{F} (left panel) and $p_{\perp}$ (right panel) for the W target. All distributions are normalised according to their integral. In this way, it is possible to get rid of the luminosity factor in the simulation and to control the shape of the distributions directly. The agreement between MC and RD data is satisfactory (less than 10% disagreement) in most of the x_{F} range. Except at very large $x_{\mathrm{F}} \gtrsim 0.8$, where the disagreement reaches approximately 20%. We note that the agreement between MC and RD as a function of $p_{\perp}$ is also reasonable.[3] A disagreement by 10-20% is observed for $p_{\perp} \lesssim 0.5$ GeV and $p_{\perp} \sim$ 2-2.5 GeV. Overall, the generated phase space is in good agreement with the RD.

Al target

Figure 5.5 shows the comparison between the MC and RD as a function of x_{F} (left panel) and $p_{\perp}$ (right panel) for the Al target. The same observations can be made compared to the W target. The disagreement between MC and RD for the Al target is slightly more pronounced compared to the W target. Overall, the agreement is satisfactory.

5.3   Drell-Yan cross section

After extracting the number of DY events as a function of x_{F} and $p_{\perp}$, these distributions must be corrected for the acceptance of the spectrometer as well for the luminosity factor. The different steps to determine the DY cross section are detailed below.

---

[3]The tuning of the $p_{\perp}$ spectrum in order to improve the agreement between the MC and RD has not been carried out within the framework of this thesis work.
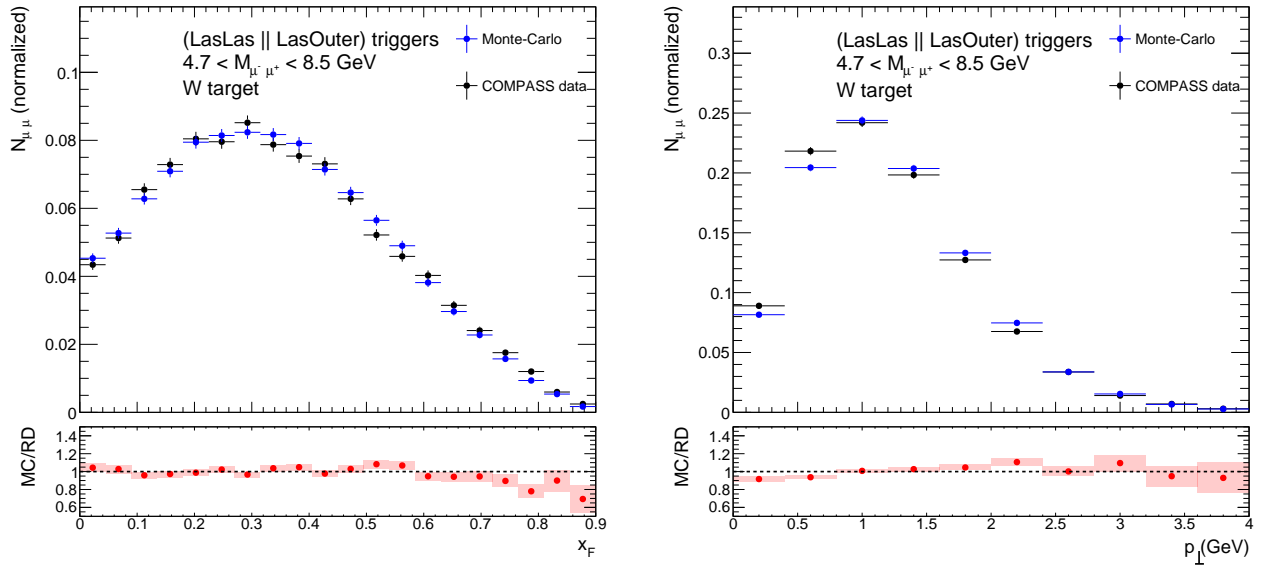
Figure 5.4: Comparison between MC and RD for the x_F (left panel) and $p_\perp$ (right panel) distributions for the W target.
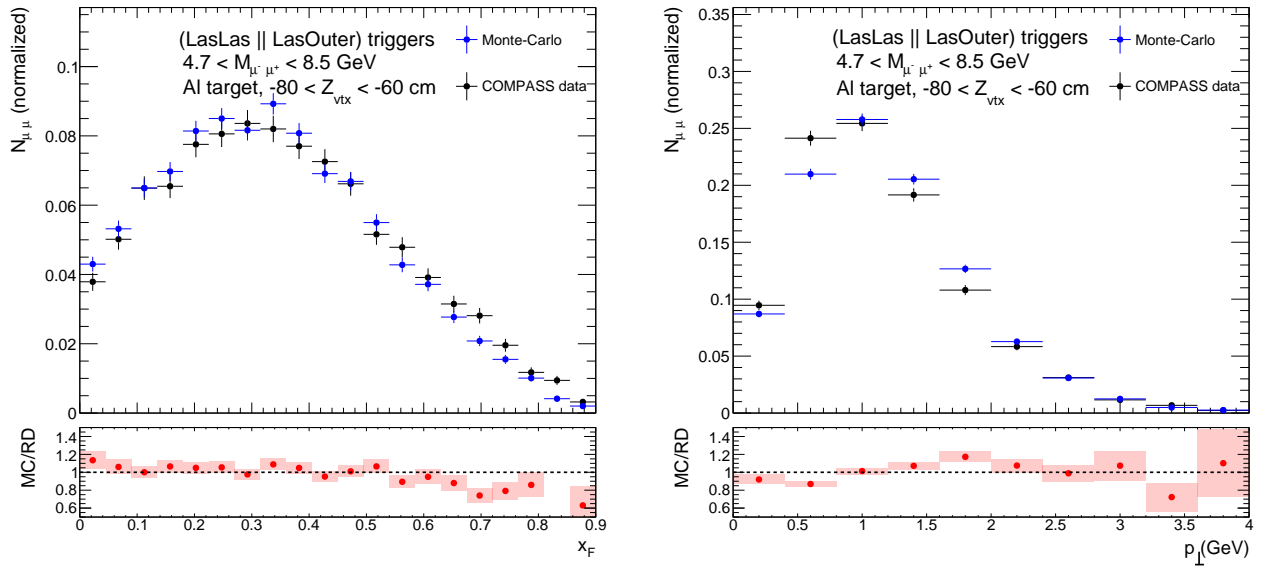
Figure 5.5: Comparison between MC and RD for the x_F (left panel) and $p_\perp$ (right panel) distributions for the Al target.

5.3.1   2D acceptance as a function of x_F and $p_\perp$

The 2D acceptance as a function of x_F and $p_\perp$ including both geometrical acceptance, trigger efficiencies and resolution effects of the spectrometer is defined as

$$\varepsilon_{x_F, p_\perp} = \frac{N(x_F, p_\perp)_{\mathrm{MC}}^{\mathrm{rec}}}{N(x_F, p_\perp)_{\mathrm{MC}}^{\mathrm{gen}}}, \tag{5.3}$$

where $N(x_F, p_\perp)^{\text{rec}}_{\text{MC}}$ is the number of *reconstructed events* by the spectrometer in $(x_F, p_\perp)$ kinematic bin and $N(x_F, p_\perp)^{\text{rec}}_{\text{gen}}$ is the number of *all generated events* in the same $(x_F, p_\perp)$ kinematic bin. *All generated events* include only the Z_{vtx} and dimuon mass selection criteria. The *reconstructed events* from MC include the kinematics cuts summarised in Table 4.1 and Table 5.5.

5.3.1.a   W target

Figure 5.6 shows the variation of high-mass DY acceptance for the W target as a function of x_F and $p_\perp$. The acceptance in quite stable at small $p_\perp \lesssim 1$ GeV. For $p_\perp \gtrsim 1$ GeV, the
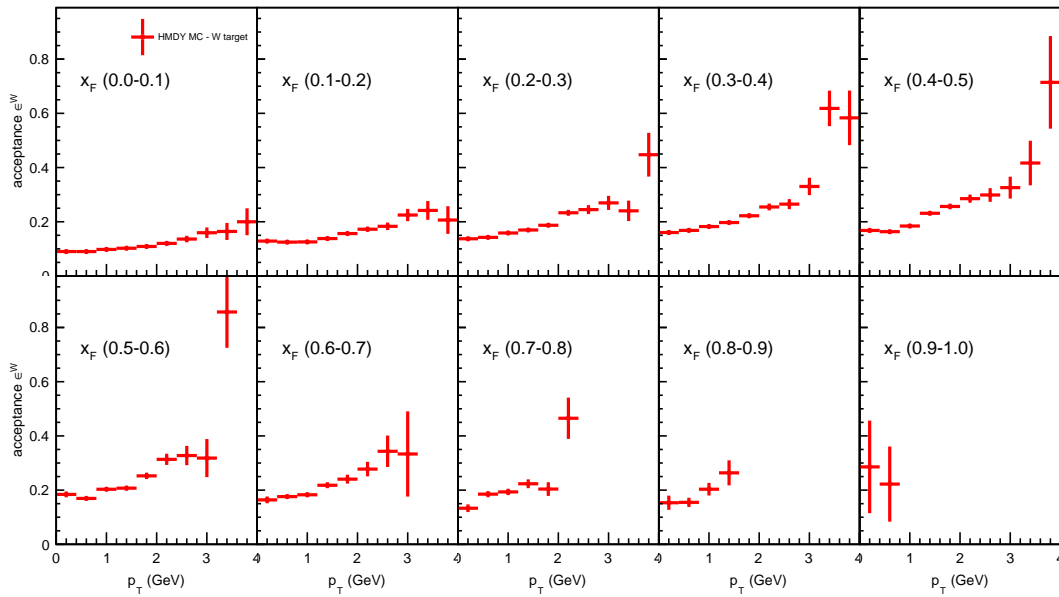
Figure 5.6: High-mass DY acceptance for the W target as a function of x_F and $p_\perp$.

acceptance increases by nearly a factor of 2 compared to the small $p_\perp$ region. In the large $p_\perp \gtrsim 3$ GeV, the acceptance starts to diverge. Since the high $p_\perp$ region is at the edge of the phase space, the statistics in the MC is limited. In addition, the acceptance in the last bin in x_F is restricted to only small $p_\perp$ values, $p_\perp \lesssim 1$ GeV.

5.3.1.b   Al target

The acceptance for the Al target as a function of x_F and $p_\perp$ is shown in Fig. 5.7. The same trends compared for the W target are observed. Moreover, the acceptance in the last bin in x_F is zero.

The ratios of the nuclear cross sections between the W and Al targets are directly related to the ratio of their acceptances (see Eq. (5.2)). The acceptance ratio between the Al and W targets is shown in Fig. 5.8 as a function of x_F and $p_\perp$. The acceptance ratio is below 1 for all x_F kinematic bins. In addition, the acceptance ratio doesn't depend on the kinematic value, it is flat as a function of x_F and $p_\perp$ and the ratio value is relatively stable. The only
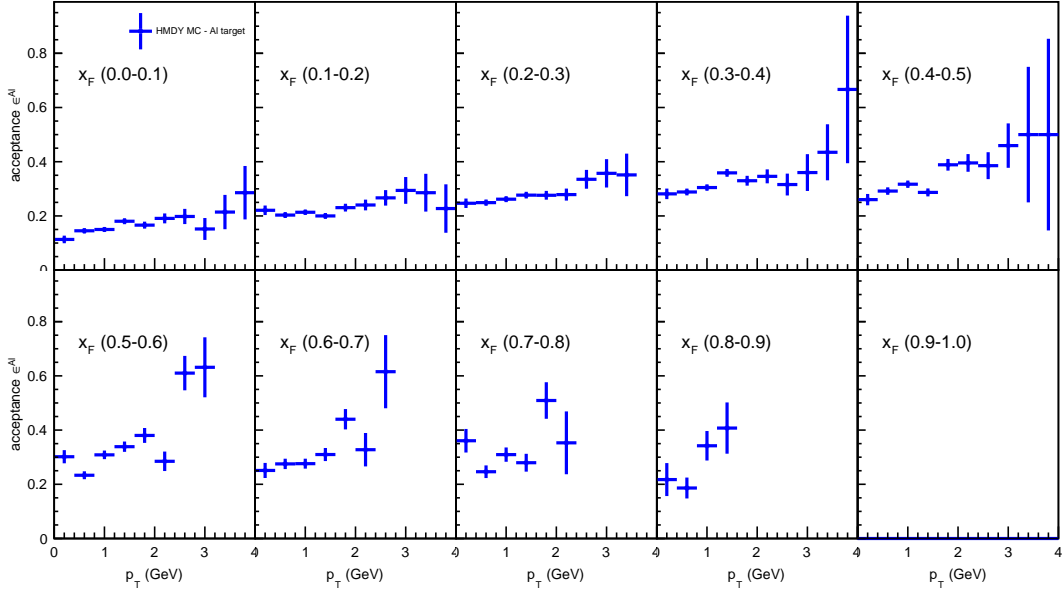
Figure 5.7: High-mass DY acceptance for the Al target as a function of x_{F} and $p_\perp$.

exception is for the $x_{\mathrm{F}} \in (0.7\text{-}0.8)$ bin, in which the acceptances ratio value is different by 15% compared to the neighbouring bins.
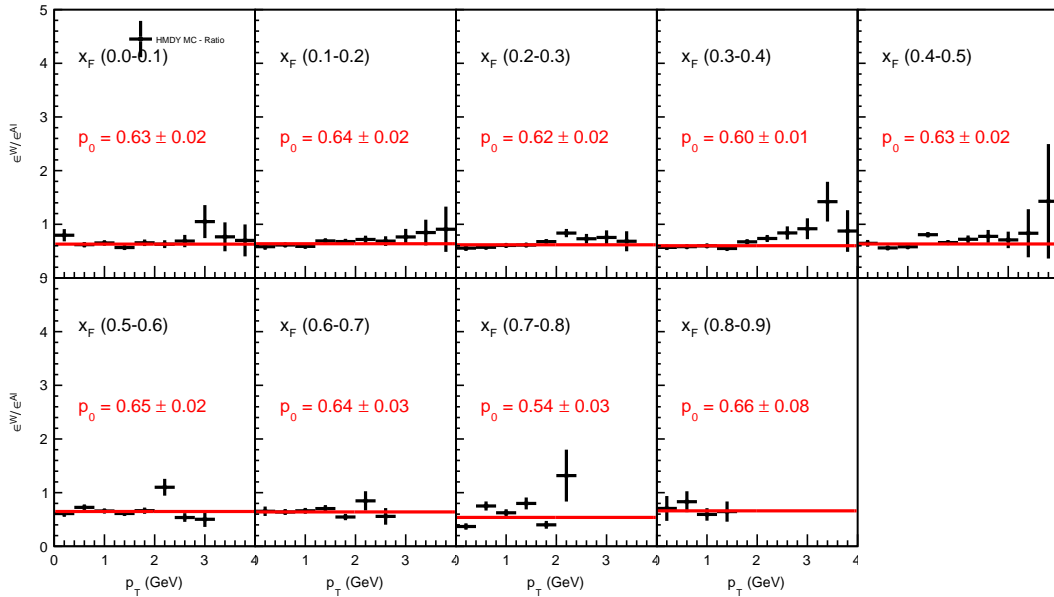
Figure 5.8: Ratio of acceptances for the W and the Al targets as a function of x_{F} and $p_\perp$ (black points). In red, constant fit function with p_0 parameter.

5.3.2 Drell-Yan cross section as a function of x_F and $p_\perp$

The extraction of DY events and the calculation of acceptances for the the W and Al were shown in the previous section. It is now possible to extract the experimental cross section, using

$$\frac{\mathrm{d}\sigma^{\pi^- A}}{\mathrm{d}x_F \mathrm{d}p_\perp}(\mathrm{DY}) \times \Phi_0 = \frac{N_{\mathrm{events}}^{\mathrm{DY}}(x_F, p_\perp)}{\epsilon^A \times \mathcal{L}} \times \Phi_0. \tag{5.4}$$

Figure 5.9 shows the absolute cross section for the W target normalised with the initial absolute flux Φ_0 as a function of x_F (left panel) and $p_\perp$ (right panel). The mean value of the x_F and $p_\perp$ distributions are $\langle x_F \rangle = 0.31$ and $\langle p_\perp \rangle = 1.12$ GeV, respectively. Figure 5.10 shows
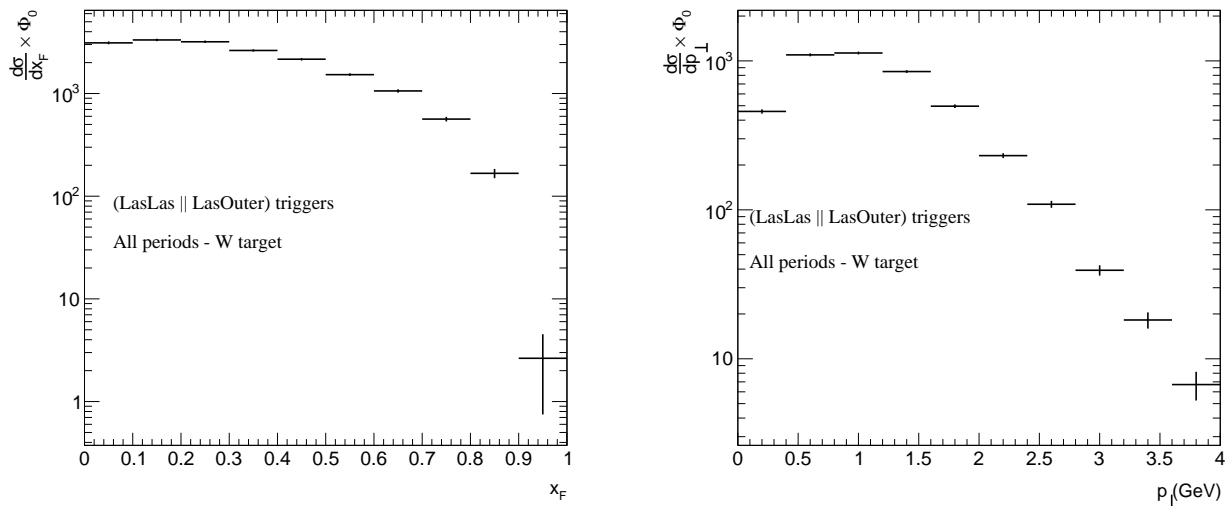
Figure 5.9: DY absolute cross section for the W target as a function of x_F (left panel) and $p_\perp$ (right panel) multiplied by the initial absolute flux Φ_0 in the for all period.

the same observable but for the Al target. The mean value of x_F and $p_\perp$ obtained are $\langle x_F \rangle = 0.32$ and $\langle p_\perp \rangle = 1.10$ GeV, respectively. By using a parametric function in the form $\propto (1 - x_F)^\alpha$, it possible to quantify the difference in the slopes between the two targets. . The fit results give $\alpha^W = 1.70 \pm 0.04$ and $\alpha^{Al} = 1.51 \pm 0.06$. The x_F distribution for the W target is more suppressed by $\sim 11\%$ compared to the Al target. The suppression observed in the DY absolute cross section at large x_F for the W target is clearly less important than in the case of the J/ψ cross section for the same target (see Sec 4.4.2), respectively of 20% and 40% in the last x_F bin.

5.3.3 Ratios of nuclear cross sections

After the extraction of the DY absolute cross sections for the W and Al targets, it is possible to calculate their ratios in order to study the nuclear dependence of the DY process. Figure 5.16 shows the W/Al cross section ratios as a function of x_F (left panel) and $p_\perp$ (right panel) for all periods. The x_F-dependence shows a slight suppression as a function of x_F. However, at large $x_F \sim 0.8$, the data exhibit a more pronounced depletion especially in the last bin in x_F. The
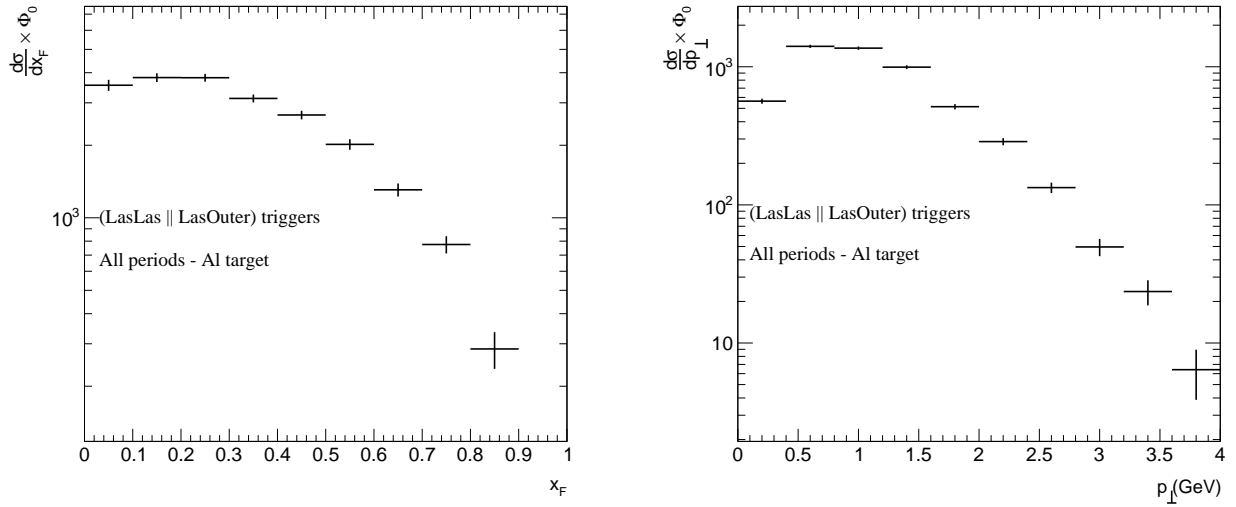
Figure 5.10: DY absolute cross section for the Al target as a function of x_F (left panel) and $p_\perp$ (right panel) multiplied by the the initial absolute flux Φ_0 in the for all period.
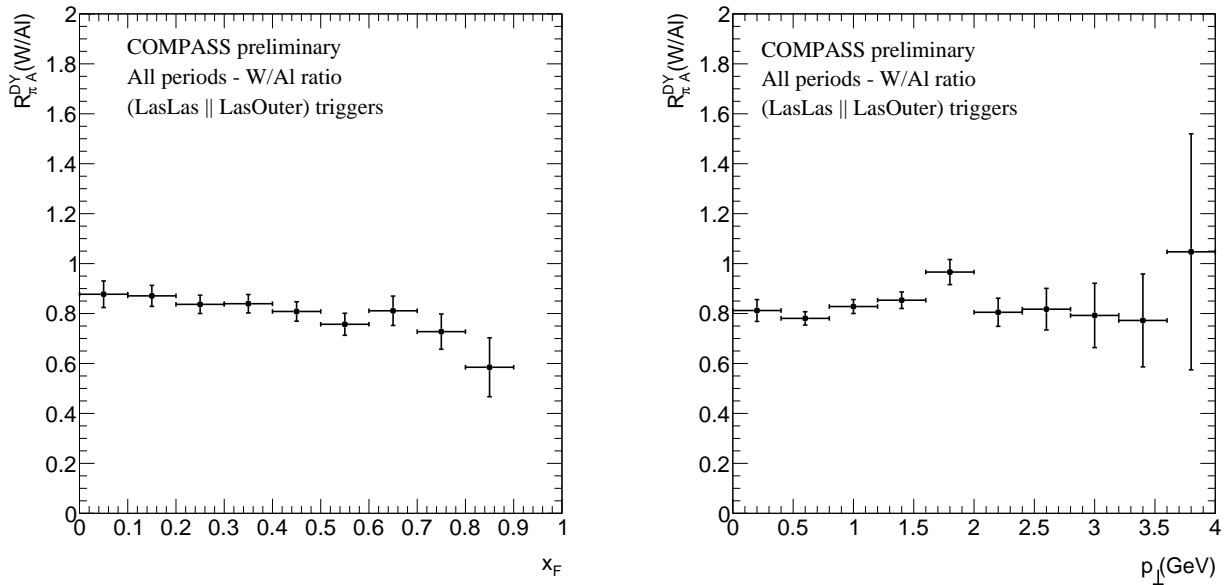
Figure 5.11: DY nuclear production ratio measured in πW normalised to πAl collisions as a function of x_F (left panel) and $p_\perp$ (right panel) for all periods and the statistical error associated.

shape of the $R_{\pi^- A}$ is different from that obtained in the x_F dependence of the J/ψ process: the suppression is much less important (see Fig. 5.17). The $p_\perp$ dependence of $R_{\pi^- A}$ is shown in the right panel of Fig. 5.16. It is rather flat, except in the region $p_\perp \in (1.5\text{-}2.0)$ GeV, in which a possible onset of a peak is observed (assimilated to the Cronin peak). The nuclear effect in the $R_{\pi^- A}$ of DY as a function of $p_\perp$ is also less pronounced than in the J/ψ case. These observations are consistent with the values of the slopes of the absolute cross sections extracted at large x_F for the W and Al targets as well as with the value of the transverse momentum broadening calculated in Table 5.8. The values of $R_{\pi^- A}$ as a function of x_F and $p_\perp$ for all periods including

only the statistical uncertainties are summarised respectively in Tables 5.6 and 5.7.

x_{F}	$\mathrm{R}^{\mathrm{DY}}_{\pi\mathrm{A}}(\mathrm{W/Al})$
0-0.1	$0.88 \pm (0.05)_{\mathrm{stat}}$
0.1-0.2	$0.87 \pm (0.04)_{\mathrm{stat}}$
0.2-0.3	$0.84 \pm (0.04)_{\mathrm{stat}}$
0.3-0.4	$0.84 \pm (0.04)_{\mathrm{stat}}$
0.4-0.5	$0.81 \pm (0.04)_{\mathrm{stat}}$
0.5-0.6	$0.76 \pm (0.04)_{\mathrm{stat}}$
0.6-0.7	$0.81 \pm (0.06)_{\mathrm{stat}}$
0.7-0.8	$0.75 \pm (0.07)_{\mathrm{stat}}$
0.8-0.9	$0.59 \pm (0.09)_{\mathrm{stat}}$

Table 5.6: $\mathrm{R}^{\mathrm{DY}}_{\pi\mathrm{A}}(\mathrm{W/Al})$ values as a function of x_{F} from all periods and the statistical uncertainty associated.

$p_{\perp}$	$\mathrm{R}^{J/\psi}_{\pi\mathrm{A}}(\mathrm{W/Al})$
0-0.4	$0.81 \pm (0.04)_{\mathrm{stat}}$
0.4-0.8	$0.78 \pm (0.03)_{\mathrm{stat}}$
0.8-1.2	$0.83 \pm (0.03)_{\mathrm{stat}}$
1.2-1.6	$0.85 \pm (0.05)_{\mathrm{stat}}$
1.6-2.0	$0.97 \pm (0.06)_{\mathrm{stat}}$
2.0-2.4	$0.81 \pm (0.08)_{\mathrm{stat}}$
2.4-2.8	$0.82 \pm (0.11)_{\mathrm{stat}}$
2.8-3.2	$0.80 \pm (0.13)_{\mathrm{stat}}$
3.2-3.6	$0.78 \pm (0.19)_{\mathrm{stat}}$
3.6-4.0	$1.05 \pm (0.47)_{\mathrm{stat}}$

Table 5.7: $\mathrm{R}^{\mathrm{DY}}_{\pi\mathrm{A}}(\mathrm{W/Al})$ values as a function of $p_{\perp}$ from all periods aand the statistical uncertainty associated.

5.3.4 Nuclear transverse momentum broadening

It is possible to calculate the value of the transverse momentum broadening induced by the nuclear medium in both nuclear targets. Figure 5.12 shows the *Kaplan fit* of the absolute cross sections as a function of $p_{\perp}$ for the Al target (left panel) and W target (right panel). The χ^2/ndf obtained are respectively 1.4 and 0.7.

Three different calculation methods are used to determine the $\langle p_{\perp}^2 \rangle$ value. The first consists in fitting the absolute cross section with a *Kaplan function*. The other two describe the integral calculation by performing a summation over the set of experimental bins (see Secs. 4.4.4 and 7.2.2 for more details).

The results for the transverse momentum broadening value calculated with the three different methods are summarised in Table 5.8. The value of the transverse momentum broadening in the case of the DY process is $\Delta p_{\perp}^2 = 0.03 \pm 0.04$ GeV^2 by using the *Kaplan method*. This

value is significantly lower compared to the transverse momentum broadening observed in the J/ψ process ($\Delta p_\perp^2 (J/\psi) = 0.21 \pm 0.04$ GeV^2).
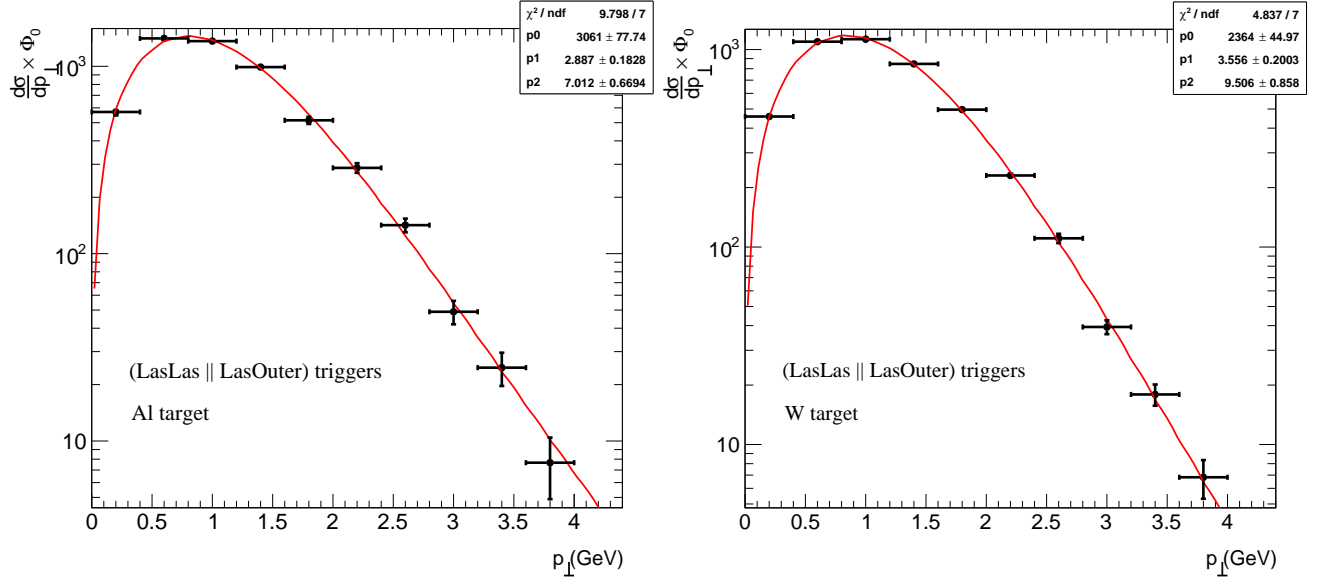
Figure 5.12: *Kaplan fit* of DY absolute cross section for the Al target (left panel) and for the W target (right panel) as a function $p_\perp$ for all periods.

Method	$\langle p_\perp^2 \rangle_{\mathrm{W}}$ (GeV^2)	$\langle p_\perp^2 \rangle_{\mathrm{Al}}$ (GeV^2)	$\Delta p_\perp^2$ (GeV^2)
Kaplan	1.66 ± 0.03	1.63 ± 0.03	0.03 ± 0.04
Bin (median)	1.65 ± 0.02	1.62 ± 0.02	0.03 ± 0.03
Bin (mean)	1.63 ± 0.02	1.60 ± 0.02	0.03 ± 0.03

Table 5.8: Determination of $\Delta p_\perp^2$ with different methods for the W and Al targets.

5.4 Systematic uncertainties

The systematic uncertainties on the $R_{\pi^- \mathrm{A}}$ ratios have been evaluated using three sources of uncertainties: (i) the impact of the trigger selection (ii) the impact of the Z_{vtx} position for the W target and finally (iii) the impact of the PDFs used in the MC for the acceptances calculation.

5.4.1 Impact of the trigger selection

Until now, all the results shown corresponded to the selection of events coming from two triggers: *LasLas or LasOuter*. As discussed in Sec 3, each trigger is associated with a specific angular region, i.e. a different phase space and therefore a different acceptance. In order to ensure the consistency of the results, the values of the $R_{\pi^- \mathrm{A}}$ as a function of x_F and $p_\perp$ obtained must be compatible trigger by trigger, i.e. *LasLas* (*LasOuter*) compared to the sum of the two, i.e. *LasLas or LasOuter*. Figure 5.13 shows the trigger dependence of the $R_{\pi^- \mathrm{A}}$ as a function of x_F (left

panel) and $p_\perp$ (right panel). The *LasOuter* trigger mainly probes the region at large $x_{\mathrm{F}} \gtrsim 0.5$, while the *LasLas* trigger dominates at moderate $x_{\mathrm{F}} \lesssim 0.5$. The trigger dependence of $R_{\pi^-\mathrm{A}}$ as a function of $p_\perp$ is more uniform, although the small $p_\perp \lesssim 1$ GeV region is essentially dominated by large $x_{\mathrm{F}} \gtrsim 0.8$ values. Tables 5.10 and 5.9 show the $R_{\pi^-\mathrm{A}}$ values, respectively, as a function of x_{F} and $p_\perp$ including statistical and systematic uncertainties due to the trigger dependence. The systematic uncertainties in each kinematic are determined by using the standard deviation defined in Eq. (4.15) for each $R_{\pi^-\mathrm{A}}$ sample calculated by trigger.
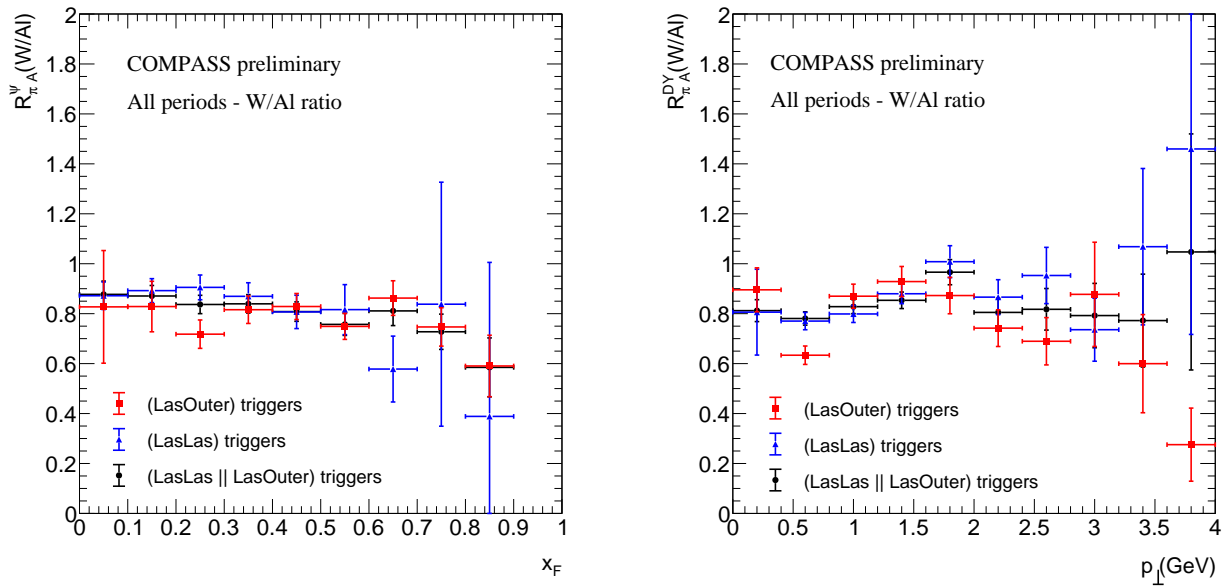
Figure 5.13: Impact of the triggers used in the $\mathrm{R}_{\pi\mathrm{A}}^{\mathrm{DY}}(\mathrm{W/Al})$ ratio as a function of x_{F} and $p_\perp$. In blue, $\mathrm{R}_{\pi\mathrm{A}}^{\mathrm{DY}}(\mathrm{W/Al})$ ratio calculated in *LasLas* trigger and in red, calculated in *LasOuter* trigger and in black, for both *LasLas or LasOuter* trigger.

x_{F}	$\mathrm{R}_{\pi\mathrm{A}}^{\mathrm{DY}}(\mathrm{W/Al})$
0-0.1	$0.88 \pm (0.05)_{\mathrm{stat}} \pm (0.02)_{\mathrm{syst}}$
0.1-0.2	$0.87 \pm (0.04)_{\mathrm{stat}} \pm (0.01)_{\mathrm{syst}}$
0.2-0.3	$0.84 \pm (0.04)_{\mathrm{stat}} \pm (0.06)_{\mathrm{syst}}$
0.3-0.4	$0.84 \pm (0.04)_{\mathrm{stat}} \pm (0.06)_{\mathrm{syst}}$
0.4-0.5	$0.81 \pm (0.04)_{\mathrm{stat}} \pm (0.05)_{\mathrm{syst}}$
0.5-0.6	$0.76 \pm (0.04)_{\mathrm{stat}} \pm (0.05)_{\mathrm{syst}}$
0.6-0.7	$0.81 \pm (0.06)_{\mathrm{stat}} \pm (0.07)_{\mathrm{syst}}$
0.7-0.8	$0.75 \pm (0.07)_{\mathrm{stat}} \pm (0.07)_{\mathrm{syst}}$
0.8-0.9	$0.59 \pm (0.09)_{\mathrm{stat}} \pm (0.09)_{\mathrm{syst}}$

Table 5.9: $\mathrm{R}_{\pi\mathrm{A}}^{\mathrm{DY}}(\mathrm{W/Al})$ as a function of x_{F} for all periods. The systematic uncertainties quoted take into account the trigger dependence only.

$p_\perp$	$\mathrm{R}^{\mathrm{DY}}_{\pi\mathrm{A}}(\mathrm{W/Al})$
0-0.4	$0.81 \pm (0.04)_{\mathrm{stat}} \pm (0.04)_{\mathrm{syst}}$
0.4-0.8	$0.78 \pm (0.03)_{\mathrm{stat}} \pm (0.07)_{\mathrm{syst}}$
0.8-1.2	$0.83 \pm (0.03)_{\mathrm{stat}} \pm (0.03)_{\mathrm{syst}}$
1.2-1.6	$0.85 \pm (0.05)_{\mathrm{stat}} \pm (0.03)_{\mathrm{syst}}$
1.6-2.0	$0.97 \pm (0.06)_{\mathrm{stat}} \pm (0.06)_{\mathrm{syst}}$
2.0-2.4	$0.81 \pm (0.08)_{\mathrm{stat}} \pm (0.05)_{\mathrm{syst}}$
2.4-2.8	$0.82 \pm (0.11)_{\mathrm{stat}} \pm (0.10)_{\mathrm{syst}}$
2.8-3.2	$0.80 \pm (0.13)_{\mathrm{stat}} \pm (0.06)_{\mathrm{syst}}$
3.2-3.6	$0.78 \pm (0.19)_{\mathrm{stat}} \pm (0.19)_{\mathrm{syst}}$
3.6-4.0	$1.05 \pm (0.47)_{\mathrm{stat}} \pm (0.50)_{\mathrm{syst}}$

Table 5.10: $\mathrm{R}^{\mathrm{DY}}_{\pi\mathrm{A}}(\mathrm{W/Al})$ as a function of $p_\perp$ for all periods. The systematic uncertainties quoted take into account the trigger dependence only.

5.4.2 Impact of Z_{vtx} position in W target

It is possible to quantify the impact of the cut in Z_{vtx} for the W target, indeed, this target measures 120 cm. The majority of events are within the first ten centimeters of the W target due to the strong beam attenuation as a function of Z_{vtx} (see Fig. 3.4). By comparing the $R_{\pi^- \mathrm{A}}$ value obtained for different slices, an estimate of the systematic error due both to the attenuation of the beam in the target and the acceptance dependence as a function of Z_{vtx} can be quantified. The impact of target length for the W target is shown in Fig. 5.14 and is negligible ($\sim 2\%$) compared to trigger dependence.
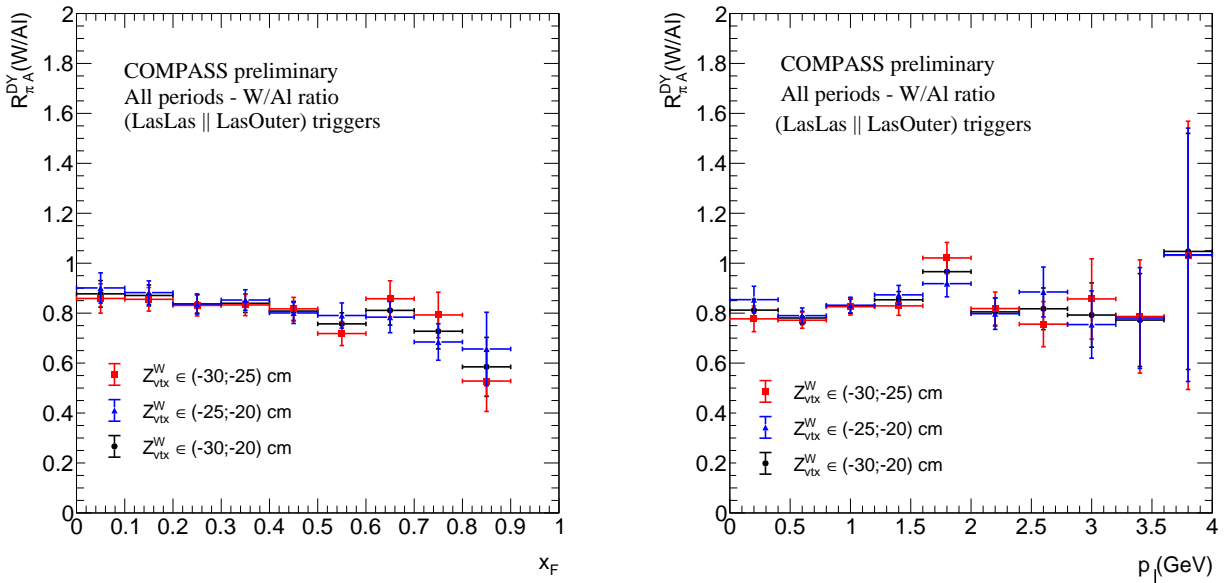
Figure 5.14: Impact of the Z_{vtx} cut of the W target on the $\mathrm{R}^{\mathrm{DY}}_{\pi\mathrm{A}}(\mathrm{W/Al})$ ratio as a function of x_{F} and $p_\perp$. In blue, $\mathrm{R}^{\mathrm{DY}}_{\pi\mathrm{A}}(\mathrm{W/Al})$ ratio calculated in second 5 cm in W target, in red, calculated in first 5 cm in W target and in black, in the first 10 cm.

5.4.3 Acceptance systematic error

In addition, the pion PDFs used in the MC is changed (GRVP1 (NLO) and GRVP0 (LO) pion PDF [34]) in order to estimate the impact of the physics model on the acceptance calculation and consequently on the ratio of nuclear cross section. The impact ($\sim 2\%$) as a function of x_{F} (left panel) and $p_\perp$ (right panel) is shown in Fig. 5.15. The impact of the PDF used in the $R_{\pi^- \mathrm{A}}$ calculation is negligible compared to the impact of the trigger dependence.
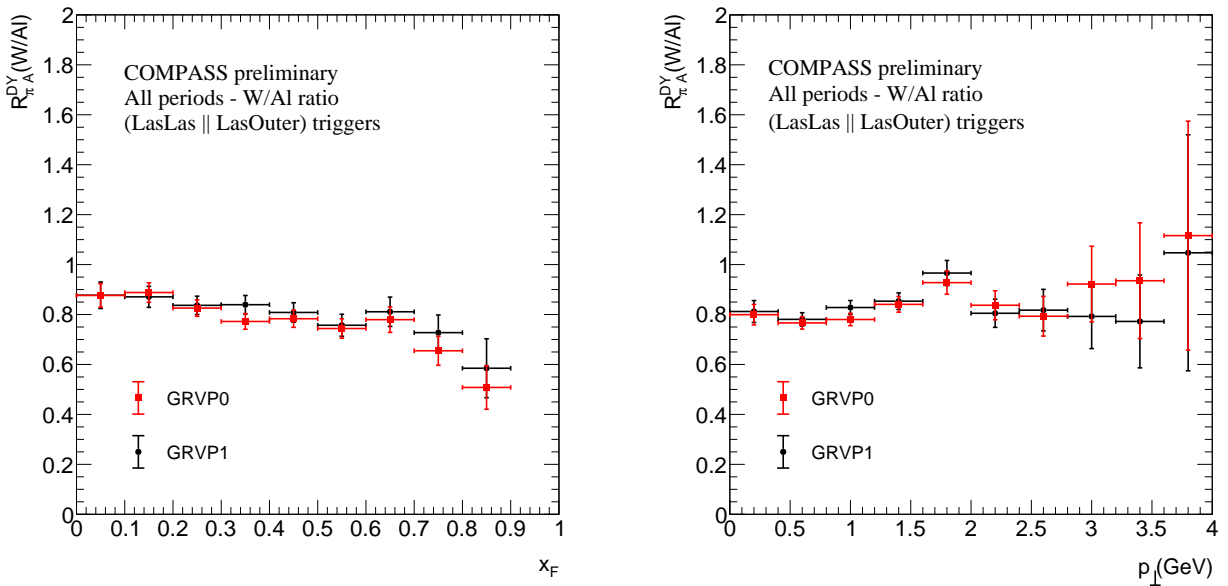
Figure 5.15: Impact of the pion PDF used in high-mass DY MC simulation on the $\mathrm{R}_{\pi \mathrm{A}}^{\mathrm{DY}}(\mathrm{W/Al})$ ratio as a function of x_{F} (left panel) and $p_\perp$ (right panel). In blue, $\mathrm{R}_{\pi \mathrm{A}}^{\mathrm{DY}}(\mathrm{W/Al})$ ratio using an acceptance calculation using GRVP1 PDF (NLO) and in red, using an acceptance calculation with GRVP0 PDF (LO).

5.4.4 Results

Ratio of cross sections

The final results of the A-dependence as a function of x_{F} (left panel) and $p_\perp$ (right panel) of the DY process are shown in Fig. 5.16. The results including the systematic error[4] associated are summarized in Table 5.10.

The comparison between the nuclear ratio cross section between $\pi^- \mathrm{W}$ and $\pi^- \mathrm{Al}$ collisions as a function of x_{F} and $p_\perp$ of the DY and the J/ψ processes is shown in Fig. 5.17. The suppression in J/ψ data is more pronounced in the entire x_{F} range. Both the DY and the J/ψ A-dependencies exhibit a ratio close to 1 in the first x_{F} bin. Likewise, the $p_\perp$ dependence shows a more pronounced suppression in the J/ψ data compared to the DY data. In both cases, the nuclear ratios seem to converge towards 1 at large $p_\perp$.

---

[4]The systematic errors from acceptance and Z_{vtx} dependence are negligible compared to the triggers dependence.
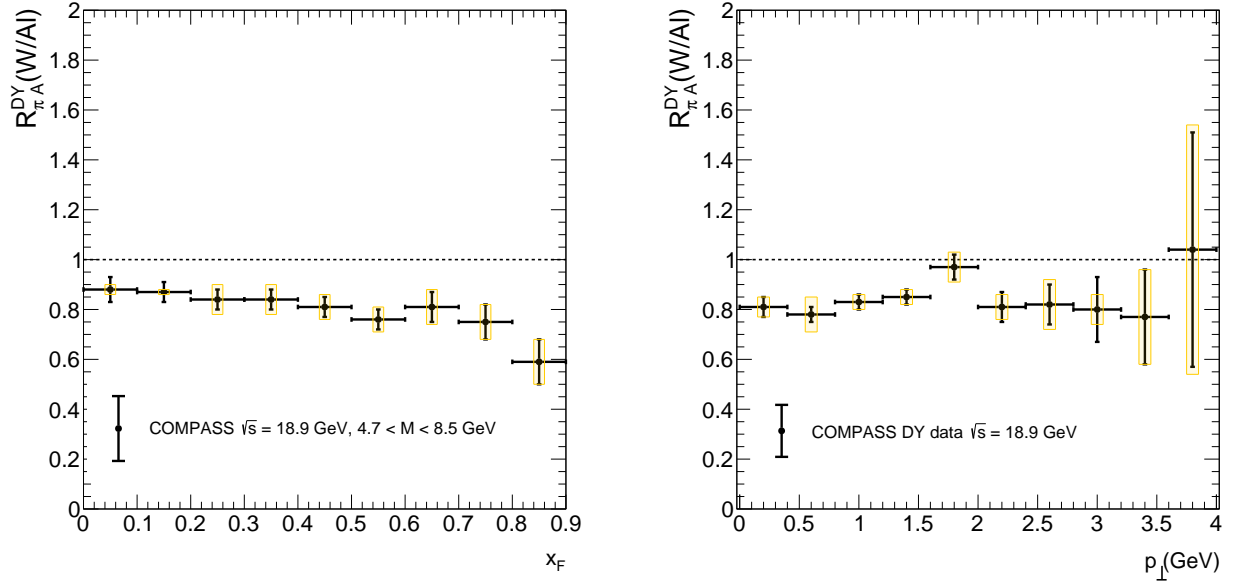
Figure 5.16: DY nuclear production ratio measured in πW normalised to πAl collisions as a function of x_F (left panel) and $p_\perp$ (right panel) for all periods. The error bars shown include statistical (black lines) and systematic (yellow rectangles) uncertainties.
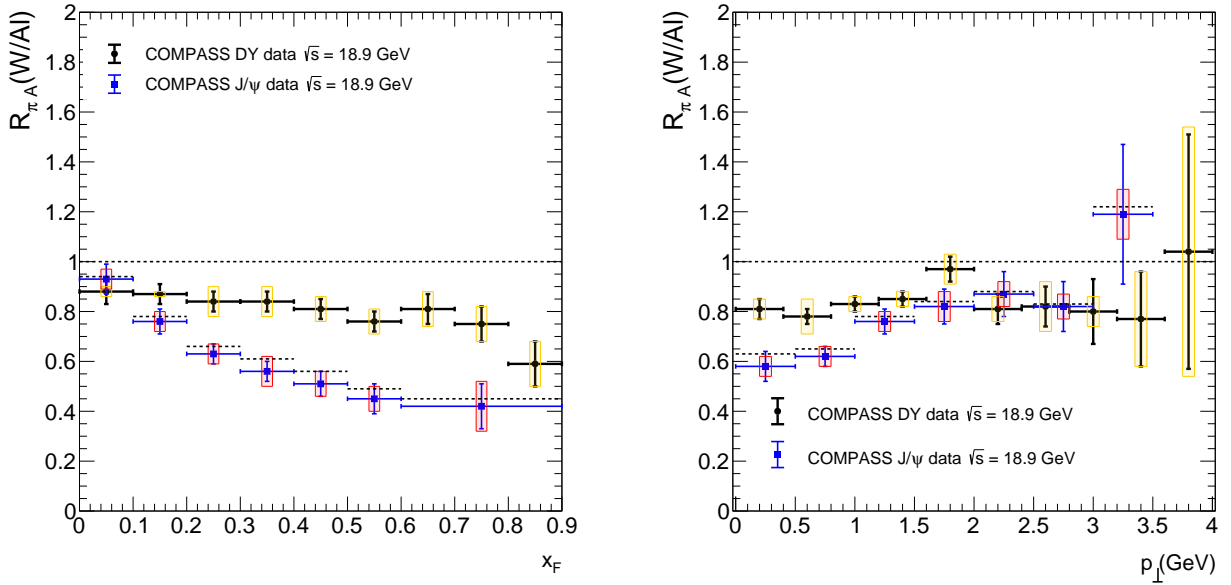
Figure 5.17: J/ψ and DY nuclear production ratios measured in πW collisions normalised to πAL collisions as a function of x_F (left panel) and $p_\perp$ (right panel), including the statistical and systematic uncertainties.

Nuclear transverse momentum broadening

The final values of $\langle p_\perp^2 \rangle_W = (1.66 \pm 0.03)$ GeV^2, $\langle p_\perp^2 \rangle_{Al} = (1.63 \pm 0.03)$ GeV^2 and $\Delta p_\perp^2 = 0.03 \pm 0.04$ GeV^2.

5.5 Conclusion

In this chapter, preliminary DY data of the COMPASS experiment were analysed. From the event selection to the Monte-Carlo (MC) analysis, the extraction of the DY cross sections ratio between $\pi^- W$ and $\pi^- Al$ collisions was discussed. The DY events extraction was performed by selecting the dimuon mass interval with the best signal background ratio.

The preliminary DY data exhibit a suppression $\sim 20\%$ at large $x_F \sim 0.8$ values in $\pi^- W$ compared to $\pi^- Al$ collisions. Whereas the DY data as a function of $p_\perp$ show a constant ratio between $\pi^- W$ and $\pi^- Al$ cross sections except for $p_\perp = $ 1-2 GeV where a slight peak can be observed.

Otherwise, the transverse momentum broadening effect between $\pi^- W$ and $\pi^- Al$ collisions is equal to $\Delta p_\perp^2 = 0.03 \pm 0.04$ GeV^2. This value is significantly lower by a factor 7 compared to the transverse momentum broadening value obtained in the J/ψ data. These preliminary results demonstrate different nuclear effects between the DY and J/ψ processes. The next two chapters have for objective to interpret these preliminary COMPASS data. They will be put into perspective in the set of DY and J/ψ existing data in hA collisions.

<div style="text-align: right; font-size: 4em; font-weight: bold;">6</div>

Initial-state energy loss effects in the Drell-Yan process

Contents

In this chapter, the radiative energy loss effect in the LPM regime will be investigated through a phenomenological analysis of Drell-Yan data in pA and πA fixed-target collisions. In the DY process, the quark propagating from the beam hadron through the nucleus is sensitive to the initial-state energy loss as discussed in section 2.4. The goal of this chapter is to make a global analysis of the existing DY data by comparing them to an initial-state energy loss model based on the BDMPS formalism and with the latest EPPS16 nPDFs [78]. Until now, no DY data in hA collisions could clearly demonstrate the presence of a radiative energy loss effect. E866/NuSea at FNAL performed high-statistics measurements of the DY process in pA collisons at $\sqrt{s} = 38.7$ GeV in the large x_F domain, $0 \lesssim x_F \lesssim 0.9$ [85, 124]. Their interpretation of an observed large suppression as a function of x_F in heavy nuclei remained elusive for a long time. This suppression could be attributed to nPDF, i.e. anti-shadowing sea quarks at $x_2 \lesssim 0.1$ as discussed in section 2.2, or to a presence of significant energy loss effect [144, 145, 146]. Thanks to the global analysis of the DY data set in hA, including new data from the COMPASS

experiment [119], I will try to provide a consistent picture of cold nuclear effects at fixed-target energy. This chapter is based on an article published in *Journal of High Energy Physics (JHEP)* prepared jointly with François Arleo and Stephane Platchkov [1].

6.1 Initial-state energy loss model

The effects of initial-state energy loss on the DY cross section in pA and πA collisions can be modelled as [147]

$$
\begin{aligned}
\frac{\mathrm{d}\sigma(\mathrm{hA})}{\mathrm{d}x_{\mathrm{F}}\,\mathrm{d}M} &= \sum_{i,j=q,\bar{q},g} \int_0^1 \mathrm{d}x_1 \int_0^1 \mathrm{d}x_2 \int_0^{(1-x_1)E_{\mathrm{b}}} \mathrm{d}\epsilon\, \mathcal{P}_i(\epsilon)\, f_i^{\mathrm{h}}\left(x_1 + \frac{\epsilon}{E_{\mathrm{b}}}\right) f_j^{\mathrm{A}}(x_2) \\
&\quad \times \frac{\mathrm{d}\widehat{\sigma}_{ij}}{\mathrm{d}x_{\mathrm{F}}\,\mathrm{d}M}(x_1 x_2 s)\,,
\end{aligned}
\tag{6.1}
$$

where E_{b} is the hadron beam energy in the rest frame of the nucleus, and $\mathcal{P}_i$ is the probability distribution in the energy loss of the parton i [42]. The latter has been determined numerically from a Poisson approximation [148, 149], using the LPM medium-induced gluon spectrum derived by BDMPS [106] as introduced in section 2.4.2. In the case of the DY process, the initial-state energy loss of the incident parton is modelled by a shift of its fraction of momentum x_1. Consequently, the beam PDF is not evaluated at x_1 but at $x_1 + \Delta x_1$, where $\Delta x_1 = \epsilon/E_{\mathrm{b}}$ encodes the energy loss effect. In the high E_{b} energy limit, it implies $\Delta x_1 \to 0$, i.e. the initial-state energy loss is suppressed.

The DY cross section in pA and πA is calculated at NLO using the DYNNLO Monte Carlo program [150, 43]. The transport coefficient expression $\hat{q}(x, Q^2)$ in Eq. (6.2) is approximated using the gluon distribution parametrisation in the nucleus at small x value as $\hat{q}(x) \propto xG(x) \propto x^{-\alpha}$, where $\alpha = 0.3$ suggested by fits to HERA data [151].[1] The transport coefficient is parametrized as (see appendix of [4]),

$$
\hat{q}(x) \equiv \hat{q}_0 \left(\frac{10^{-2}}{x}\right)^{0.3} \;;\quad x = \min(x_{\mathrm{A}}, x_2)\;;\quad x_A \equiv \frac{1}{2m_p L}\,,
\tag{6.2}
$$

with $m_p \equiv 1\,\mathrm{GeV}$, is the proton mass. The medium length is $L = (3/4)R$ where $R = r_0\,A^{1/3}$, the nuclear radius in a hard sphere nuclear density approximation with $r_0 = (4\pi\rho/3)^{-1/3} = 1.12$ fm and ρ is the nuclear matter density [3]. At $x_2 \lesssim x_{\mathrm{A}}$, the transport coefficient $\hat{q}(x)$ is considered as frozen as its Q^2 energy scale dependence at low scales $\hat{q}L \lesssim 1\mathrm{GeV}^2$.[2] The only free parameter of the model is the transport coefficient $\hat{q}_0$ evaluated at $x = 10^{-2}$. It was extracted from J/ψ data within the FCEL approach, $\hat{q}_0 = 0.07$-$0.09\ \mathrm{GeV}^2/\mathrm{fm}$ [152].

---

[1] The scale at which $xG(x)$ should be evaluated is semi-hard $Q^2 \sim \hat{q}L \sim 1\ \mathrm{GeV}^2$.
[2] The condition is satisfied in low beam energy, see [2].

6.2 Uncertainties computation

To calculate the uncertainties from the energy loss model, a prescription suggested by [153] is used. It is defined as

$$
\begin{aligned}
\left(\Delta R_{h\mathrm{A}}^{+}\right)^2 &= \sum_k \left[\max\left\{R_{h\mathrm{A}}\left(S_k^+\right) - R_{h\mathrm{A}}\left(S^0\right), R_{h\mathrm{A}}\left(S_k^-\right) - R_{h\mathrm{A}}\left(S^0\right), 0\right\}\right]^2 \\
\left(\Delta R_{h\mathrm{A}}^{-}\right)^2 &= \sum_k \left[\max\left\{R_{h\mathrm{A}}\left(S^0\right) - R_{h\mathrm{A}}\left(S_k^+\right), R_{h\mathrm{A}}\left(S^0\right) - R_{h\mathrm{A}}\left(S^-\right), 0\right\}\right]^2,
\end{aligned}
\tag{6.3}
$$

with $S_0 \equiv \{\hat{q}_0, n\}$, $S_1^\pm = \left\{\hat{q}_0^\pm, n\right\}$ and $S_2^\pm = \{\hat{q}_0, n^\pm\}$. The systematic uncertainties due to the transport coefficient is determined by varying it between $\hat{q}_0^- = 0.07$ GeV^2/fm and $\hat{q}_0^+ = 0.09$ GeV^2/fm. The central value of the transport coefficient is determined according to the best fit value extracted in J/ψ suppression from E866/NuSea experiment [86, 129] as discussed in section 2.4, i.e. $\hat{q}_0 = 0.075$ GeV^2/fm. To complete the systematic errors calculation, several beam PDF sets at NLO are used. For the proton PDF, the CT14 [28] set is used as the central value calculation (labelled n). The MMHT2014 [26] and nCTEQ [70] sets are used as error sets calculation (labelled $n^\pm$). For the pion PDF, the GRV set [34] is used as central value calculation (labelled n). The SMRS [30] and BSMJ [38] sets (labelled $n^\pm$) give almost identical results as long as the valence quark PDFs slope at large $x \to 1$ is the same, i.e. $xu_v^{\pi^-}(x) \sim (1-x)^1$.

6.3 DY Rapidity dependence

In this section, the DY cross section in Eq. (1.18) is calculated considering the isospin effect from Eq. (2.3) using CT14 free proton PDF [28] (labelled CT14 in the figures), the nPDF effect from Eq. (2.17) using EPPS16 [78] and their associated error sets and the energy loss effect modelled in Eq. (6.1). Each effect is computed separately but both nPDFs and the energy loss effects can be taken into account.

The present analysis includes data from E906/SeaQuest [118] at $E_{\mathrm{beam}} = 120$ GeV, E866/NuSea [124] at $E_{\mathrm{beam}} = 800$ GeV, NA10 [120] at $E_{\mathrm{beam}} = 140$ GeV, COMPASS at $E_{\mathrm{beam}} = 190$ GeV (see Chap. 5) and E615 [89] at $E_{\mathrm{beam}} = 251$ GeV. In addition, predictions for the AFTER@LHC [154] experiment will be shown. Finally, a discussion on extracting meson PDFs using DY nuclear data will also be made.

6.3.1 E906 experiment

The E906/SeaQuest experiment collected preliminary DY data as a function of x_{F} using a proton beam at $\sqrt{s} = 15$ GeV on C, Fe and W targets. The experimental acceptance coverage is $0.5 \lesssim x_1 \lesssim 0.8$, $0.1 \lesssim x_2 \lesssim 0.3$, $0.7 \lesssim p_\perp \lesssim 0.8$ GeV and $4.5 \lesssim M \lesssim 5.5$ GeV. Figure 6.1 shows R_{pA} (Fe/C) and R_{pA} (W/C) as a function of x_{F}. The data exhibit a suppression at large x_{F} for both Fe and W targets. The suppression is more pronounced for the heavier W nucleus.

In both R_{pA}, the isospin effect predicts a slight dependence as a function of x_F and a ratio close to 1. This is because the sea quarks of the nucleus are mainly probed in pA collisions (see Sec. 2.1.3). A weak isospin effect is therefore expected, it increases as function of x_F due to the antiquark flavour asymmetry in the nucleon sea i.e. $f_{\bar{d}}^p > f_{\bar{u}}^p$, discussed in Chap. 2.1.2,

On the other hand, the nPDF calculation shows a ratio rather flat as a function of x_F compatible with the isospin effect only. The x_2 range probed by these data essentially encompasses the EMC and the antishadowing regions. In both R_{pA}, the nPDF central set curve is above the isospin curve and increases the larger x_F becomes. This is due to the fact that at large $x_F \approx 0.8$, corresponding to the lower limit of the x_2 interval, the nPDF calculation highlights the antishadowing effect, for which $R_{pA} \gtrsim 1$. While at small $x_F \approx 0.1$, i.e. $x_2 \sim 0.3$, the nPDF effect decreases compared to the isospin effect due to the EMC effect, $R_{pA} \lesssim 1$. These
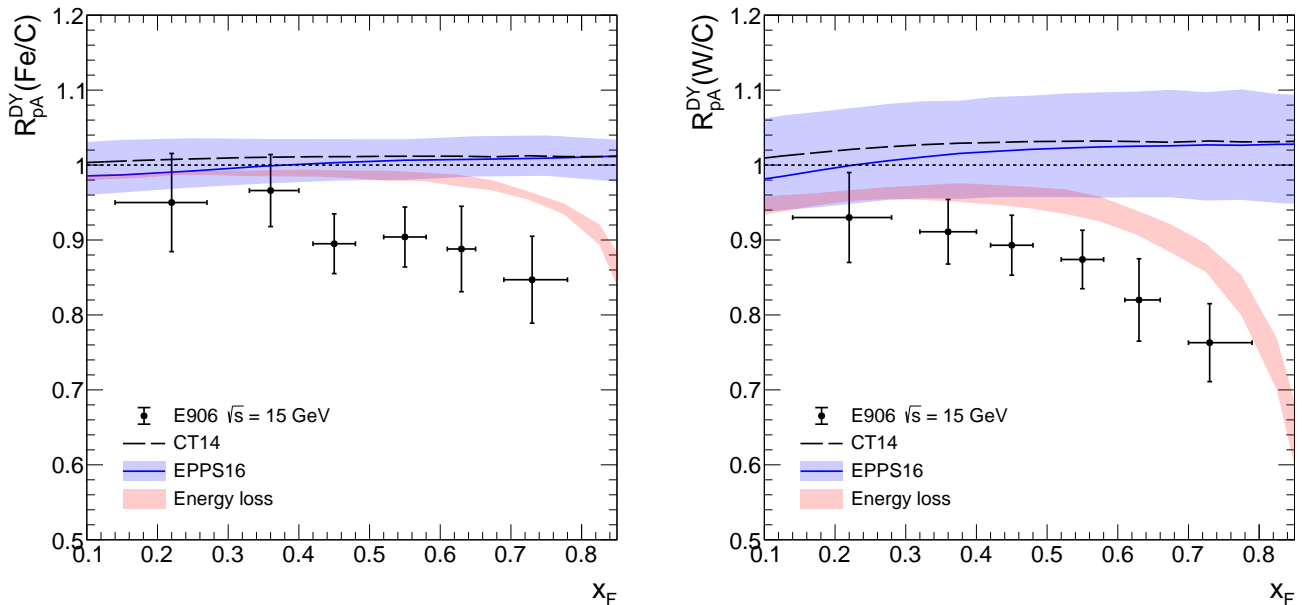
Figure 6.1: E906 nuclear production ratio measured in pFe (left panel) and pW (right panel) normalised to pC collisions at $\sqrt{s} = 15$ GeV compared to the EPPS16 nPDF calculation (blue band), isospin (dashed line) and energy loss effects (red band).

preliminary DY data show for the first time a clear disagreement with the nPDF calculation. The same calculation was performed using the nCTEQ nPDF [70]. The results obtained are compatible with narrower error bands.

The LPM initial-state energy loss model is shown in red band assuming the transport coefficient interval $\hat{q}_0 = 0.07$-0.09 GeV^2/fm. The calculation predicts a strong suppression as a function of x_F, compatible with the slope of the preliminary DY data. The agreement between the initial-state energy loss model and the data is better for the W than Fe target by roughly 5% and 10% respectively. The remarkable agreement between the slope of the suppression in data and the model hints at the presence of LPM energy loss effect, for the first time in the DY process.

The relative disagreement of the normalisation could be explained by three reasons: (i) a slight contribution of the anti-shadowing effect could reduce the normalisation of R_{pA}, (ii) a lack of the antiquark flavour asymmetry effect in the proton, (iii) a slightly higher transport coefficient would improve the agreement with data. These three reasons together might explain a part of the observed disagreement. Finally, a last observation can be made about the difference in agreement between the energy loss model and the data in the Fe and W targets. The *L*-dependence of the energy loss model does not seem to reproduce correctly the data. Nonetheless, the final DY data from E906 experiment are not still available. An additional contribution of the FCEL energy loss from Eq. (2.39), expected at NLO in the $q\bar{q} \to \gamma^{\star}g$ process, can play a role in suppression at large x_{F}.

6.3.2 E866 experiment

The E866/NuSea experiment collected DY data on a wide range in x_{F}, $0.1 \lesssim x_{\mathrm{F}} \lesssim 0.9$ using a proton beam at $\sqrt{s} = 38.7$ GeV on Be, Fe and W targets [85, 124]. The integrated mass range is $4 < M < 8$ GeV, with an additional kinematic cut $0.02 \lesssim x_2 \lesssim 0.10$. These data probe a x_2 range dominated by the shadowing effect, i.e. $R_{\mathrm{pA}} \lesssim 1$. The comparison between calculations and data is shown in Fig. 6.2.

The agreement between the data and the nPDF calculation is satisfactory for the two ratios[3]. The nPDF effect follow the same trend as the data. The higher x_{F} values are related to smaller $x_2 \sim 0.02$ where the shadowing effect contributes.

On the other hand, the LPM initial-state energy loss model shows a weaker suppression as a function of x_{F} compared to the kinematics of E906/SeaQuest, $\langle\epsilon\rangle_{\mathrm{LPM}}/E_{\mathrm{b}} \to 0$ in the high E_{b} beam energy limit. Consequently, this effect is negligible for both ratios except at large $x_{\mathrm{F}} \gtrsim 0.8$ for the heavier W nucleus. At this beam energy, and above, the initial-state energy loss effect is suppressed. Therefore, the DY data in pA collisions seem relevant to be included in the global nPDF fit analyses. Recently [155], new DY data have been collected in pA collisions as a function of y from the CMS experiment at $\sqrt{s} = 8.16$ TeV in $15 < \mathrm{M} < 60$ GeV and $-3 < y < 2$. As expected, the data do not provide evidence of suppression whose origin would be due to a LPM energy loss effect.

6.3.3 NA10 experiment

The NA10 experiment collected DY data on two nuclear W and D targets at $\sqrt{s} = 16.2$ GeV. The experimental acceptance coverage is $4.35 < M < 15$ GeV excluding the Υ peak region $8.5 < M < 11$ GeV.

---

[3]However, these data are used in the global fit of EPPS16 as discussed in Sec. 2.2.1
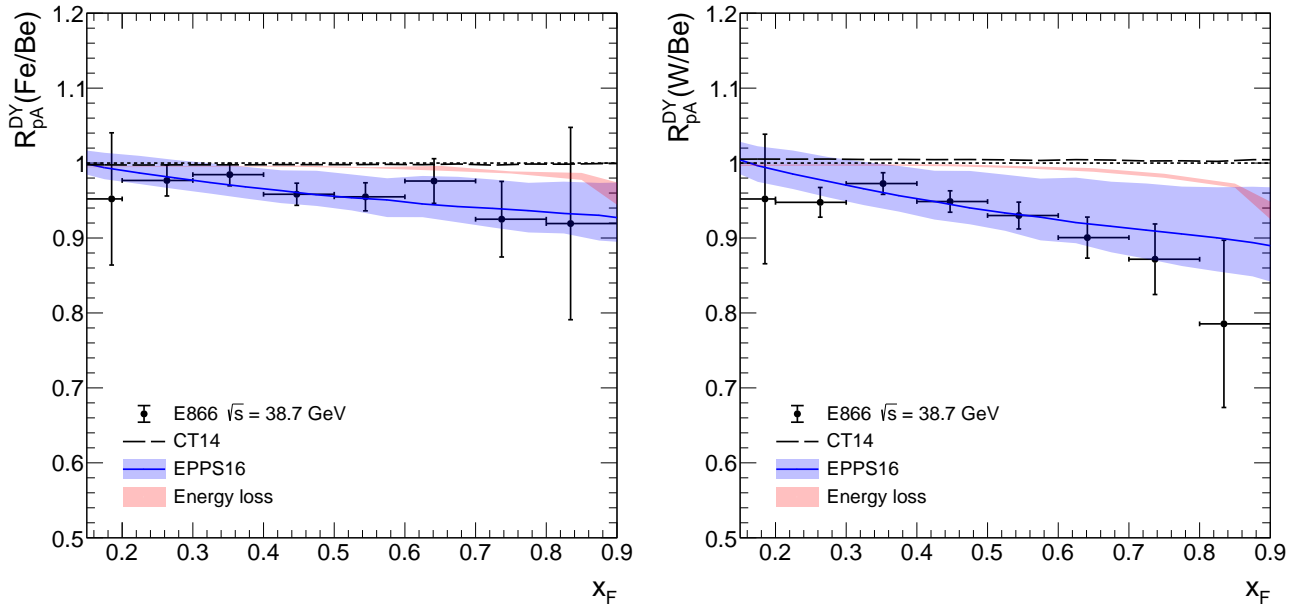
Figure 6.2: E866 nuclear production ratio measured in pFe (left panel) and pW (right panel) normalised to pBe collisions at $\sqrt{s} = 38.7$ GeV compared to the EPPS16 nPDF calculation (blue band), isospin (dashed line) and energy loss effects (red band).

These measurements were corrected for isospin effects due to the W target [88] (see Chap. 2.1.1). As in [156], an isospin correction is applied to all calculations and defined as

$$R_{\pi^-}^{\text{NLO-isospin corrected}}(\text{W/D}) = R_{\pi^-}^{\text{LO}}(\text{W}^{\text{isoscalar}}/\text{W})_{\text{no nPDF}} \times R_{\pi^-}^{\text{NLO}}(\text{W/D}), \qquad (6.4)$$

where $R_{\pi^-}^{\text{LO}}(\text{W}^{\text{isoscalar}}/\text{W})_{\text{no nPDF}}$ is calculated at LO in an "isospin-symmetrized" W nucleus ($Z = A/2$) over that in a W nucleus. Figure 6.3 clearly shows that the data are significantly below the nPDF calculation. A rescaling of 12.5% is applied by Paakkinen et al. [156] in their calculation in order to reproduce the data. This rescaling is larger than the normalization uncertainty of 6% reported by NA10.

On the other hand, the energy loss model predicts a constant contribution as a function of x_2. The suppression usually observed at large $x_F \sim 0.8 - 0.9$ is outside the acceptance of the experiment, $x_2 \lesssim 0.1$. The data show only the moderate $x_F \lesssim 0.8$ region where the energy loss effect is constant, $R_{\pi^- \text{A}} \approx 0.97$. The effect of energy loss is overall more marked in pion beam than in proton beam. This is due to the fact that the slope of the pion PDF at large x is less steep. Yet, the present calculations show that the initial-state energy loss effect exhibits an effect of the same magnitude as the nPDF effect.

As discussed in Sec. 2.1.3 and 2.2, the DY cross section in π^- A collisions is dominated by the contribution of valence quark PDFs of the target. All current nPDFs show a strong constraint on the valence quark nPDFs in this x_2 region thanks to the DIS data. Therefore, the existence of a nPDF effect is beyond doubt. If both the energy loss and nPDF effects are taken into account in the present calculation, the rescaling factor would become about 9%, closer to the
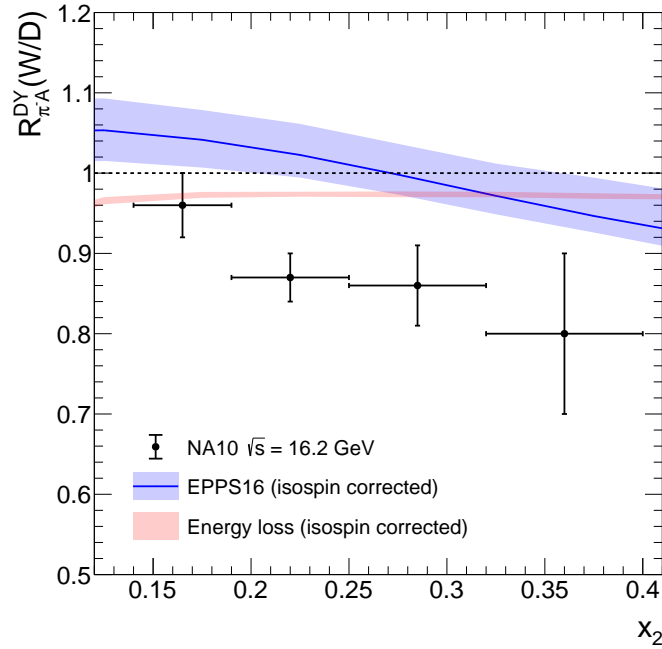
Figure 6.3: NA10 nuclear production ratio, corrected for isospin effects, measured in πW, normalised to πD, collisions at $\sqrt{s} = 16.2$ GeV compared to the EPPS16 nPDF calculation (blue band) and energy loss effects (red band).

systematic experimental error, compared to the 12.5% mentioned by EPPS16 group. Although the energy loss effect is independent of x_2 in this specific interval, its contribution must be taken into account in order to achieve a clean extraction of the nPDFs.

6.3.4 COMPASS experiment

The COMPASS experiment collected DY data using a pion beam at $\sqrt{s} = 18.9$ GeV on NH_3, Al and W targets as discussed in Chap. 5. The acceptance coverage of the experiment enables a wide kinematic range to be probed in x_F, $0 < x_F < 0.9$ and $0.1 < x_2 < 0.5$ probing mainly the anti-shadowing and EMC effects. The integrated mass range is $4.7 < M < 8.5$ GeV.

Figure 6.4 shows the calculations for the $R_{\pi^- A}$ (W/NH_3) and the $R_{\pi^- A}$ (W/Al) ratios. The isospin effect is larger in the first ratio, as in NH_3 the number of protons is larger than the number of neutrons. In contrast, in the second ratio, the isospin effect is smaller due to Al target, the $R_{\pi^- A}$ (W/Al) ~ 0.95.

In both ratios, in the $0.1 < x_F < 0.9$ interval, the nPDF calculation is always above the isospin effect due to the anti-shadowing effect, $R_{\pi^- A} \gtrsim 1$. The EMC effect is not visible in Fig. 6.4. It is probed at smaller $x_F \lesssim 0.1$ values. As in the NA10 data, the energy loss effect is small but of the same magnitude as the nPDFs at moderate $x_F \lesssim 0.7$. At large $x_F \gtrsim 0.7$, the initial-state energy loss model exhibits a large suppression, $R_{\pi^- A} \sim 0.8$ at $x_F \sim 0.9$.
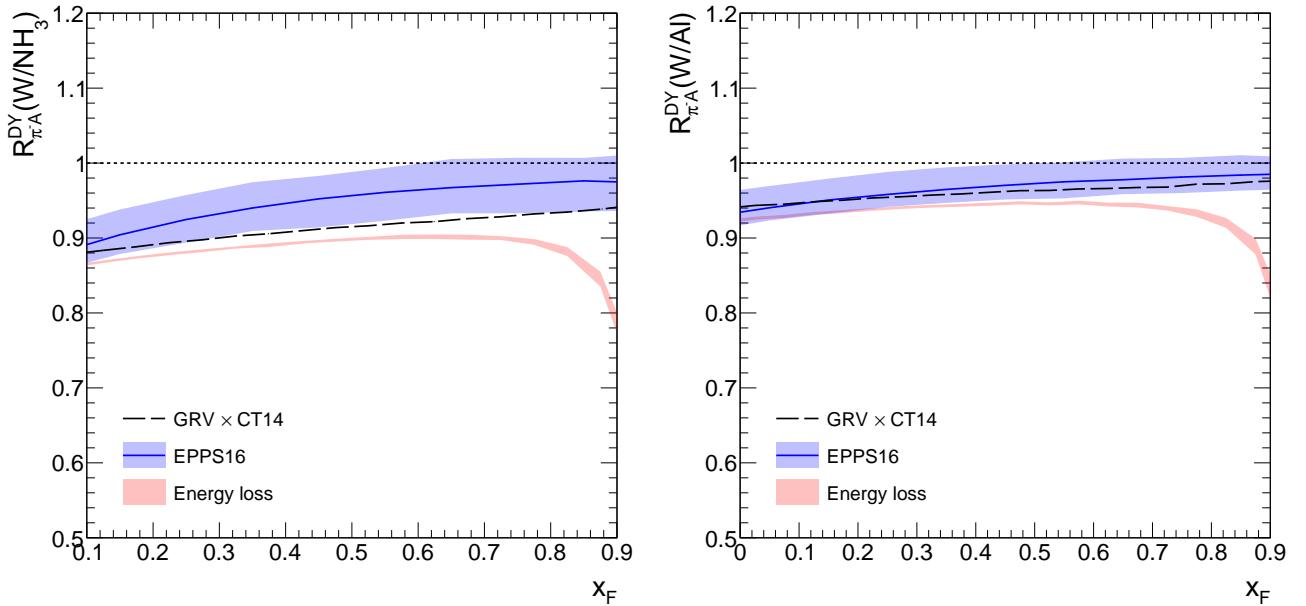
Figure 6.4: Nuclear production ratio in πW, normalised to πNH_3 (left panel) and to πAl (right panel) collisions at $\sqrt{s} = 18.9$ GeV compared to the EPPS16 nPDF calculation (blue band), isospin (dashed line) and energy loss effects (red band)

COMPASS Preliminary DY data

Figure 6.5 shows the comparison between the $R_{\pi^- A}$ (W/Al) ratio as a function of x_F for the preliminary DY data analyzed in Chap. 5 and the initial-state energy loss, nPDF and isospin calculations. A 20% disagreement in normalization is observed between the calculations and the data. However, the data show a suppression of about 20% at large x_F. These data seem to indicate a disagreement with the predictions of nPDF at large x_F. Despite (i) the limited statistics due to the reference Al target and (ii) the fact that the initial-state energy loss effect in πA collisions is significantly lower than in pA collisions, these data will add an upper limit on the transport coefficient.

6.3.4.a AFTER experiment

Measurement of DY data has been proposed by the AFTER collaboration using a proton beam on several nuclear targets at a collision energy $\sqrt{s} = 115$ GeV [154] in $-3 \lesssim y \lesssim 3$ rapidity interval and in $4 < M < 5$ GeV mass range. Depending on the rapidity region, the nuclear effects are different. The AFTER experiment would explore a typical range in $10^{-3} \lesssim x_2 \lesssim 0.8$, embracing both the shadowing, the anti-shadowing and the EMC regions. First, the initial-state energy loss effect vanishes at forward rapidity ($y \gtrsim 0$) at this beam energy. In contrast at backward rapidity ($y \lesssim 0$) a not negligible effect is expected.

In Fig. 6.6, the initial-state energy loss and isospin effects at backward rapidity are shown. First, a large isospin effect is observed when comparing Pb and p targets. The backward
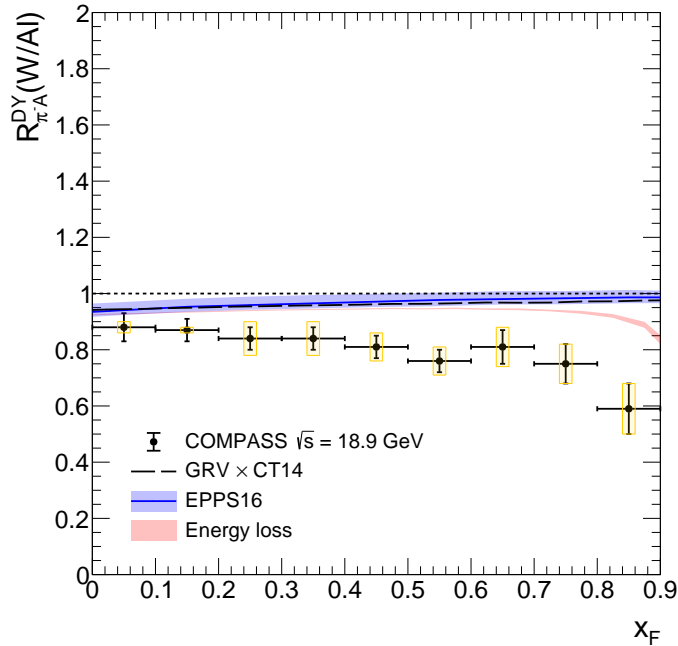
Figure 6.5: Nuclear production ratio measured in πW normalised to πAl collisions at $\sqrt{s} = 18.9$ GeV compared to the EPPS16 nPDF calculation (blue band), isospin (dashed line) and energy loss effects (red band).

rapidity enables to probe large $x_2 \sim 0.7$ where the DY cross section is dominated by the valence quark PDFs of the target.

Second, the initial-state energy loss effect is non-negligible and contributes to 10 % in the R_{pA} at $y \sim -2.5$. This effect is of the same order as the nPDF effects expected in the x_2 range associated. It is therefore necessary to take it into account in any theoretical prediction.

6.3.5 E615 experiment

The E615 experiment collected DY data in both π^- and π^+ collisions at $\sqrt{s} = 21.7$ GeV on a W target [89]. The acceptance coverage of $0.04 < x_2 < 0.36$ covers mainly the anti-shadowing region. The ratio between DY cross sections in π^-W and π^+W collisions enables to access the ratio between valence and sea quarks in the nucleon via,

$$R^{DY}_{\pi^+ A / \pi^- A} \approx \frac{\bar{d}^{\pi^+}(x_1) d^A(x_2) + 4 u^{\pi^+}(x_1) \bar{u}^A(x_2)}{4 \bar{u}^{\pi^-}(x_1) u^A(x_2) + d^{\pi^-}(x_1) \bar{d}^A(x_2)} \tag{6.5}$$

$$\approx \frac{d^A(x_2) + 4 \bar{u}^A(x_2)}{\bar{d}^A(x_2) + 4 u^A(x_2)}. \tag{6.6}$$

Figure 6.7 shows the comparison between the data and nPDF calculation. The ratio decreases quickly between $0.05 < x_2 \lesssim 0.15$ then slows down at $x_2 \gtrsim 0.15$. This observation is explained by the fact that sea quark PDFs contribution $(\bar{u}(x), \bar{d}(x))$ vanish at large x_2. Consequently, Eq. 6.5 can approximate like the ratio between $d(x)/u(x) \sim 0.3 - 0.4$ as illustrated in Fig. 2.1 (right panel). The agreement between the calculation with the EPPS16 nPDF and data is
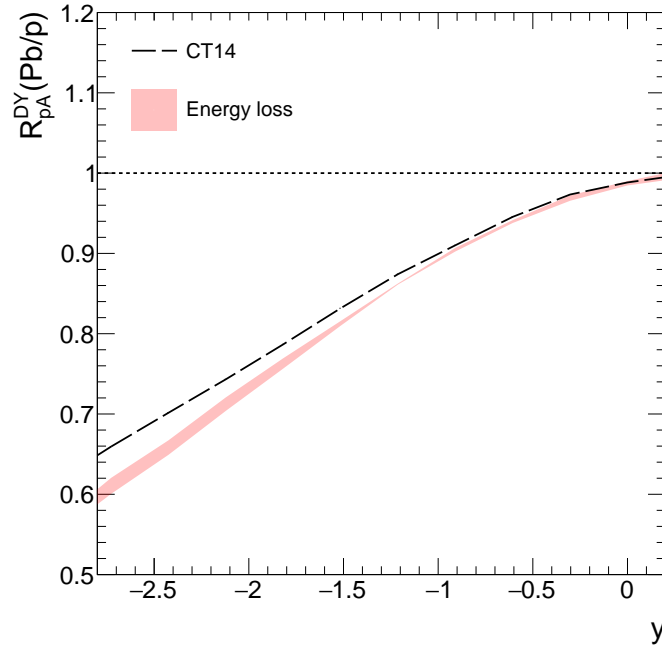
Figure 6.6: Nuclear production ratio measured in pPb normalised to pp, collisions at $\sqrt{s} = 115$ GeV compared to isospin (dashed line) and energy loss effects (red band)
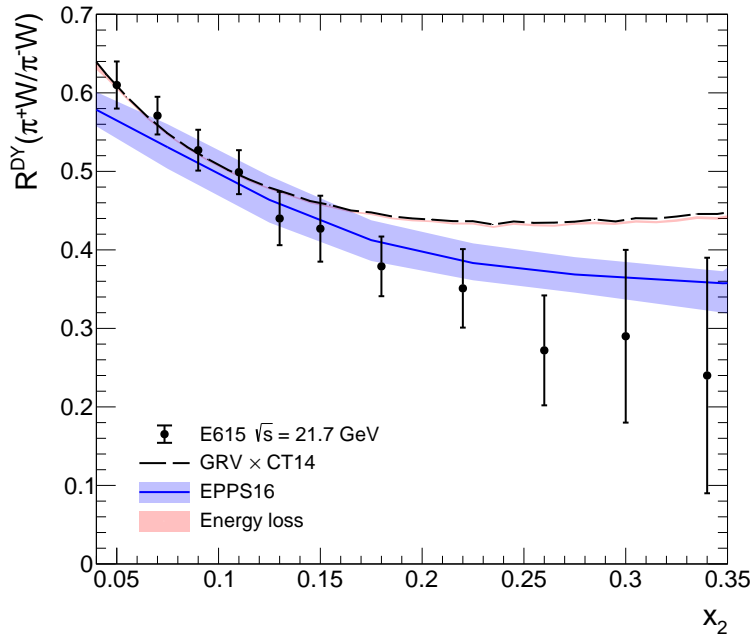
Figure 6.7: Nuclear production ratio measured in π^+W normalised to π^-W collisions at $\sqrt{s} = 21.7$ GeV compared to nPDF effect (blue band) and energy loss effects (red band).

good for all x_2 values except at small $x_2 \sim 0.05$.

The initial-state energy loss effect is suppressed due the SU(2) symmetry in the pion, i.e. $\bar{u}^{\pi^-}(x_1) = \bar{d}^{\pi^+}(x_1) = d^{\pi^-}(x_1) = u^{\pi^+}(x_1)$. As can be seen in Eq. (6.5) the π beam PDF cancel in the ratio, energy loss effects are negligible on this observable.

6.3.6 Discussion about meson PDF at large x

The NA3 collaboration collected DY data on a Pt target with two different meson beams at $\sqrt{s} = 16.7$ GeV: pion and kaon [157]. Figure 6.8 shows the ratio between the DY cross sections in π^-Pt and K$^-$Pt collisions as a function of x_1. At large x_1, the data exhibit a large suppression giving $\sigma_{K^-}^{\mathrm{DY}}/\sigma_{\pi^-}^{\mathrm{DY}} \sim 0.5$. In this x_1 domain, the DY cross section is dominated by the valence quark PDFs from the beam,

$$\sigma_{K^-A}^{\mathrm{DY}} \propto \frac{4}{9}\bar{u}^{K^-}(x_1)\,u^{A}(x_2) + \frac{1}{9}s^{K^-}(x_1)\,\bar{s}^{A}(x_2). \tag{6.7}$$

According to Eq. (2.10) and Eq. (6.7) neglecting the second term, the DY nuclear ratio can be written as

$$\frac{\sigma_{K^-A}^{\mathrm{DY}}}{\sigma_{\pi^-A}^{\mathrm{DY}}} \propto \frac{\bar{u}_{K^-}(x_1)u_A(x_2)}{\bar{u}_{\pi^-}(x_1)u_A(x_2)} \propto \frac{(1-x_1)^{\beta}}{(1-x_1)^{\alpha}}, \tag{6.8}$$

by neglecting $s^{K^-}(x_1)$ at large $x_1 \to 1$. The suppression observed can be interpreted like the $\bar{u}_{K^-}$ PDF is steeper compared to $\bar{u}_{\pi^-}$ PDF, i.e. with $\beta \gtrsim \alpha$. Moreover, at this beam energy, the initial-state energy loss is not negligible. As discussed in Sec. 6.1, the effect of the initial-state energy loss depends on the slope of the beam PDF at large x_1. Consequently, if the slope of the $\bar{u}_{K^-}$ PDF differs compared to the $\bar{u}_{\pi^-}$ PDF, the energy loss effect is not cancelled out in the ratio shown in Fig. 6.8. The suppression observed in these data may be due both to the difference in the slope of the $\bar{u}_{K^-}$ and $\bar{u}_{\pi^-}$ PDFs but also to the initial-state energy loss effect. To quantify the first effect and indirectly the second effect, it is necessary to determine precisely the slope of the pion PDF at large x, but it is still an open topic. Indeed, recent pion PDF extraction study at NLL exhibits a power law at large x like $(1-x)^2$ [158] due to the dominant small $p_\perp$ contribution. Indeed, in this $p_\perp$ region the cross section must be resummed as discussed in Sec. 1.1.5. The global fit at NLO from GRV [30], SMRS [34], JAM [38] or xFitter [159], using DY data to constrain, predict a $(1-x)^{\alpha}$ slope with $\alpha \sim 1$ at large x.

The schematic impact of the initial-state energy loss on the DY process in hA collisions at large x_1 can be written like

$$\sigma_{\mathrm{Eloss}}^{\mathrm{DY}}(x_1) \propto (1 - x_1 + \Delta x_1)^{\alpha}. \tag{6.9}$$

where Δx_1 encodes the initial-state energy loss impact (see Eq. (6.1)). Figure 6.8 (right panel) shows the energy loss suppression at LO as a function of x_F in $R_{K^-\mathrm{Pt}/\pi^-\mathrm{Pt}}$ for an α value fixed at 1 (corresponding to the pion PDF slope) and for different $\beta = (1.1, 1.3, 1.5)$ values. Only the energy loss model is included in this calculation, without nPDF and isospin effects. The energy loss rate is more pronounced in the case where $\beta = 1.5$. The effect is about 10% at $x_F \sim 0.9$. Depending on the slope of $\bar{u}_{K^-}$ at large x, i.e. on the β value, the initial-state energy loss impact varies between 2% to 10% at $x_F \sim 0.9$.
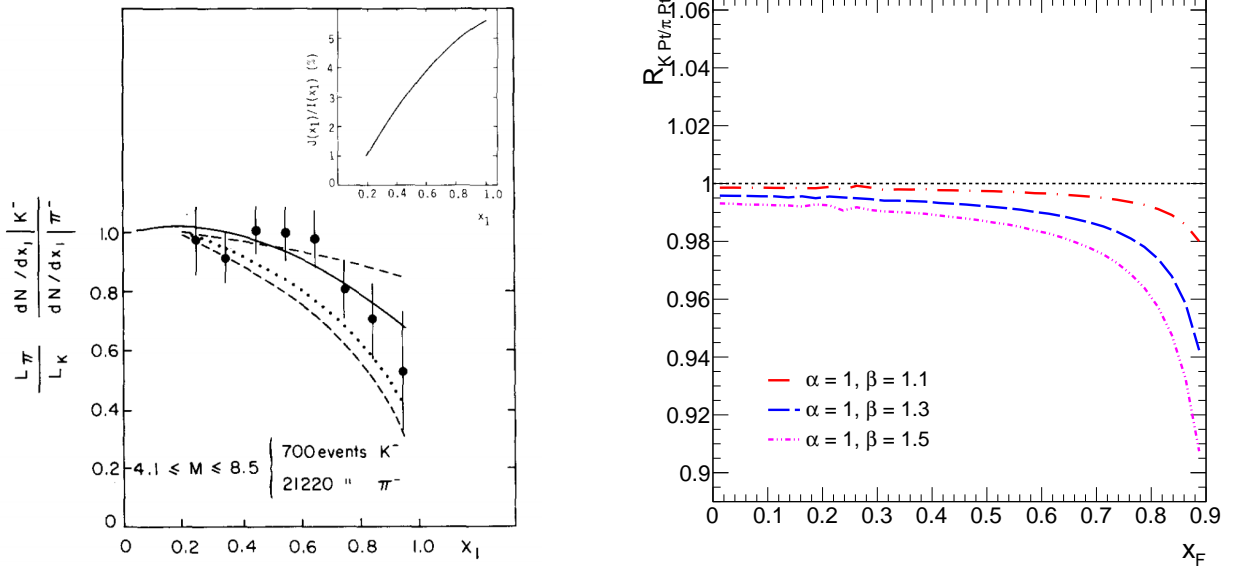
Figure 6.8: DY nuclear production ratio measured in K^-Pt normalised to π^-Pt collisions at $\sqrt{s} = 16.7$ GeV from NA3 experiment [157] (left panel) and the impact of α and β values on the initial-state energy loss model calculation at LO using Pt nucleus at $\sqrt{s} = 16.7$ GeV (right panel).

Consequently, the suppression observed in Fig. 6.8 need to be interpreted by taking into account the initial-state energy loss. In particular, if the slope of $\bar{u}_{K^-}$ is more pronounced at large x_1 compared to $\bar{u}_{\pi^-}$. A cleaner slope extraction will be more safe in light target but in this case, the statistics will be weaker.

6.4 x_2 scaling in Drell-Yan production

In the previous section, we showed that the initial-state energy loss plays an important role in the interpretation of data at low beam energy, typically at $E_{\text{beam}} < 1$ TeV. Preliminary data from E906/SeaQuest show for the first time a clear disagreement with the nPDF calculation. Otherwise, the nPDF calculation exhibits a good agreement with DY data from E866/NuSea. One of the strong hypotheses of the nPDF formalism consists in considering that the QCD factorization is verified at all energies and therefore a proper extraction of the nPDFs is possible. The factorised expression for the DY cross section can be written independently of the center-of-mass energy of the collision. At forward rapidity, we have

$$\begin{aligned}
\frac{\mathrm{d}\sigma(\mathrm{pA})}{\mathrm{d}x_{\mathrm{F}}\,\mathrm{d}M} &\simeq f_q^{\mathrm{p}}(x_{\mathrm{F}}) \times \left(\sum_{j=q,\bar{q},g} \int \mathrm{d}x_2\, f_j^{\mathrm{A}}(x_2) \frac{\mathrm{d}\hat{\sigma}_{qj}}{\mathrm{d}x_{\mathrm{F}}\,\mathrm{d}M}(x_{\mathrm{F}}x_2 s) \right) \\
&\simeq f_q^{\mathrm{p}}(x_{\mathrm{F}}) \times \left(\sum_{j=q,\bar{q},g} f_j^{\mathrm{A}}(x_2) \frac{\mathrm{d}\hat{\sigma}_{qj}}{\mathrm{d}x_{\mathrm{F}}\,\mathrm{d}M}(M^2) \right)
\end{aligned} \tag{6.10}$$

by considering at forward rapidity region, $x_{\mathrm{F}} \sim x_1 \gg x_2$ and $x_2 \approx \hat{s}/(x_{\mathrm{F}}s)$. The DY cross section approximation in Eq. (6.10) depends exclusively on the dimuon invariant mass M.

Consequently, $R_{pA} \propto \sum_j f_j^A(x_2) / \sum_j f_j^B(x_2)$ should exhibit a scaling as a function of x_2, it is independent of the beam energy used to collect the DY data. When M and x_2 are fixed, the value of R_{pA} should be universal.

Figure 6.9 shows R_{pA} data as a function of x_2 for E866/NuSea, E772 and E906 experiments at two different beam energy, respectively $\sqrt{s} = 38.7$ and 15 GeV. A comparison with a NLO DY calculation using the central set of EPPS16 is also shown. The small differences between the calculations are due to the slight energy scale dependence of the nPDF. Indeed, the integrated mass ranges differ from one experiment to another. The calculations show a scaling as a function of x_2 for the 3 experiments. However, the comparison between E866, E772 on the other hand and E906 data on the other hand shows clearly an absence of x_2 scaling at large $x_2 \sim 0.1$. The initial-state energy loss effect is a natural candidate to explain this observation as discussed in Sec. 6.3.
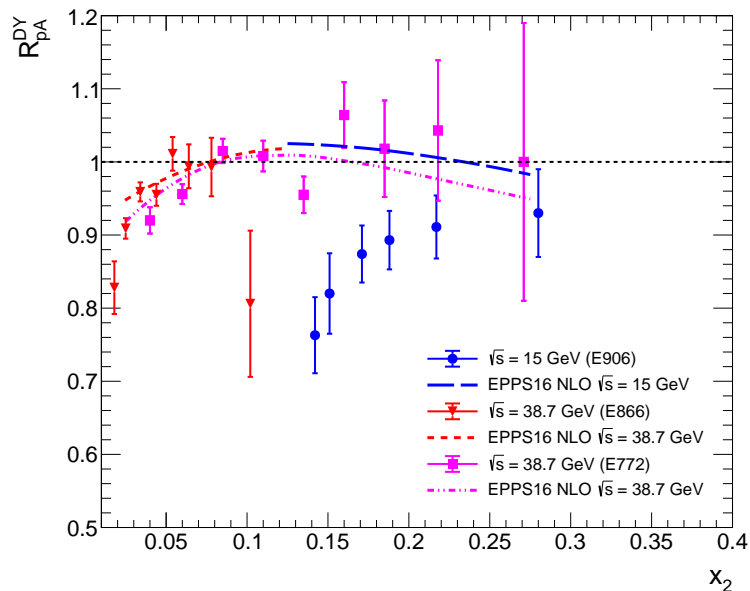
Figure 6.9: Comparison between DY nuclear production ratio measured by E772 [85], E866 [124], E906 [118] and NLO calculation using the central set of EPPS16 nPDF, plotted as a function of x_2.

6.5 Conclusion

The initial-state energy loss effect in DY data in πA and pA collisions at fixed-target energy were investigated based on the BDMPS formalism. A systematic comparison with the most recent PDF of EPPS16 was also shown. The main conclusions are

- Preliminary DY data from E906/SeaQuest in pA collisions exhibiting a large suppression in R_{pA} (W/C) and R_{pA} (Fe/C) disagree with nPDF expectations. The initial-state energy loss model reproduces qualitatively the data suppression slope, especially for the W target. These data highlight for the first time a strong indication in favor of the initial-state energy loss effect. On the other hand, the absence of scaling as a function of x_2 observed when

comparing the E866, E772 and E906 data also indicates that an effect, other than the nPDF, is at work;

- The DY data from E866/NuSea show that at a beam energy of 800 GeV, the initial energy loss effect becomes negligible, $\langle \epsilon \rangle_{\mathrm{LPM}}/E \rightarrow 0$. Except at very large $x_{\mathrm{F}} \sim 0.8\text{-}0.9$, a region in which it is necessary to take this effect into account. In general, these data are relevant to extract nPDFs in a clean way;

- The DY data in $\pi \mathrm{A}$ are less suitable for easily demonstrating the initial-state energy loss. Indeed, due to the fact that the slope of the pion PDF at large x is less steep than that of the proton, the energy loss effect in these collisions is less pronounced. Apart from this point, the DY data from the NA10 experiment show that it was necessary to take into account the energy loss effect in the interpretation of the data. This effect has a magnitude similar to that of the nPDF contribution. The preliminary DY data from the COMPASS experiment exhibit a suppression at large $x_{\mathrm{F}} \gtrsim 0.8$ whose amplitude is compatible (for the suppression slope) with the initial-state energy loss effect. However, a difference of 20% in the normalization persists between the calculations and the preliminary data.

- The AFTER collaboration projects to collect DY data in a range at high enough rapidity to be able to constrain EMC, anti-shadowing and shadowing effects. The energy loss model predicts in the most backward rapidity region an effect of around 10%. The magnitude of the effect is comparable to the expected nPDF effect in this region. It is therefore necessary to take this effect into account in order to be able to perform a clean and relevant nPDF extraction;

- The PDF extraction of mesons at large x is performed mainly using the DY nuclear data on heavy nucleus for better statistics. However, the initial-state energy loss plays a significant role that must be taken into account.

7

Transverse momentum broadening effect in world data

Contents

When a parton enters in a QCD medium, it interacts via multiple scattering inducing radiative energy loss and broadening effects. The first effect was investigated in Chap. 6. The main goal of this chapter is to analyse the nuclear broadening using available Drell-Yan (DY) and quarkonium data in pA and πA collisions. The simple observable in order to study the nuclear broadening effect value in hA collisions reads

$$\Delta p_\perp^2 = \left\langle p_\perp^2 \right\rangle_{\mathrm{hA}} - \left\langle p_\perp^2 \right\rangle_{\mathrm{hp}} . \tag{7.1}$$

This analysis of all of this data will allow to (i) extract the transport coefficient value and (ii) probe the saturation scale in large nuclei and its energy dependence. This chapter is based on an article published in *Journal of High Energy Physics (JHEP)* prepared jointly with François Arleo [2].

7.1 Model

7.1.1 Broadening definition

The total momentum broadening acquired by a parton (in color representation R) traversing a length L in a nuclear medium is given by Eq. (2.34)

$$\Delta p_\perp^2 = \hat{q}_R L, \tag{7.2}$$

where $\hat{q}_R$ is the transport coefficient introduced in Eq. (6.2). By defining $\hat{q}$ as the transport coefficient of a gluon, the broadening expression becomes

$$\Delta p_\perp^2 = \frac{C_R}{N_c} \hat{q} L, \tag{7.3}$$

where C_R is the color charge of the parton crossing the nuclear medium ($C_R = C_F = 4/3$ for a quark and $C_R = N_c = 3$ for a gluon). In practice, the value of the broadening obtained in
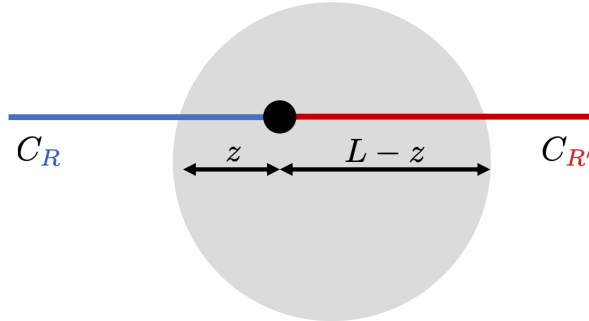
Figure 7.1: Sketch of the nuclear broadening at small coherence length.

hA collisions compared to hB collisions, where B is the reference target, is simply

$$\Delta p_\perp^2 = \frac{C}{N_c} (\hat{q}_A L_A - \hat{q}_B L_B) \tag{7.4}$$

where $\hat{q}_A$ and $\hat{q}_B$ are respectively the transport coefficient of the nucleus A and B.[1] The nuclear length $L = 3/2R$ is calculated assuming the hard sphere approximation with $R = 1.12 \times A^{1/3}$ fm. The color factor C corresponds to the average value of the color state of the initial (C_R) and final partonic states ($C_{R'}$) [160],

$$C = \frac{C_R + C_{R'}}{2}. \tag{7.5}$$

---

[1]In the case of pp collisions, the value of $\hat{q}_p L_p$, although small, due to the proton medium is obtained by taking, L_p=1.5 fm. [3, 4].

7.1.2 Coherence length

The length L appearing in Eq. (7.4) is sensitive to the coherence length of the hard process, $\ell_{\mathrm{coh}} \sim 1/(2m_p x)$, where $m_p \approx 1$ GeV is the proton mass, to resolve the size of the QCD medium. At high-energy, the choice of the medium length crossed by a color charge is delicate because $\ell_{\mathrm{coh}} \gg L$.

The limit kinematic domain in which $\ell_{\mathrm{coh}} \sim L$ corresponds to the PHENIX experiment [125] case. Depending on the rapidity region, the coherence length is of the same order or even greater than the length of a heavy nucleus $L \sim 10$ fm (see Table 7.1). In the remainder of the analysis, the low energy picture from Eq. (7.5) will be assumed to the high energy case.

Experiment.	y range	x_2 range	ℓ_{coh} range (fm)
PHENIX	$-2.2 < y < -1.2$	$0.10 \lesssim x_2 \lesssim 0.05$	$1.0 \lesssim \ell_{\mathrm{coh}} \lesssim 2.0$
	$|y| < 0.35$	$0.01 \lesssim x_2 \lesssim 0.02$	$4.8 \lesssim \ell_{\mathrm{coh}} \lesssim 10$
	$1.2 < y < 2.2$	$2 \times 10^{-3} \lesssim x_2 \lesssim 5 \times 10^{-3}$	$23 \lesssim \ell_{\mathrm{coh}} \lesssim 61$

Table 7.1: Coherence length ℓ_{coh} for the intermediate beam energy at the PHENIX experiment [125].

7.1.3 Hard processes

7.1.3.a Drell-Yan production

In the DY process at LO, the (anti-)quark of a color charge C_{F} coming from the beam and crossing the nuclear medium undergoes a nuclear broadening effect. The virtual photon produced is colourless, i.e. $C_{\mathrm{R'}} = 0$. It doesn't contribute to the total broadening momentum induced by the medium. Consequently the total color charge for the DY process appearing in Eq. (7.4) is $\mathcal{C}^{\mathrm{DY}} = C_F/2$.

However, the Compton process $qg \to q\gamma^\star$ contributes to the DY cross section at NLO. It can modify the nuclear broadening due to the incident gluon of a color charge N_c. We note that the DY data used in this chapter were measured at small $p_\perp \lesssim M$ where a significant contribution from the Compton process is not expected. In addition, at positive x_{F} values, this process is dominated by the scattering of an incoming quark from the beam hadron as discussed in Sec. 2.1.3.

7.1.3.b Quarkonium production

Quarkonium production describes the annihilation of two partons in the initial state followed by the production of a heavy-quark pair $Q\bar{Q}$ pair in the final state. Thus, the broadening effect in quarkonium production at low coherence length originates from two partonic states: (i) the color of the initial partonic state and (ii) from the color of the $Q\bar{Q}$ pair produced in the final state.

First, as discussed in Sec. 2.1.4, as much the initial partonic state in pA collisions is clear, i.e. gluon fusion ($C_{\mathrm{R}} = 3$), in πA collisions the question remains open. In the latter, depending on both the production model and also the pion PDF, the dominant partonic channel can be

gg either or $q\bar{q}$. In this analysis and according to the Fig. 2.3, the $q\bar{q}$ channel is considered as dominant in the quarkonium production cross section in πA collisions ($C_{\mathrm{R}} = 4/3$).

Secondly, in the final state, the $Q\bar{Q}$ pair can be produced in a *singlet* ($C_{\mathrm{R'}} = 0$) or *octet* ($C_{\mathrm{R'}} = 3$) color state depending on the production model. In the CEM or the NRQCD, the $Q\bar{Q}$ pair is essentially produced in an *octet* color state. Consequently, the $Q\bar{Q}$ pair must neutralize its color before hadronizing[2], i.e. $\ell_8 \gg \ell_{Q\bar{Q}}$, where ℓ_{had} and $\ell_{Q\bar{Q}}$ are respectively the hadronisation and coherence lengths. Whilst in the CSM model, the $Q\bar{Q}$ is already produced in a *singlet* color state, i.e. $\ell_1 \sim \ell_{Q\bar{Q}}$. In this study, we assume that the $Q\bar{Q}$ pair is produced mainly in a color octet state during its propagation throughout the nucleus, but the *singlet* picture will be investigated too.

Table 7.2 summarises the color factors used for the DY and quarkonium in *octet* and *singlet* production in πA and pA collisions.

Process	Collision	$\mathcal{C}$
DY	πA/ pA	$C_F/2$
Quarkonium	πA	$(C_F + N_c)/2$
Quarkonium	pA	N_c
Quarkonium (*singlet*)	πA/ pA	$N_c/2$

Table 7.2: Color factors used for the DY and quarkonium in *octet* and *singlet* production in πA and pA collisions.

7.2 Extraction of the nuclear broadening from data

7.2.1 Data

The present analysis includes world quarkonium data from fixed-target (NA3, NA10 and E772) to collider (PHENIX, ALICE and LHCb) energies for different rapidity domains and projectiles (π and p hadron beams). In addition, DY data from NA10 and E772 are included in this analysis. The forward data at RHIC ($1.2 < y < 2.2$) and at LHC ($2 < y < 4$ for LHCb experiment) probe smallest x_2 values, $x_2 \approx 3 \times 10^{-3}$ and $x_2 \approx 2 \times 10^{-5}$, respectively. These data investigate the x-dependence of the transport coefficient in Eq. (6.2). A factor of 400 in $\sqrt{s}$ is observed between the data from SPS to LHC energies.

7.2.2 Method extraction

By definition, the average transverse momentum squared in Eq. (7.1) is defined as

$$\left\langle p_\perp^2 \right\rangle = \left(\int_0^\infty \mathrm{d}p_\perp p_\perp^2 \frac{\mathrm{d}\sigma}{\mathrm{d}p_\perp} \right) / \left(\int_0^\infty \mathrm{d}p_\perp \frac{\mathrm{d}\sigma}{\mathrm{d}p_\perp} \right). \tag{7.6}$$

---

[2]For example in the CEM model at LO, the $Q\bar{Q}$ pair produced in color *octet* state neutralizes its color by emitting a gluon before being hadronized, $Q\bar{Q} \to g + J/\psi$.

Exp.	Proj.	Target	$\sqrt{s}$ (GeV)	Process	Ref.
NA3	p	Pt	19.4	J/ψ	[120]
	π^-	Pt	16.8/19.4/22.9	J/ψ	
	π^+	Pt	19.4	J/ψ	
NA10	π^-	W	16.2/23.2	DY	[122]
	π^-	W	23.2	J/ψ	
E772	p	Ca, Fe, W	38.7	DY	[123]
	p	Ca, Fe, W	38.7	Υ	
PHENIX	d	Au	200	J/ψ	[125]
ALICE	p	Pb	5020	J/ψ	[126]
LHCb	p	Pb	8160	J/ψ	[128]

Table 7.3: Data sets included in the present analysis.

Due to the finite $p_\perp$ acceptance of each experiment, it is not possible to integrate the $p_\perp$ cross section up to infinity. The integral is then approximated by performing a summation over the set of experimental bins as

$$\left\langle p_\perp^2 \right\rangle_{\text{bins}} = \left(\sum_{i=1}^{N_{\text{bins}}} \Delta p_\perp^i \times \left(\hat{p}_\perp^i \right)^2 \frac{\mathrm{d}\sigma^i}{\mathrm{d}p_\perp} \right) \Big/ \left(\sum_{i=1}^{N_{\text{bins}}} \Delta p_\perp^i \times \frac{\mathrm{d}\sigma^i}{\mathrm{d}p_\perp} \right), \tag{7.7}$$

where $\Delta p_\perp^i$ is the bin width, $\hat{p}_\perp^i$ the typical $p_\perp$ value in that bin width and $\frac{\mathrm{d}\sigma^i}{\mathrm{d}p_\perp}$, the measured cross section of the bin i. This method has its limits. Indeed, the value of the $\hat{p}_\perp^i$ chosen depends on the width of the experimental bin. In the case where the experimental bin is large, opting for a value of $p_\perp$ corresponding to the median $p_\perp$ value does not take into account the cross section behaviour in the bin. The solution to this problem is to take the mean $p_\perp$ value in each experimental bin. In order to determine the mean $\hat{p}_\perp^i$ value, the cross section is fitted using the *Kaplan* function defined as

$$\frac{\mathrm{d}\sigma_{\text{fit}}\left(p_\perp\right)}{p_\perp \mathrm{d}p_\perp} = \mathcal{N} \left(\frac{p_0^2}{p_0^2 + p_\perp^2} \right)^m \tag{7.8}$$

where m and p_0 are the only two relevant parameters due to the fact that $\langle p_\perp^2 \rangle$ is independent of the cross section normalisation. Thanks to this method, the definition in Eq. (7.6) can be used.

PHENIX experiment

The PHENIX collaboration published $\Delta p_\perp^2$ values for J/ψ production in pp and dAu collisions at $\sqrt{s} = 200$ GeV for different bins in rapidity [125] (see Table 7.1). By using the absolute cross section published in pp and dAu collisions [125, 66] and Eq. (7.7) including the median $p_\perp$ value, the nuclear broadening values quoted in [125] are recovered. However, since the experimental

bins at $p_\perp \gtrsim 5$ GeV are large, it is necessary to take into account the average $p_\perp$ value in Eq. (7.7). In this case, the value of broadening changes significantly (5% of difference at backward and forward rapidity and 10% at mid rapidity). In order to avoid the dependence in the choice of the $p_\perp$ value appearing in Eq. (7.7), the data are fitted using the Kaplan parametrization Eq. (7.8). The broadening values are summarised in Table 7.4.

ALICE experiment

The ALICE collaboration published $\Delta p_\perp^2$ values for J/ψ production in pp and pPb collisions at $\sqrt{s} = 5.02$ TeV at backward, $-4.46 < y < -2.96$ and forward $2.03 < y < 3.53$ rapidity. In pPb collisions system, the $\Delta p_\perp^2$ values are published for different bins in centrality [126]. In order to calculate the integrated broadening for the whole domain of centrality, the $\langle p_\perp^2 \rangle_{\mathrm{pPb}}$ value reads

$$\left\langle p_\perp^2 \right\rangle_{\mathrm{pPb}} = \sum_{\mathcal{C}} \left\langle p_\perp^2 \right\rangle_{\mathcal{C}} \sigma_{\mathcal{C}} / \sum_{\mathcal{C}} \sigma_{\mathcal{C}} \tag{7.9}$$

where $\sigma_{\mathcal{C}}$ is the J/ψ integrated absolute cross section measured in centrality bin $\mathcal{C}$. Furthermore, it has been checked beforehand that by using Eq. (7.8), the $\langle p_\perp^2 \rangle_{\mathrm{pp}}$ value obtained are consistent with those published [126]. The broadening values extracted are summarised in Table 7.4.

LHCb experiment

Finally, LHCb collaboration published absolute cross sections for J/ψ production in pp and pPb collisions at $\sqrt{s} = 8.16$ GeV at backward, $-4.5 < y < -2.5$ and forward $2 < y < 4$ rapidity. The nuclear broadening value is again calculated by performing the *Kaplan fit* using Eq. (7.8).

Experiment	y range	$\Delta p_\perp^2$ (GeV^2)
PHENIX	$-2.2 < y < -1.2$	0.43 ± 0.08
	$|y| < 0.35$	0.71 ± 0.20
	$1.2 < y < 2.2$	0.43 ± 0.08
LHCb	$-4.5 < y < -2.5$	0.79 ± 0.12
	$2 < y < 4$	2.05 ± 0.12
ALICE	$-4.46 < y < -2.96$	0.68 ± 0.33
	$2.03 < y < 3.53$	1.91 ± 0.42

Table 7.4: Determination of $\Delta p_\perp^2$ from PHENIX, LHCb and ALICE measurements.

7.2.3 Uncertainty of the broadening calculation

The uncertainty on the broadening value for the bin method in Eq. (7.7) is

$$\left\langle p_\perp^2 \right\rangle_{\mathrm{err}} = \sqrt{\left[\sum_{i=1}^{N_{\mathrm{bins}}} \left(\frac{(p_\perp^i)^2 \Delta p_\perp^i}{\sigma_{\mathrm{tot}}^\alpha} + \frac{\sigma_{\mathrm{tot}}^\beta}{\sigma_{\mathrm{tot}}^\alpha} \right)^2 (\sigma^i)^2 \right]}, \tag{7.10}$$

where $\Delta p_\perp^i$ is the width of the $p_\perp$ bin i, σ^i the experimental error in the bin i and

$$\sigma_{\text{tot}}^\alpha = \sum_{i=1}^{N_{\text{bins}}} \left[\left(\frac{\mathrm{d}\sigma}{\mathrm{d}p_\perp} \right)^i \Delta p_\perp^i \right], \tag{7.11}$$

and

$$\sigma_{\text{tot}}^\beta = \sum_{i=1}^{N_{\text{bins}}} \left[\left(\frac{\mathrm{d}\sigma}{\mathrm{d}p_\perp} \right)^i (p_\perp^i)^2 \Delta p_\perp^i \right]. \tag{7.12}$$

The uncertainty calculation using the *Kaplan method* in Eq. (7.8) depends on two correlated parameters m and p_0. The error calculation reads

$$\left\langle p_\perp^2 \right\rangle_{\text{Kaplan}}^{\text{err}} \approx \sqrt{\left[\left(\frac{\partial}{\partial p_0} \left(\frac{\mathrm{d}\sigma_{\text{fit}}}{\mathrm{d}p_\perp} \right) \right)^2 \delta p_0^2 + \left(\frac{\partial}{\partial m} \left(\frac{\mathrm{d}\sigma_{\text{fit}}}{\mathrm{d}p_\perp} \right) \right)^2 \delta m^2 - 2 \left(\frac{\partial}{\partial p_0} \left(\frac{\mathrm{d}\sigma_{\text{fit}}}{\mathrm{d}p_\perp} \right) \right) \left(\frac{\partial}{\partial m} \left(\frac{\mathrm{d}\sigma_{\text{fit}}}{\mathrm{d}p_\perp} \right) \right) \sigma_{p_0,m} \right]} \tag{7.13}$$

where $\sigma_{p_0,m}$ is the covariance matrix given by the fit. The partial derivatives are

$$\frac{\partial}{\partial m} \left(\frac{\mathrm{d}\sigma_{\text{fit}}}{\mathrm{d}p_\perp} \right) = \frac{-p_0^2}{(-2+m)^2} \tag{7.14}$$

and

$$\frac{\partial}{\partial p_0} \left(\frac{\mathrm{d}\sigma_{\text{fit}}}{\mathrm{d}p_\perp} \right) = \frac{2p_0}{-2+m}. \tag{7.15}$$

The uncertainty values quoted in Table 7.4 are calculated with Eq. (7.13).

7.3 Extraction of the transport coefficient $\hat{q}_0$

7.3.1 Global fit

A global fit of the world nuclear broadening data summarized in Tables 7.3 and 7.4 is performed by using the $\hat{q}$ transport coefficient modelled as in Chap. 6. The broadening expression in Eq. (7.4) by using the simple power law of $xG(x) \propto x^{-\alpha}$ can be written as

$$\Delta p_\perp^2 = \frac{\hat{q}_0}{N_c} \times \left(\frac{10^{-2}}{x} \right)^\alpha \times \mathcal{C}\Delta L; \quad \Delta L = L_A - L_p' \tag{7.16}$$

where $\hat{q}_0$ is the transport coefficient at $x = 10^{-2}$ and the $\mathcal{C}$ color factor values from Table 7.2. According to Eq. (6.2),

$$L_p' = L_p \left(\frac{\min(x_A, x_2)}{\min(x_p, x_2)} \right)^\alpha. \tag{7.17}$$

At $x_2 \lesssim x_A$, namely at PHENIX (mid and forward rapidity) and LHC energies, the transport coefficient is sensitive to the parameter α of $xG(x)$. The transverse momentum broadening values induced by the nuclear medium for the DY, J/ψ and Υ processes in πA and pA collisions as a function of $\mathcal{C}\Delta L/x^\alpha$ in *octet* (left panel) and in *singlet* (right panel) pictures is shown Fig. 7.2. All the data follow a linear function showing remarkable scaling despite a factor
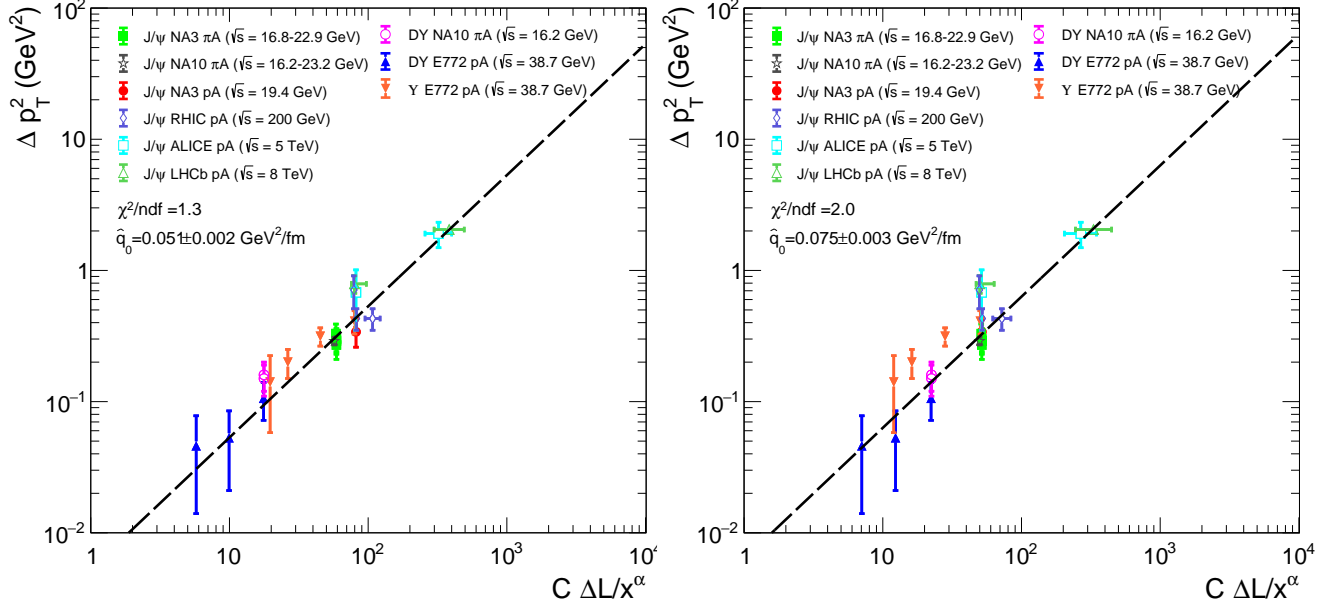
Figure 7.2: Scaling of the nuclear $p_\perp$-broadening in DY and quarkonium production in *octet* and *singlet* state to the left and the right panel respectively using the color assumptions in Table 7.2.

of 400 in $\sqrt{s}$ when going from SPS to LHC energies. The main part of the data is located in a x_2 domain where $x = \min(x_A, x_2) = x_A$.

The best fits in *octet* and *singlet* pictures give, respectively, $\hat{q}_0 = 0.051 \pm 0.02$ GeV^2/fm ($\alpha = 0.25 \pm 0.01$) and $\hat{q}_0 = 0.075 \pm 0.03$ GeV^2/fm ($\alpha = 0.30 \pm 0.02$). The χ^2/ndf obtained from the fit assuming the prevalence of the *singlet* state in the quarkonium production exhibits a degraded value (χ^2/ndf =2.0) compared to the *octet* state hypothesis (χ^2/ndf =1.3). Finally, an additional fit is performed excluding the nuclear broadening data[3] for which the $\ell_{\text{coh}} \gtrsim L/2$ in order to highlight the non-dependence on our assumptions on the extraction of the $\hat{q}_0$ transport coefficient. The value of the $\hat{q}_0$ transport coefficient doesn't change significantly, less than 2% in both pictures. Fit results are shown in Table 7.5.

	Data set	$\hat{q}_0$ (GeV^2/fm)	α	χ^2/ndf
Color *octet*	All	0.051 ± 0.002	0.25 ± 0.01	1.3
	$\ell_c < L/2$	0.050 ± 0.002	(0.25)	0.8
Color *singlet*	All	0.075 ± 0.003	0.30 ± 0.02	2.0
	$\ell_c < L/2$	0.074 ± 0.003	(0.30)	1.3

Table 7.5: Results of the fits to all and selected ($\ell_c < L/2$) data sets, assuming color *octet* or color *singlet* $Q\bar{Q}$ production.

An extraction of $\hat{q}_0$ is performed individually, using the value of the broadening of each experiment. The result is shown in Fig. 7.3. The agreement is overall very satisfactory. However, some tensions can be observed especially for the backward point of the LHCb experiment.

---

[3]Namely PHENIX mid/backward rapidity and LHC data.
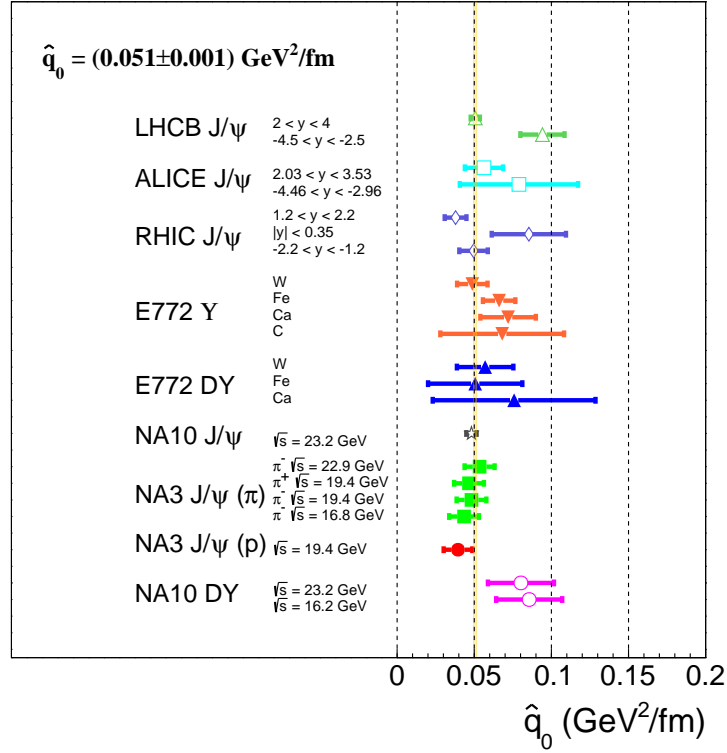
Figure 7.3: Extracted values of $\hat{q}_0$ from each measurement of $\Delta p_\perp^2$. Experiments are plotted in descending order of $\sqrt{s}$ energy, data points in ascending order of atomic number (E772) and rapidity (PHENIX, ALICE, LHCb).

7.3.2 Nuclear broadening from the COMPASS experiment

Nuclear broadening from the Drell-Yan process

The preliminary DY broadening value between the W and the Al targets from the COMPASS experiment at $\sqrt{s} = 18.9$ GeV is equal to $\Delta p_\perp^2 = 0.03 \pm 0.04$ GeV^2 (see Chap. 5). It is possible to compare the experimental value obtained with the expected nuclear broadening value following Sec. 7.1.

The typical $\langle x_2 \rangle$ value of DY COMPASS data is 0.19. Consequently, the transport coefficient is frozen according to Eq. (6.2). By taking $L_W = 9.55$ fm and $L_{Al} = 5.04$ fm, the DY expected value of broadening, using the central value of the transport coefficient from Fig. 7.2 in the *octet* picture, i.e. $\hat{q}_0 = 0.051$ GeV^2, is equal to $\Delta p_\perp^2 = 0.06$ GeV^2. Whereas, the $\hat{q}_0$ value from the *singlet* picture leads to a nuclear broadening value slightly larger, $\Delta p_\perp^2 = 0.09$ GeV^2. Table 7.6 summarizes the nuclear broadening values from the NA10 and E772 experiments. Compared to previous experiments, the value of DY nuclear broadening obtained at COMPASS is significantly lower. Indeed, the effects of broadening in the Al target are not negligible. If the reference target had been a light target, typically a hydrogen target, the broadening value would have been equal to $\Delta p_\perp^2 = 0.09$ GeV^2. The preliminary broadening value extracted via the DY analysis at COMPASS in Chap. 5 is compatible with the expected theoretical value calculated based on the quarkonium production model dominated by the *octet* state.

Exp.	Proj.	Targets	$\sqrt{s}$ (GeV)	$\Delta p_\perp^2$	Ref.
NA10	π	D, W	16.2	0.15 ± 0.03	[122]
	π	D, W	23.2	0.16 ± 0.03	
E772	p	H, W	38.7	0.106 ± 0.034	[123]
COMPASS	π	Al, W	18.9	0.03 ± 0.04	Chap. 5

Table 7.6: DY broadening values from NA3, E772 and COMPASS experiments.

Nuclear broadening from the J/ψ process

The preliminary J/ψ broadening value between W and Al targets from the COMPASS experiment at $\sqrt{s} = 18.9$ GeV is equal to $\Delta p_\perp^2 = 0.21 \pm 0.04$ GeV^2 (see Sec. 2.1.4). The typical $\langle x_2 \rangle$ value of the J/ψ COMPASS data is ~ 0.1.[4] Consequently, the transport coefficient is also frozen according to Eq. (6.2), compared to DY data. The expected value of nuclear broadening, using the central value of transport coefficient from Fig. 7.2 in the *octet* picture ($\hat{q}_0 = 0.051$ GeV^2) leads to $\Delta p_\perp^2 = 0.18$ GeV^2 while the $\hat{q}_0$ value from the *singlet* picture leads to a nuclear broadening value clearly larger, $\Delta p_\perp^2 = 0.28$ GeV^2. The preliminary COMPASS nuclear broadening value for the J/ψ process is compatible with the expected value in the *octet* picture.

The broadening value expected at the COMPASS experiment if the reference target for COM-PASS had been a light target, typically a hydrogen target[5], would have been equal to $\Delta p_\perp^2 = 0.30$ GeV^2.

Exp.	Proj.	Targets	$\sqrt{s}$ (GeV)	$\Delta p_\perp^2$ (GeV^2)	Ref.
NA10	π	D, W	23.2	0.29 ± 0.02	[122]
NA3	π	H, Pt	16.8	0.27 ± 0.06	[120]
	π	H, Pt	19.3	0.30 ± 0.06	
	π	H, Pt	19.3	0.29 ± 0.06	
	π	H, Pt	22.9	0.33 ± 0.06	
	p	H, Pt	19.3	0.34 ± 0.08	
COMPASS	π	Al, W	18.9	0.21 ± 0.04	Chap. 4

Table 7.7: J/ψ broadening values from NA3 and NA10 experiments.

Finally, Fig. 7.4 shows that the preliminary values of the $\hat{q}_0$ transport coefficient extracted from the COMPASS experiment from the DY and J/ψ processes are in line with the global fit results shown above.

7.4 nPDF and radiative energy loss effects

The nuclear broadening is independent of the normalization of the cross section in pA and πA collisions. However, radiative energy loss and nPDF effects can distort the $p_\perp$-spectra. The

---

[4]This value is determined by using $\langle x_F \rangle = 0.20$ from Sec. 4.4.2, $x_F \simeq 2M_{J/\psi}/\sqrt{s} \times \sinh y$ and $x_2 \approx M/\sqrt{s} \times e^{-y}$ definitions.

[5]$L_H = 1.5$ fm is used.
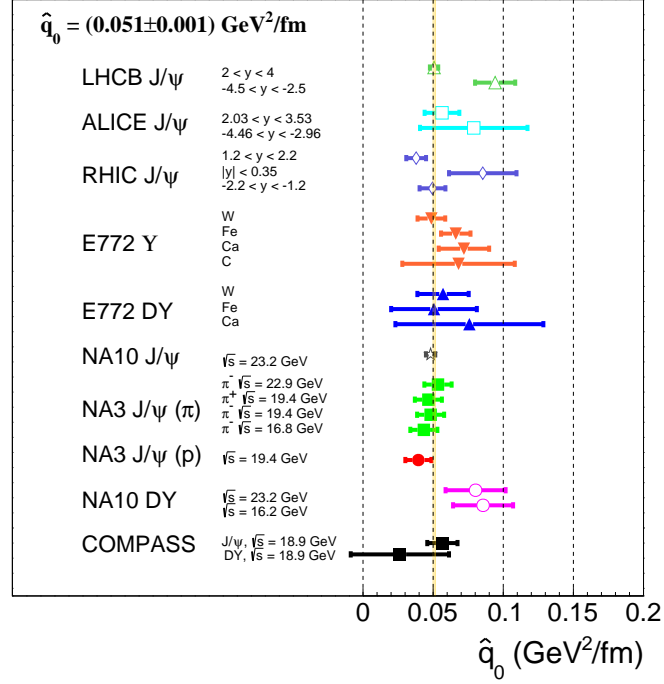
Figure 7.4: Extracted values of $\hat{q}_0$ from each measurement of $\Delta p_\perp^2$ including preliminary results from the COMPASS experiment (in black). Experiments are plotted in descending order of $\sqrt{s}$ energy, data points in ascending order of atomic number (E772) and rapidity (PHENIX, ALICE, LHCb).

initial-state energy loss in fixed-target DY data in hA collisions exhibits a tiny effect, except at large x_F (see Chap. 6). This effect therefore doesn't have an impact on the DY nuclear broadening.

Nevertheless, the Fully Coherent Energy Loss (FCEL) affects the quarkonium $p_\perp$-spectrum.[6] Indeed, the average FCEL energy loss is suppressed at large $p_\perp \gtrsim M$, $\langle\epsilon\rangle^{\text{FCEL}} \propto 1/M_\perp$.

Finally, the nPDF effect, when $p_\perp \lesssim M$, depends slightly on $p_\perp$ and shows a constant contribution affecting only the normalisation of R_{pA}. At PHENIX and LHC energies, when $p_\perp \gtrsim M$, the nPDF can affect the slope of the $p_\perp$-spectra.

In order to quantify the FCEL and nPDF effects in the quarkonium production at RHIC and LHC energies, the cross section in pA collisions can be modelled as

$$\frac{1}{A}\frac{\mathrm{d}\sigma_{\text{pA}}^{\text{FCEL}}(p_\perp, y)}{\mathrm{d}p_\perp\,\mathrm{d}y} = R_{\text{pA}}^{\text{FCEL}}(p_\perp, y) \times \frac{\mathrm{d}\sigma_{\text{pp}}(p_\perp, y)}{\mathrm{d}p_\perp\,\mathrm{d}y}, \tag{7.18}$$

$$\frac{1}{A}\frac{\mathrm{d}\sigma_{\text{pA}}^{\text{nPDF}}(p_\perp, y)}{\mathrm{d}p_\perp\,\mathrm{d}y} = R_g^A\left(x_2 = \frac{M_\perp + p_\perp}{\sqrt{s}}e^{-y}, Q = M_\perp + p_\perp\right) \times \frac{\mathrm{d}\sigma_{\text{pp}}(p_\perp, y)}{\mathrm{d}p_\perp\,\mathrm{d}y}.$$

The FCEL effect in quarkonium production is computed from [4] and the nPDF effect by using the gluon nuclear modification factor R_g^A from EPPS16 [78]. In order to take into account the region at large $p_\perp \gtrsim M$, the calculations are performed by considering a $2 \to 2$ kinematics. The double differential cross section of J/ψ production in pp collisions is parametrized as [129]

$$\frac{\mathrm{d}\sigma_{\text{pp}}(p_\perp, y)}{\mathrm{d}y\mathrm{d}p_\perp} \propto p_\perp \times \left(\frac{p_0^2}{p_0^2 + p_\perp^2}\right)^m \times \left(1 - \frac{2M_\perp}{\sqrt{s}}\cosh y\right)^n, \tag{7.19}$$

---

[6]In fixed-target data, $p_\perp \lesssim M$, the FCEL affects only the normalisation of the R_{pA} as a function of $p_\perp$ [129].

where the values of $\mathcal{N}$, n, m and p_0 parameters were extracted from the LHC data in [129]. Figure 7.5 shows the FCEL and the EPPS16 nPDF effects at backward (left panel) and forward (right panel) rapidities at LHCb energy ($\sqrt{s} = 8160$ GeV). The FCEL calculation, in both rapidity ranges, exibits a constant R_{pA} for $p_\perp \gtrsim 5$ GeV. For $p_\perp \lesssim M$, R_{pA} shows a small depletion, more accentuated at forward compared to backward rapidity. The nPDF calculation also shows a $R_{\mathrm{pA}} \lesssim 1$ increasing as a function of $p_\perp$ (x_2) due to the shadowing effect at forward rapidity. At backward rapidity, the R_{pA} slightly increases and decreases around 1 as a function of $p_\perp$ mainly due to the anti-shadowing and EMC regions.[7]

The impact of these effects on the broadening calculation using Eq. (7.18) in PHENIX and LHC data is summarized in Table 7.8. Although the FCEL and nPDF effects (with a large

Experiment	System	y range	$\Delta p_\perp^2\big|_{\mathrm{FCEL}}$ (GeV^2)	$\Delta p_\perp^2\big|_{\mathrm{nPDF}}$ (GeV^2)
PHENIX	dAu	$-2.2 < y < -1.2$	0.1	[-0.2 ; 0]
	dAu	$|y| < 0.35$	0.1	[0.1 ; 0.4]
	dAu	$1.2 < y < 2.2$	0.1	[0.1 ; 0.4]
LHCb	pPb	$-4.5 < y < -2.5$	0.2	[0.1 ; 0.6]
	pPb	$2 < y < 4$	[0.5 ; 0.6]	[0.1 ; 0.7]

Table 7.8: Calculation of $\Delta p_\perp^2\big|_{\mathrm{FCEL}}$ and $\Delta p_\perp^2\big|_{\mathrm{nPDF}}$ at RHIC and LHC.

uncertainty) may impact the nuclear broadening value of the J/ψ process, the results show a weak effect. This shows that nuclear broadening is the dominant effect in the data. Furthermore, a strong correlation coefficient (0.7) for each EPPS16 error set in the broadening calculation interval is observed between backward and forward rapidity at LHC. A better constraint of nPDFs in one of these two ranges in rapidity will impact them in the same way.

7.5 Relation between the broadening and the gluon distribution

The transport coefficient $\hat{q}$ is directly related to the gluon distribution $xG(x)$ of the nucleon in Eq. (6.2). It is therefore possible to use recent PDFs of the proton in order to test the relationship between $\hat{q}$ and $xG(x)$ and also their scale dependence. From Eq. (7.4) and Eq. (6.2), the broadening reads

$$\Delta p_\perp^2 \propto \mathcal{C}\alpha_s\left(Q^2\right)\left[xG\left(x,Q^2\right)L_{\mathrm{A}} - x'G\left(x',Q^2\right)L_{\mathrm{p}}\right] \equiv \mathcal{C}\alpha_s\Delta(xGL). \quad (7.20)$$

The scale Q^2 appearing in Eq. (7.20) should be of the order of magnitude of $\Delta p_\perp^2$. At low-scales[8], $\Delta p_\perp^2 \lesssim 1$ GeV^2, Q^2 is frozen at the input scale[9] of the proton PDF, according to $Q^2 = \min\left(Q_0^2, \lambda\Delta p_\perp^2\right)$. Figure 7.6 shows the fit of nuclear broadening data in the *octet* picture using the

---

[7]By considering $p_\perp = 0$ GeV and $\langle y \rangle$=-3.5, $x_2 \sim 0.1$ and at $p_\perp = 20$ GeV, $x_2 \sim 0.8$. This $p_\perp$ region embracing both antishadowing effect mainly at small $p_\perp$ and EMC effect at large $p_\perp$.

[8]All the data used are in this regime, except the LHC data at forward rapidity.

[9]Typically, $Q_0^2 = 1 - 2$ GeV^2.
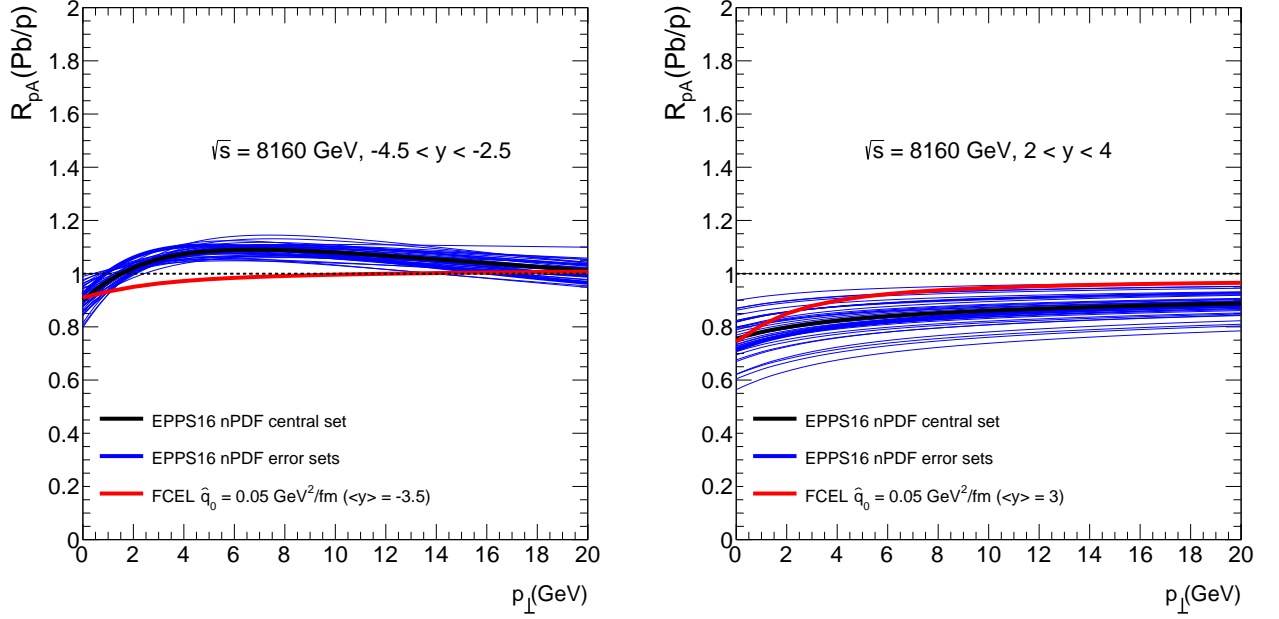
Figure 7.5: $R_{pA}^{J/\psi}(Pb/p)$ as a function of $p_\perp$ calculated with the EPPS16 nPDF and FCEL effects at $\sqrt{s}$ = 8160 GeV in backward, $-4.5 < y < -2.5$, (left panel) and forward, $2 < y < 4$ (right panel) rapidity.

CT14 PDF[10] set at LO [28]. The best agreement is found using a value of $\lambda \approx 2.5$ (χ^2/ndf=1.2). The value of the transport coefficient at $x = 10^{-2}$ obtained, $\hat{q}_0 = 0.049 \pm 0.002$ GeV^2/fm, is compatible with the previous estimate by using a simple parameterization of $xG(x) \propto x^{-\alpha}$.

In addition, a fit of the gluon distribution $xG(x)$ evaluated at $Q^2 \sim 2.5\ \Delta p_\perp^2$, with $\Delta p_\perp^2$ at LHC forward rapidity ~ 2 GeV^2, is performed at small x, $10^{-6} < x < 10^{-4}$, as illustrated in Fig. 7.6 (right panel). The slope obtained is slightly below 0.25, $xG(x) \propto x^{-0.18\pm0.05}$. It is also compatible with $\hat{q}(x_2) \propto x_2^{-0.17}$ from [161].

7.6 R_{pA} as a function of $p_\perp$ in the Drell-Yan process

7.6.1 Model

The R_{hA} ratio as a function of $p_\perp$ can be determined by incorporating the nuclear transverse broadening effect in the hp[11] cross section. The simple differential cross section in hp collisions as a function of $p_\perp$ can be parameterized as

$$\frac{d\sigma_{hp}}{d^2\vec{p}_\perp} = \mathcal{N} \times \left(\frac{p_0^2}{p_0^2 + p_\perp^2}\right)^m \equiv \mathcal{N} \times \mu(p_\perp). \tag{7.21}$$

By using Eq. (7.21), R_{hA} as a function of $p_\perp$ reads [129],

$$R_{hA}^{\text{Broadening}}(p_\perp) = \int_0^{2\pi} \frac{d\varphi}{2\pi} \frac{\mu(|\vec{p}_\perp - \Delta\vec{p}_\perp|)}{\mu(p_\perp)}, \tag{7.22}$$

---

[10]Q_0^2 is equal to 1.69 GeV^2 for CT14 proton PDF.

[11]Or in hA collisions, where A is a light nucleus in order to minimise nuclear effects
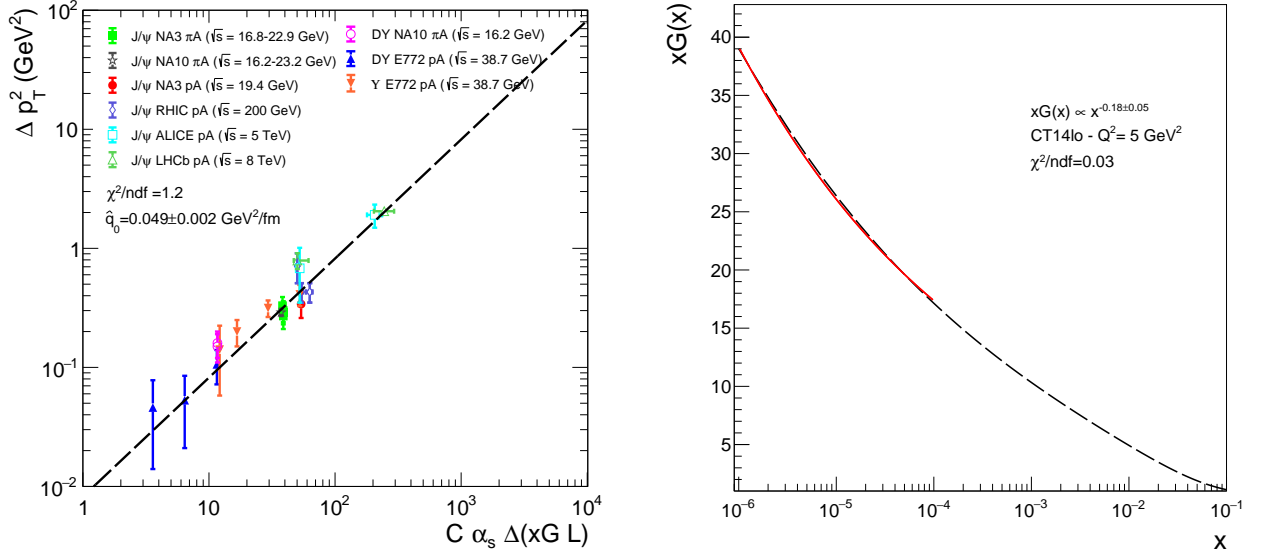
Figure 7.6: Scaling of the nuclear $p_\perp$-broadening in DY and quarkonium production using the CT14 LO gluon distribution (left panel). Fit of the gluon distribution $xG(x)$ between $10^{-6} < x_2 < 10^{-4}$ using CT14 PDF set at LO [28] (right panel)

where φ is the azimutal angle integrated between $\vec{p_\perp}$ and $\Delta \vec{p}_\perp$.[12] The nPDF effect is also taken into account. The DY cross section at LO in pA collisions is sensitive to the $\bar{u}(x_2)$ quarks nPDF. In π^-A collisions, it sensitive to the the $u(x_2)$ quarks nPDF (see Sec. 2.1.3). R_{hA} as a function of $p_\perp$ are respectively defined like

$$R_{pA}^{nPDF}(p_\perp) \approx \frac{\bar{u}^A(x_2(p_\perp), Q^2)}{\bar{u}^B(x_2(p_\perp), Q^2)} \qquad (7.23)$$

and

$$R_{\pi^-A}^{nPDF}(p_\perp) \approx \frac{u^A(x_2(p_\perp), Q^2)}{u^B(x_2(p_\perp), Q^2)}, \qquad (7.24)$$

where $Q^2 = \left(\sqrt{M^2 + p_\perp^2} + p_\perp\right)^2$ and $x_2(p_\perp)$ is calculated using the typical value of $\langle x_2 \rangle$. Because when $p_\perp \lesssim M$, $x_2 \propto Q$ slightly depends on the $p_\perp$ value. In the next section, R_{pA} as a function of $p_\perp$ including the broadening and nPDF effects will be compared to the DY data from E866/NueSea at $E_{beam} = 800$ GeV ($\sqrt{s} = 38.7$ GeV) [124], to recent data from PHENIX at $\sqrt{s} = 200$ GeV [124] and from preliminary COMPASS data at $E_{beam} = 190$ GeV ($\sqrt{s} = 18.9$ GeV) obtained in Chap. 5.

7.6.2 E866/NuSea experiment

In order to calculate the transverse momentum broadening effect, the reference absolute cross section as a function of $p_\perp$ is determined by E772 experiment in pp collisions at the same dimuon mass domain and beam energy as the E866/NuSea experiment. The fit using the Kaplan parametrisation function from Eq. (7.8) is shown in Fig. 7.7. The fit results are shown in Table 7.9. Figure 7.8 shows the comparison between the calculation of the broadening effect.[13]

---

[12]The nuclear broadening effect doesn't have a privileged direction in the φ plane.

Figure 7.7: Fit of the absolute cross section as a function of $p_\perp$ from E722 experiment integrated in $5 < M < 6$ GeV dimuon invariant mass range.

for R_{pA} (Fe/Be) and R_{pA} (W/Be). In both cases, the best χ^2/ndf value (1.2 for Fe/W ratio and 1.5 for W/Be ratio) is obtained by using the transport coefficient value $\hat{q}_0 = 0.09$ GeV^2/fm. This value is higher compared to the value extracted in Fig. 7.2.

In addition, an estimation of $\bar{u}$ quarks nPDF effect on these data by using the central set from EPPS16 nPDF[14] is also shown. The calculation exhibits an nPDF effect lower than 5%.

7.6.3 PHENIX experiment

PHENIX experiment collected DY data in pp and dAu collisions at $\sqrt{s} = 200$ GeV [162]. The integrated dimuon mass range is $4.8 < M < 8.2$ GeV. The absolute cross section as a function of $p_\perp$ in pp collisions is fitted using the Kaplan function in Eq. (7.8) as illustrated in 7.9. Figure 7.10 shows the comparison between the calculation of the broadening effect and Au/p DY nuclear production ratio from PHENIX experiment as a function of $p_\perp$ at forward rapditiy[15], $1.2 < y < 2.2$. The best χ^2/ndf value (1.6) is obtained with $\hat{q}_0 = 0.09$ GeV^2/fm. However, the experimental errors bar are too large to conclude. In addition, the nPDF effect is more pronounced in comparison to E866 experiment case for several reasons. First, in the case of E866 experiment, we calculated the ratio of two nuclei whose nPDF central sets are totally correlated, so the final nuclear effect will be weaker. The data from E866 cover mainly te antishadowing region, $R_{pA} \sim 1$.

---

[13]Here, the reference target is a light nucleus (Be) The broadening effect due to this target is not negligible and is taken into account in the calculation via $\Delta p_\perp^2 \propto (\hat{q}_A L_A - \hat{q}_B L_{Be})$.

[14]The mean x_2 value in E866/NuSea DY data is $\langle x_2 \rangle = 0.038$ [124].

[15]The x_2 mean value is $\langle x_2 \rangle = 0.005$.
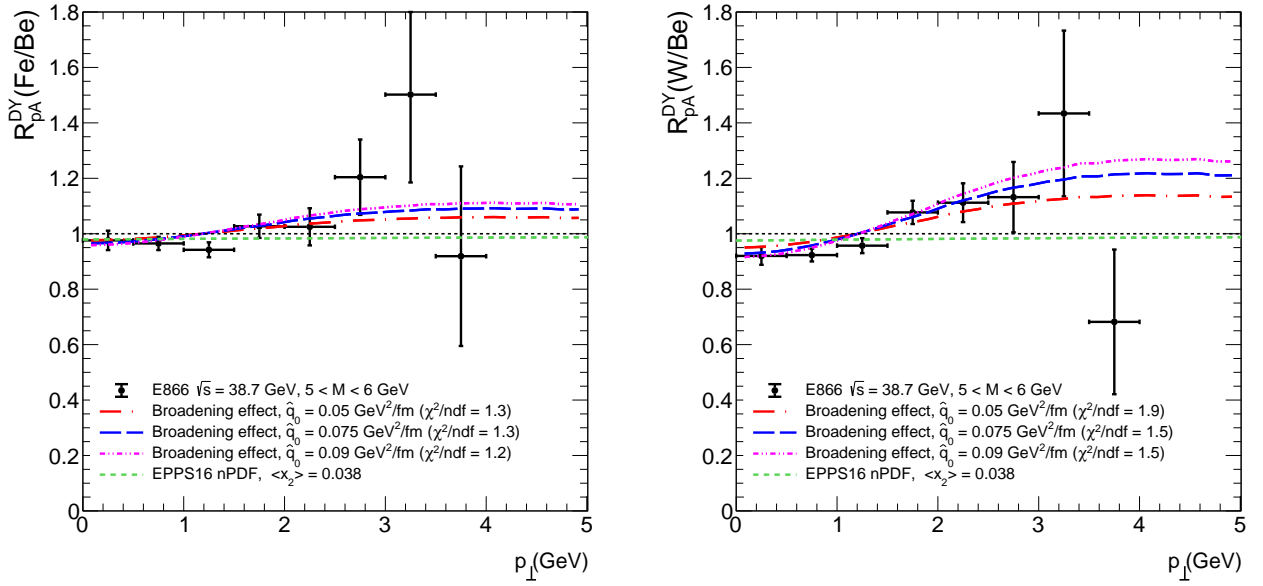
Figure 7.8: Comparison between DY R_{pA} as a function of $p_\perp$ from E866/NuSea experiment for Fe/Be (left panel) and W/Be (right panel) ratios with the broadening calculation using $\hat{q}_0 \in (0.05, 0.075, 0.09)$ GeV^2/fm and the nPDF effect using the central set from EPPS16.
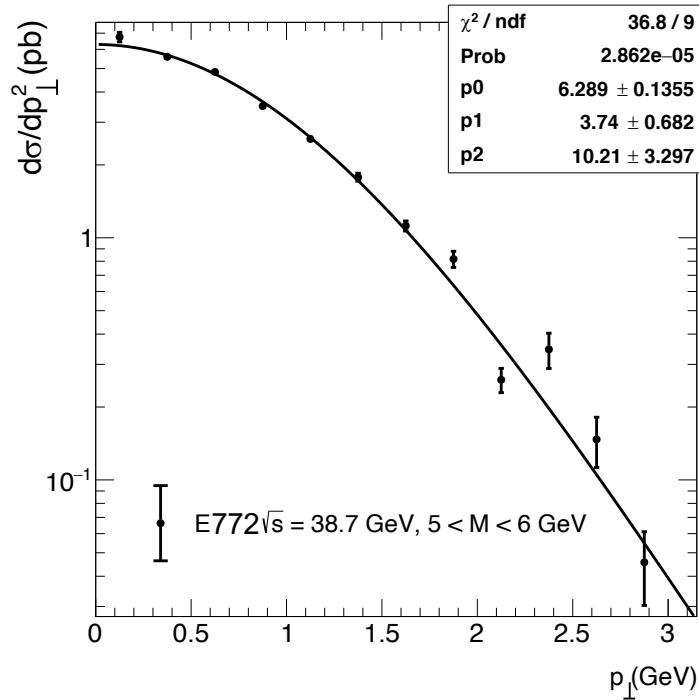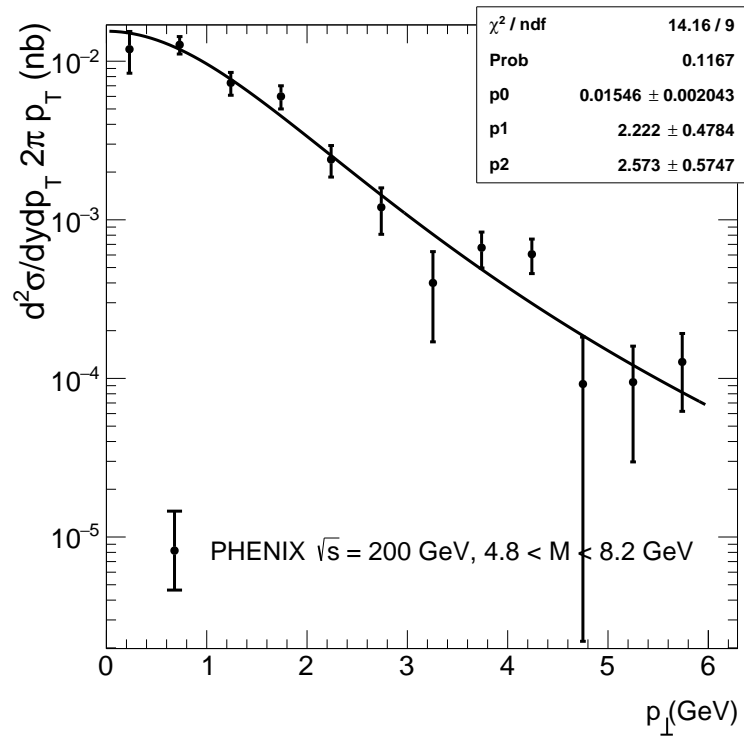

Figure 7.9: Fit of absolute cross section as a function of $p_\perp$ from PHENIX experiment integrated in $4.8 < M < 8.2$ GeV dimuon invariant mass range at forward rapidity $1.2 < y < 2.2$.

In contrast, the mean value $\langle x_2 \rangle = 0.005$ enables to probe at PHENIX experiment the shadowing region, $R_{pA} \lesssim 1$. The nPDF effect therefore contributes for about $\sim 20\%$ to the R_{pA} calculation.
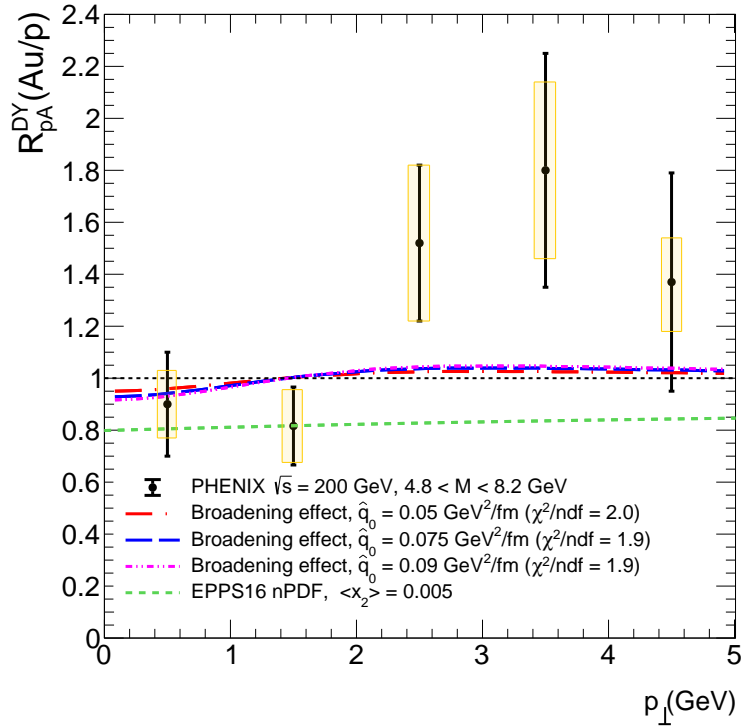
Figure 7.10: Comparison between DY R_{pA} as a function of $p_\perp$ from PHENIX experiment for Au/d ratio with the broadening using $\hat{q}_0 \in (0.05, 0.075, 0.09)$ GeV^2/fm and the nPDF effect using the central set from EPPS16.

7.6.4 COMPASS experiment

COMPASS experiment measured preliminary W/Al nuclear production ratio as a function of $p_\perp$ in $\pi^- $A collisions at $\sqrt{s} = 18.9$ GeV (see Chap. 5). The integrated dimuon mass range is $4.7 < M < 8.5$ GeV. The comparison between $R_{\pi^- \mathrm{A}}$ as a function of $p_\perp$ from the COMPASS data, the broadening effect using $\hat{q}_0$=(0.05,0.075,0.09) GeV^2/fm and the nPDF effect using the central set from EPPS16 is shown in Fig. 7.11. The normalization of the $R_{\pi^- \mathrm{A}}$ as a function of $p_\perp$ from the data is in below the theoretical prediction by $\sim 20\%$. This discrepancy is not visible in the value of the nuclear broadening extracted in Sec. 7.3.2 because its value is independent of the normalization of the $R_{\pi^- \mathrm{A}}$ (see Eq. (7.6)).

Exp.	$\sqrt{s}$ (GeV)	p_0 (GeV)	m	χ^2/ndf
COMPASS	18.9	2.9 ± 0.2	7.0 ± 0.7	1.4
E772	37.8	3.7 ± 0.7	10.2 ± 3.3	4.1
PHENIX	200	2.2 ± 0.5	2.6 ± 0.6	1.6

Table 7.9: Fit results of the DY absolute cross section as a function of $p_\perp$.
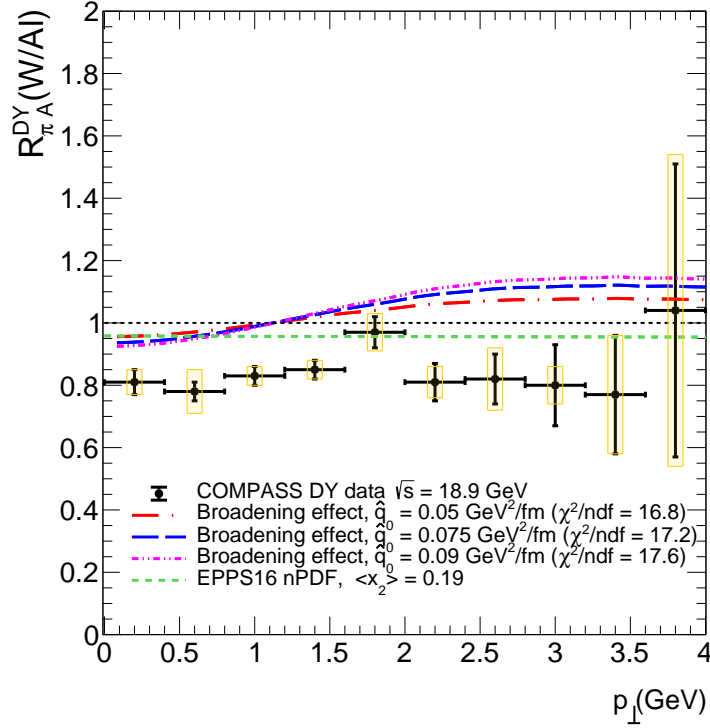
Figure 7.11: Comparison between DY R_{pA} as a function of $p_\perp$ from the COMPASS experiment for W/Al ratio with the broadening using $\hat{q}_0 \in (0.05, 0.075, 0.09)$ GeV^2/fm and the nPDF effect using the central set from EPPS16.

7.7 Conclusion

The nuclear broadening effect of the DY and quarkonium processes in pA and πA collisions has been systematically investigated. The validity of the model was tested via the assumptions made on the color factors, the x-dependence of the transport coefficient and the different nuclei analysed. The main conclusions are

- Despite a factor of 400 between the $\sqrt{s}$ value of SPS and LHC, a remarkable scaling is found. This made it possible to precisely extract a value of the transport coefficient $\hat{q}_0$ with a good χ^2/ndf ($\hat{q}_0 = 0.051 \pm 0.02$ in *octet* picture and $\hat{q}_0 = 0.075 \pm 0.03$ in *singlet* picture);

- Furthermore, thanks to the nuclear broadening data from PHENIX and LHC experiments, the x-dependence of the transport coefficient has been constrained. Based on the assumptions about the dominant color states in quarkonia production, a slope of $xGx \propto x^{-\alpha}$ with $\alpha = 0.25$-0.30 was found. This slope is compatible with the results from previous studies [161, 163];

- The preliminary COMPASS data from the DY and J/ψ processes are consistent with the value of the transport coefficient extracted via the global analysis of nuclear broadening data;

- The $p_\perp$ dependence of R_{hA} has also been investigated. A compatibility was found between the broadening calculation using $\hat{q}_0$=(0.05,0.075,0.09) GeV^2/fm transport coefficient interval and the DY data at E866, PHENIX and COMPASS experiments. A weak nPDF effect is observed as a function of $p_\perp$ at E866 and COMPASS experiments. A more pronounced effect is shown at PHENIX experiment due to the strong shadowing effect at $x_2 \sim 0.005$.

8

Conclusion

Thirty years after the last data collected in πA published by the NA10 experiment, preliminary data from the 2018 run as a function of x_{F} and $p_\perp$ of the Drell-Yan (DY) and J/ψ processes from the COMPASS experiment on two nuclear targets, W and Al, were analyzed. From the signal extraction to the evaluation of cross sections, including Monte Carlo simulations, each step of the experimental analysis have been presented. Using a multidimensional analysis and simulating each physical process participating in the dimuon mass spectrum, the evolution of the J/ψ number as a function of x_{F} and $p_\perp$ was quantified in $\pi^- \mathrm{W}$ and $\pi^- \mathrm{Al}$ collisions.

These preliminary J/ψ data, collected in a large amount, highlight a strong suppression of the cross section in both $p_\perp$ and x_{F} variables in the $\pi^- \mathrm{W}$ collisions compared to the $\pi^- \mathrm{Al}$ collisions. *A contrario*, preliminary DY data show less suppression. $R_{\pi^- \mathrm{A}}^{\mathrm{DY}}(\mathrm{W/Al})$ ratio exhibits a slight depletion at large x_{F} and a Cronin peak at $p_\perp = $ 1-2 GeV. Due to large experimental errors, the latter is compatible with $\Delta p_\perp^2 = 0$. In both analyzes, the calculation of the value of the nuclear transverse momentum broadening shows a compatibility with previous experiments, $\Delta p_\perp^2(J/\psi) = 0.21 \pm 0.04$ GeV^2 and $\Delta p_\perp^2(\mathrm{DY}) = 0.03 \pm 0.04$ GeV^2.

The cold nuclear matter effects in the DY and quarkonium productions as a function of the rapidity and transverse momentum from fixed-target to collider energies was investigated. In two phenomenological studies Refs. [1] and [2], the first one is a study of the initial-state energy loss effects in DY data from fixed target experiments. For the first time, the preliminary data from the Fermilab E906/SeaQuest experiment demonstrate, without ambiguity, an energy loss effect in pA collisions in DY data.

Finally, the second one is a study of the nuclear transverse momentum dependence in the DY and quarkonium production highlights a unique effect present at all collisions energies: nuclear broadening. A precise extraction of the transport coefficient has been performed

using color and octet quarkonium production assumption. The latter is compatible with the previous radiative energy loss studies.

The interpretation of nuclear data in hA collisions is limited by the size of the uncertainties in nPDF effect. The measurement of Deep Inelastic scattering (DIS) data proposed by the Electron-Ion-Collider (EIC) collaboration should add constrains on the nPDF allowing to considerably reduce their error bands [93, 94]. Future DY data at low beam energy ($E_{beam} \lesssim 100$ GeV) can bring constraints on the transport coefficient. Indeed, at these energies, the initial-state energy loss effect dominates the ratio of nuclear DY cross sections as a function of x_F. Using a proton beam versus a pion beam leads to a stronger effects.

Bibliography

[1] F. Arleo, C.-J. Naïm and S. Platchkov, *Initial-state energy loss in cold QCD matter and the Drell-Yan process*, *JHEP* **01** (2019) 129 [1810.05120].

[2] F. Arleo and C.-J. Naïm, *Nuclear $p_\perp$-broadening of Drell-Yan and quarkonium production from SPS to LHC*, *JHEP* **07** (2020) 220 [2004.07188].

[3] F. Arleo and S. Peigne, *J/ψ suppression in p-A collisions from parton energy loss in cold QCD matter*, *Phys. Rev. Lett.* **109** (2012) 122301 [1204.4609].

[4] F. Arleo and S. Peigné, *Heavy-quarkonium suppression in pA collisions from parton energy loss in cold QCD matter*, *JHEP* **03** (2013) 122 [1212.0434].

[5] J. H. Christenson, G. S. Hicks, L. M. Lederman, P. J. Limon, B. G. Pope et al., *Observation of massive muon pairs in hadron collisions*, *Phys. Rev. Lett.* **25** (1970) 1523.

[6] J. H. Christenson, G. S. Hicks, L. M. Lederman, P. J. Limon, B. G. Pope et al., *Observation of muon pairs in high-energy hadron collisions*, *Phys. Rev. D* **8** (1973) 2016.

[7] S. D. Drell and T.-M. Yan, *Massive Lepton Pair Production in Hadron-Hadron Collisions at High-Energies*, *Phys. Rev. Lett.* **25** (1970) 316.

[8] F. Ravndal, *Feynman and the quark model*, *Int. J. Mod. Phys. A* **8** (1993) 4369.

[9] **E598** collaboration, J. Aubert et al., *Experimental Observation of a Heavy Particle J*, *Phys. Rev. Lett.* **33** (1974) 1404.

[10] **SLAC-SP-017** collaboration, J. Augustin et al., *Discovery of a Narrow Resonance in e^+e^- Annihilation*, *Phys. Rev. Lett.* **33** (1974) 1406.

[11] J. D. Bjorken, ed., *In Conclusion: A Collection of Summary Talks in High Energy Physics*. 2003.

[12] S. Ting, *The Discovery of the J Particle: A Personal Recollection*, *Rev. Mod. Phys.* **49** (1977) 235.

[13] G. Abrams et al., *The Discovery of a Second Narrow Resonance in e+ e- Annihilation*, *Phys. Rev. Lett.* **33** (1974) 1453.

[14] J. D. Bjorken, *CURRENT ALGEBRA AT SMALL DISTANCES, Conf. Proc.* **C670717** (1967) 55.

[15] H. D. Politzer, *Reliable Perturbative Results for Strong Interactions?*, *Phys. Rev. Lett.* **30** (1973) 1346.

[16] D. J. Gross and F. Wilczek, *Ultraviolet Behavior of Nonabelian Gauge Theories*, *Phys. Rev. Lett.* **30** (1973) 1343.

[17] **H1** collaboration, F. Aaron et al., *Inclusive Deep Inelastic Scattering at High Q^2 with Longitudinally Polarised Lepton Beams at HERA*, *JHEP* **09** (2012) 061 [`1206.7007`].

[18] **CTEQ** collaboration, R. Brock et al., *Handbook of perturbative QCD: Version 1.0*, *Rev. Mod. Phys.* **67** (1995) 157.

[19] L. N. Lipatov, *The parton model and perturbation theory, Sov. J. Nucl. Phys.* **20** (1975) 94.

[20] V. N. Gribov and L. N. Lipatov, *Deep inelastic e p scattering in perturbation theory, Sov. J. Nucl. Phys.* **15** (1972) 438.

[21] S. Catani and M. Grazzini, *Collinear factorization and splitting functions for next-to-next-to-leading order QCD calculations*, *Phys. Lett.* **B446** (1999) 143 [`hep-ph/9810389`].

[22] S. Moch, J. A. M. Vermaseren and A. Vogt, *The three-loop splitting functions in QCD: The non-singlet case*, *Nucl. Phys.* **B688** (2004) 101 [`hep-ph/0403192`].

[23] A. Vogt, S. Moch and J. A. M. Vermaseren, *The three-loop splitting functions in QCD: The singlet case*, *Nucl. Phys.* **B691** (2004) 129 [`hep-ph/0404111`].

[24] G. Altarelli and G. Parisi, *Asymptotic Freedom in Parton Language*, *Nucl. Phys. B* **126** (1977) 298.

[25] R. Field, *Applications of Perturbative QCD*, vol. 77. 1989.

[26] L. A. Harland-Lang, A. D. Martin, P. Motylinski and R. S. Thorne, *Parton distributions in the LHC era: MMHT 2014 PDFs*, *Eur. Phys. J.* **C75** (2015) 204 [`1412.3989`].

[27] D. Stump et al., *Inclusive jet production, parton distributions, and the search for new physics*, *JHEP* **10** (2003) 046 [`hep-ph/0303013`].

[28] S. Dulat, T.-J. Hou, J. Gao, M. Guzzi, J. Huston et al., *New parton distribution functions from a global analysis of quantum chromodynamics*, *Phys. Rev.* **D93** (2016) 033006 [`1506.07443`].

[29] **NNPDF** collaboration, R. D. Ball et al., *Parton distributions from high-precision collider data*, *Eur. Phys. J. C* **77** (2017) 663 [`1706.00428`].

[30] P. Sutton, A. D. Martin, R. Roberts and W. Stirling, *Parton distributions for the pion extracted from Drell-Yan and prompt photon experiments*, *Phys. Rev. D* **45** (1992) 2349.

[31] **NA10** collaboration, B. Betev et al., *Differential Cross-section of High Mass Muon Pairs Produced by a 194-GeV/cπ⁻ Beam on a Tungsten Target*, *Z. Phys.* **C28** (1985) 9.

[32] J. S. Conway et al., *Experimental Study of Muon Pairs Produced by 252-GeV Pions on Tungsten*, *Phys. Rev.* **D39** (1989) 92.

[33] **WA70** collaboration, E. Bonvin et al., *DOUBLE PROMPT PHOTON PRODUCTION AT HIGH TRANSVERSE MOMENTUM BY pi- ON PROTONS AT 280-GeV/c*, *Z. Phys.* **C41** (1989) 591.

[34] M. Glück, E. Reya and A. Vogt, *Pionic parton distributions*, *Z. Phys.* **C53** (1992) 651.

[35] M. Gluck, E. Reya and I. Schienbein, *Pionic parton distributions revisited*, *Eur. Phys. J. C* **10** (1999) 313 [`hep-ph/9903288`].

[36] **ZEUS** collaboration, S. Chekanov et al., *Leading neutron production in e+ p collisions at HERA*, *Nucl. Phys.* **B637** (2002) 3 [`hep-ex/0205076`].

[37] **H1** collaboration, F. D. Aaron et al., *Measurement of Leading Neutron Production in Deep-Inelastic Scattering at HERA*, *Eur. Phys. J.* **C68** (2010) 381 [`1001.0532`].

[38] P. C. Barry, N. Sato, W. Melnitchouk and C.-R. Ji, *First Monte Carlo Global QCD Analysis of Pion Parton Distributions*, *Phys. Rev. Lett.* **121** (2018) 152001 [`1804.01965`].

[39] I. R. Kenyon, *The Drell-Yan Process*, *Rept. Prog. Phys.* **45** (1982) 1261.

[40] Y. L. Dokshitzer, V. A. Khoze, A. H. Mueller and S. Troian, *Basics of perturbative QCD*. 1991.

[41] R. Ellis, W. Stirling and B. Webber, *QCD and collider physics*, vol. 8. Cambridge University Press, 2, 2011.

[42] R. Baier, Y. L. Dokshitzer, A. H. Mueller and D. Schiff, *Quenching of hadron spectra in media*, *JHEP* **09** (2001) 033 [`hep-ph/0106347`].

[43] S. Catani, L. Cieri, G. Ferrera, D. de Florian and M. Grazzini, *Vector boson production at hadron colliders: a fully exclusive QCD calculation at NNLO*, *Phys. Rev. Lett.* **103** (2009) 082001 [`0903.2120`].

[44] **PHENIX** collaboration, C. Aidala et al., *Measurements of $\mu\mu$ pairs from open heavy flavor and Drell-Yan in $p + p$ collisions at $\sqrt{s} = 200$ GeV*, *Phys. Rev. D* **99** (2019) 072003 [`1805.02448`].

[45] S. Gavin et al., *Production of the Drell-Yan pairs in high-energy nucleon- nucleon collisions*, *Int. J. Mod. Phys.* **A10** (1995) 2961 [`hep-ph/9502372`].

[46] Y. L. Dokshitzer, D. Diakonov and S. I. Troian, *Hard Processes in Quantum Chromodynamics*, *Phys. Rept.* **58** (1980) 269.

[47] J. C. Collins, D. E. Soper and G. F. Sterman, *Transverse Momentum Distribution in Drell-Yan Pair and W and Z Boson Production*, *Nucl. Phys.* **B250** (1985) 199.

[48] S. Catani, D. de Florian, G. Ferrera and M. Grazzini, *Vector boson production at hadron colliders: transverse-momentum resummation and leptonic decay*, *JHEP* **12** (2015) 047 [`1507.06937`].

[49] M. Kramer, *Charmonium production at high-energy colliders*, *Pramana* **51** (1998) 145.

[50] R. Vogt, *The x_F dependence of ψ and Drell-Yan production*, *Phys. Rev.* **C61** (2000) 035203 [`hep-ph/9907317`].

[51] Y.-Q. Ma and R. Vogt, *Quarkonium Production in an Improved Color Evaporation Model*, *Phys. Rev.* **D94** (2016) 114029 [`1609.06042`].

[52] C.-H. Chang, *Hadronic production of J/ψ associated with a gluon*, *Nucl. Phys.* **B172** (1980) 425.

[53] J. Lansberg, *J/ψ production at sqrt(s)=1.96 and 7 TeV: Color-Singlet Model, NNLO* and polarisation*, *J. Phys. G* **38** (2011) 124110 [`1107.0292`].

[54] G. T. Bodwin, E. Braaten and G. P. Lepage, *Rigorous QCD analysis of inclusive annihilation and production of heavy quarkonium*, *Phys. Rev.* **D51** (1995) 1125 [`hep-ph/9407339`].

[55] W. Buchmuller and S. H. H. Tye, *Quarkonia and Quantum Chromodynamics*, *Phys. Rev.* **D24** (1981) 132.

[56] E. J. Eichten and C. Quigg, *Quarkonium wave functions at the origin: an update*, `1904.11542`.

[57] **CDF** collaboration, F. Abe et al., *J/ψ and $\psi(2S)$ production in $p\bar{p}$ collisions at $\sqrt{s} = 1.8$ TeV*, *Phys. Rev. Lett.* **79** (1997) 572.

[58] P. Nason et al., *Bottom production*, in *1999 CERN Workshop on standard model physics (and more) at the LHC, CERN, Geneva, Switzerland, 25-26 May: Proceedings*, pp. 231–304, 1999, `hep-ph/0003142`.

[59] F. Maltoni et al., *Analysis of charmonium production at fixed-target experiments in the NRQCD approach*, *Phys. Lett.* **B638** (2006) 202 [`hep-ph/0601203`].

[60] **NuSea** collaboration, J. Webb et al., *Absolute Drell-Yan dimuon cross-sections in 800 GeV / c pp and pd collisions*, `hep-ex/0302019`.

[61] **CMS** collaboration, A. M. Sirunyan et al., *Measurement of the differential Drell-Yan cross section in proton-proton collisions at $\sqrt{s}$ = 13 TeV*, *JHEP* **12** (2019) 059 [`1812.10529`].

[62] **ATLAS** collaboration, G. Aad et al., *Measurement of the Z/γ^* boson transverse momentum distribution in pp collisions at $\sqrt{s}$ = 7 TeV with the ATLAS detector*, *JHEP* **09** (2014) 145 [`1406.3660`].

[63] **CMS** collaboration, V. Khachatryan et al., *Measurement of the transverse momentum spectra of weak vector bosons produced in proton-proton collisions at $\sqrt{s}$ = 8 TeV*, *JHEP* **02** (2017) 096 [`1606.05864`].

[64] **PHENIX** collaboration, U. Acharya et al., *J/ψ and $\psi(2S)$ production at forward rapidity in p+p collisions at $\sqrt{s}$ = 510 GeV*, *Phys. Rev. D* **101** (2020) 052006 [`1912.13424`].

[65] **PHENIX** collaboration, S. Adler et al., *J/ψ production from proton proton collisions at $\sqrt{s}$ = 200-GeV*, *Phys. Rev. Lett.* **92** (2004) 051802 [`hep-ex/0307019`].

[66] **PHENIX** collaboration, A. Adare et al., *Ground and excited charmonium state production in $p + p$ collisions at $\sqrt{s}$ = 200 GeV*, *Phys. Rev. D* **85** (2012) 092004 [`1105.1966`].

[67] **LHCb** collaboration, R. Aaij et al., *Measurement of J/ψ production in pp collisions at $\sqrt{s}$ = 7 TeV*, *Eur. Phys. J. C* **71** (2011) 1645 [`1103.0423`].

[68] **LHCb** collaboration, R. Aaij et al., *Production of J/psi and Upsilon mesons in pp collisions at sqrt(s) = 8 TeV*, *JHEP* **06** (2013) 064 [`1304.6977`].

[69] **NuSea** collaboration, E. Hawker et al., *Measurement of the light anti-quark flavor asymmetry in the nucleon sea*, *Phys. Rev. Lett.* **80** (1998) 3715 [`hep-ex/9803011`].

[70] K. Kovarik et al., *nCTEQ15 - Global analysis of nuclear parton distributions with uncertainties in the CTEQ framework*, *Phys. Rev.* **D93** (2016) 085037 [`1509.00792`].

[71] **SeaQuest** collaboration, C. Aidala et al., *The SeaQuest Spectrometer at Fermilab*, *Nucl. Instrum. Meth. A* **930** (2019) 49 [`1706.09990`].

[72] B. P. Dannowitz, *Nuclear Dependence of Proton-Induced Drell-Yan Dimuon Production at 120 GeV at Seaquest*, Ph.D. thesis, Illinois U., Urbana, 2016. 10.2172/1294515.

[73] **NuSea** collaboration, L. Zhu et al., *Measurement of Υ Production for $p + p$ and $p + d$ Interactions at 800 GeV/c*, *Phys. Rev. Lett.* **100** (2008) 062301 [`0710.2344`].

[74] A. Martin, W. Stirling, R. Thorne and G. Watt, *Parton distributions for the LHC*, *Eur. Phys. J.* **C63** (2009) 189 [`0901.0002`].

[75] **European Muon** collaboration, J. J. Aubert et al., *The ratio of the nucleon structure functions F_{2n} for iron and deuterium*, *Phys. Lett.* **B123** (1983) 275.

[76] **CLAS** collaboration, B. Schmookler et al., *Modified structure of protons and neutrons in correlated pairs*, *Nature* **566** (2019) 354.

[77] D. de Florian, R. Sassot, P. Zurita and M. Stratmann, *Global Analysis of Nuclear Parton Distributions*, *Phys. Rev.* **D85** (2012) 074028 [`1112.6324`].

[78] K. J. Eskola, P. Paakkinen, H. Paukkunen and C. A. Salgado, *EPPS16: Nuclear parton distributions with LHC data*, *Eur. Phys. J.* **C77** (2017) 163 [`1612.05741`].

[79] **PHENIX** collaboration, S. S. Adler et al., *Centrality dependence of pi0 and eta production at large transverse momentum in $\sqrt{s_{NN}} = $200 GeV dAu collisions*, *Phys. Rev. Lett.* **98** (2007) 172302 [`nucl-ex/0610036`].

[80] **STAR** collaboration, B. I. Abelev et al., *Inclusive π^0, η, and direct photon production at high transverse momentum in $p + p$ and $d+Au$ collisions at $\sqrt{s_{NN}} = 200$ GeV*, *Phys. Rev.* **C81** (2010) 064904 [`0912.3838`].

[81] **CMS** collaboration, V. Khachatryan et al., *Study of W boson production in pPb collisions at $\sqrt{s_{NN}} = 5.02$ TeV*, *Phys. Lett.* **B750** (2015) 565 [`1503.05825`].

[82] **CMS** collaboration, V. Khachatryan et al., *Study of Z boson production in pPb collisions at $\sqrt{s_{NN}} = 5.02$ TeV*, *Phys. Lett.* **B759** (2016) 36 [`1512.06461`].

[83] **ATLAS** collaboration, G. Aad et al., *Z boson production in p+Pb collisions at $\sqrt{s_{NN}} = 5.02$ TeV measured with the ATLAS detector*, *Phys. Rev.* **C92** (2015) 044915 [`1507.06232`].

[84] **CMS** collaboration, S. Chatrchyan et al., *Studies of dijet transverse momentum balance and pseudorapidity distributions in pPb collisions at $\sqrt{s_{NN}} = 5.02$ TeV*, *Eur. Phys. J.* **C74** (2014) 2951 [`1401.4433`].

[85] **E772** collaboration, D. M. Alde et al., *Nuclear dependence of dimuon production at 800 GeV in the E772 experiment*, *Phys. Rev. Lett.* **64** (1990) 2479.

[86] **E866** collaboration, M. J. Leitch et al., *Measurement of differences between J/ψ and ψ' suppression in pA collisions*, *Phys. Rev. Lett.* **84** (2000) 3256 [`nucl-ex/9909007`].

[87] **NA3** collaboration, J. Badier et al., *Test of nuclear effects in hadronic dimuon production*, *Phys. Lett.* **B104** (1981) 335.

[88] **NA10** collaboration, P. Bordalo et al., *Nuclear Effects on the Nucleon Structure Functions in Hadronic High Mass Dimuon Production*, *Phys. Lett.* **B193** (1987) 368.

[89] J. Heinrich et al., *Measurement of the Ratio of Sea to Valence Quarks in the Nucleon*, *Phys. Rev. Lett.* **63** (1989) 356.

[90] K. J. Eskola, H. Paukkunen and C. A. Salgado, *EPS09 - a New Generation of NLO and LO Nuclear Parton Distribution Functions*, *JHEP* **04** (2009) 065 [`0902.4154`].

[91] K. J. Eskola, I. Helenius, P. Paakkinen and H. Paukkunen, *A QCD analysis of LHCb D-meson data in p+Pb collisions*, `1906.02512`.

[92] R. Sassot, M. Stratmann and P. Zurita, *Fragmentations Functions in Nuclear Media*, *Phys. Rev. D* **81** (2010) 054001 [`0912.1311`].

[93] A. Deshpande, R. Milner, R. Venugopalan and W. Vogelsang, *Study of the fundamental structure of matter with an electron-ion collider*, *Ann. Rev. Nucl. Part. Sci.* **55** (2005) 165 [`hep-ph/0506148`].

[94] A. Accardi et al., *Electron Ion Collider: The Next QCD Frontier*, *Eur. Phys. J.* **A52** (2016) 268 [`1212.1701`].

[95] F. Karsch and H. Satz, *The Spectral analysis of strongly interacting matter*, *Z. Phys.* **C51** (1991) 209.

[96] H. Satz, *Colour deconfinement and quarkonium binding*, *J. Phys.* **G32** (2006) R25 [`hep-ph/0512217`].

[97] T. Matsui and H. Satz, *J/ψ suppression by Quark–Gluon plasma formation*, *Phys. Lett.* **B178** (1986) 416.

[98] A. Capella, J. A. Casado, C. Pajares, A. V. Ramallo and J. Tran Thanh Van, *Nuclear effects in J/ψ suppression*, *Phys. Lett.* **B206** (1988) 354.

[99] F. Arleo and V.-N. Tram, *A systematic study of J/ψ suppression in cold nuclear matter*, *Eur. Phys. J.* **C55** (2008) 449 [`hep-ph/0612043`].

[100] V.-N. Tram and F. Arleo, *Global analysis of J/ψ suppression in cold nuclear matter*, *Eur. Phys. J.* **C61** (2009) 847 [`0907.0043`].

[101] A. Majumder and M. Van Leeuwen, *The Theory and Phenomenology of Perturbative QCD Based Jet Quenching*, *Prog. Part. Nucl. Phys.* **66** (2011) 41 [`1002.2206`].

[102] Y. Mehtar-Tani, J. G. Milhano and K. Tywoniuk, *Jet physics in heavy-ion collisions*, *Int. J. Mod. Phys.* **A28** (2013) 1340013 [`1302.2579`].

[103] N. Armesto and E. Scomparin, *Heavy-ion collisions at the Large Hadron Collider: a review of the results from Run 1*, *Eur. Phys. J. Plus* **131** (2016) 52 [`1511.02151`].

[104] G.-Y. Qin and X.-N. Wang, *Jet quenching in high-energy heavy-ion collisions*, *Int. J. Mod. Phys.* **E24** (2015) 1530014 [`1511.00790`].

[105] R. Baier, Y. L. Dokshitzer, A. H. Mueller, S. Peigné and D. Schiff, *Radiative energy loss of high energy quarks and gluons in a finite-volume quark-gluon plasma*, *Nucl. Phys.* **B483** (1997) 291 [`hep-ph/9607355`].

[106] R. Baier, Y. L. Dokshitzer, A. H. Mueller, S. Peigné and D. Schiff, *Radiative energy loss and $p_\perp$ broadening of high energy partons in nuclei*, *Nucl. Phys.* **B484** (1997) 265 [`hep-ph/9608322`].

[107] F. Arleo and S. Peigné, *Quarkonium suppression from coherent energy loss in fixed-target experiments using LHC beams*, *Adv. High Energy Phys.* **2015** (2015) 961951 [`1504.07428`].

[108] P. Arnold, G. D. Moore and L. G. Yaffe, *Photon emission from ultrarelativistic plasmas*, *JHEP* **11** (2001) 057 [`hep-ph/0109064`].

[109] P. Arnold, G. D. Moore and L. G. Yaffe, *Photon and gluon emission in relativistic plasmas*, *JHEP* **06** (2002) 030 [`hep-ph/0204343`].

[110] R. Baier, Y. L. Dokshitzer, A. H. Mueller and D. Schiff, *Medium induced radiative energy loss: Equivalence between the BDMPS and Zakharov formalisms*, *Nucl. Phys.* **B531** (1998) 403 [`hep-ph/9804212`].

[111] M. Gyulassy, P. Levai and I. Vitev, *NonAbelian energy loss at finite opacity*, *Phys. Rev. Lett.* **85** (2000) 5535 [`nucl-th/0005032`].

[112] M. Gyulassy, P. Levai and I. Vitev, *Jet quenching in thin quark gluon plasmas. 1. Formalism*, *Nucl. Phys.* **B571** (2000) 197 [`hep-ph/9907461`].

[113] M. Gyulassy, P. Levai and I. Vitev, *Reaction operator approach to nonAbelian energy loss*, *Nucl. Phys.* **B594** (2001) 371 [`nucl-th/0006010`].

[114] U. A. Wiedemann, *Gluon radiation off hard quarks in a nuclear environment: Opacity expansion*, *Nucl. Phys.* **B588** (2000) 303 [`hep-ph/0005129`].

[115] U. A. Wiedemann, *Jet quenching versus jet enhancement: A quantitative study of the bdmps-z gluon radiation spectrum*, *Nucl. Phys.* **A690** (2001) 731 [`hep-ph/0008241`].

[116] X. Guo and X.-N. Wang, *Multiple scattering, parton energy loss and modified fragmentation functions in deeply inelastic e a scattering*, *Phys. Rev. Lett.* **85** (2000) 3591 [`hep-ph/0005044`].

[117] X.-N. Wang and X.-f. Guo, *Multiple parton scattering in nuclei: Parton energy loss*, *Nucl. Phys.* **A696** (2001) 788 [`hep-ph/0102230`].

[118] P.-J. Lin, *Measurement of Quark Energy Loss in Cold Nuclear Matter at Fermilab E906/SeaQuest*, Ph.D. thesis, Colorado U., 2017. 10.2172/1398791.

[119] **COMPASS** collaboration, M. Aghasyan et al., *First measurement of transverse-spin-dependent azimuthal asymmetries in the Drell-Yan process*, *Phys. Rev. Lett.* **119** (2017) 112002 [`1704.00488`].

[120] **NA3** collaboration, J. Badier et al., *Experimental J/ψ Hadronic Production from 150 GeV/c to 280 GeV/c*, *Z. Phys.* **C20** (1983) 101.

[121] **NA3** collaboration, J. Badier et al., *MEASUREMENT OF THE TRANSVERSE MOMENTUM OF DIMUONS PRODUCED BY HADRONIC INTERACTIONS AT 150-GEV/C, 200-GEV/C AND 280-GEV/C*, *Phys. Lett.* **117B** (1982) 372.

[122] **NA10** collaboration, P. Bordalo et al., *OBSERVATION OF A NUCLEAR DEPENDENCE OF THE TRANSVERSE MOMENTUM DISTRIBUTION OF MASSIVE MUON PAIRS PRODUCED IN HADRONIC COLLISIONS*, *Phys. Lett.* **B193** (1987) 373.

[123] P. L. McGaughey, J. M. Moss and J. C. Peng, *High-energy hadron induced dilepton production from nucleons and nuclei*, *Ann. Rev. Nucl. Part. Sci.* **49** (1999) 217 [`hep-ph/9905409`].

[124] **E866** collaboration, M. A. Vasilev et al., *Parton energy loss limits and shadowing in Drell-Yan dimuon production*, *Phys. Rev. Lett.* **83** (1999) 2304 [`hep-ex/9906010`].

[125] **PHENIX** collaboration, A. Adare et al., *Transverse-Momentum Dependence of the J/ψ Nuclear Modification in dAu Collisions at $\sqrt{s_{NN}}$ = 200 GeV*, *Phys. Rev.* **C87** (2013) 034904 [`1204.0777`].

[126] **ALICE** collaboration, J. Adam et al., *Centrality dependence of inclusive J/ψ production in p-Pb collisions at $\sqrt{s_{\mathrm{NN}}}$ = 5.02 TeV*, *JHEP* **11** (2015) 127 [`1506.08808`].

[127] **ALICE** collaboration, M. Tarhini, *Charmonium production in Pb–Pb and p–Pb collisions at forward rapidity measured with ALICE*, *Nucl. Phys. A* **967** (2017) 588.

[128] **LHCb** collaboration, R. Aaij et al., *Prompt and nonprompt J/ψ production and nuclear modification in pPb collisions at* $\sqrt{s_{NN}} = 8.16$ *TeV*, *Phys. Lett. B* **774** (2017) 159 [1706.07122].

[129] F. Arleo, R. Kolevatov, S. Peigné and M. Rustamova, *Centrality and* $p_\perp$ *dependence of J/ψ suppression in proton-nucleus collisions from parton energy loss*, *JHEP* **05** (2013) 155 [1304.0901].

[130] **NA58 Collaboration** collaboration, G. Baum, J. Kyynäräinen and A. Tripet, *COMPASS: a proposal for a common muon and proton apparatus for structure and spectroscopy*, Tech. Rep. CERN-SPSLC-96-14. SPSLC-P-297, CERN, Geneva, 1996.

[131] G. Baum, J. Kyynäräinen and A. Tripet, *COMPASS: Common Muon and Proton Apparatus for Structure and Spectroscopy; Add. 1*, Tech. Rep. CERN-SPSLC-96-30. SPSLC-P-297-Add-1, CERN, Geneva, 1996.

[132] **COMPASS** collaboration, F. Gautheron et al., *COMPASS-II Proposal*, .

[133] H. W. Atherton, C. Bovet, N. T. Doble, L. Piemontese, A. Placci et al., *Precise measurements of particle production by 400 GeV/c protons on beryllium targets*, CERN Yellow Reports: Monographs. CERN, Geneva, 1980, 10.5170/CERN-1980-007.

[134] **COMPASS** collaboration, P. Abbon et al., *The COMPASS experiment at CERN*, *Nucl. Instrum. Meth. A* **577** (2007) 455 [hep-ex/0703049].

[135] R. Longo, *Measurement of spin effects in the Drell-Yan process at the COMPASS experiment*, Ph.D. thesis, Turin U., 2018.

[136] **Particle Data Group** collaboration, M. Tanabashi et al., *Review of Particle Physics*, *Phys. Rev. D* **98** (2018) 030001.

[137] P. Lösel and R. Müller, *Design and construction of large size micromegas chambers for the upgrade of the ATLAS muon spectrometer*, .

[138] F. Thibaud et al., *Performance of large pixelised Micromegas detectors in the COMPASS environment*, *JINST* **9** (2014) C02005.

[139] J. Marroncle, *La grande chambre à dérive DC4*, *Saclay* (2008) .

[140] *Experimental determination of the townsend coefficient for argon-co2 gas mixtures at high fields*, .

[141] G. Braun et al., *F1: An Eight channel time to digital converter chip for high rate experiments*, in *5th Workshop on Electronics for the LHC Experiments (LEB 99)*, pp. 383–387, 9, 1999, `hep-ex/9911009`.

[142] T. Sjostrand, S. Mrenna and P. Z. Skands, *A Brief Introduction to PYTHIA 8.1*, *Comput. Phys. Commun.* **178** (2008) 852 [`0710.3820`].

[143] A. Ito et al., *Measurement of the Continuum of Dimuons Produced in High-Energy Proton - Nucleus Collisions*, *Phys. Rev. D* **23** (1981) 604.

[144] M. B. Johnson, B. Z. Kopeliovich, I. K. Potashnikova, P. L. McGaughey, J. M. Moss et al., *Energy loss versus shadowing in the Drell-Yan reaction on nuclei*, *Phys. Rev.* **C65** (2002) 025203 [`hep-ph/0105195`].

[145] R. Neufeld, I. Vitev and B.-W. Zhang, *A possible determination of the quark radiation length in cold nuclear matter*, *Phys.Lett.* **B704** (2011) 590 [`1010.3708`].

[146] L.-H. Song and L.-W. Yan, *Constraining the transport coefficient in cold nuclear matter with the Drell-Yan process*, *Phys. Rev.* **C96** (2017) 045203.

[147] F. Arleo, *Constraints on quark energy loss from Drell-Yan data*, *Phys. Lett.* **B532** (2002) 231 [`hep-ph/0201066`].

[148] F. Arleo, *Tomography of cold and hot QCD matter: Tools and diagnosis*, *JHEP* **11** (2002) 044 [`hep-ph/0210104`].

[149] C. A. Salgado and U. A. Wiedemann, *Calculating quenching weights*, *Phys. Rev.* **D68** (2003) 014008 [`hep-ph/0302184`].

[150] S. Catani and M. Grazzini, *An NNLO subtraction formalism in hadron collisions and its application to Higgs boson production at the LHC*, *Phys. Rev. Lett.* **98** (2007) 222002 [`hep-ph/0703012`].

[151] K. J. Golec-Biernat and M. Wüsthoff, *Saturation effects in deep inelastic scattering at low Q^2 and its implications on diffraction*, *Phys. Rev.* **D59** (1998) 014017 [`hep-ph/9807513`].

[152] F. Arleo and S. Peigné, *Quarkonium suppression in heavy-ion collisions from coherent energy loss in cold nuclear matter*, *JHEP* **10** (2014) 73 [`1407.5054`].

[153] J. Pumplin, D. Stump, R. Brock, D. Casey, J. Huston et al., *Uncertainties of predictions from parton distribution functions. 2. The Hessian method*, *Phys. Rev. D* **65** (2001) 014013 [`hep-ph/0101032`].

[154] C. Hadjidakis et al., *Physics opportunities with a fixed target experiment at the LHC (AFTER@LHC)*, *PoS* **PSTP2017** (2018) 035.

[155] **CMS Collaboration** collaboration, *Differential measurements of the Drell–Yan process in the muon channel in pPb collisions at $\sqrt{s_{NN}}$ = 8.16 TeV*, Tech. Rep. CMS-PAS-HIN-18-003, CERN, Geneva, 2020.

[156] P. Paakkinen, K. J. Eskola and H. Paukkunen, *Applicability of pion nucleus Drell-Yan data in global analysis of nuclear parton distribution functions*, *Phys. Lett.* **B768** (2017) 7 [1609.07262].

[157] **Saclay-CERN-College de France-Ecole Poly-Orsay** collaboration, J. Badier et al., *Measurement of the K^-/π^- Structure Function Ratio Using the Drell-Yan Process*, *Phys. Lett. B* **93** (1980) 354.

[158] M. Aicher, A. Schafer and W. Vogelsang, *Soft-gluon resummation and the valence parton distribution function of the pion*, *Phys. Rev. Lett.* **105** (2010) 252003 [1009.2481].

[159] I. Novikov et al., *Parton Distribution Functions of the Charged Pion Within The xFitter Framework*, 2002.02902.

[160] F. Cougoulic and S. Peigné, *Nuclear $p_\perp$-broadening of an energetic parton pair*, 1712.01953.

[161] P. Ru, Z.-B. Kang, E. Wang, H. Xing and B.-W. Zhang, *A global extraction of the jet transport coefficient in cold nuclear matter*, 1907.11808.

[162] Y. H. Leung, *PHENIX measurements of charm, bottom, and Drell-Yan via dimuons in p+p and p+Au collisions at $\sqrt{s_{\mathrm{NN}}}$ = 200 GeV*, *PoS* **HardProbes2018** (2019) 160.

[163] K. J. Golec-Biernat and M. Wusthoff, *Saturation in diffractive deep inelastic scattering*, *Phys. Rev.* **D60** (1999) 114023 [hep-ph/9903358].

Titre: Effets de la matière nucléaire froide dans le processus Drell-Yan et la production de J/ψ

Mots clés: Chromodynamique quantique, production de paires de letpons, interaction hadron-hadron, structure des hadrons, nPDF, perte d'énergie, charmonium, Drell-Yan

Résumé: Le phénomène de perte d'énergie des quarks et des gluons se propageant dans un milieu en interaction forte a été mis en évidence pour la première fois dans les collisions d'ions lourds par les expériences auprès des accélérateurs RHIC et LHC. Une autre manière de sonder les propriétés de la matière nucléaire est d'étudier la production de processus durs dans les collisions hadron-noyau. En effet, dans ce cas, le milieu nucléaire est simple : sa densité ainsi que sa taille sont connues. Dans cette thèse, le processus Drell-Yan et la production de J/ψ ont été étudiés à travers une analyse expérimentale et phénoménologique. La collaboration COMPASS au CERN a collecté un nombre significatif d'événements Drell-Yan et J/ψ en utilisant un faisceau de pions négatifs d'énergie égale à 190 GeV sur deux cibles nucléaires : aluminium (Al) et tungstène (W). De l'analyse des événements à l'extraction des rapports des sections efficaces nucléaires, en passant par l'analyse Monte-Carlo, cette thèse décrit chaque étape de l'analyse expérimentale. Enfin, une analyse basée sur l'ensemble des données DY et J/ψ existantes, incluant celles de l'expérience COMPASS, a permis de réaliser une extraction précise des propriétés de transport de la matière nucléaire froide.

Title: Cold nuclear matter effects in Drell-Yan process and J/ψ production

Keywords: Quantum chromodynamics, lepton pair production, hadron-hadron collisions, hadron structure, nPDF, energy loss, charmonium, Drell-Yan

Abstract: The Jet Quenching phenomenon observed in the heavy ions collisions at the LHC and RHIC made it possible to highlight the radiation energy loss effects of quarks and gluons propagating in a QCD medium. Another way to the properties of the nuclear matter is to consider the production of hard processes in hadron-nuclei collisions. In this case, the nuclear medium, the cold nuclear matter, is simple; its density and size are known. The Drell-Yan process and charmonium production are investigated in this thesis through an experimental and phenomenological study. The COMPASS collaboration at CERN collected the Drell-Yan and J/ψ events in high statistics in pion-nuclei collisions on two nuclear targets: tungsten (W) and aluminium (Al). From the signal extraction to the evaluation of nuclear dependence of the cross sections, including Monte Carlo simulations, each step of the experimental analysis is discussed. Finally, a global analysis of the Drell-Yan and J/ψ nuclear world data, including the COMPASS preliminary data, was performed. It highlighted the radiative energy loss and transverse momentum broadening effects. A precise extraction of the properties of the transport in the nuclear matter was carried-out.